

Tetrathiafulvalene and 2,2'-Bipyridine: Bridging both Worlds in the Pursuit of Novel Molecular Materials

Roger Gumbau-Brisa

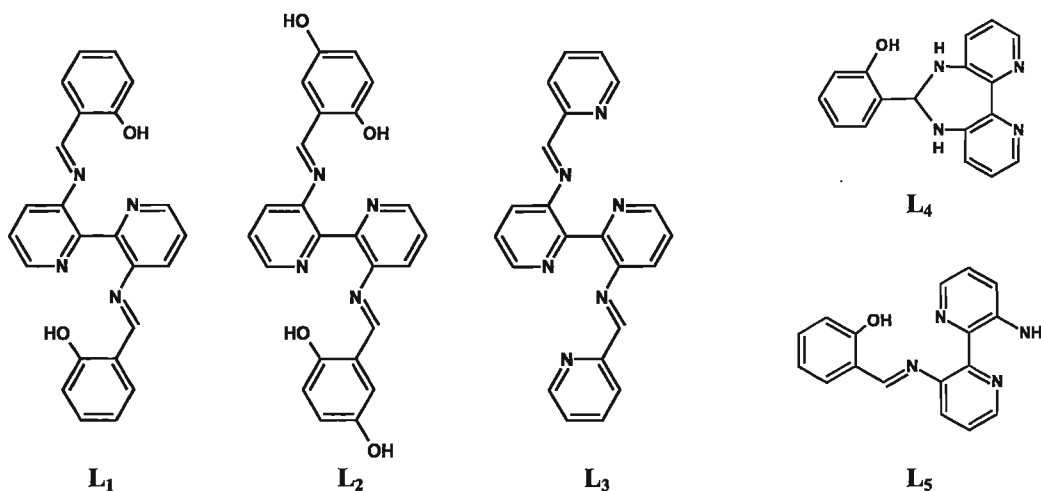
Thesis submitted to the Department of Chemistry in partial fulfillment of the
requirements for the degree of Doctor of Philosophy

Supervised By
Professor Melanie Pilkington
Brock University
St. Catharines, Ontario, Canada
June 2012

© Roger Gumbau-Brisa, 2012

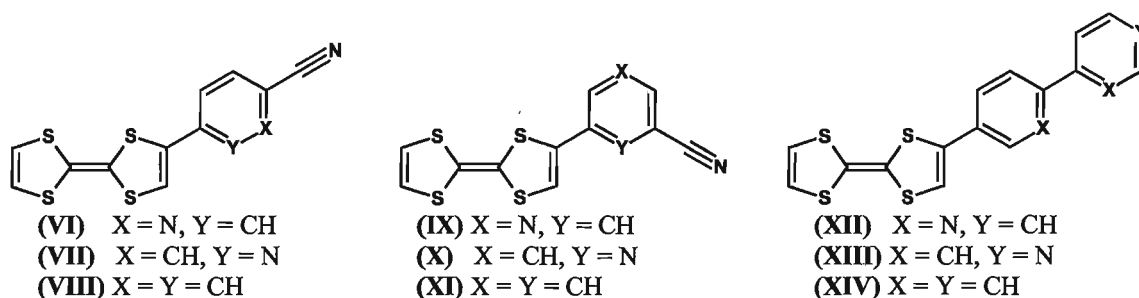
Abstract

The preparation and characterization of two families of building blocks for molecule-based magnetic and conducting materials are described in three projects. In the first project the synthesis and characterization of three *bis*-imine ligands **L**₁ – **L**₃ is reported. Coordination of **L**₁ to a series of metal salts afforded the five novel coordination complexes Sn(**L**₄)Cl₄ (**I**), [Mn(**L**₄)(μ-Cl)(Cl)(EtOH)]₂ (**II**), [Cu(**L**₄)(μ-sal)]₂(ClO₄)₂ (sal = salicylaldehyde anion) (**III**), [Fe(**L**₅)₂]Cl (**IV**) and [Fe(**L**₁)₂(μ-O) (**V**). All complexes have been structurally and magnetically characterized. X-ray diffraction studies revealed that, upon coordination to Lewis acidic metal salts, the imine bonds of **L**₁ are susceptible to nucleophilic attack. As a consequence, the coordination complexes (**I**) – (**IV**) contain either the cyclised ligand **L**₄ or hydrolysed ligand **L**₅.

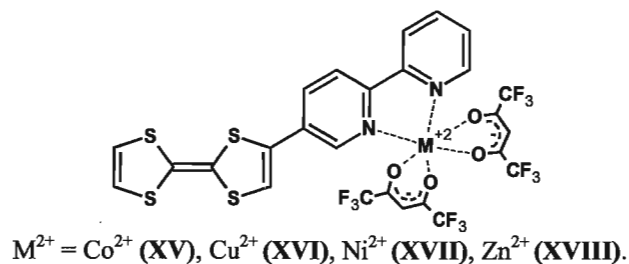


In contrast, the dimeric Fe³⁺ complex (**V**) comprises two intact ligand **L**₁ molecules. In this complex, the ligand chelates two Fe(III) centres in a *bis*-bidentate manner through the lone pairs of a phenoxy oxygen and an imine nitrogen atom. Magnetic studies of complexes (**II**-**V**) indicate that the dominant interactions between neighbouring metal centres in all of the complexes are antiferromagnetic.

In the second project the synthesis and characterization two families of TTF donors, namely the cyano aryl compounds (VI) - (XI) and the *bis*-aryl TTF derivatives (XII) - (XIV) are reported. The crystal structures of compounds (VI), (VII), (IX) and (XII) exhibit regular stacks comprising of neutral donors. The UV-Vis spectra of compounds (VI) - (XIV) present an ICT band, indicative of the transfer of electron density from the TTF donors to the aryl acceptor molecules.



Chemical oxidation of donors (VI), (VII), (IX) and (XII) with iodine afforded a series of CT salts that where possible have been characterized by single crystal X-ray diffraction. Structural studies showed that the radical cations in these salts are organized in stacks comprising of dimers of oxidized TTF donors. All four salts behave as semiconductors, displaying room temperature conductivities ranging from 1.852×10^{-7} to $9.620 \times 10^{-3} \text{ S cm}^{-1}$. A second series of CT salts were successfully prepared via the technique of electrocrystallization. Following this methodology, single crystals of two CT salts were obtained. The single crystal X-ray structures of both salts are isostructural, displaying stacks formed by trimers of oxidized donors. Variable temperature conductivity measurements carried out on this series of CT salts reveal they also are semiconductors with conductivities ranging from 2.94×10^{-7} to $1.960 \times 10^{-3} \text{ S cm}^{-1}$ at room temperature.



In the third project the synthesis and characterization of a series of $M^{II}(hfac)_2$ coordination complexes of donor ligand **(XII)** where $M^{2+} = Co^{2+}$, Cu^{2+} , Ni^{2+} and Zn^{2+} are reported. These complexes crystallize in a head-to-tail arrangement of TTF donor and bipyridine moieties, placing the metal centres and hfac ligands are located outside the stacks. Magnetic studies of the complexes **(XV)** - **(XVIII)** indicate that the bulky hfac ligands prevent neighbouring metal centres from assembling in close proximity, and thus they are magnetically isolated.

Acknowledgements

There are many people who have been important in the completion of this thesis. Although I mention a number of people below, please don't be offended if your name is not among them. The contribution of many people cannot be explicitly stated, but rather they were part of the positive environment and human interaction necessary to help this thesis crystallize (and keep its author sane). I would like to express my gratitude to those of you who fall within this category.

In first place I would like to thank Prof. Pilkington for her help and guidance during this thesis. I would also like to thank her for letting me take care and play around with the X-ray diffractometer. I am also indebted to Prof. van der Est and Prof. Lemaire for their advice through my thesis and for answering with patience all my (sometimes vague and random) questions. I would also like to acknowledge Prof. Gordon for joining my supervisory committee in the very last stage of my thesis and for her kindness and advice through my years at Brock University.

I must express my most sincere gratitude to Tim Jones and Razvan Siminoescu for their efforts finding my products. Without their assistance this thesis would've been much shorter. I would like to thank Dr. Poddutoori and Sam Mula for collecting the EPR spectra of my products. I would also like apologize for not showing any of them in my thesis. X-ray crystallography is not an easy subject, and I must acknowledge the help received from Prof. Wallis and Dr. Britten in this topic. I would also like to thank Prof. Murugesu, Prof. Rawson, Dr. Alberola, and the Razavi group for their help with the SQUID experiments, and for the helpful discussions about the results. The conductivity measurements would've not been possible without the assistance of Prof. Turner, and I would like to express my most sincere gratitude for his work.

The members of the Pilkington group have been my family at Brock University. They have my endless gratitude for enduring me over the years and for being my friends. In particular, the desire to have twenty(!) wives and his love for calimochos certainly made Roland Acha the spice of the group. I would like to thank Dr. Wang for sharing his

experimental expertise and smooth sense of humour. I would also like to thank Shari Venneri and Nick Hurley for adding their Canadian point of view to the Pilkington melting pot of cultures. And last but not least, I would like to express my gratitude Emma Gavey for taking part on the somewhat shocking, but always hilarious conversations about unexpected and controversial topics we had during the endless hours we spent in the lab.

I must thank the Spares family for their help in far too many aspects of my life in Canada to recount here. You guys know everything you have done for me, and if anyone else wants to know I'll just bring them to one of your family parties.

The foundations of who I am can only be traced back to my parents and my brothers. From them I have learned more than I can recall, and they helped me shape the person I am today. Although geographically distant, their constant support and advice have been instrumental in reaching this point in my life. I cannot express with words how grateful I am to them for being there for me over the years.

I would like to thank my wife Heather for waiting patiently outside my Ph.D. bubble, and for reminding me from time to time that I have a life with her in the outside world. This thesis would've never materialized without her love and support.

Finally, I would like to thank my most gifted undergraduate students, for asking if the water is boiling.

Table of Contents

Abstract.....	i
Acknowledgments.....	iv
Table of Contents.....	vi
List of Figures.....	x
List of Tables.....	xx
List of Schemes.....	xxiii
List of Abbreviations.....	xxv
List of Compounds.....	xxviii
Table of Atomic Colours.....	xxxii
CHAPTER 1 - Introduction to molecular magnetism and multifunctional materials.....	1
1.1 Introduction	1
1.2 Introduction to magnetism	1
1.2.1 A macroscopic view of magnetism.....	1
1.2.2 Molecular magnetism.....	3
1.3 Introduction to ligand design for molecular materials	12
1.3.1 Hexacyanometalates.....	12
1.3.2 Ligand design applied to the derivatization of 2,2'-bipyridine.....	19
1.3.3 Strategies for the preparation of magnetic and conductive molecular materials	37
1.4 Organization of this thesis.....	59
CHAPTER 2 - Novel bis-imine ligands for magnetic molecular materials.....	60
2.1 Introduction	60

2.2	Synthesis and characterization of the <i>bis</i> -imine ligands	61
2.2.1	Synthesis of the <i>bis</i> -imine ligands	61
2.2.2	Spectroscopic characterization of ligands 2.2 and 2.3	62
2.2.3	X-ray characterization of the <i>bis</i> -imine ligands 1.40 , 2.2 and 2.3	63
2.3	Coordination chemistry of the <i>bis</i> -imine ligand 2.2	69
2.3.1	Synthesis and characterization of complex 2.4	70
2.3.2	Synthesis and characterization of complex 2.6	73
2.3.3	Synthesis and characterization of complex 2.7	80
2.3.4	Synthesis and characterization of complex 2.8	85
2.3.5	Synthesis and characterization of complex 2.11	89
2.4	Conclusions	93
CHAPTER 3 - Preparation and characterization of a family of π-extended TTF derivatives and their CT salts		95
3.1	Introduction	95
3.2	Preparation and characterization of novel cyanoaryl derivatives of TTF	98
3.2.1	Synthesis of 3.2-3.5	98
3.2.2	Single-crystal X-ray characterization of cyanopyridyl derivatives	100
3.2.3	Spectroscopic characterization	113
3.2.4	Electrochemical characterization	117
3.3	Novel π -extended <i>bis</i> -aryl TTF systems: rational ligand design for the preparation of magnetic hybrid electrical conductors.	118
3.3.1	Synthesis of 3.8-3.10	118
3.3.2	Spectroscopic characterization	122
3.3.3	Electrochemical characterization	123
3.4	Synthesis and characterization of charge transfer salts	124
3.4.1	Oxidation of 3.2 , 3.3 and 3.8 with I ₂	127
3.4.2	Electrochemical synthesis of CT salts	129

3.4.3	X-ray characterization of CT salts 3.15 and 3.16	130
3.4.4	Additional characterization of CT salts of cyanopyridyl donors	141
3.4.5	X-ray characterization of CT salts 3.17 , 3.21 , 3.22	144
3.4.6	Additional characterization of the CT salts 3.19-3.22	156
3.5	Conclusions	157
CHAPTER 4 - Synthesis and characterization of a family of electroactive TTF-based transition metal complexes.....		159
4.1	Introduction	159
4.2	Coordination of 3.8 and characterization of complexes 4.1-4.4	160
4.2.1	Coordination of 3.8	160
4.2.2	Single-crystal X-ray diffraction	161
4.2.3	Spectroscopic characterization.....	175
4.2.4	Electrochemical characterization	177
4.2.5	Magnetic characterization	177
4.3	Conclusions	181
CHAPTER 5 - Summary and conclusions.....		183
CHAPTER 6 - Experimental.....		186
6.1	General considerations	186
6.2	Instrumentation.....	186
6.3	Experimental for Chapter 2	188
6.3.1	Synthesis of 3,3'-diamino-2,2'-bipyridine.....	188
6.3.2	Synthesis of <i>E,E</i> -N3,N3'-Bis(2-pyridylmethylene)-(2,2'-bipyridine)-3,3'-diamine (1.40)	188
6.3.3	Synthesis of <i>E,E</i> -N3,N3'-Bis(phenol-2-ylmethylene)-(2,2'-bipyridine)-3,3'-diamine (2.2)	189
6.3.4	Synthesis of <i>E,E</i> -N3,N3'-Bis(phen-1,4-diol-2-ylmethylene)-(2,2'-bipyridine)-3,3'-diamine (2.3)	190

6.3.5	Synthesis of complex $\text{Sn}(\mathbf{2.5})\text{Cl}_4$ (2.4)	191
6.3.6	Synthesis of complex $[\text{Mn}(\mathbf{2.5})\text{Cl}(\mu\text{-Cl})\text{OHEt}]_2$ (2.6)	192
6.3.7	Synthesis of complex $[\text{Cu}(\mathbf{2.5})(\mu\text{-salald})]_2(\text{ClO}_4)_2$ (2.7).....	193
6.3.8	Synthesis of complex $[\text{Fe}(\mathbf{2.9})_2]\text{Cl}$ (2.8)	194
6.3.9	Synthesis of complex $\text{Fe}_2(\mathbf{2.2})_2(\mu\text{-O})$ (2.11)	195
6.4	Experimental for Chapter 3	196
6.4.1	Synthesis of tetrathiafulvalene, TTF (1.47)	196
6.4.2	General procedure for the preparation of TTF-cyanopyridines 3.2-3.5	196
6.4.3	Synthesis of stannyl-tetrathiafulvalene (3.11)	201
6.4.4	General procedure for the preparation of TTF-benzonitriles 3.6, 3.7	201
6.4.5	Synthesis of 4-bromo-2,2'-bipyridine (3.12)	204
6.4.6	Synthesis of 5-(2-(1,3-dithiol-2-ylidene)-1,3-dithiol-4-yl)-2,2'-bipyridine (3.8).....	205
6.4.7	Synthesis of 4-(p-bromophenyl)pyridine (3.13)	206
6.4.8	Synthesis of 4-{4-(2-(1,3-dithiol-2-ylidene)-1,3-dithiol-4-yl)phenyl}pyridine (3.9).....	206
6.4.9	Synthesis of 4-(biphenyl-4-yl)-2-(1,3-dithiol-2-ylidene)-1,3-dithiole (3.10).....	207
6.4.10	General procedure for the preparation of single crystals of CT salts	208
6.4.11	General procedures for the preparation CT salts as powders	208
6.5	Experimental for Chapter 4	216
6.5.1	General procedure for the preparation of complexes 4.1-4.4	216
CHAPTER 7 - References		220
Appendix A - Crystallographic tables		238

List of Figures

Figure 1.1 Magnetic field lines for a) paramagnet and b) diamagnet.	2
Figure 1.2 Schematic illustration of spin interactions for the four most common types of magnetic behaviours: a) paramagnetic, b) ferromagnetic, c) antiferromagnetic, d) ferrimagnetic.	4
Figure 1.3 Plot of $1/\chi$ vs. T for Curie and Curie-Weiss magnetic behaviour.....	5
Figure 1.4 Plot of χT vs. T for paramagnetic, ferromagnetic, antiferromagnetic and ferrimagnetic behaviour.....	5
Figure 1.5 Diagram showing magnetic domains in a ferromagnet. The arrows indicate the orientation of the magnetic moment of each domain.	7
Figure 1.6 Schematic representation of a hysteresis loop.....	8
Figure 1.7 Crystal field splitting for an octahedral coordination geometry.....	8
Figure 1.8 Spectrochemical series showing a small set of ligands. Ligand field increases from left to right.....	9
Figure 1.9 Diagram of the electron distribution for an Fe^{2+} ion in high and low spin states.	9
Figure 1.10 Diagram showing five possible spin transition curves for SCO systems in the solid state: (a) gradual; (b) abrupt; (c) with hysteresis; (d) with steps; (e) incomplete. γ_{HS} corresponds to the molar fraction of high spin state complexes in the sample. Figure adapted from reference ⁶ with permission.....	10
Figure 1.11 a) Structure of Mn_{12} SMM, b) double well of spin states. Adapted with permission from ¹⁶ . Copyright 2003 American Chemical Society.	11
Figure 1.12 Schematic representation of the crystal structure of a prussian blue analog. Reprinted from ³⁷ with permission from Elsevier.....	13
Figure 1.13 Structures of ligands 1.1 , bpm, cyclam and treten (top row) and examples of their coordination modes (bottom row). L represents a labile ligand(s). .	14
Figure 1.14 Isomers Δ and Λ of a <i>tris</i> -oxalate complex.....	16

Figure 1.15 a) 2-D honeycomb layer of <i>tris</i> -oxalate metal complexes, b) 3-D decagon cavity of <i>tris</i> -oxalate metal complexes. Metal centres are shown as light blue balls, oxalate ligands are shown as black sticks.	16
Figure 1.16 The family of bipyridine regioisomers.	19
Figure 1.17 Potential a) symmetrical and b) asymmetrical binding modes of 3,3'-disubstituted 2,2'-bipyridine.	21
Figure 1.18 Partial structure of complexes 1.13 and 1.14 . Carbon atoms are white spheres, nitrogen atoms are striped spheres, oxygen atoms are dotted spheres and ruthenium atoms are large spheres. Adapted from reference ⁷³ - Reproduced by permission of The Royal Society of Chemistry.	22
Figure 1.19 Molecular structure of a fragment of the 1-D chains of the cerium nitrate complex of ligand 1.11 . Nitrate counterions and water molecules shown as a wireframe for simplicity. Hydrogen atoms are omitted for simplicity.	23
Figure 1.20 Crystal structure of the isostructural trinuclear clusters 1.15 and 1.16 alkoxides. The alkoxide ligands are shown as a grey sticks. Hydrogen atoms are omitted for clarity.	23
Figure 1.21 Molecular structure of the coordination polymer of 1.18 , a) the coordination environment of one ligand, b) view of copper chain, c) packing diagram viewed down the <i>b</i> -axis. Hydrogen atoms are omitted for clarity.	25
Figure 1.22 a) Typical structure of a <i>tris</i> -chelated 1.12 metal complex. b) Best plane of the pyridine ring shown in green.	29
Figure 1.23 A structural overlay of the two ligands and Cu ²⁺ atoms obtained from the crystal structures 1.45 (red) and 1.46 (green).	36
Figure 1.24 Packing diagram of the TTF-TCNQ CT salt viewed down the <i>c</i> -axis.	38
Figure 1.25 Molecular structures of TTF and some common derivatives.	39
Figure 1.26 Temperature dependence of the resistance of (BEDT-TTF) ₄ (H ₂ O)Fe(C ₂ O ₄) ₃ ·C ₆ H ₅ CN for the 5-200 K range. Adapted with permission from ¹¹¹ . Copyright 1995 American Chemical Society.	40
Figure 1.27 Crystal structure of (BEDT-TTF) ₃ [CrMn(ox) ₃]. a) View of the [CrMn(ox) ₃] ⁻ network layers. The filled and open circles represent the	

two types of metals. b) Slanted stacks of 1.49 forming layers. c) View along the <i>c</i> -axis of the alternating layers. Reprinted with permission from Macmillan Publishers Ltd: Nature ¹¹⁰ , copyright 2000.	41
Figure 1.28 Packing diagram of (1.53b)PF ₆ . Figure adapted from reference ¹²⁷ - Reproduced by permission of The Royal Society of Chemistry.	44
Figure 1.29 Crystal structure of complex [Mn(hfac) ₂ (1.54) ₂]. Reprinted from reference ¹¹³ with permission from Elsevier.	46
Figure 1.30 1-D chain present in [Cu(hfac) ₂ (1.54) ₂](PF ₆) and [Cu(hfac) ₂ (1.54) ₂](BF ₄) ₂ . Hydrogen and fluorine atoms not shown for simplicity.	47
Figure 1.31 Schematic representation of the charge disproportionated chains for [Cu(hfac) ₂ (1.54) ₂](PF ₆) and [Cu(hfac) ₂ (1.54) ₂](BF ₄) ₂ . Figure reprinted fom reference ¹³⁷ with kind permission from Springer Science and business Media.....	48
Figure 1.32 a) Planar zig-zag chains of the complex CuCl ₂ (1.57), b) stacking of the CuCl ₂ (1.57) complexes down the <i>c</i> -axis.	49
Figure 1.33 a) Arrangement of TTF ligand 1.58 molecules roughly perpendicular to each other, b) stacking arrangement with parallel ligand 1.58 , c) dimers of ligand molecules of the same polymorph as in b).	51
Figure 1.34 Schematic drawing of: (a) oxidation of a TTF ligand bearing paramagnetic centres; (b) stack of oxidized TTF ligand bearing paramagnetic centres, showing itinerant electrons moving through the stack. Adapted from reference ¹⁴³ with permission.	54
Figure 1.35 a) Molecular structure of 1.60 showing the dihedral angle θ , b) dependency of <i>J</i> with θ . Reprinted from reference ¹⁴⁶ with permission from Elsevier.	55
Figure 1.36 Calculated spin density distributions for [Mn(hfac) ₂ (1.63)]. Spin density shown as dark blue lobes. Reprinted with permission from ¹⁵¹ . Copyright 2010 American Chemical Society.	58
Figure 2.1 UV-Vis spectra of 10 ⁻⁵ M solutions of 2.2 and 2.3 in methanol.....	63

Figure 2.2 a) ORTEP plot of the molecular structure of 1.40 showing the corresponding numbering scheme. Thermal ellipsoids plotted at 50% probability. b) Unit cell of 1.40 . Hydrogen atoms are omitted for clarity....	64
Figure 2.3 a) ORTEP plot of the molecular structure of 2.2 showing the corresponding numbering scheme and the hydrogen bonds between the hydroxyl and imine groups. Thermal ellipsoids plotted at 50% probability. b) Unit cell of 2.2 . c) Short contacts between neighbouring 2.2 molecules shown as dashed red lines. Hydrogen atoms not involved in intramolecular H-bonds are omitted for clarity.....	65
Figure 2.4 a) ORTEP plot of the molecular structure 2.3 showing the corresponding numbering scheme and the hydrogen bonds between the hydroxyl and imine groups. Thermal ellipsoids plotted at 50% probability. b) Unit cell of 2.3 , showing the ligand domains separated by solvent molecules. c) Short contacts and hydrogen bonds are shown as red dotted lines. Some hydrogen atoms and isopropyl alcohol molecules are omitted for clarity....	68
Figure 2.5 UV-Vis spectrum of an approximately 10^{-5} M solution of complex 2.4 in methanol.	70
Figure 2.6 a) ORTEP plot of the molecular structure of the Sn^{4+} complex 2.4 showing the corresponding numbering scheme. Thermal ellipsoids plotted at 50% probability. b) Unit cell of 2.4 . Ethanol molecules and hydrogen atoms are omitted for clarity. c) diazepine ligand 2.5 resulting from the intramolecular cyclization of 2.2	71
Figure 2.7 UV-Vis spectrum of an approximately 10^{-5} M solution of complex 2.6 in methanol.	74
Figure 2.8 a) ORTEP plot of the molecular structure 2.6 showing the corresponding numbering scheme. Thermal ellipsoids plotted at 50% probability. b) Unit cell of 2.6 . c) Hydrogen bonding interactions between hydroxyl groups and axial chloride ions show as red dotted lines. Hydrogen atoms are omitted for clarity except where necessary.....	75
Figure 2.9 Variation of $1/\chi$ versus temperature for 2.6 . The fit to the Curie-Weiss law is shows as a red line.	77

Figure 2.10 Variation of χT versus temperature for complex 2.6 . The fit to the van Vleck equation is shown as a red line.....	78
Figure 2.11 UV-Vis spectrum of a 10^{-5} M solution of complex 2.7 in methanol.	80
Figure 2.12 ORTEP plot of the molecular structure of Cu^{2+} complex 2.7 showing the corresponding numbering scheme. Thermal ellipsoids plotted at 50% probability. The hydrogen atoms and perchlorate counterions are omitted for clarity.	81
Figure 2.13 Perchlorate disorder types A and B. Chlorine and oxygen atoms are shown in green and red respectively. The atoms belonging to the second component of the disorder are shown in light blue.....	82
Figure 2.14 a) View of the unit cell of 2.7 down the a -axis, c) view of the unit cell down the c -axis. The hydrogen atoms and perchlorate counterions are omitted for clarity.	82
Figure 2.15 Variation of χT versus temperature for complex 2.7 . The fit to the van Vleck equation is shown as a red line.....	84
Figure 2.16 a) ORTEP plot of the molecular structure of 2.8 showing the corresponding numbering scheme. Thermal ellipsoids are plotted at 50% probability. b) Schematic representation of the molecular structure of ligand 2.9 . c) Hydrogen bonding interactions between amino groups and chloride counterions shown as red dashed lines. d) Intrastack acetonitrile short contacts between neighbouring complex molecules. The hydrogen atoms, chloride counterion and acetonitrile molecules are omitted for clarity where necessary.	86
Figure 2.17 Variation of the $1/\chi$ product versus temperature for complex 2.8 . The fit to the Curie-Weiss law is shown as a red line.....	89
Figure 2.18 Variation of the χT product versus temperature for complex 2.8	89
Figure 2.19 UV-Vis spectrum of a 10^{-5} M solution of complex 2.11 in methanol.	90
Figure 2.20 a) ORTEP plot of the molecular structure of 2.11 showing the corresponding numbering scheme. Thermal ellipsoids are plotted at 50% probability. b) Unit cell of 2.11 . c) View of the packing diagram of 2.11	

on the <i>bc</i> plane. The hydrogen atoms and acetonitrile molecules are omitted for clarity when necessary.	91
Figure 3.1 ORTEP plot of the molecular structure of 3.2 showing the corresponding numbering scheme. Thermal ellipsoids plotted at 50% probability. Hydrogen atoms are omitted for clarity.	100
Figure 3.2 a) Unit cell of 3.2 , b) view of the stacks along the <i>b</i> -axis, c) side view of one stack. Hydrogen atoms are omitted for clarity.	102
Figure 3.3 a) Interstack short contacts of 3.2 shown as red dotted lines, along the <i>c</i> -axis between atoms N2-S2a, and b) along the <i>b</i> -axis between atoms S4-S3b. Hydrogen atoms are omitted for clarity.	103
Figure 3.4 ORTEP plot of the molecular structure of 3.3 showing the corresponding numbering scheme. Thermal ellipsoids plotted at 50% probability. Hydrogen atoms are omitted for clarity.	103
Figure 3.5 a) Unit cell of 3.3 , b) view of the stacks along the <i>b</i> -axis, c) view of one stack along the <i>c</i> -axis.	104
Figure 3.6 Interstack short contacts of 3.3 shown as red dotted lines, a) along the <i>c</i> -axis between atoms C2a-H2a...N2 ($x, 1/2-y, -1/2+z$), and b) along the <i>b</i> -axis between atoms S2-S1b. Hydrogen atoms shown when necessary, otherwise they are omitted for clarity.	106
Figure 3.7 ORTEP plot of 3.4 showing the corresponding numbering scheme. Thermal ellipsoids plotted at 50% probability. Hydrogen atoms are omitted for clarity.	107
Figure 3.8 a) Unit cell of 3.4 , b) view along the <i>c</i> -axis of the stacks, c) view of one stack along its long side, showing the head-to-tail arrangement of the stack. Hydrogen atoms are omitted for clarity.	108
Figure 3.9 Interstack short contacts of 3.4 shown as red dotted lines. a) N...H and bifurcated S...S interactions. Hydrogen atoms shown when necessary, otherwise they are omitted for clarity.	109
Figure 3.10 a) Hydrogen bonding interactions of aldehydes in the solid state and b) CN...H contacts in 3.4	110

Figure 3.11 ORTEP plot of the molecular structure of 3.5 showing the corresponding numbering scheme. Thermal ellipsoids plotted at 50% probability. Hydrogen atoms are omitted for clarity.	110
Figure 3.12 a) Unit cell of 3.5 , b) unit cell down the <i>a</i> -axis showing the green and white molecules over the pink and yellow molecules, c) four chains in different colours showing the C-H...N hydrogen bond along the <i>c</i> -axis in dotted red lines. Hydrogen atoms shown when necessary as coloured sticks, otherwise they are omitted for clarity.	112
Figure 3.13 UV-Vis spectra of 10 ⁻⁵ M solutions of derivatives 3.2-3.7 and TTF in acetonitrile.	115
Figure 3.14 ORTEP plot of the molecular structure of 3.8 showing the corresponding numbering scheme. Thermal ellipsoids plotted at 50% probability. Hydrogen atoms are omitted for clarity.	120
Figure 3.15 a) Unit cell of 3.8 , b) view of the stacks along the <i>b</i> -axis. Hydrogen atoms are omitted for clarity.	120
Figure 3.16 UV-Vis spectra of 10 ⁻⁵ M solutions of derivatives 3.8-3.10 and TTF in acetonitrile.	123
Figure 3.17 ORTEP plot of the asymmetric unit of 3.15a , showing the corresponding numbering scheme. Thermal ellipsoids plotted at 50% probability. Hydrogen atoms are omitted for clarity.	131
Figure 3.18 a) Unit cell of 3.15a , b) Stack of dimers of 3.15a showing the S...S short contacts between TTF moieties as dashed red lines. c) I ₅ ⁻ anions between stacks of derivatives.	133
Figure 3.19 Molecular structure showing in different colours the overlapped components of the positional disorder of an I ₅ ⁻ counterion.	134
Figure 3.20 TTF dimers in 3.15 . Cyanopyridyl moieties and counterions are omitted for clarity. The C=C bond lengths and S...S contacts for the TTF molecules are shown in Å.	135
Figure 3.21 a) ORTEP plot of molecular structure of the asymmetric unit of 3.16 , showing the corresponding numbering scheme. Thermal ellipsoids	

plotted at 50% probability. Hydrogen atoms are omitted for clarity. b)	
Unit cell of 3.16 .	138
Figure 3.22 Dimer of 3.3⁺⁺ .	139
Figure 3.23 Layers of molecules of 3.16 that run along the b-axis of the unit cell.	139
Figure 3.24 UV-Vis spectra of 10 ⁻⁵ M solutions of polyiodine CT salts 3.15c , 3.16a , 3.18b , 3.18c in acetonitrile.	143
Figure 3.25 ORTEP plot of the asymmetric unit of 3.17 , showing the appropriate numbering scheme. Thermal ellipsoids are plotted at 50% probability. Hydrogen atoms and iodine disorder are omitted for clarity.	144
Figure 3.26 a) Unit cell of 3.17 , disorder in the counterions is not shown, b) chains of derivative dimers running along the direction [011], c) TTF dimer S...S short contacts are shown as dashed lines, distances are shown in Å.	146
Figure 3.27 a) Short S...I and I...I contacts showing also a TTF dimer, b) molecular model showing in different colours the overlapped components of the disorder of a I ₃ ⁻ anions. The iodine atom in purple is shared by both components of the disorder.	146
Figure 3.28 ORTEP plot of the asymmetric unit of 3.21 , showing the corresponding numbering scheme and type of donor A and B. Thermal ellipsoids plotted at 50% probability. Hydrogen atoms and PF ₆ ⁻ counterions are omitted for clarity.	148
Figure 3.29 a) Unit cell of 3.21 , b) view of the intratrimer S...S distances shown as green dashed lines, distances are in Å c) view of the stacks down the <i>a</i> - axis.	149
Figure 3.30 ORTEP plot of the asymmetric unit of 3.22 , showing the corresponding numbering scheme and type of donor A and B. Thermal ellipsoids plotted at 50% probability. Hydrogen atoms and PF ₆ ⁻ anions are omitted for clarity.	152
Figure 3.31 a) Unit cell of 3.22 , b) view of the intratrimer S...S distances shown as green dashed lines, distances are in Å, c) view of the stacks in 3.22 down the <i>a</i> -axis. The disorder of the PF ₆ ⁻ anions is not shown.	153

- Figure 3.32** The PF_6^- counterions in the structure of **3.22**: a) anisotropic PF_6^- showing no disorder, b) isotropic PF_6^- showing the positional disorder of fluoride atoms as small green spheres not bonded to the central phosphorus atom. 155
- Figure 3.33** UV-Vis spectra of 10^{-5}M solutions of CT salts **3.19-3.22** in acetonitrile.156
- Figure 4.1** Sample radical ligands. From left to right: nitronyl nitroxide, verdazyl, DTDA and 3,5-di-tert-butyl-o-quinone.159
- Figure 4.2** a) ORTEP plot of the molecular structure of **4.1** showing the corresponding numbering scheme, b) unit cell of **4.1**. Thermal ellipsoids plotted at 50% probability. Hydrogen and fluorine atoms are omitted for clarity.162
- Figure 4.3** a) Top view of a dimer of **4.1**, showing the green molecule is on top of the red molecule. b) View of the slanted stacks of TTF dimers on the *ac* plane, c) view of the same slanted stacks along the *b*-axis showing the chelated Co^{2+} centered occupying the space between adjacent stacks of donors. Hfac ligands omitted when necessary for clarity, except for their oxygen atoms. Hydrogen atoms are omitted for clarity.164
- Figure 4.4** ORTEP plot of the molecular structure of **4.2** showing the corresponding numbering scheme. Thermal ellipsoids plotted at 50% probability. Hydrogen and fluorine atoms are omitted for clarity.165
- Figure 4.5** a) Unit cell of complex **4.2**, b) view of the slanted stacks on the *ac* plane. Hfac ligands omitted when necessary for clarity, with the exception of their oxygen atoms. Hydrogen atoms are omitted for clarity.167
- Figure 4.6** a) ORTEP plot of the molecular structure of the two independent molecules of **4.3** showing the corresponding numbering scheme. b) Unit cell of **4.3**. No disorder shown for clarity. Thermal ellipsoids plotted at 50% probability. Hydrogen and fluorine atoms are omitted for clarity.168
- Figure 4.7** a) Image showing in blue the first signs of B component during refinement of **4.3**, overlapped with the A component of the disorder. b) Diagram showing the overlap of TTF-A with an incomplete, misshapen TTF-B (right).169

Figure 4.8 Overlapped component of the disorder A (solid bonds) and B (dashed bonds) of 4.3. Thermal ellipsoids plotted at 50% probability. Hydrogen and fluorine atoms are omitted for clarity.	169
Figure 4.9 a) Top view of a dimer of 4.3, showing the green molecule is on top of the red molecule. b) View of the slanted stacks in the <i>ac</i> plane. Hfac ligands omitted when necessary for clarity, except for their oxygen atoms. Hydrogen atoms are omitted for clarity. The B component of disorder is not shown for clarity.	171
Figure 4.10 Short contacts between the rings of non-disordered 4.3 complexes.	172
Figure 4.11 a) ORTEP plot of the molecular structure of 4.4 showing the corresponding numbering scheme. Thermal ellipsoids plotted at 50% probability. b) Unit cell of 4.4. Hydrogen and fluorine atoms are omitted for clarity when necessary.	173
Figure 4.12 a) View of the stacks of 4.4 down the <i>b</i> -axis. b) View of the stacks down the <i>a</i> -axis showing the fluorine atoms as green spheres. Hydrogen and hfac ligands are omitted for clarity when necessary.	175
Figure 4.13 UV-Vis spectra of 10 ⁻⁵ M solutions of derivatives 4.1-4.4 in acetonitrile. ..	176
Figure 4.14 Variation of 1/ χ versus temperature for 4.1. The fit to the Curie law is shows as a red line.	178
Figure 4.15 Variation of χT versus temperature for complex 4.1.	179
Figure 4.16 Variation of 1/ χ versus temperature for 4.3. The fit to the Curie law is shows as a red line.	180
Figure 4.17 Variation of χT versus temperature for complex 4.3. The fit to the van Vleck equation is shown as a red line.	181

List of Tables

Table 1.1 Selected bond lengths and angles for helicates 1.20 - 1.23	27
Table 1.2 Cyclic voltammetric data for 1.49, 1.59 and $[\text{Fe}(\mathbf{1.59})_2](\text{SCN})_2$	53
Table 2.1 Selected bond lengths (Å) and angles (°) for ligand 1.40	64
Table 2.2 Selected bond lengths (Å) and angles (°) for ligand 2.2	66
Table 2.3 Distance d and angle α of the hydrogen bonds for ligand 2.3	68
Table 2.4 Selected bond lengths (Å) and angles (°) for ligand 2.3	69
Table 2.5 Selected bond lengths (Å) and angles (°) for complex 2.4	72
Table 2.6 Selected bond lengths (Å) and angles (°) for complex 2.6	76
Table 2.7 Magnetic coupling J and structural parameters for chloro-bridged octahedral Mn^{2+} complexes.....	79
Table 2.8 Selected bond lengths (Å) and angles (°) for complex 2.7	83
Table 2.9 Selected bond lengths (Å) and angles (°) for complex 2.8	87
Table 2.10 Selected bond lengths (Å) and angles (°) for complex 2.11	92
Table 2.11 Distance d and angle α of the $\text{C-H}\cdots\text{X}$ short contacts in 2.11	93
Table 3.1 Selected bond lengths (Å) and angles (°) for 3.2	101
Table 3.2 Selected bond lengths (Å) and angles (°) for 3.3	105
Table 3.3 Selected bond lengths (Å) and angles (°) for 3.4	109
Table 3.4 Selected bond lengths (Å) and angles (°) for 3.5	111
Table 3.5 Distance d and angle θ of the $\text{CN}\cdots\text{HC}$ short contacts of derivative 3.5	112
Table 3.6 UV-Vis ICT λ_{max} (nm) in different solvents for derivatives 3.2-3.7	116
Table 3.7 Influence of heterocycle substituents on TTF for derivatives 3.2-3.7 . $Y =$ 'yes', $N =$ 'no'.	116
Table 3.8 FT-IR nitrile stretching frequencies (cm^{-1}) and UV-Vis ICT λ_{max} (nm) for derivatives 3.2-3.7	117
Table 3.9 FT-IR nitrile stretching (cm^{-1}), UV-Vis ICT λ_{max} (nm) and cyclic voltammetry oxidation potentials (V) for derivatives 3.2-3.7	118
Table 3.10 Selected bond lengths (Å) and angles (°) for 3.8	121
Table 3.11 UV-Vis ICT λ_{max} (nm) in different solvents for derivatives 3.8-3.10	123

Table 3.12 Uv-Vis ICT λ_{max} (nm) and cyclic voltammetry oxidation potentials (V) for derivatives 3.8-3.10	124
Table 3.13 Selected bond lengths (Å) and angles (°) for 3.15	132
Table 3.14 Distance d and angle α of the CH \cdots N short contacts in 3.15	133
Table 3.15 CT calculations for the neutral derivatives 3.2-3.5	135
Table 3.16 CT calculations for 3.2 and 3.15	136
Table 3.17 Selected bond lengths (Å) and angles (°) for 3.16	140
Table 3.18 Distance d and angle θ for the CH \cdots N short contacts in 3.16	141
Table 3.19 CT calculations for the neutral 3.3 and 3.3⁺	141
Table 3.20 IR nitrile stretching (cm ⁻¹) for the corresponding neutral donor and CT salts 3.15b , 3.15c , 3.16a , 3.16b , 3.18a-c , 3.19 , 3.20 and the stoichiometry of the CT salts.	142
Table 3.21 Electrical conductivity measurements (S cm ⁻¹) at room temperature of pressed pellets of the CT salts 3.15c , 3.16a , 3.18b and 3.18c	143
Table 3.22 Selected bond lengths (Å) and angles (°) for 3.17	145
Table 3.23 Summary of bond lengths of 3.8 and bond length changes for different oxidation states. The column headings indicate bonds as in Scheme 3.10. Bond length changes are compared to the bond lengths of 3.8²⁺	147
Table 3.24 CT calculations for 3.17	147
Table 3.25 Selected bond lengths (Å) and angles (°) for 3.21	150
Table 3.26 CT calculation for 3.21	151
Table 3.27 Selected bond lengths (Å) and angles (°) for 3.22	154
Table 3.28 CT calculations for 3.22	155
Table 3.29 Electrical conductivity measurements (S cm ⁻¹) at room temperature of pressed pellets of the CT salts 3.19 , 3.20 , 3.21 and 3.22	157
Table 4.1 Selected bond lengths (Å) and angles (°) for complex 4.1	163
Table 4.2 Selected bond lengths (Å) and angles (°) for complex 4.2	166
Table 4.3 Selected bond lengths (Å) and angles (°) for the molecule of 4.3 showing no disorder.	170
Table 4.4 Selected bond lengths (Å) and angles (°) for complex 4.4	174
Table 4.5 UV-Vis ICT λ_{max} in different solvents for complexes 4.1-4.4	177

Table 4.6 Cyclic voltammetry oxidation potentials for complexes 4.1-4.4	177
Table I Crystal data and structure refinement parameters for compounds 1.40, 2.2 and 2.3	239
Table II Crystal data and structure refinement parameters for compounds 2.4 and 2.6	240
Table III Crystal data and structure refinement parameters for compounds 2.7, 2.8 and 2.11	241
Table IV Crystal data and structure refinement parameters for compounds 3.2 and 3.3	242
Table V Crystal data and structure refinement parameters for compounds 3.4 and 3.5	243
Table VI Crystal data and structure refinement parameters for compounds 3.8 and 3.15a	244
Table VII Crystal data and structure refinement parameters for compounds 3.16a and 3.17a	245
Table VIII Crystal data and structure refinement parameters for compounds 3.21 and 3.22	246
Table IX Crystal data and structure refinement parameters for compounds 4.1 and 4.2	247
Table X Crystal data and structure refinement parameters for compounds 4.3 and 4.4	248

List of Schemes

Scheme 1.1 Schematic representation of the cationic and anionic layers in the 2-D layered structure of an oxalate salt.	17
Scheme 1.2 Demethoxylation reaction of 1.17 . Reaction conditions: 1 eq. 1.17 , 2 eq. $\text{Cu}(\text{COOCH}_3)_2$, H_2O , 160°C , 7 days.....	24
Scheme 1.3 Reaction diagram of the Zn^{2+} complex 1.31 with acetone to afford 1.33 . Reaction conditions: acetonitrile, room temperature.	31
Scheme 1.4 Reaction diagram of the metal-catalyzed intramolecular cyclization reaction of 1.34 into 1.35 . Reaction conditions: i) NiCl_2 , DMSO, heating.	31
Scheme 1.5 Reaction scheme of the formation of the family of luminescent complexes 1.38 . $\text{M}^{n+} = \text{Li}^+, \text{Na}^+, \text{K}^+, \text{Mg}^{2+}, \text{Ca}^{2+}, \text{Ba}^{2+}, \text{Fe}^{3+}, \text{Co}^{2+}, \text{Ni}^{2+}, \text{Cu}^{2+}, \text{Zn}^{2+}, \text{Cd}^{2+}, \text{Hg}^{2+}$	32
Scheme 1.6 Reaction diagram for the synthesis of ligand 1.40 . Reaction conditions: toluene, 4 Å molecular sieves, reflux, 4days.....	33
Scheme 1.7 Proposed mechanism for the rearrangement of the 1.40 to afford complex 1.41	35
Scheme 1.8 Oxidation states of TTF.	37
Scheme 1.9 Phase alternation diagram explaining antiferro and ferromagnetic interactions in $[\text{Mn}(\text{hfac})_2(\mathbf{1.62})]$ and $[\text{Mn}(\text{hfac})_2(\mathbf{1.63})]$. ^{150,151}	58
Scheme 2.1 Reaction diagram for the synthesis of 2.2 and 2.3 . Reaction conditions: for 2.2 : methanol, r.t. overnight; for 2.3 : methanol, reflux, overnight.	62
Scheme 2.2 Potential binding modes of ligands 2.2	69
Scheme 2.3 Proposed mechanism for the intramolecular cyclization of ligand 2.2 to form ligand 2.5	73
Scheme 3.1 Scheme of the supramolecular diad AlPor- C_{60} . Adapted with permission from ¹⁹² . Copyright 2011 American Chemical Society.	98
Scheme 3.2 Reagents and conditions: i) 1.2 eq. LDA, THF, -82°C , 1 h, ii) 1.2 eq. Bu_3SnCl , THF, -82°C , 1 h, iii) 1.2 eq. Bromo-cyanopyridine, 0.1 eq. $\text{Pd}(\text{PPh}_3)_4$, THF, -82°C to r.t., overnight.	99

Scheme 3.3 Reagents and conditions: i) 1.2 eq. LDA, THF, -82°C, 1 h, ii) 1.2 eq. ZnCl ₂ , THF, -82°C, 1 h, iii) 1.2 eq. Bromo-cyanopyridine, 0.1 eq. Pd(PPh ₃) ₄ , THF, -82°C to r.t., overnight.	99
Scheme 3.4 Numbering scheme of the cyanopyridyl derivatives 3.2-3.5	113
Scheme 3.5 a) Intramolecular H5···N1 hydrogen bond in CDCl ₃ . b) Intramolecular hydrogen bonding between N1 and surrounding MeOD molecules.	114
Scheme 3.6 Reagents and conditions: i) 1.2 eq. LDA, THF, -82°C, 1 h, ii) 1.2 eq. ZnCl ₂ , THF, -82°C, 1 h, iii) 1.2 eq. 3.12 , 0.1 eq. Pd(PPh ₃) ₄ , THF, -82°C to r.t., overnight.	119
Scheme 3.7 Reagents and conditions: 1.4 eq. 3.12 , 0.1 eq. Pd(PPh ₃) ₄ , toluene, reflux, 24h.	119
Scheme 3.8 Reagents and conditions for: a) 3.9 : 1.2 eq. 3.13 , 0.1 eq. Pd(PPh ₃) ₄ , toluene, reflux, 24h, b) 3.10 : 0.86 eq. 3.14 , 0.1 eq. Pd(PPh ₃) ₄ , toluene, reflux, 12h.	122
Scheme 3.9 Scheme showing the SOMO of TTF. ¹⁴⁰	124
Scheme 3.10 Schematic representation of the bonds used for the CT calculations.	125
Scheme 3.11 Diagram showing the electrocrystallization process of the electroactive species B into the CT salt BX. The single crystal is represented as a green shape.	126
Scheme 3.12 Schematic representation of the electrocrystallization H-cell used in this work.	127
Scheme 3.13 Reaction scheme for the formation of radical cation salts <i>via</i> the first method namely slow diffusion of the TTF derivative and the iodine solutions.	128
Scheme 3.14 Reaction scheme for the formation of radical cation salts <i>via</i> the second method namely direct reactions between the TTF derivative and iodine.	129
Scheme 3.15 Reaction scheme for the preparation of CT salts 3.19-3.22 <i>via</i> electrocrystallization.	130
Scheme 4.1 Reaction scheme for the preparation of 4.1-4.4 . Reagents and conditions: 1.0 eq. M(hfac) ₂ , THF, reflux, overnight.	161

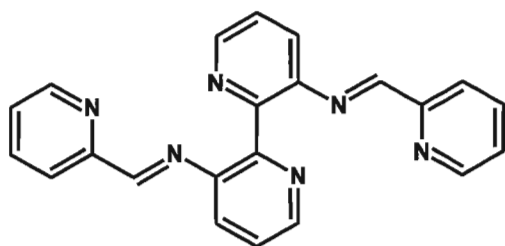
List of Abbreviations

1-D	One-dimensional
2-D	Two-dimensional
3-D	Three-dimensional
α	Angle
Å	Ångstrom
BEDT- TTF	Bis(ethylenedithio)tetrathiafulvalene
bipy	Bipyridine
B.M.	Bohr magneton
C	Curie constant
CT	Charge transfer
CN ⁻	Cyanide
COSY	Correlation spectroscopy
C ₂ O ₄ ⁻	Oxalate
C ₆₀	Fullerene
CV	Cyclic voltammetry
°C	Degree Celsius
DCM	Dichloromethane
DFT	Density Functional Theory
d	Doublet
dd	Doublet of doublet
e	Electron
EI	Electron impact ionization
emu	Electromagnetic unit
EPR	Electron paramagnetic resonance
ϵ	Molar absorptivity
FAB	Fast-Atom Bombardment
g	Grams
g	g-factor, proportionality constant
HMBC	Heteronuclear Multiple Bond Correlation
HOMO	Highest Occupied Molecular Orbital

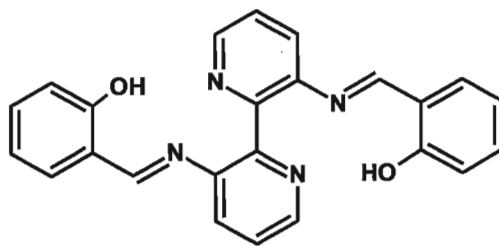
HR-MS	High Resolution Mass Spectroscopy
HSQC	Heteronuclear Single Quantum Correlation
HS	High Spin
IR	Infrared
ICT	Intramolecular Charge Transfer
<i>J</i>	Coupling constant (NMR), magnetic exchange parameter
K	Kelvin
LDA	Lithium diisopropyl amide
LIESST	Light-Induced Excited State Spin Trapping
LMCT	Ligand to Metal Charge Transfer
LS	Low Spin
LUMO	Lowest Unoccupied Molecular Orbital
<i>m</i>	Multiplet
M	Molar
mL	Milliliters
MLCT	Metal to Ligand Charge Transfer
mmol	Millimole
M.p.	Melting point
M_r	Remnant magnetization
M_s	Saturated magnetization
MS	Mass Spectroscopy
<i>m/z</i>	Mass/charge ratio
NMR	Nuclear Magnetic Resonance
Oe	Oersted
ORTEP	Oak Ridge Thermal Ellipsoid Plot
ppm	Parts per million
R	Agreement factor
r.t.	Room temperature
s	Singlet
S	Siemens
<i>S</i>	Spin quantum number
SCO	Spin crossover
SMM	Single Molecule Magnet

SQUID	Superconducting Quantum Interference Device
str	Stretching
t	Triplet
T	Temperature
T_c	Critical temperature
τ	Trigonality index
TCNQ	Tetracyanoquinodimethane
THF	Tetrahydrofuran
θ	Weiss constant
TTF	Tetrathiafulvalene
$TTF^{\cdot+}$	Tetrathiafulvalene radical cation
TTF^{2+}	Tetrathiafulvalene dication
TMTSF	Tetramethyltetraselenafulvalene
UV-Vis	Ultra violet-visible spectroscopy
μ_B	Bohr magneton
μ_{eff}	Magnetic moment
λ	Wavelength
χ	Magnetic susceptibility
χ_m	Molar magnetic susceptibility

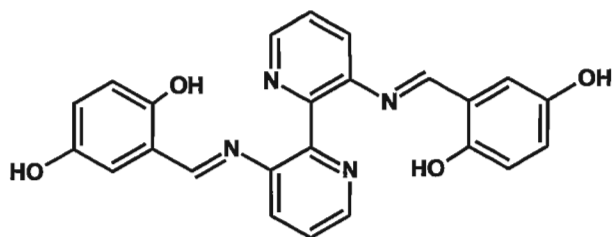
List of Compounds



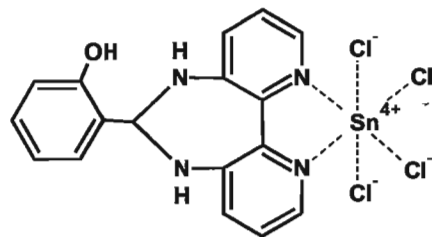
1.40



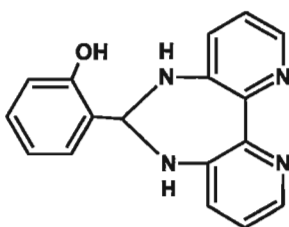
2.2



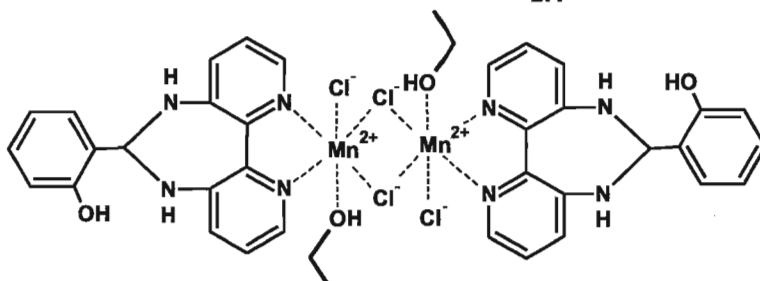
2.3



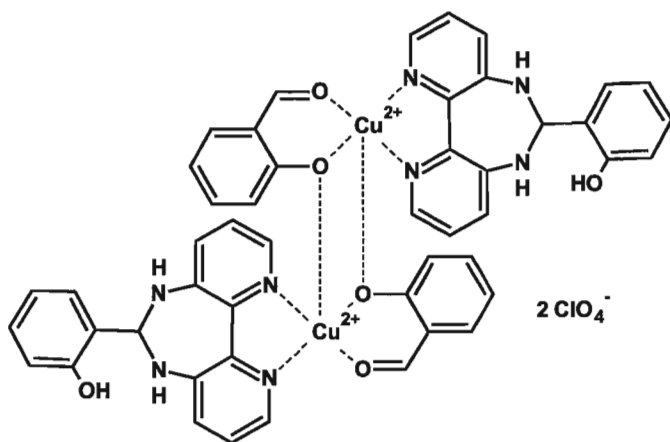
2.4



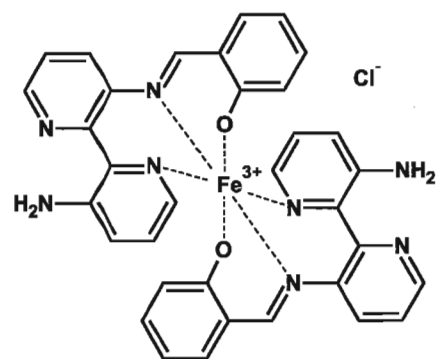
2.5



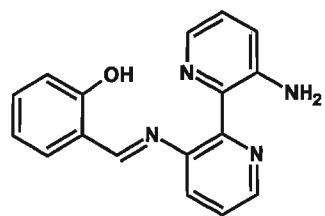
2.6



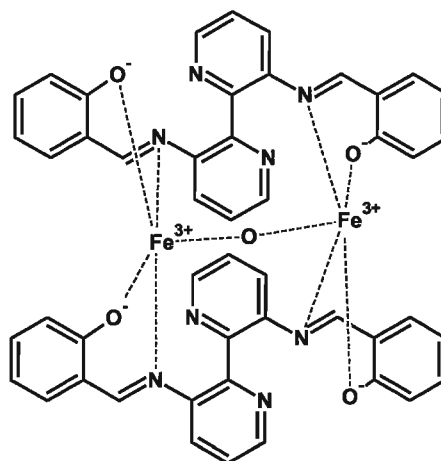
2.7



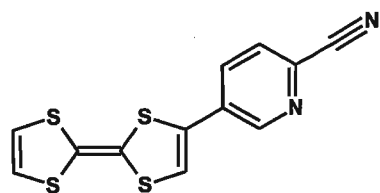
2.8



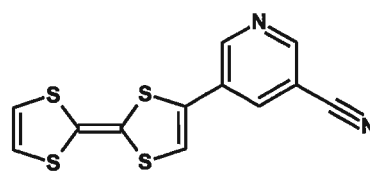
2.9



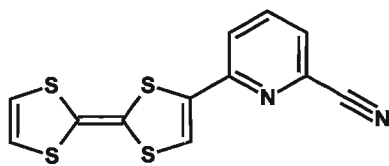
2.11



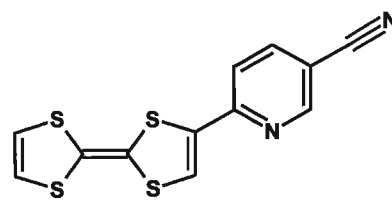
3.2



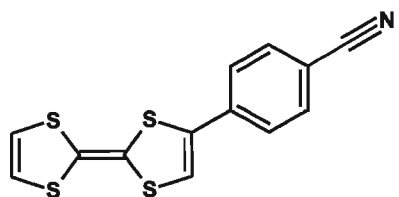
3.3



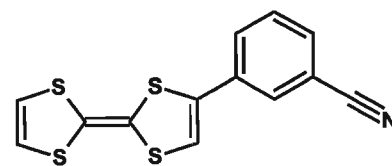
3.4



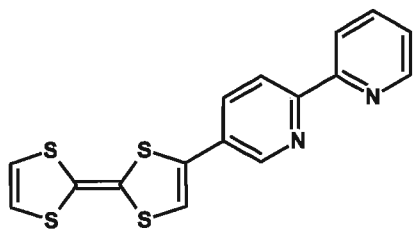
3.5



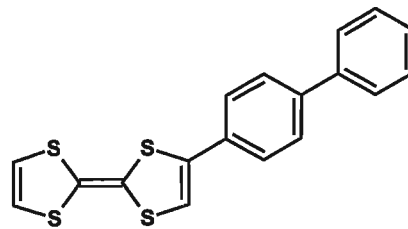
3.6



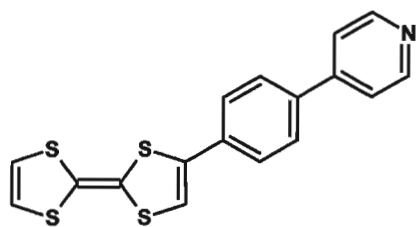
3.7



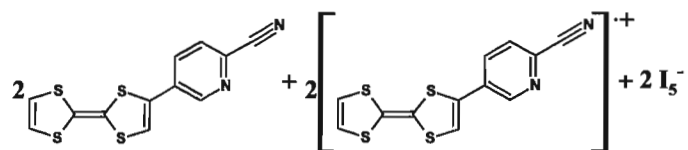
3.8



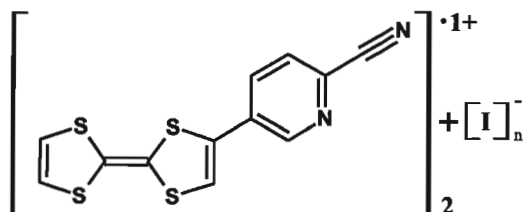
3.9



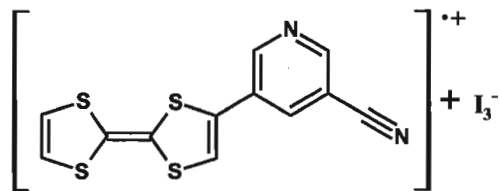
3.10



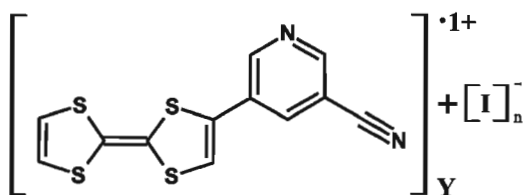
3.15a



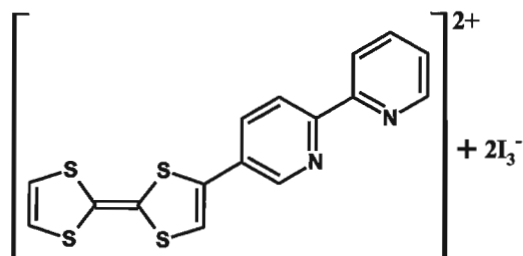
3.15b n = 7; 3.15c n = 5



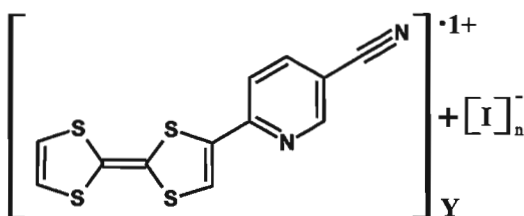
3.16



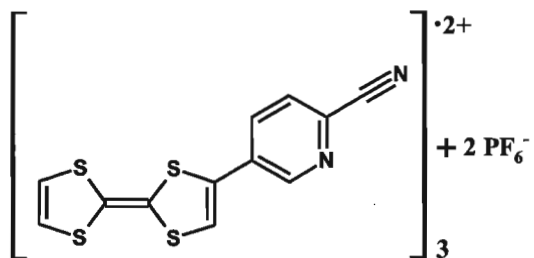
3.16a n = 3, Y = 1; 3.16b n = 7, Y = 3



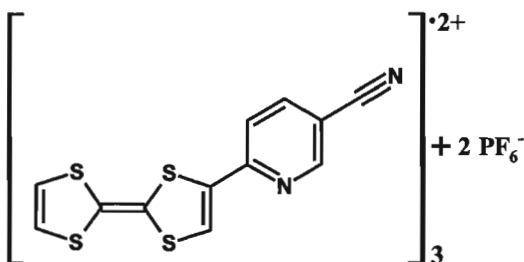
3.17



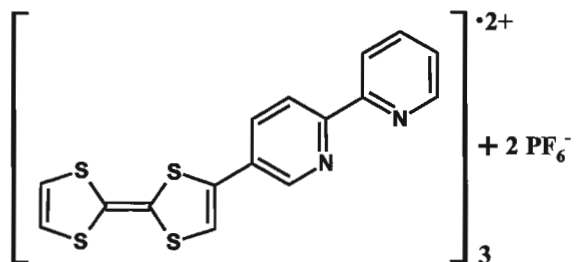
3.18a n = 7, Y = 2; 3.18b n = 5, Y = 2;
3.18c n = 3, Y = 1



3.19



3.20



3.21

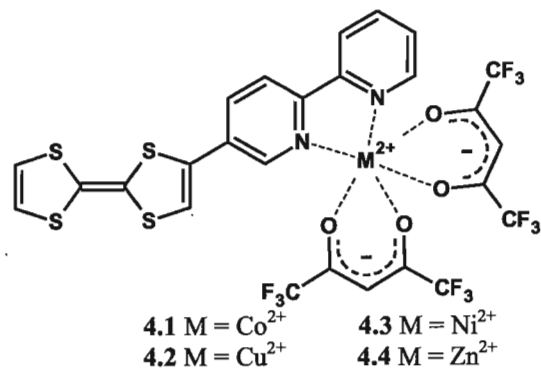
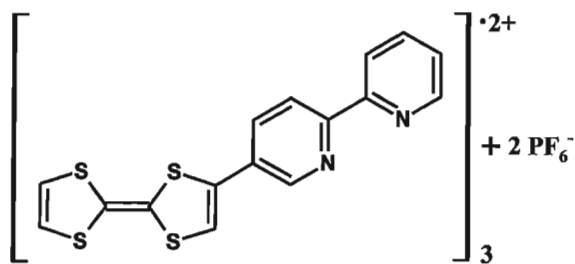



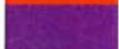

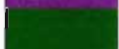














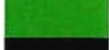

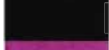


Table of atomic colours

Element symbol	[Red,Green,Blue]		Element symbol	[Red,Green,Blue]	
H	[170,255,255]		Fe	[255,99,8]	
Li	[204,128,255]		Co	[195,0,234]	
C	[145,145,145]		Ni	[255,198,65]	
N	[143,143,255]		Cu	[255,135,75]	
F	[194,255,0]		Zn	[170,85,0]	
O	[255,0,0]		Zr	[0,0,0]	
Na	[171,92,242]		Cd	[255,217,143]	
P	[255,128,0]		Sn	[102,128,128]	
S	[255,247,0]		I	[181,0,181]	
Cl	[31,240,31]		Ba	[0,201,0]	
Ti	[0,0,0]		Ce	[255,255,199]	
Mn	[255,0,255]				

CHAPTER 1

Introduction to molecular magnetism and multifunctional materials

1.1 Introduction

Magnetism is a physical property that has quietly established itself in our everyday life, playing a major role in appliances such as fridges and loudspeakers, or in more technologically advanced applications such as wind turbines and magnetic resonance imaging (MRI) scanners. Along with magnetism, electrical conductivity has also permeated our society to such an extent that only few aspects of our professional and private lives do not involve the use of an electrical device. During the last two decades a great deal of effort has been invested in developing molecule-based alternatives to the widespread inorganic magnets and electrical conductors.^{1,2} The possibility of designing molecular magnets and/or electrical conductors with physical properties tailored for a particular application has attracted the attention of research groups from around the world, due to the dramatic technological advances these materials represent.^{1,3,4} In particular, multifunctional molecular materials, that is, molecule-based materials that present interplay between two or more physical properties, have received a great deal of attention because of the challenge involved in preparing these materials. Not only it is necessary to design molecular building blocks with the desired physical properties, but the building blocks must organize in the solid state so that their physical properties will manifest and interact with each other.^{5,6} The work presented in this thesis targets the preparation and characterization of molecular magnets and molecular conductors as precursors for multifunctional molecular materials.

1.2 Introduction to magnetism

1.2.1 A macroscopic view of magnetism

Placing a material inside a magnetic field can result in the material being attracted or repelled by the magnetic field. Macroscopically, we can define the quantity, magnetic induction B , as the extent to which an isotropic material can be magnetized by a homogeneous external magnetic field according to the expression:

$$B = H + 4\pi M \quad (1.1)$$

where H is the applied magnetic field and M is the volume magnetization of the sample. If we divide both sides of Equation 1 by the magnetic field H , we have:

$$\frac{B}{H} = 1 + 4\pi \frac{M}{H} \quad (1.2)$$

then

$$\frac{M}{H} = \chi_v \quad (1.3)$$

and

$$\frac{B}{H} = \mu \quad (1.4)$$

where χ_v in equation (1.3) is the volume magnetic susceptibility and μ in equation (1.4) is the magnetic permeability of the material.⁷ A derivative magnitude more commonly used for practical reasons is the molar magnetic susceptibility χ_m , and we will refer to this magnitude from now on as magnetic susceptibility or simply susceptibility.

A material that has $\chi > 0$ and is placed in a magnetic field experiences a net magnetization, which increases the magnetic flux lines going through it, Figure 1.1 a). These materials are paramagnetic, and are attracted by the magnetic field. For the case in which $\chi < 0$, the number of magnetic flux lines inside the material decrease and the material is not attracted to the magnet, Figure 1.1 b). These materials are considered diamagnetic.

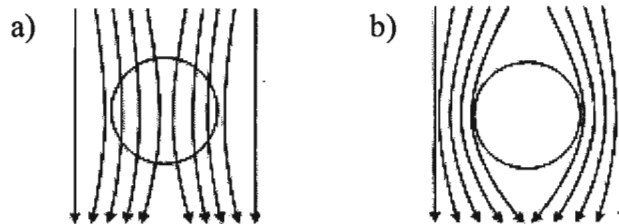


Figure 1.1 Magnetic field lines for a) paramagnet and b) diamagnet.

The temperature dependency of the magnetic susceptibility in some paramagnetic substances was reported by Curie in 1895, and can be represented by equation (1.5). This

equation shows that the magnetic susceptibility of a substance is inversely proportional to the temperature T , and directly proportional to the substance-dependent Curie constant C^7

$$\chi = \frac{C}{T} \quad (1.5)$$

The applicability of this law was, however, limited to a small group of paramagnetic substances. The Curie-Weiss law shown in equation (1.6) includes a Weiss temperature parameter θ that acts as a correction term to accommodate deviations from the Curie law. This parameter is introduced based on the mean field theory, in which all the interactions between the magnetic components of a substance are ‘averaged’ and treated as a perturbation.^{8,9}

$$\chi = \frac{C}{T - \theta} \quad (1.6)$$

Although equations 1.5 and 1.6 describe the behaviour of paramagnets, they do not explain them. These macroscopic descriptions of the magnetic susceptibility do not give any insight into its origin or on how to manipulate the composition of matter in order to change its magnetic properties. It is therefore necessary to take a more in-depth look at the sources of magnetism in order to understand how the magnetic susceptibility can be influenced by the chemical composition, molecular structure and the arrangement of the molecules in the solid state.

1.2.2 Molecular magnetism

Magnetism arises from the presence of uncompensated magnetic moments generated by the spin and orbital motions of unpaired electrons.^{8,9} The magnetic moments of each electron in an electron pair cancel each other, and the field-induced electron circulation of paired electrons generates a magnetic field that opposes the applied field. This diamagnetic behaviour is present in all substances, and is one of the components of the measured magnetic susceptibility χ_{total} , as shown in equation (1.7):

$$\chi_{\text{total}} = \chi_{\text{dia}} + \chi_{\text{para}} \quad (1.7)$$

where χ_{dia} is the diamagnetic susceptibility and χ_{para} is the paramagnetic susceptibility. The diamagnetic component of a paramagnetic substance can be determined in two different ways: i) measuring the susceptibility of only the diamagnetic part of a sample (e.g. the diamagnetic ligand of a paramagnetic complex), or ii) calculating the diamagnetic component of the sample by adding the numerical diamagnetic contribution for each atom and bond type known as Pascal's constants.⁸⁻¹⁰

The magnetic properties of a paramagnetic substance depend on how the unpaired electrons in the substance interact with each other when placed inside a magnetic field. Paramagnets that follow Curie's law present unpaired electrons that do not interact with each other, so their spins will not show any organized alignment, Figure 1.2 a). Many paramagnets deviate from Curie law due to the short range interactions between their magnetic spins. Below a critical temperature T_c the randomization of the magnetic spins caused by the thermal energy $k_B T$ decreases and the interactions between magnetic spins in the paramagnetic material can be observed. Three general scenarios exist for these interactions: i) the spins align parallel to each other, resulting in ferromagnetic interactions (Figure 1.2 b)), ii) the spins align antiparallel to each other giving a net zero magnetic moment (Figure 1.2 c)), resulting in antiferromagnetic interactions and , iii) the spins align antiparallel to each other, but there is not complete cancellation of the magnetic moments, resulting in ferrimagnetic interactions (Figure 1.2, d)).⁸⁻¹⁰

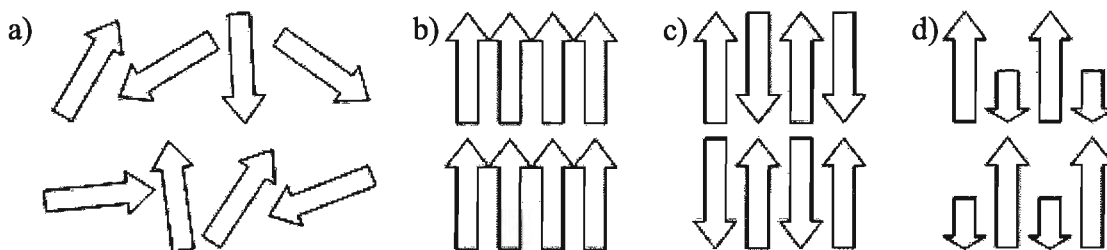


Figure 1.2 Schematic illustration of spin interactions for the four most common types of magnetic behaviours: a) paramagnetic, b) ferromagnetic, c) antiferromagnetic, d) ferrimagnetic.

Visual identification of each interaction is carried out by plotting $1/\chi$ vs. T as shown in Figure 1.3 or by plotting χT vs. T as in Figure 1.4. Plotting $1/\chi$ vs. T , all classes of behaviour give straight lines of slope C , and the point where the line crosses the

temperature axis indicates the presence of paramagnetic ($\theta = 0$), ferromagnetic ($\theta > 0$) or antiferromagnetic ($\theta < 0$) behaviour.^{8,9}

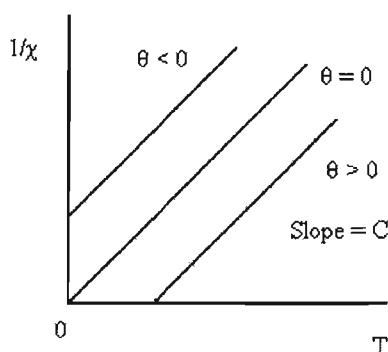


Figure 1.3 Plot of $1/\chi$ vs. T for Curie and Curie-Weiss magnetic behaviour.

In the second case, plotting χT vs. T gives a straight line for a pure paramagnetic behaviour, which intersects the y axis at the value of C . For a ferromagnetic response, the product χT increases as temperature decreases. χT shows the opposite tendency for an antiferromagnetic response as the temperature decreases. The ferrimagnetic response can be explained by the initial onset of short range antiferromagnetic interactions, causing a lowering of χT . As the correlation length increases, the antiferromagnetic interactions give rise to a coparallel alignment of spins between next nearest neighbours that increases the value of χT upon lowering the temperature further.

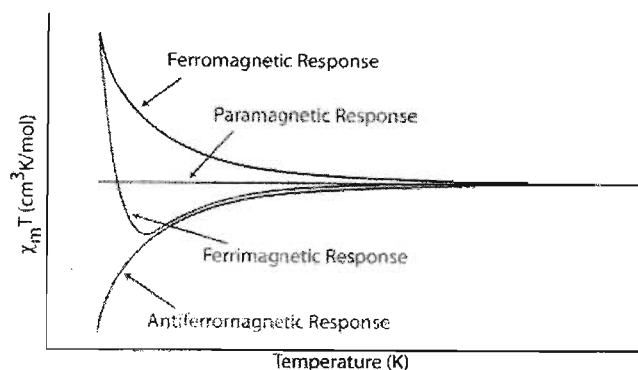


Figure 1.4 Plot of χT vs. T for paramagnetic, ferromagnetic, antiferromagnetic and ferrimagnetic behaviour.

Following a quantum mechanical approach to the modelling of the magnetic susceptibility, van Vleck considered that the magnetic moment M of a sample inside a magnetic field H was the result of the contributions of the magnetic moments μ_n of the spin-carrying population in each energy state n , weighed by their Boltzmann distribution;

$$M = N \sum_{m_s} \mu_n P_n \quad (1.8)$$

In equation (1.8) P_n is the Boltzmann distribution:

$$P_n = \frac{N_n}{N} = \frac{\exp\left(\frac{-E_n}{k_B T}\right)}{\sum_n \exp\left(\frac{-E_n}{k_B T}\right)} \quad (1.9)$$

where N_n in equation (1.9) is the population of the state n , N is the total population of all the states and E_n is the energy of each energy level.

The van Vleck equation (1.10) can be used to explain more complex magnetic behaviour, as it allows for the introduction of phenomena such as zero-field splitting or spin-orbit coupling in the modelling of the magnetic susceptibility

$$\chi_m = N_A \frac{\sum_n \left(\frac{E_n^{(1)2}}{k_B T} - 2E_n^{(2)} \right) \exp\left(\frac{-E_n^{(0)}}{k_B T}\right)}{\sum_n \exp\left(\frac{-E_n^{(0)}}{k_B T}\right)} \quad (1.10)$$

where the term $E_n^{(0)}$ corresponds to the ground state energy of the system, and $E_n^{(1)}$ and $E_n^{(2)}$ correspond to the first and second order Zeeman terms.⁸⁻¹⁰

1.2.2.1 Long range magnetic ordering

The interactions described in the previous section take place between the nearest or next nearest neighbours in the lattice, and they only manifest below T_c when the paramagnetic material is in a magnetic field. But although a paramagnet may display ferromagnetic interactions, it does not mean that it is capable of maintaining long range magnetic ordering. Ferromagnets can display long range cooperativity of the magnetic

spins in the material below their critical temperature T_c in the absence of a magnetic field, which results in the permanent magnetization of the material.⁷ In practice, a ferromagnet may not display any degree of magnetization below its T_c . Below this temperature the ferromagnet is divided into magnetic domains which have randomly aligned magnetic moments, Figure 1.5. These individual magnetic moments cancel each other out, resulting in a ferromagnet that displays no net magnetization.⁷

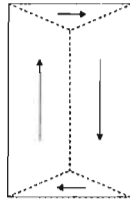


Figure 1.5 Diagram showing magnetic domains in a ferromagnet. The arrows indicate the orientation of the magnetic moment of each domain.

When an external magnetic field is applied, the domains whose magnetic moments are closer to the field direction will grow at the expense of other domains, resulting in the net magnetization of the ferromagnet. If the applied magnetic field is strong enough, the saturation of magnetization M_s of the ferromagnet will be reached, and the ferromagnet will only present one domain.⁷ The ferromagnet will remain magnetized once the magnetic field is removed, but heating above T_c will result in the loss of the net magnetization. This is caused by the formation of randomised magnetic moments which lead to loss of the domain structure and the sample behaves as a paramagnet above T_c . A magnetized ferromagnet will have a remnant magnetization M_r that may be different from the saturation of the magnetization M_s . The remnant magnetization can be suppressed by applying a magnetic field of the appropriate strength, known as the coercive field H_c .⁷ The magnitude of H_c can be used to classify magnetic materials as hard or soft magnets, depending on whether the coercive field is large or small. The effect of M_r and H_c on the M vs. H curve gives rise to the hysteresis loop shown in Figure 1.6.

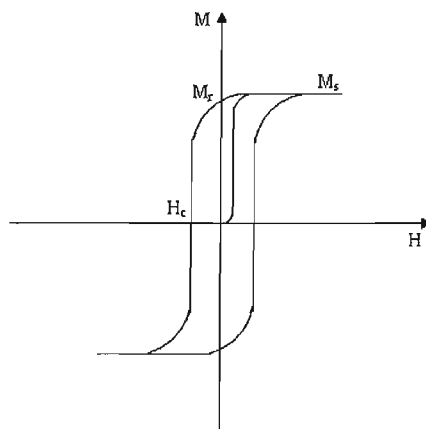


Figure 1.6 Schematic representation of a hysteresis loop.

1.2.2.2 Spin-crossover complexes.

Coordination of transition metal ions to a set of ligands causes the splitting of the d orbitals into a number of sets of orbitals with different energies. This splitting is called the crystal field splitting. The number of sets of orbitals formed depends on the symmetry of the coordination environment caused by the ligand. Generally, the orbitals that fall directly along the coordination axis between the lone pairs of the ligand and the metal centre gain energy, whereas the ligands that lie outside a coordination axis lose energy. Figure 1.7 shows the crystal field splitting for a metal complex with octahedral coordination. The orbitals d_{z^2} and $d_{x^2-y^2}$ gain energy because they lie on the axial and equatorial positions of the octahedron respectively.¹¹

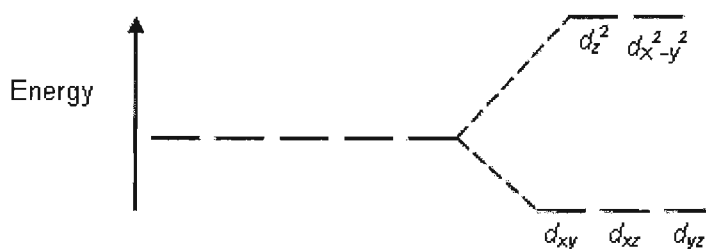


Figure 1.7 Crystal field splitting for an octahedral coordination geometry.

The magnitude of the crystal field splitting, Δ_{oct} , depends on the type of metal ion and its oxidation state, the symmetry of the coordination environment of the metal ion,

and the nature of the ligand(s). Figure 1.8 shows the spectrochemical series for a selected group of ligands. Ligands on the left of the series generate a weak crystal field splitting, and the ligands on the right generate a much larger (stronger) crystal field splitting.¹¹

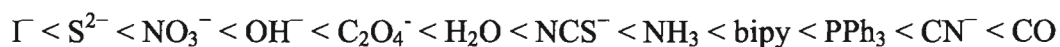


Figure 1.8 Spectrochemical series showing a small set of ligands. Ligand field increases from left to right.

For transition metal ions with electronic configurations d^4 - d^7 in an octahedral environment, it is possible to distribute their electrons among the orbital sets depending on the strength of the crystal field splitting. As shown in Figure 1.9, for an Fe^{2+} ion in a weak field (caused by I^- for example) four of the six d electrons of the Fe^{2+} ion are in the t_{2g} level and two electrons are in the e_g level, giving a high spin (HS) state. If the same ion is in a strong field (caused by CN^- , for example), the six electrons will be in the t_{2g} level and the complex will be in the low spin (LS) state. In any case, electrons will form pairs only if the pairing energy P is smaller than the crystal field splitting Δ_{oct} , otherwise their distribution among the orbitals will follow Hund's rule.¹¹

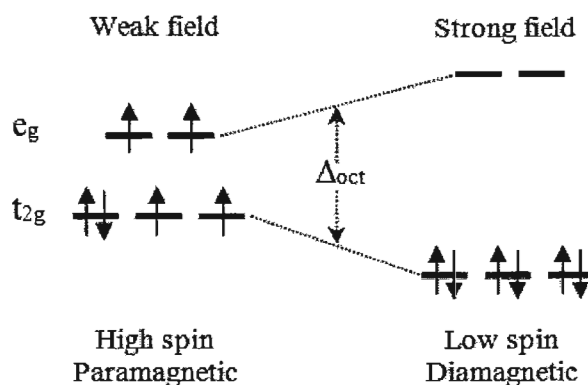


Figure 1.9 Diagram of the electron distribution for an Fe^{2+} ion in high and low spin states.

Careful choice of ligands and metal ions can give rise to a situation in which $\Delta_{\text{oct}} \approx P$. In this scenario, the spin state of the complex depends on the temperature, and two spin states with different magnetic moments are accessible. Complexes of this kind are called 'spin crossover' (SCO) meaning that their spin state can switch from HS to LS

in a reversible manner. This transition can also be triggered by changes in pressure, magnetic field or by irradiation with light. Currently, SCO complexes of Co^{2+} , Co^{3+} , Mn^{3+} , Fe^{2+} , Fe^{3+} can be found in the literature, but Fe^{2+} complexes are the most common.⁶ Given the difference in magnetic moments between spin states, it is possible to follow SCO behaviour using a magnetometer. The transition between high and low spin states can happen with different degrees of abruptness or completeness as show in Figure 1.10.

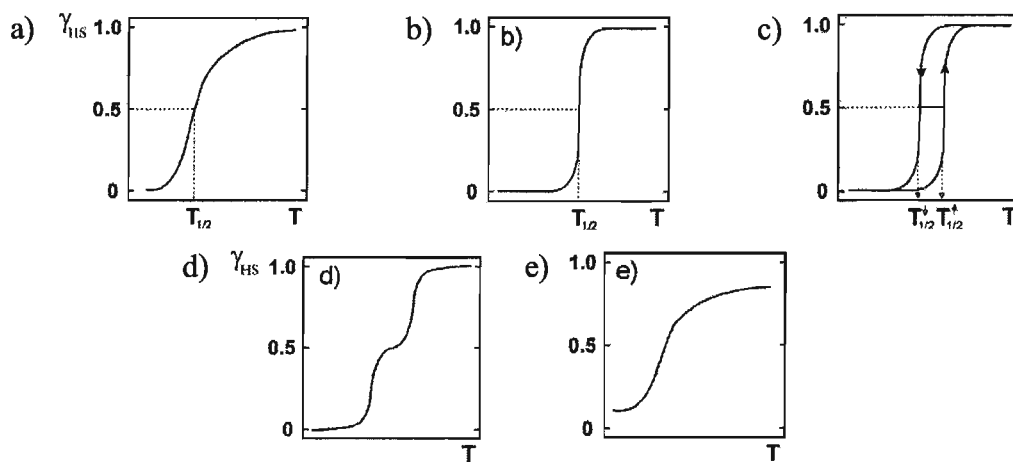


Figure 1.10 Diagram showing five possible spin transition curves for SCO systems in the solid state: (a) gradual; (b) abrupt; (c) with hysteresis; (d) with steps; (e) incomplete. γ_{HS} corresponds to the molar fraction of high spin state complexes in the sample. Figure reproduced from reference 6 with permission.

The curve in Figure 1.10 c) is of particular interest. This curve shows magnetic hysteresis, that is, the temperature $T_{1/2}$ at which the molar fraction $\gamma_{\text{HS}} = 0.5$ depends on whether that temperature is reached by cooling or heating the sample. The cause of this hysteresis is the bond length and bond angle changes due to the HS-LS transitions. Population of antibonding orbitals in the HS state weakens the ligand-metal bonds, causing a lengthening of these bonds. The transition to the LS state depopulates the antibonding orbitals and, as a consequence, the bond lengths decrease. These changes propagate through the lattice *via* cooperative intermolecular interactions such as hydrogen bonding or intermolecular π - π interactions. This magnetic bistability presents SCO complexes as potential candidates for magnetic storage devices and switches.^{6,12-14}

1.2.2.3 Cluster-based single-molecule magnets (SMMs).

In 1991, Caneschi *et al.* reported the slow relaxation of the magnetization of the cluster $\text{Mn}_{12}\text{O}_{12}(\text{O}_2\text{CMe})_{16}(\text{H}_2\text{O})_4$ or Mn12 for short, at liquid helium temperatures.¹⁵ The cluster is formed by an outer ring of eight Mn^{3+} ions and a central core of four Mn^{4+} ions. This cluster was the first SMM discovered, and it paved the way for a whole new field of magnetochemistry. In general, SMM behaviour results from magnetically isolated clusters that have a large ground spin state S , a negative axial zero field splitting parameter D and the presence of an easy axis of magnetization.⁴ For Mn12, the antiferromagnetic coupling between the eight Mn^{3+} ions and the four Mn^{4+} ions results in a ground spin state $S = 10$ which becomes populated at low temperatures. The Jahn-Teller distortion axis of the eight Mn^{3+} ions are aligned nearly parallel, causing the anisotropy that generates an easy axis of magnetization. The negative zero-field splitting parameter D generates a double well of spin states with a barrier for magnetization reversal that hinders the inversion of the magnetization below the blocking temperature T_B .¹⁵

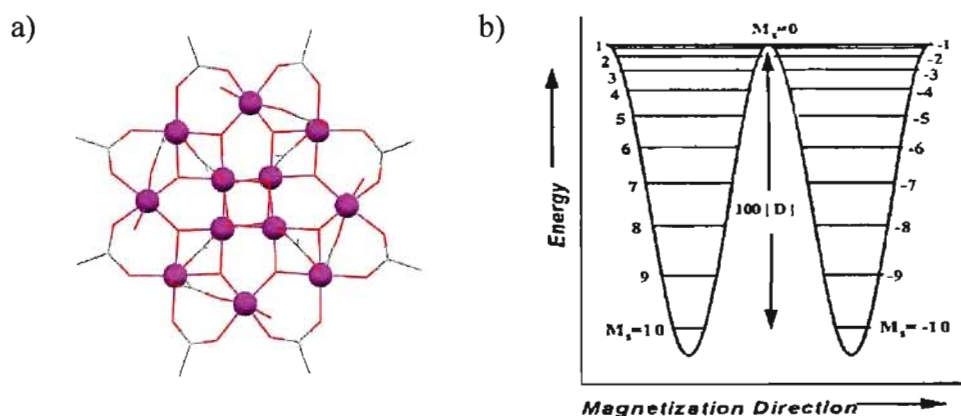


Figure 1.11 a) Structure of Mn12 SMM, b) double well of spin states. Adapted with permission from 16. Copyright 2003 American Chemical Society.

The family of Mn12 derivatives with stoichiometry $\text{Mn}_{12}\text{O}_{12}(\text{O}_2\text{CR})_{16}$ ($R = \text{alkyl, aryl}$) is the most studied one,^{4,17} but families of Fe_4 , Mn_4 and Mn_6 SMMs have also been reported in the literature,^{4,18,19} along with SMMs of other $3d$ metal ions and lanthanides.^{20,21} The generation of this kind of systems relies on a fair amount of serendipity, as it is not currently possible to predict the presence of SMM behaviour based only on the topology of the ligand and the coordinated metal centres.⁴ Still,

although a fully rational design of the desired cluster is not possible, it is possible to use ligands and metal ions with the appropriate traits to obtain a cluster with these properties. The ligands used for the preparation of SMMs are often small, structurally flexible and polypodal in order to promote the formation of clusters with high nuclearities, The correct choice of metal ions is important in order to aim for SMM behaviour; single-ion anisotropy in, for example, Ni^{2+} , Co^{2+} , Fe^{2+} or Mn^{3+} is desirable as the alignment of the anisotropy axis in the final cluster can result in the formation of an easy axis of magnetization.^{4,18,20}

An important driving force in the research of new SMMs is their potential application in magnetic storage devices. The freezing of the magnetization reversal makes these materials suitable candidates for such an application, but the current blocking temperatures are still too low for any commercial use.²² Recently, the use of SMMs as potential contrast agents for magnetic resonance imaging (MRI) has been reported.²³⁻²⁶ The large magnetic moments of these clusters is expected to enhance the relaxivity of water molecules, and the low toxicity of 3d transition metal ions as compared to that of Gd^{3+} ^{23,26} makes them suitable candidates for this application. At the moment, cluster stability in water is an issue,^{24,26} and more research must be done to ensure biocompatibility and optimal *in vivo* activity before any medical application can be realistically envisaged.^{23,27}

1.3 Introduction to ligand design for molecular materials

1.3.1 Hexacyanometalates

The possibility of engineering devices, by designing their molecular components with tailored physical properties, is the main driving force for the development of this field. Molecular systems capable of switching between accessible magnetic states could result in the drastic miniaturization of technology beyond the dimensions currently commercially viable for devices. The magnetic properties of molecular magnets depend on the exchange interactions between their paramagnetic components mediated by the bridging ligands. Ligand choice is therefore crucial in order to achieve the necessary lattice topologies that will give the desired magnetic properties.²⁸⁻³²

Cyanide is a small, dissymmetrical *bis*-monodentate ligand capable of coordinating virtually any metal ion in the periodic table. This ligand forms strong metal–carbon bonds, and stable mononuclear polycyano metal complexes of known stoichiometry.³³⁻³⁵ These complexes can be used as building blocks for the preparation of molecular magnets and 1-D, 2-D or 3-D magnetic architectures thanks to the N coordination of cyanide to metal cations, forming μ -cyanide bridges of the style A–CN–B (where A and B are paramagnetic metal cations). These bridges permit strong magnetic exchange interactions between the magnetic spins of the coordinated metals.³⁵ In particular, many of these 3-D networks are related to Prussian blue (PB), a mixed-valence ferrocyanate complex of formula $\text{Fe}_4^{\text{III}}[\text{Fe}^{\text{II}}(\text{CN})_6]_3 \cdot 15\text{H}_2\text{O}$ that displays long-range ferromagnetic ordering at $T_c = 5.6$ K and has a face-centered cubic lattice.³⁶ PB analogs can be prepared substituting the Fe ions in PB by other paramagnetic metals ions; these analogues are usually isostructural with PB, Figure 1.12.³⁵

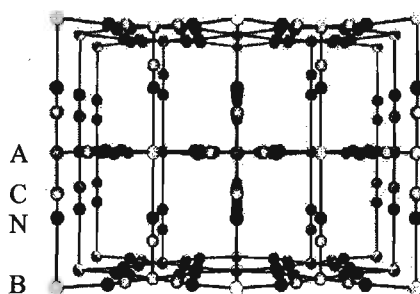


Figure 1.12 Schematic representation of the crystal structure of a prussian blue analog. Reprinted from 37 with permission from Elsevier.

Bringing the T_c of these analogs closer to room temperature has driven the research of groups from around the world. The first compound displaying a Curie temperature above liquid nitrogen temperature was $\text{Cs}^{\text{I}}\text{Mn}^{\text{II}}[\text{Cr}^{\text{III}}(\text{CN})_6]$, $T_c = 90$ K, reported by Babel *et al.*³⁸ The T_c of the analogs was increased by applying the orbital model by Kahn⁹ to the design of new stoichiometries and by improving the crystallinity of the samples. In 1999, Holmes and Girolami reported the highest T_c to-date for the ferrimagnet $\text{KV}^{\text{II}}[\text{Cr}^{\text{III}}(\text{CN})_6] \cdot 2\text{H}_2\text{O}$, which has a $T_c = 376$ K.³⁹ The Co-Fe PB analog family have also received a great deal of attention due to their photomagnetic properties. Hashimoto *et al.* showed that excitation of the PB analog, using a red light, caused an

electron exchange between the Fe^{2+} and Co^{3+} ions in the lattice. This results in the diamagnetic $\text{Fe}^{2+}\text{-Co}^{3+}$ pairs becoming paramagnetic $\text{Fe}^{3+}\text{-Co}^{2+}$ pairs and the Curie temperature of the irradiated analog is increased by 4 K as a result. Irradiation with blue light was shown to be enough to switch the analog back to the initial state.⁴⁰ Apart from 3-D networks, the literature is rich in examples of molecular, 1-D chains and 2-D layers built from PB analogs. Control over the dimensionality of the product is exerted by using complexes containing labile and capping ligands. Capping ligands such as ethylenediamine,⁴¹ 2,2'-bipyridine,⁴² bpm (*bis*(1-pyrazolyl)methane),⁴³ cyclam (1,4,8,11-tetraazacyclotetradecane)^{44,45} or treten (tetraethylenepentamine)⁴⁶ direct the reactivity of the incoming N-cyanide ligand towards the labile positions around the metal centre. Figure 1.13 shows the structures of these ligands together with examples of complexes present in the literature. The positions and number of the labile ligands L in the coordination environment of the metal cation M^{n+} is limited by the capping ligands. This results in the programming of building blocks with specific angular and dimensional information that, upon reaction with cyanometallate ions, direct the self-assembly of the PB analog network.

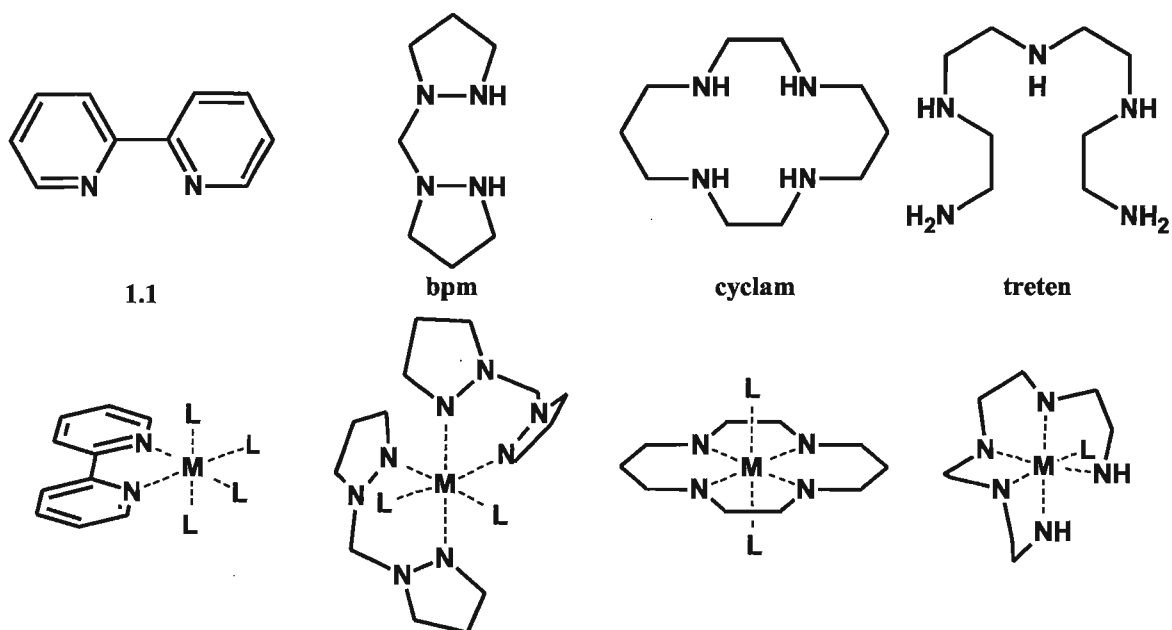


Figure 1.13 Structures of ligands 1.1, bpm, cyclam and treten (top row) and examples of their coordination modes (bottom row). L represents a labile ligand(s).

Far from being restricted to the aesthetically pleasing octahedral hexacyanometallate ion, usually formed by 3d metals ions, cyanide complexes of 4d and 5d metal ions are receiving an increasing amount of attention.³⁴ The larger diameter of these ions allows coordination spheres with a higher number of cyanide ligands, which expands the possible geometries beyond the predictable 90° angles of the 3d hexacyanometallate anions. Moreover, 4d and 5d metal ions present more radially extended valence orbitals, capable of enhanced magnetic exchange between magnetic centres compared to 3d metal ions. The larger spin–orbit coupling present in the heavier transition metals can give rise to higher anisotropy of magnetic exchange between magnetic spins, and the richer redox and photochemical behaviour of these metal ions are parameters added to an already complex field that can result in new kinds of magnetic molecular materials.³⁴

The oxalate (ox) ligand is also a good mediator of magnetic interactions between paramagnetic metal ions. This symmetrical ligand can coordinate in a *bis*-bidentate manner bridging two metal cations, and has been extensively used in the self-assembly of 1-D chains, 2-D layers and 3-D networks. The last two types of frameworks have received the most attention due to their potential in forming multifunctional materials following a rational design approach.³⁵

The fundamental building block of the 2-D and 3-D oxalate frameworks is the homoleptic octahedral complex $[M^{n+}(ox)_3]^{(6-n)-}$ (M = transition metal). The relative arrangement of the isomers Λ and Δ of the octahedral anion (Figure 1.14) in the framework determines its dimensionality; the alternating isomer arrangements $\Lambda\Delta$ usually lead to a 2-D honeycomb layered structure, whereas the homochiral configurations $\Lambda\Lambda$ and $\Delta\Delta$ lead to a 3-D network, see Figure 1.15. Therefore the dimensionality of the final product depends on the capacity of the components of the network to template the anionic framework during the self-assembly process.³⁵

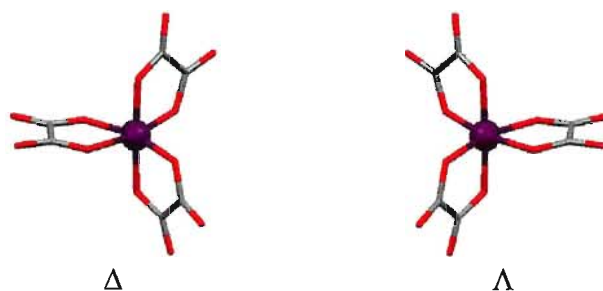


Figure 1.14 Isomers Δ and Λ of a *tris*-oxalate complex.³⁵

In this respect, monocationic species such as $[\text{XR}_4]^+$ ($\text{X} = \text{N}, \text{P}$; $\text{R} = \text{phenyl}, \text{n-alkyl}$) promote the formation of 2-D honeycomb layers of *tris*-oxalate complexes interleaved by layers of the cation, Scheme 1.1. The general formula of the framework is $[\text{XR}_4][\text{M}^{\text{II}}\text{M}^{\text{III}}(\text{ox})_3]$ ($\text{M}^{\text{II}} = \text{V}, \text{Mn}, \text{Fe}, \text{Co}, \text{Ni}, \text{Cu}$; $\text{M}^{\text{III}} = \text{V}, \text{Cr}, \text{Mn}, \text{Fe}, \text{Co}, \text{Ru}$), and ferro-, antiferro- and ferrimagnetic long-range ordering have been observed in these compounds.^{35,47,48} Their magnetic properties can be tailored by carefully choosing M^{II} , M^{III} , and the organic cation. For example, compounds presenting $[\text{Fe}^{\text{III}}(\text{ox})_3]^-$ show ferrimagnetic (e.g. $\text{M}^{\text{II}} = \text{Ni}$, $T_c = 28 \text{ K}$)⁴⁹ or antiferromagnetic ordering (e.g. $\text{M}^{\text{II}} = \text{Mn}$, $T_c = 55 \text{ K}$)⁵⁰, whereas compounds with $[\text{Cr}^{\text{III}}(\text{ox})_3]^-$ show ferromagnetic ordering (e.g. $\text{M}^{\text{II}} = \text{Mn}$, $T_c = 6 \text{ K}$)⁵¹ or no long range ordering for $\text{M}^{\text{II}} = \text{Cr}$.⁵²

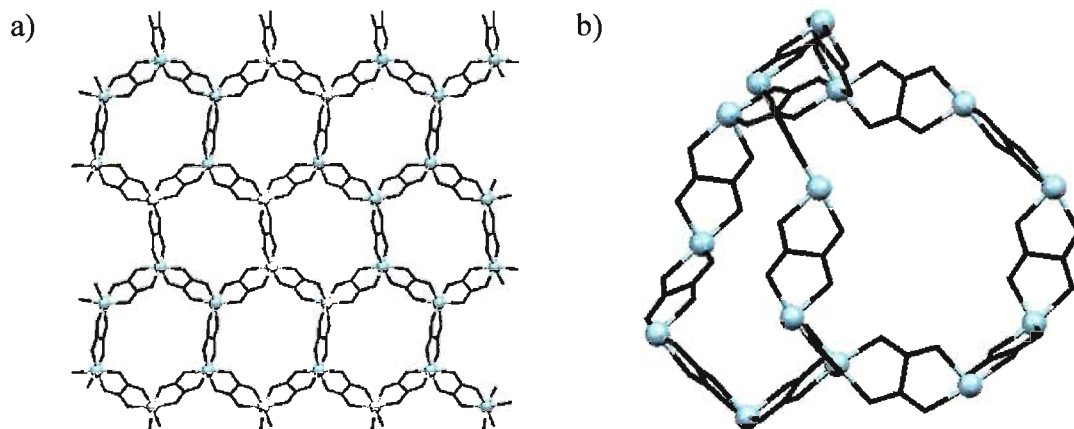
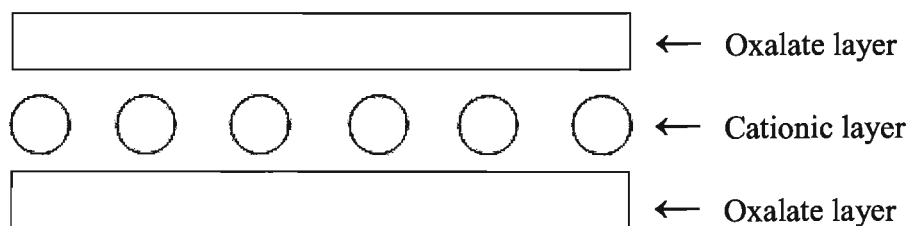
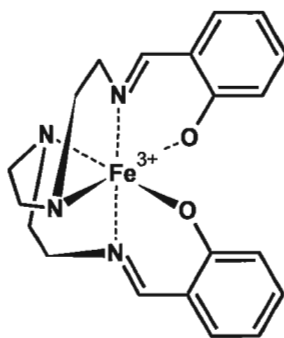


Figure 1.15 a) 2-D honeycomb layer of *tris*-oxalate metal complexes, b) 3-D decagon cavity of *tris*-oxalate metal complexes. Metal centres are shown as light blue balls, oxalate ligands are shown as black sticks.³⁵



Scheme 1.1 Schematic representation of the cationic and anionic layers in the 2-D layered structure of an oxalate salt.

Beyond the $[\text{XR}_4]^+$ cation, cations displaying magnetism or other physical properties have also been used to form hybrid multifunctional molecular materials that present 2-D oxalate layers. The possibility of building such materials from rationally designed building blocks has attracted much attention during the last two decades due to the possibility of discovering new physical phenomena and their potential technological applications.^{5,48} More specifically, the preparation of hybrid multifunctional molecular materials that show synergy between two or more physical properties has driven researchers from around the world to use oxalate frameworks to obtain these materials. Taking advantage of the self-assembly processes of oxalate frameworks, cations bearing, for example, magnetism, conductivity or photonic properties have been successfully used instead of $[\text{XR}_4]^+$ cations. Examples of cations used for the preparation of multifunctional materials include chiral, non-linear-optics-active, photochromic molecules and SCO cationic complexes.^{5,47,48} The possibility of tuning the magnetic properties of an oxalate-based product with an external stimulus such as temperature change led to the preparation of $[\text{Fe}(\mathbf{1.2})]_2[\text{Mn}_2(\text{ox})_3]$.⁵³ Magnetic and Mössbauer characterization of this complex showed that the cation preserved its SCO behaviour in the compound, showing a SCO transition at about 60 K for the Fe^{3+} centres, while the oxalate layers remained paramagnetic. Further cooling revealed the onset of antiferromagnetic interactions between Mn^{2+} ions, to finally show spontaneous magnetization at 10 K.



1.2

The 3-D oxalate networks present cavities delineated by the *tris*-oxalate complexes with homochiral configurations $\Lambda\Lambda$ or $\Delta\Delta$ in the form of a three-dimensional decagon framework of D_3 symmetry, Figure 1.15 b).³⁵ These cavities can be achieved by templating the oxalate network with racemic mixtures of cationic *tris*-bisimine metal complexes of D_3 symmetry or by using optically pure cationic *tris*-bisimine complexes of the same symmetry.³⁵ The preparation of 3-D networks using racemic mixtures of cationic complexes is possible because the cations template the oxalate network, making it assemble around them. Magnetic studies of 3-D networks usually show paramagnetic or antiferromagnetic behaviours although ferromagnetism has also been described.⁵⁴ In all cases, the value of T_c for the 3-D networks is lower than for the 2-D layers; this effect has been recently attributed to the relative orientation of the magnetic orbitals.⁵⁵ An uncommon example of SCO behaviour controlled by the lattice pressure of 3-D oxalate networks was reported by Sieber *et al.*⁵⁶ The magnetic characterization of $[\text{Co}(\text{bpy})_3][\text{LiCr}(\text{ox})_3]$ shows that the cationic complex $[\text{Co}^{\text{II}}(\text{bpy})_3]^{2+}$ undergoes a SCO transition as the temperature decreases, whereas it remains high spin in $[\text{Co}(\text{bpy})_3][\text{NaCr}(\text{ox})_3]$ down to 2 K. This effect was attributed to the more confining nature of the cavities in the Li^+ analogue, resulting in the destabilization of the high spin state so the low spin state becomes the ground state. The high spin state, however, remains thermally accessible, giving rise to the SCO behaviour.

1.3.2 Ligand design applied to the derivatization of 2,2'-bipyridine

The bipyridine family of ligands is comprised of six regioisomers of the *bis*-pyridine structure, Figure 1.16. Coordination through the lone pair on the nitrogen atoms makes these ligands σ -donors, and the presence of π^* orbitals of the aromatic rings that can accept electron density from a coordinated metal centre *via* back donation makes these molecules also π -acceptor ligands.

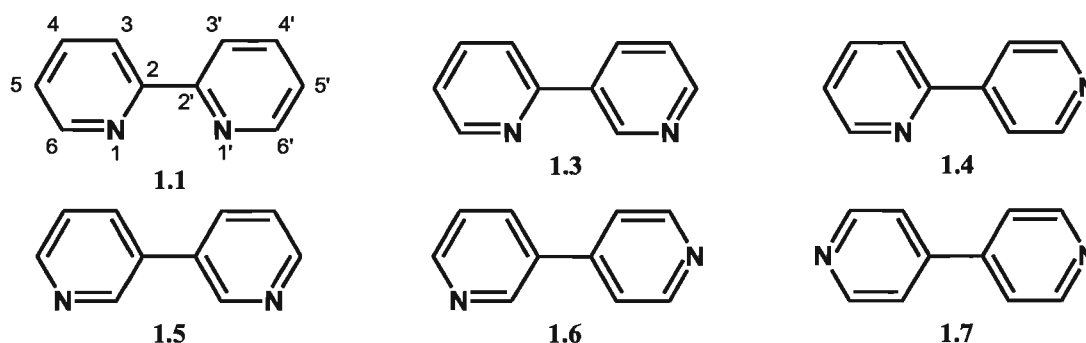
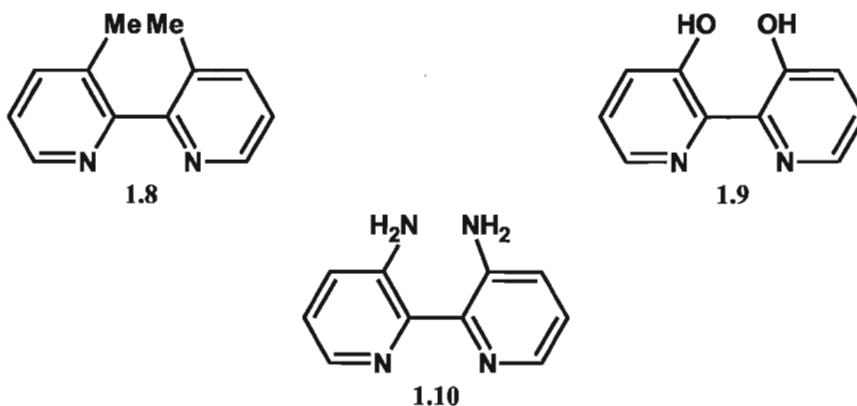


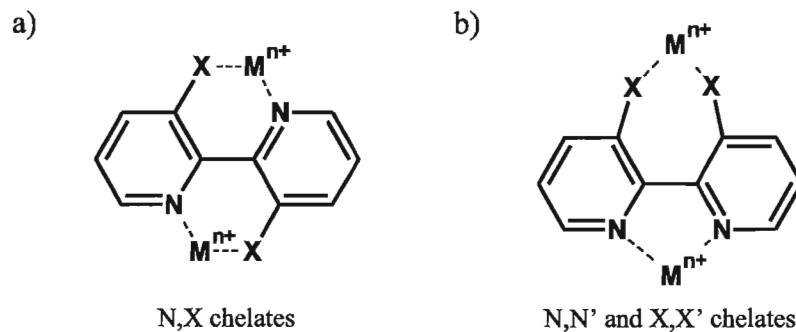
Figure 1.16 The family of bipyridine regioisomers.

The coordination chemistry of 2,2'-bipyridine (1.1) has been extensively researched due to its highly predictable coordination chemistry and the stability of the resulting complexes.^{57,58} The substitution of the 4-, 5- and 6- positions of the bipyridine molecule with additional binding sites has been actively investigated during the last two decades,⁵⁹⁻⁶² and has resulted in applications of 1.1 and its derivatives in supramolecular and macromolecular chemistry,⁶⁰ catalysis,⁶¹ molecular sensors,^{63,64} molecular recognition,⁶⁵ luminescent devices,⁶⁶ and optoelectronics.⁶⁷ Exploitation of the 3-positions for the preparation of derivatives has been much less explored. This was initially due to the misconception that the steric hindrance caused by the presence of substituents in the 3,3' positions would keep the pyridine rings in a conformation too twisted to engage in coordination chemistry.⁶⁰ In 1988, Craig *et al.* showed that 3,3'-dimethyl-2,2'-bipyridine can coordinate Fe^{2+} giving the complex $[\text{Fe}(\mathbf{1.8})_3]^{2+}$.⁶⁸ The single crystal structure of this complex showed the anticipated twisting of the pyridine rings within one bipyridine unit by about 31° , compared to the $3\text{--}12^\circ$ torsion angles in the unsubstituted complex $[\text{Fe}(\mathbf{1.1})_3]^{2+}$. Variable temperature magnetic and Mössbauer characterization of the perchlorate and hexafluorophosphate salts of $[\text{Fe}(\mathbf{1.8})_3]^{2+}$ showed a

gradual SCO transition from low spin to high spin as the temperature increased, whereas the unsubstituted complex $[\text{Fe}(\mathbf{1.1})_3]^{2+}$ displayed no SCO behaviour.⁶ The presence of the SCO transition was attributed to the reduction in coplanarity between the Fe^{2+} ion and the pyridine ring. This would cause a decrease in orbital overlap between metal and ligand, resulting in a smaller energy difference between the t_{2g} and e_g levels that falls within the SCO range. The electronic spectra of the complexes $[\text{Ni}(\mathbf{1.8})]^{2+}$ and $[\text{Ni}(\mathbf{1.1})_3]^{2+}$ were used to determine that the ligand field strength of **1.8** was actually lower compared to the field strength of **1.1**. More recently, the exploration of a range of substitutions at the 3,3' positions has gained momentum, and small substituents such as carboxylic acids,⁶⁹ esters,⁷⁰ hydroxyl⁷¹ (**1.9**) or amino⁷² (**1.10**) groups show no indication of hindering coordination to metal ions *via* the lone pairs on the nitrogen atoms of the bipyridine ligands.



The insertion of additional binding sites into the 3,3' positions opens the possibility of forming bridges using the symmetrical or asymmetrical coordination modes of the disubstituted bipyridine, as shown in Figure 1.17. In the following examples, we will focus our discussion on derivatives bearing hydroxyl and amino groups in the 3,3' positions.



1.11 X = OH, 1.12 X = NH₂

Figure 1.17 Potential a) symmetrical and b) asymmetrical binding modes of 3,3'-disubstituted 2,2'-bipyridine.

Even though the dihydroxy ligand **1.11** is a potential bridging ligand, its coordination chemistry is dominated by the N,N' chelation of the bipyridine ring, usually leaving the hydroxyl groups uncoordinated.⁷¹ The following examples show how this derivative can form N,X chelates, and how the rational derivatization of 2,2'-bipyridine can lead to interesting ligand behaviour, beyond the predictable 5-membered N,N' chelate ring.

In 1996, Thompson *et al.* prepared the mononuclear and dinuclear complexes [Ru(**1.1**)₂(**1.11**)]²⁺ (**1.13**) and [{Ru(**1.1**)₂}₂(μ-**1.11**)]²⁺ (**1.14**) in which **1.11** formed an N,N' chelate or two bridging N,O' chelates, depending on the stoichiometry of the reaction.⁷³ The ¹H NMR spectra of the complexes showed the expected signals based on the molecular symmetry for each case, and elemental analysis supported the expected composition. Single crystal X-ray diffraction was also used to characterize both products, but the authors could only report a partial refinement of the two structures due to the poor quality of the data.

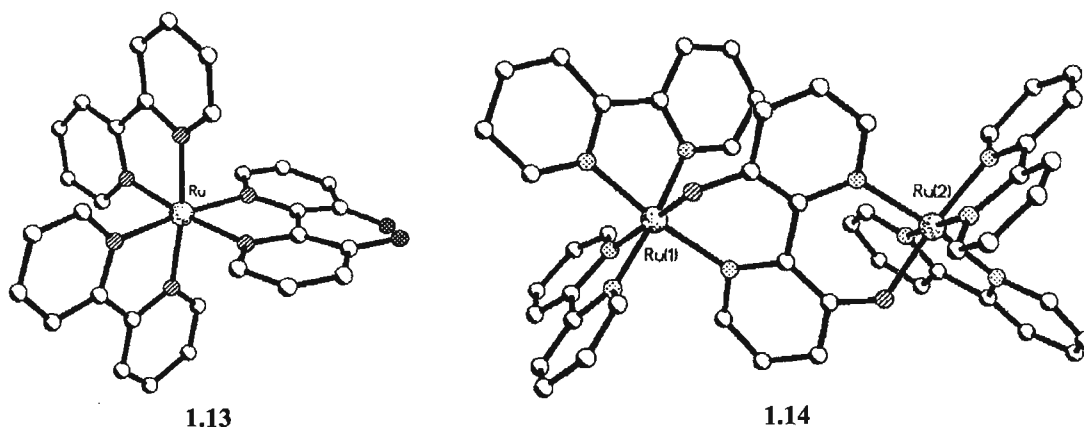


Figure 1.18 Partial structure of complexes **1.13** and **1.14**. Carbon atoms are white spheres, nitrogen atoms are striped spheres, oxygen atoms are dotted spheres and ruthenium atoms are large spheres. Adapted from reference 73 - Reproduced by permission of The Royal Society of Chemistry.

The influence of solvent over the chelation mode of **1.11** has been investigated spectroscopically for the Zn^{2+} and Cd^{2+} complexes. The results showed that the preference of the ligand for N,N'chelation over N,O chelation increased with decreasing proticity of the solvent, following the order water < ethanol < acetonitrile.⁷⁴ Lanthanide coordination chemistry has many potential applications that include luminescent probes, photochemistry, contrast agents, magnetic molecular materials, and catalysts.⁷⁵⁻⁷⁷ Taking advantage of the oxophilicity of cerium, $\text{Ce}(\text{NO}_3)_3$ was slowly reacted with ligand **1.11** in solution to afford single crystals of a complex that adopts an unusual 'castle-wall'-like topology, Figure 1.19.⁷⁸ The cerium atom coordinates two oxygen atoms of neighbouring **1.11** ligands, with an O-Ce-O' angle of $140.7(2)^\circ$, and the closest bipyridine nitrogen over 4.29 \AA away. The ligand is almost coplanar, with a torsion angle between the bipyridine rings close to half a degree.

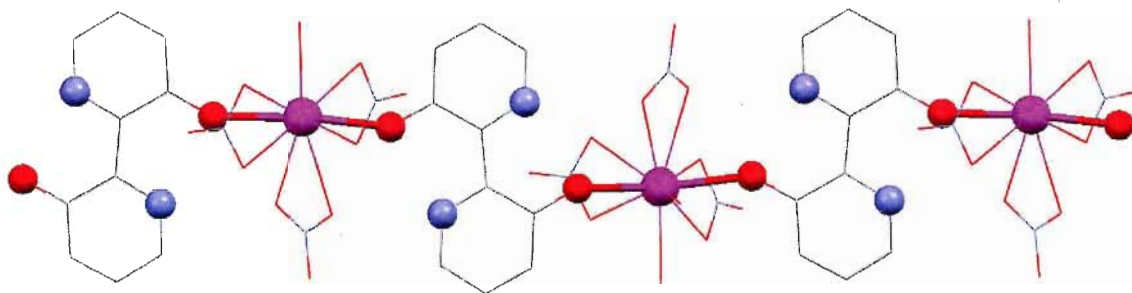
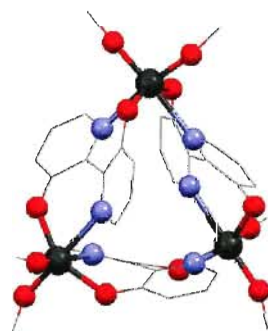


Figure 1.19 Molecular structure of a fragment of the 1-D chains of the cerium nitrate complex of ligand **1.11**. Nitrate counterions and water molecules shown as a wireframe for simplicity. Hydrogen atoms are omitted for clarity.⁷⁸

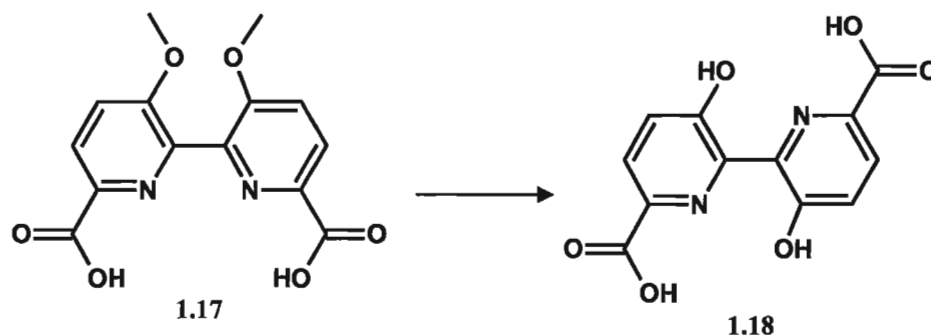
Ligand **1.11** has also been studied as a potential component of precursors for ceramic materials. Control over the structure of metal alkoxides is necessary in order to optimize their reaction rates and obtain ceramic films of good quality, but often the formation of undesired clusters and oligomers in the precursors gives undesired results.⁷⁹ Reaction of Zr^{4+} or Ti^{4+} alkoxides with **1.11** gave the two isostructural complexes shown in Figure 1.20.⁸⁰ In this case, the ligand acts as tetradentate N,O chelating bridge, forming a trinuclear cluster with C_{3v} symmetry. For both metals the coordination geometry is a distorted octahedron, with two bipyridine ligands coordinating each metal atom in the cluster. Each metal atom coordinates two pyridine N atoms and two alkoxide ligands in a *cis* manner, and two pyridine O atoms coordinating in a *trans* arrangement. In these clusters the geometrical requirements to coordinate the metal centres force the bipyridine rings to twist away from each other, adopting torsion angles in the range 27.0-32.9°.



1.15 $\text{M} = \text{Zr}^{4+}$, **1.16** $\text{M} = \text{Ti}^{4+}$

Figure 1.20 Crystal structure of the isostructural trinuclear clusters **1.15** and **1.16** alkoxides. The alkoxide ligands are shown as a grey sticks. Hydrogen atoms are omitted for clarity.⁸⁰

Metal organic frameworks (MOFs) are crystalline solids that consist of networks formed by bridging organic ligands that coordinate discrete metal ions or clusters. The nature of these bridges has been the focus of intense research, as their modification should allow researchers to chemically tune the physico-chemical properties of MOFs.⁸¹⁻⁸³ Transition metals and open shell organic ligands can be used to introduce magnetic properties in the MOF, but in order to go beyond isolated paramagnetic centres it is fundamental to control the connectivity and distances between the magnetic centres.⁸² Carboxylate ligands have been intensively studied for the wide variety of possible ligand topologies and together with the robustness of the MOFs they form. Ji *et al.*⁸⁴ prepared a MOF using ligand **1.17**, Scheme 1.2, in order to study how the rotational flexibility of the C-C bipyridine bridge would affect the dimensionality of the resulting framework and the nature of magnetic interactions between the paramagnetic metal centres. Reaction under hydrothermal conditions resulted in the demethoxylation of ligand **1.17**, affording ligand **1.18**, which forms the framework of a coordination polymer of general formula $\{[\text{Cu}_3(\mathbf{1.18})(\text{OH})_2(\text{H}_2\text{O})]_3 \cdot 2\text{H}_2\text{O}\}_n$, Scheme 1.2.



Scheme 1.2 Demethoxylation reaction of **1.17**. Reaction conditions: 1 eq. **1.17**, 2 eq. $\text{Cu}(\text{COOCH}_3)_2$, H_2O , 160°C , 7 days.⁸⁴

Ligand **1.18** acts as a *bis*-tridentate bridge, with a torsion angle of about 1.44° between the pyridine rings, Figure 1.21, a). In this structure, each ligand acts as a bridge between two infinite chains of Cu^{2+} ions. The ligand chelates one Cu^{2+} ion with each tridentate pocket formed by a pyridine nitrogen, one deprotonated hydroxyl group and one oxygen atom from a carboxylate group. This same oxygen atom also coordinates a second Cu^{2+} ion. Each cluster is formed by a central chain of oxo-bridge Cu^{2+} ions, with two ancillary Cu^{2+} ions between each step along the chain, Figure 1.21 b). The

$\text{Cu}^{2+} \cdots \text{Cu}^{2+}$ distances range from 2.94 to 3.32 Å. The packing diagram viewed down the *b*-axis, shows channels in the structure filled with water molecules. Magnetic susceptibility studies revealed that the χT value at room temperature was 0.79 emu K mol⁻¹, lower than the expected spin-only value for three non-interacting Cu^{2+} ions, indicating antiferromagnetic interactions between the magnetic centres.

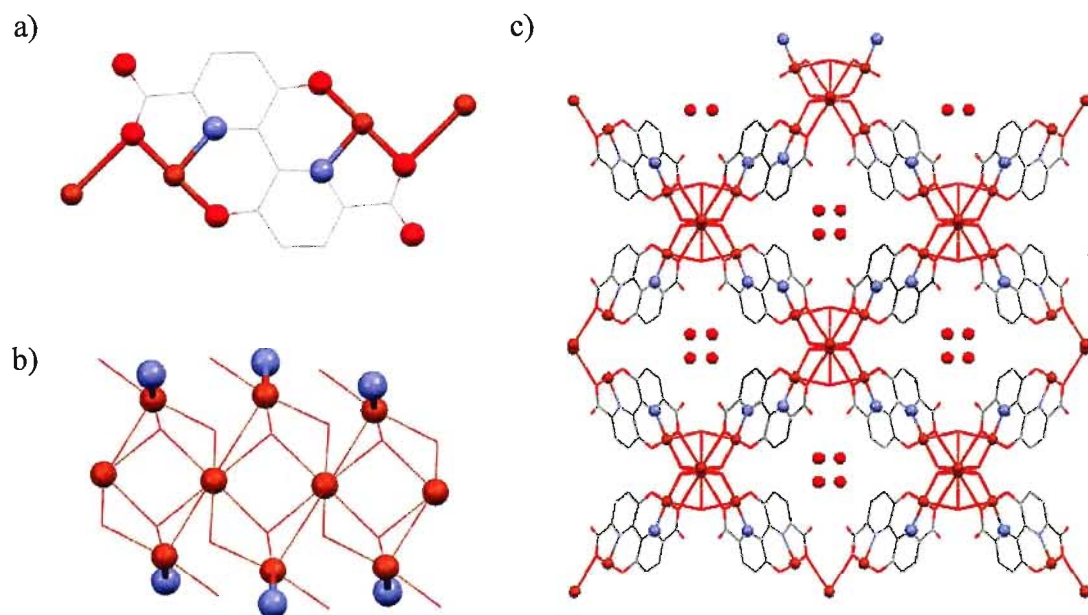
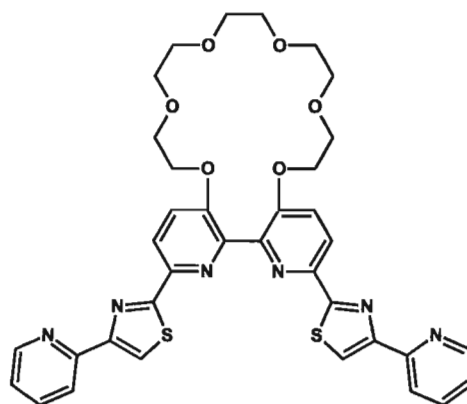


Figure 1.21 Molecular structure of the coordination polymer of **1.18**, a) the coordination environment of one ligand, b) view of copper chain, c) packing diagram viewed down the *b*-axis. Hydrogen atoms are omitted for clarity.⁸⁴

The steric hindrance caused by the substituents in the 3,3' positions has been successfully used to control the twist between the pyridine rings. Derivatization of ligand **1.11** affords the polydentate crown ether-type ligand **1.19**.⁸⁵ Coordination of this ligand with $\text{Cu}(\text{ClO}_4)_2$ gives a dinuclear double helicate complex of formula $[\text{Cu}_2(\mathbf{1.19})_2](\text{ClO}_4)_4$ (**1.20**), that has been characterized by single crystal X-ray diffraction. The crystal structure shows that the binding sites of the ligand are split into two *bis*-tridentate pockets that coordinate two different Cu^{2+} ions. The metal centres are in a distorted octahedral coordination environment formed by two *bis*-tridentate pockets from different ligand molecules. Reaction of Li^+ , Na^+ or Ba^{2+} salts in solution with the Cu^{2+} complex **1.20** resulted in the coordination of the cations by the crown ether affording complexes

1.21 - 1.23 respectively. The X-ray crystal structure showed that coordination of the crown ether to the *s*-group cation causes an increase of the torsion angle between pyridine rings of the ligand. This additional twist caused an elongation of the helicate, moving the Cu²⁺ ions away from each other. Table 1.1 shows how the distance between the paramagnetic centres changes depending on the metal cation chelated by the crown ether.



1.19

Coordination to a metal centre causes a conformational change in the crown ether, the extent of which depends on how good a match is the cation to the size of the macrocycle. A better size match means that the cation is coordinated by more oxygen atoms of the crown ether. As the crown ether becomes more rigid due to better coordination to the metal centre, it starts twisting the pyridine rings of the ligand away from coplanarity, much like as if the crown ether is functioning like the bridle of a horse steering the pyridine rings. This cation dependency is an uncommon feature, as normally the final structure of the helicate is set by the ligand topology and metal coordination geometry.³⁵ In this respect, modification of the helicate usually requires the modification of the ligand or coordination to a different metal centre.⁸⁶ The authors pointed out that even though an allosteric effect seemed to be dictating the structural changes, electrostatic repulsion between the charges of the Ba²⁺ ions could not be ruled out.

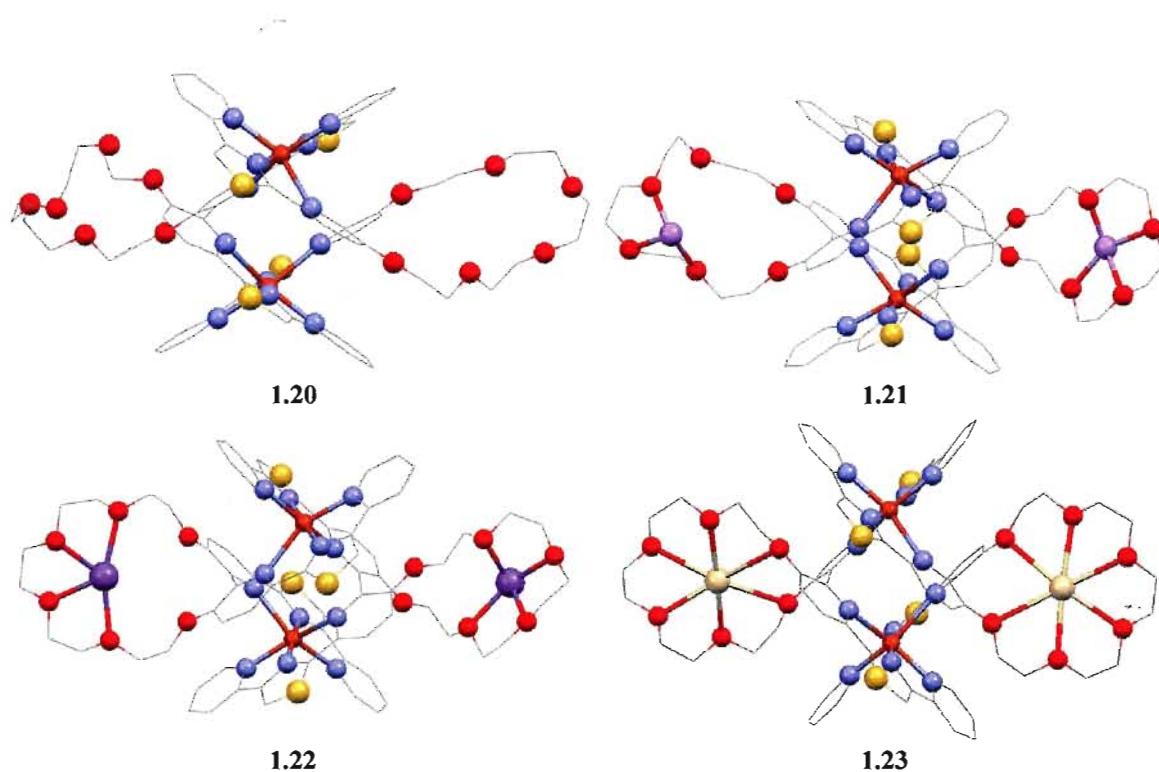


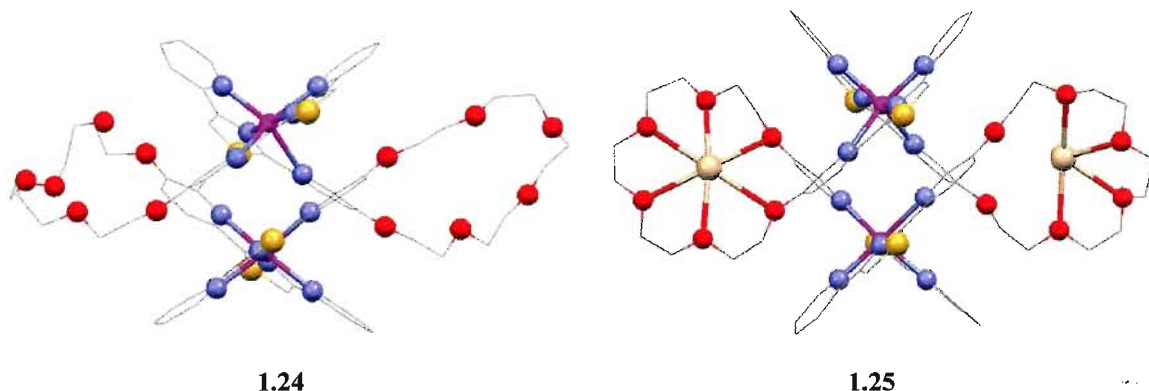
Table 1.1 Selected bond lengths and angles for helicates **1.20** - **1.23**.⁸⁵

	Cu-Cu distance (Å)	NCCN torsion angles ^a (°)
1.20	4.871(1)	62.0
1.21 (Li ⁺)	5.034(1)	66.1
1.22 (Na ⁺)	5.043(1)	70.3
1.23 (Ba ²⁺)	5.261(1)	80.2

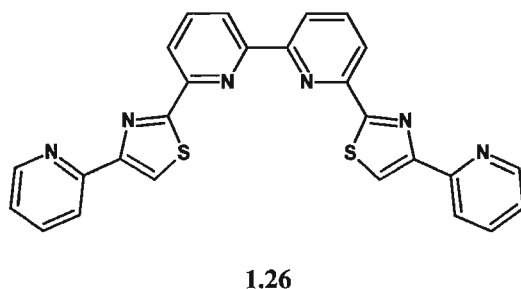
^a Average of the two NCCN torsion angles.

The effect of the s-group cation over the coordination chemistry of **1.19** also seems to be dependent on the nature of the transition metal ion.⁸⁷ Coordination of this ligand to Zn²⁺ gave the double strand helicate **1.24** and, upon reaction with Ba²⁺, formed the corresponding salt **1.25**. As expected, the coordination of the crown ether caused an increase in the distance between Zn²⁺ ions in the helicate, from 4.812(1) to 5.142(1) Å. Monitoring of a reaction of a mixture of ligands **1.19** and **1.26** with Zn²⁺ ions in solution by ¹H NMR revealed that each ligand formed preferentially homoleptic complexes,, and only about 5% of heteroleptic complex seemed to be present. This result was ascribed to the difference in coordination behaviour between both ligands. While the substituents in

the 3,3' positions force the pyridine rings of ligand **1.19** away from coplanarity, allowing it to behave as a *bis*-tridentate ligand, the pyridine rings of ligand **1.26** have no such restrictions and remain mostly coplanar, resulting in *bis*-bidentate coordination.^{88,89}



Although five-coordinate Zn^{2+} cations are also possible, there are no precedents for ligands **1.19** and **1.26** forming Zn^{2+} complexes with this coordination number. Addition of a large excess of Ba^{2+} ions to this mixture caused an increase of the heteroleptic complex in solution, and the amount of homoleptic complexes decreased by the same amount as seen by ^1H NMR spectroscopy. In order to rule out an allosteric effect as the driving force for the loss of ligand self-recognition, K^+ was added to a mixture of **1.19** and **1.26** instead of Ba^{2+} . The resulting mixture showed no increase in the amount of heteroleptic complex, even though the K^+ ion has a very similar ionic radius to the Ba^{2+} cation. This indicated that the main driving force for the loss of self-recognition seemed to be the electrostatic repulsion between cations caused by the addition of Ba^{2+} cations in the homoleptic complex.



Amines have been traditionally incorporated into ligands as binding sites for metal cations, but reports describing the coordination chemistry of the amines in 3,3'-

diamino-2,2'-bipyridine (**1.12**) indicate that the amino groups in this molecule do not play a very active role in its coordination chemistry. The pool of metal complexes for **1.12** present in the literature is dominated by the coordination of bipyridine to metal centres,⁷² with only two accounts of coordination by the amino functionalities.⁹⁰ The typical structure of a *tris*-chelated **1.12** metal complex **1.27** is shown in Figure 1.22. The molecular structure of this complex reveals that the amino groups of the ligands show almost no pyramidalization, indicated by how close the amino hydrogen atoms are to the plane of the pyridine rings, Figure 1.22, b). This is a trait that all complexes share with the structure of the uncoordinated ligand, pointing at a very strong delocalization of the nitrogen lone pair through the bipyridine backbone.

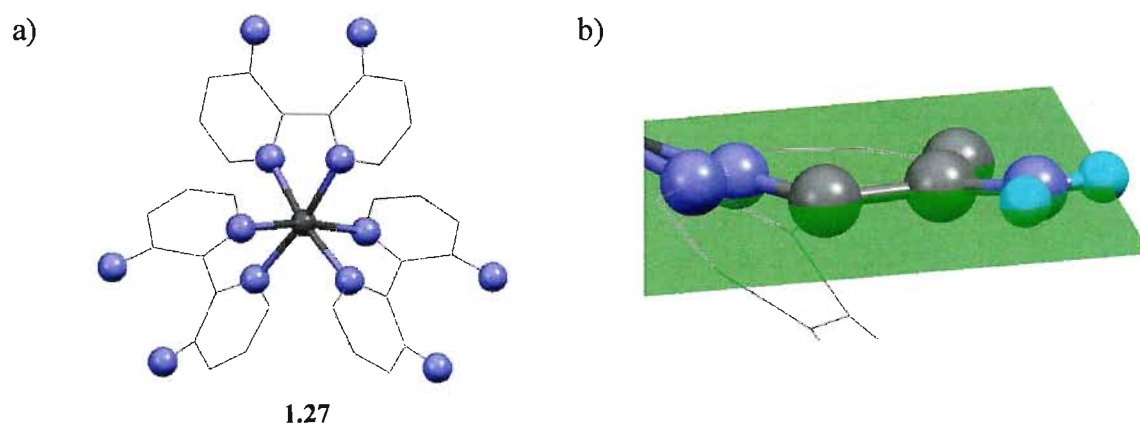
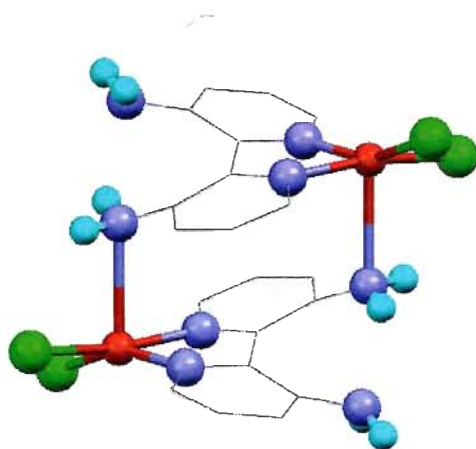
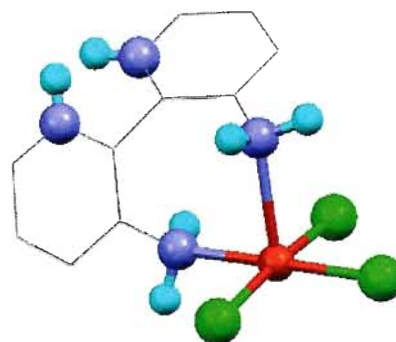


Figure 1.22 a) Typical structure of a *tris*-chelated **1.12** metal complex. b) Best plane of the pyridine ring shown in green.^{72c}

The only two examples of amino coordination of ligand **1.12** have been reported by Pilkington *et al.*^{72c} Complex **1.28** is a dimer of Cu^{2+} ions which adopts a distorted square pyramidal coordination geometry. The apical positions are occupied by an amino group of the *other* ligand molecule in the dimer. Interestingly, the hydrogen atoms of the amino groups are not coplanar with their corresponding pyridine ring, showing a marked degree of pyramidalization. This applies not only to the coordinated amino group, but also to the uncoordinated amino group in the same ligand molecule. Complex **1.29** was obtained by reacting ligand **1.12** with CuCl_2 in dilute hydrochloric acid. In this case, the bipyridine nitrogen atoms are protonated, and *both* amino groups coordinate the same Cu^{2+} ion.

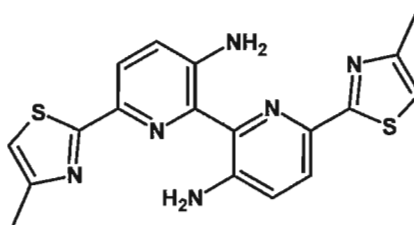


1.28

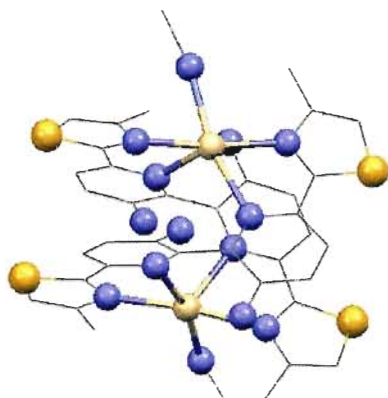


1.29

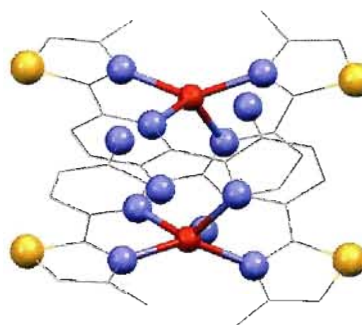
As for the dihydroxy ligand **1.11** previously reviewed, the introduction of additional binding sites to enhance the coordination capability of the amino groups of **1.12** is a strategy that has been exploited. The addition of two thiazole rings in this manner affords ligand **1.30** shown below.⁹¹ This potentially *bis*-tridentate ligand coordinates Cd^{2+} and Cu^+ ions, affording the corresponding complexes **1.31** and **1.32** respectively. In both complexes, the ligand behaves as a *bis*-bidentate ligand, leaving the amino groups uncoordinated, but the presence of the amino groups does have an impact in the coordination chemistry of this ligand.



1.30

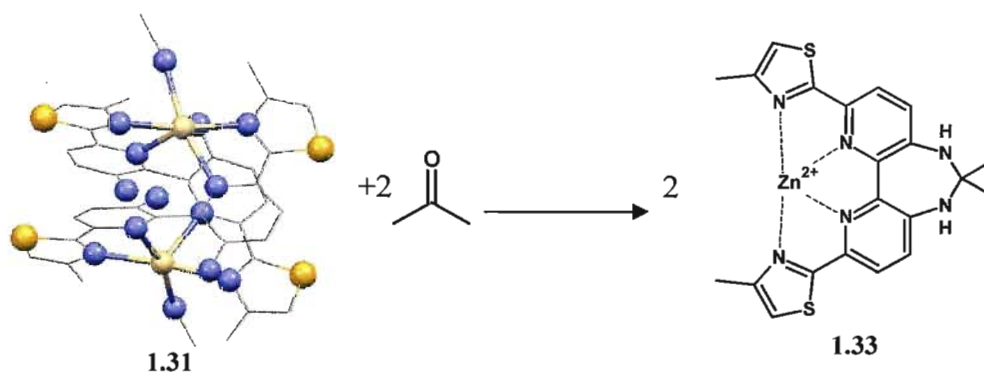


1.31



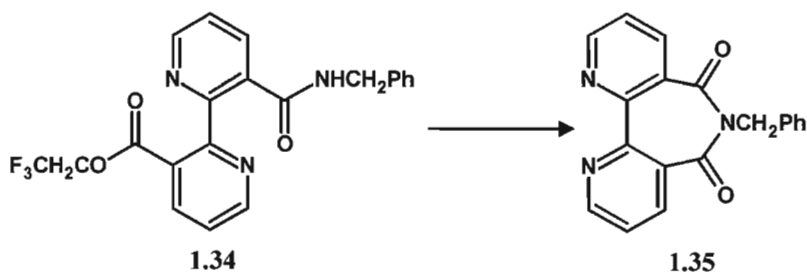
1.32

For the Cd^{2+} complex **1.31**, ^1H NMR studies revealed that in solution the helicate complex afforded an equilibrium between helicate and mononuclear species. Addition of this mixture to acetone resulted in the formation of **1.33**, where both free amino groups are now part of a 7-membered macrocycle. This reaction was reported not to occur with the Cu^+ complex **1.32**. The author attributed this to the preference of Cu^+ ions for tetrahedral over square planar coordination geometry. The author proposed⁹¹ the formation of the 7-membered macrocycle *via* the formation of an imine bond between one amino group and one acetone molecule and posterior nucleophilic attack of the second amino group, but no proof was provided.



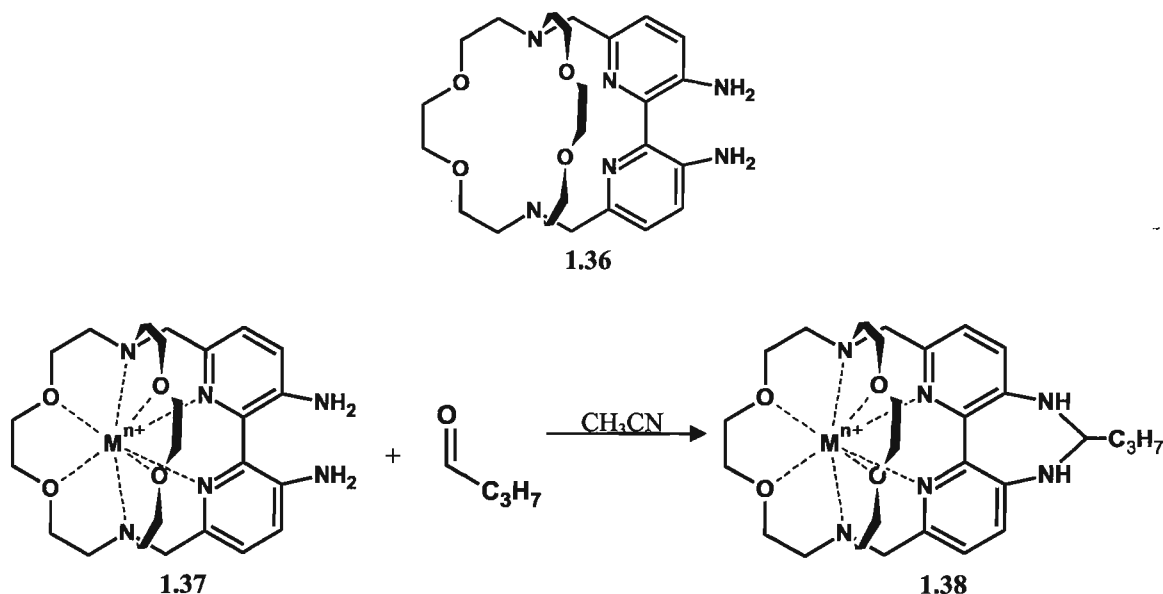
Scheme 1.3 Reaction diagram of the Zn^{2+} complex **1.31** with acetone to afford **1.33**. Reaction conditions: acetonitrile, room temperature.⁹¹

The proposed mechanism is supported by the work reported by Rebek *et al.*⁹² concerning metal-catalyzed intramolecular cyclization reactions. In this respect, Rebek showed that the rate of intramolecular cyclization of the model system **1.34**, in which an aminobenzyl arm functions as a nucleophile and a trifluoroacetate arm is the electrophile, could be enhanced by coordination of the bipyridine backbone to NiCl_2 (Scheme 1.4).



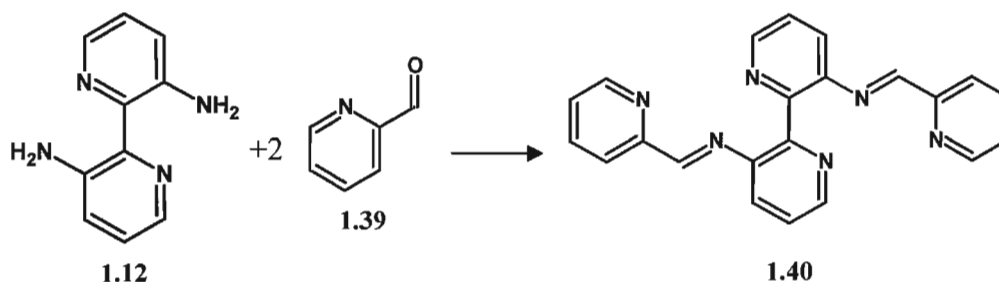
Scheme 1.4 Reaction diagram of the metal-catalyzed intramolecular cyclization reaction of **1.34** into **1.35**. Reaction conditions: i) NiCl_2 , DMSO, heating.⁹²

A related approach has been used for the preparation of luminescent cryptane complexes. Coordination of the non-luminescent ligand **1.36** with a host of metal cations, resulted in a series of cryptane complexes (**1.37**) capable of undergoing a cyclization with butanal to afford 7-membered macrocyclic cryptane complexes (**1.38**).⁹³ These complexes display highly metal-dependent luminescence properties.



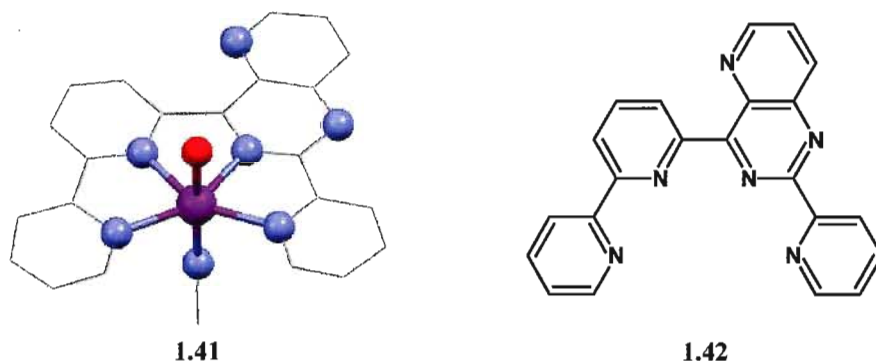
Scheme 1.5 Reaction scheme of the formation of the family of luminescent complexes **1.38**. $M^{n+} = Li^+, Na^+, K^+, Mg^{2+}, Ca^{2+}, Ba^{2+}, Fe^{3+}, Co^{2+}, Ni^{2+}, Cu^{2+}, Zn^{2+}, Cd^{2+}, Hg^{2+}$.⁹³

One strategy to encourage the amino nitrogen atoms to play a role in coordination is to transform them into Schiff-bases. Ligands presenting Schiff-bases have been used extensively in coordination chemistry.^{6,94} The condensation of **1.12** with 2-pyridylaldehyde **1.39** was used by the Pilkington group to prepare the potentially *bis*-tridentate ligand **1.40**, Scheme 1.6.⁹⁵ Reaction of this ligand with an excess of $Co(ClO_4)_2$ led to an unusual rearrangement of ligand **1.40** to yield the quarterpyridine-type complex **1.41**.

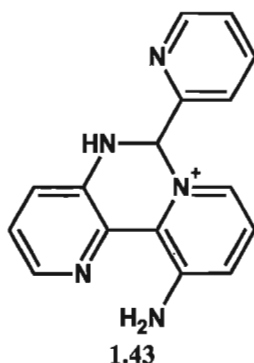


Scheme 1.6 Reaction diagram for the synthesis of ligand **1.40**. Reaction conditions: toluene, 4 Å molecular sieves, reflux, 4 days.⁹⁵

The Co^{2+} ion is coordinated in the equatorial plane by three pyridine rings and one pyrido[2,3-d]pyrimidine ring of the ligand **1.42**. The distorted octahedral environment of the metal centre is completed by water and acetonitrile solvent molecules coordinating in the axial positions.

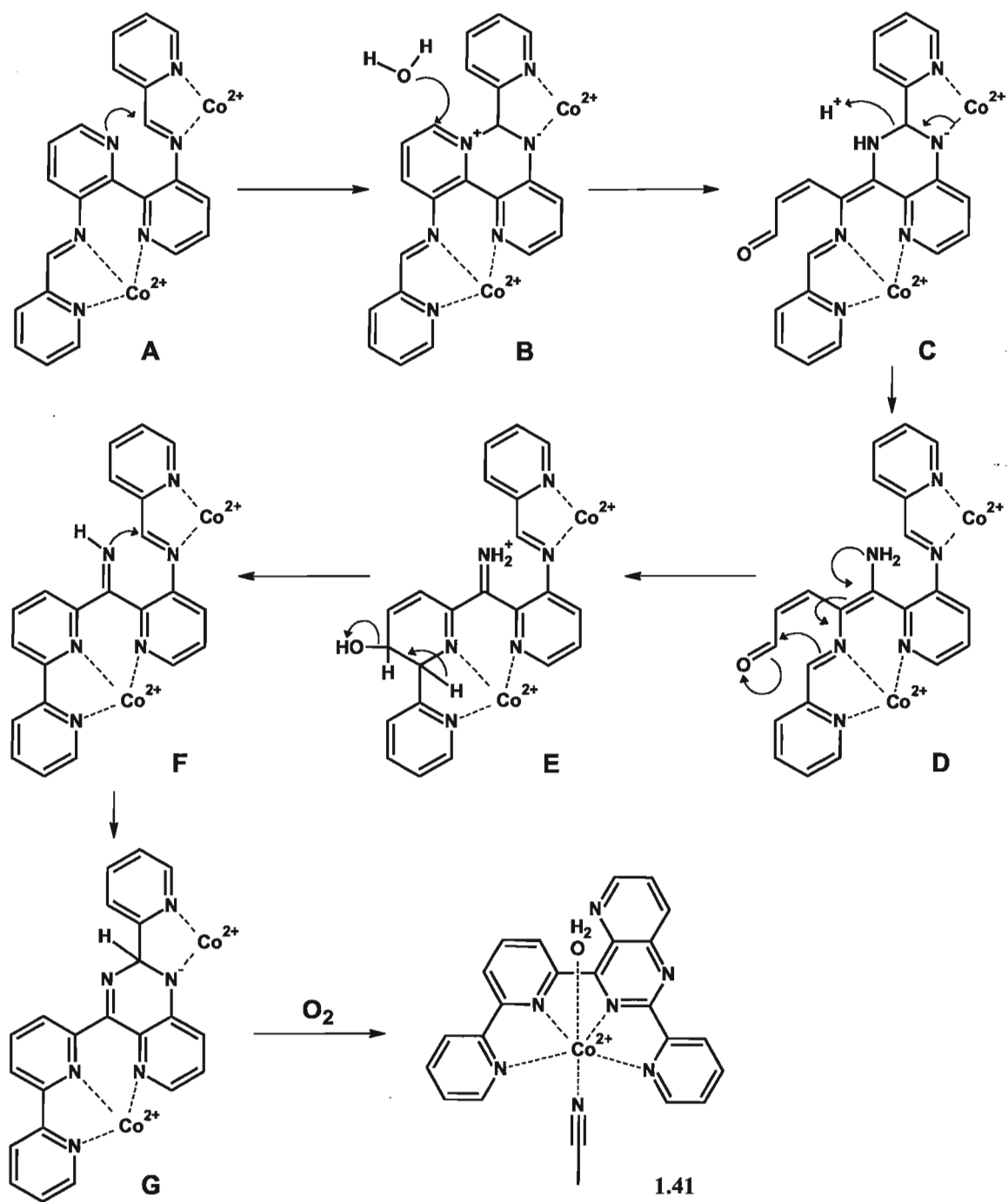


The proposed mechanism for the formation of **1.42** is illustrated in Scheme 1.7. In the first step, a pyridine nitrogen does an intramolecular nucleophilic attack on an iminic carbon, affording the pyrididinium salt **B**. The crystal structure of the pyridinium salt **1.43** was provided as support for the formation of **B**. Although **1.43** was prepared in the presence of dilute HCl, the authors suggested that the presence of the Lewis acidic Co^{2+} ions may have played a similar role, enhancing the electrophilicity of specific bonds through coordination.⁹⁵

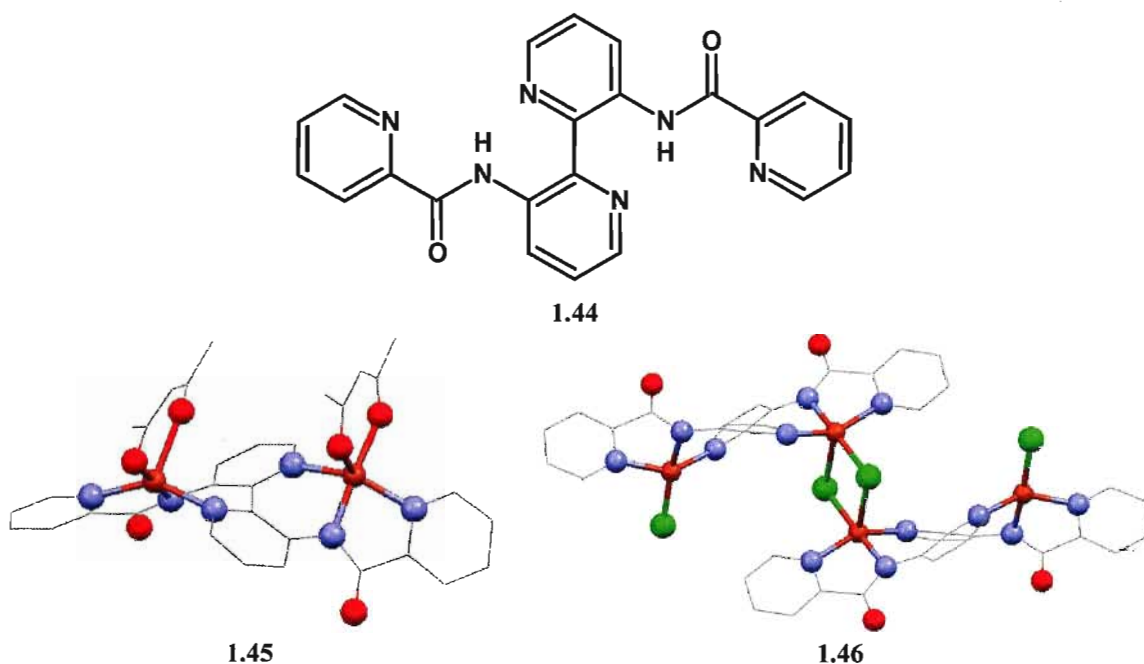


The pyridinium ring is then hydrolyzed to give aldehyde **D**, which after a series of rearrangements affords the *ter*-pyridine-like ligand in **F**. The activated (coordinated) imine in **F** then undergoes a nucleophilic addition with the neighbouring imine, and a subsequent oxidation affords the fourth aromatic ring in **1.41**.

Following a different approach, the Pilkington group also targeted the derivatization of the amino groups of **1.12** into carboxamide functionalities in order to take advantage of the greater robustness of this functional group.⁹⁶ In this respect, reaction of 2-pyridinecarbonyl chloride with **1.12** yielded the potentially *bis*-tridentate ligand **1.44** that was subsequently reacted with Cu(hfac)₂ and CuCl₂ salts to obtain complexes **1.45** and **1.46**.⁹⁶ In both cases the ligand coordinates in a *bis*-tridentate manner, forming dinuclear complexes of Cu²⁺.



Scheme 1.7 Proposed mechanism for the rearrangement of the 1.40 to afford complex 1.41.⁹⁵



The overlay presented in Figure 1.23 shows how in both complexes ligand **1.44** coordinates the two Cu^{2+} ions in a very similar manner. In complex **1.45**, the structure is monomeric because the two hfac ligands complete the 6-coordinated environment of the Cu^{2+} ions. In contrast, in complex **1.46**, two of the four chloride ions act as bridging ligands, facilitating the formation of a dimer. Magnetic susceptibility measurements revealed weak inter- and intramolecular antiferromagnetic interactions present in **1.45** probably due to the isolated nature of the paramagnetic centres. In **1.46**, a fitting of the magnetic characterization revealed strong ferromagnetic interactions between the chloro-bridged Cu^{2+} ions and weak antiferromagnetic interaction between these Cu^{2+} ions and the non-bridged Cu^{2+} ions.

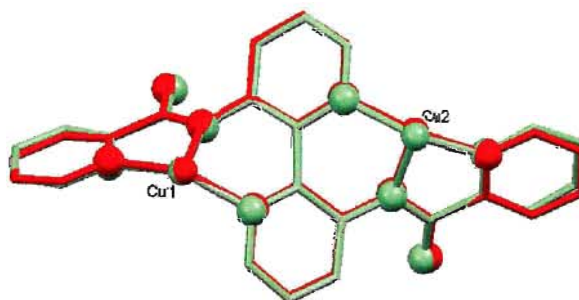
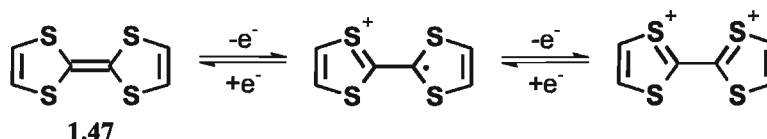


Figure 1.23 A structural overlay of the two ligands and Cu^{2+} atoms obtained from the crystal structures **1.45** (red) and **1.46** (green).

1.3.3 Strategies for the preparation of magnetic and conductive molecular materials

In the previous sections, examples in which particular ligands have been modified in order to change their coordination chemistry and/or the magnetic properties of their complexes have been discussed. In this section, electroactive multifunctional materials will be introduced, and examples of ligand design applied for the preparation of multifunctional materials will be illustrated.

Although organic materials are normally insulators, during the last three decades, new types of organic materials have appeared that behave as semiconductor, metallic conductors and superconductors.^{5,97} In this respect, charge-transfer (CT) salts are organic molecular materials formed by the transfer of electron density from a donor to an acceptor. The electrical conductivity these materials display arises from the movement through the lattice of unpaired electrons present in the donor, acceptor or both.^{98,99} Tetrathiafulvalene (TTF, **1.47**) has been intensely researched for the preparation of CT salts and has been used to introduce conductive properties into molecular materials.^{5,99-102} TTF is a nonaromatic 14- π -electron system with three stable oxidation states accessible reversibly at low potentials, which can be finely tuned by modifying the parent molecule with electron-donating or electron-withdrawing groups, Scheme 1.8.¹⁰³ It is also important that the planarity of TTF and its derivatives allows for the formation of dimers or highly ordered stacks, stabilized by π - π and sulfur-sulfur interactions.¹⁰³ In general, the oxidation of TTF can be carried out chemically or electrochemically, and only the radical cation state affords itinerant electrons that can give rise to electrical conductivity.¹⁰³



Scheme 1.8 Oxidation states of TTF.¹⁰⁰

In 1973 the charge transfer (CT) complex TTF-TCNQ (TCNQ stands for 7,7,8,8-tetracyano-p-quinodimethane) was reported as the first organic conductor to display

metallic conductivity ($\sigma_{\text{H}} = 400 \text{ } \Omega \text{ cm}^{-1}$).¹⁰⁴ In this CT salt, TTF was only partially oxidized, presenting a charge transfer of $\rho = 0.59$.¹⁰⁵ The structure of TTF-TCNQ, shown in Figure 1.24, comprises segregated stacks of TTF donors and TCNQ acceptors. The overlap of the molecular orbitals of TTF and TCNQ happens mainly along the stack direction and is much weaker between stacks.¹⁰⁵ This means that the electrical conductivity is highly anisotropic, that is, the electrical conductivity measured parallel to the crystallographic direction of the stacks is orders of magnitude higher than the electrical conductivity measured perpendicular to the stacks. High anisotropy of electrical conduction is a common trait among many TTF-based CT salts, which are considered quasi-1D electrical conductors.^{105a}

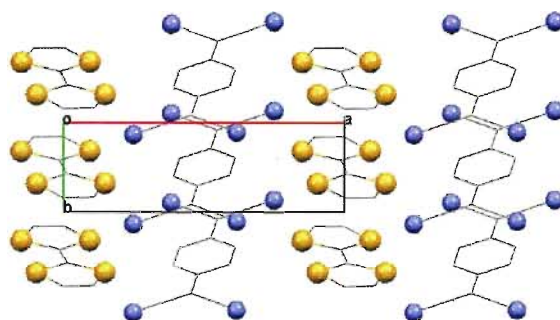


Figure 1.24 Packing diagram of the TTF-TCNQ CT salt viewed down the *c*-axis.^{105b}

The replacement of sulfur by selenium in TTF derivatives resulted in CT salts with higher electrical conductivities.^{105a} This effect is due to the reduced on-site electron repulsion caused by the higher electron polarizability of the heavier chalcogens. This led to the discovery of superconductivity in the related (TMTSF)(PF₆)¹⁰⁶ (TMTSF = tetramethyltetraselenafulvalene, **1.48**) radical cation salt. This product was obtained by electrocrystallization, and its crystal structure displays stacks of TMTSF radical cations separated by PF₆[−] counterions. The electrical conductivity of this salt is also very anisotropic due to the lack of intermolecular contacts between TMTSF stacks, which makes it also a quasi-1D electrical conductor.

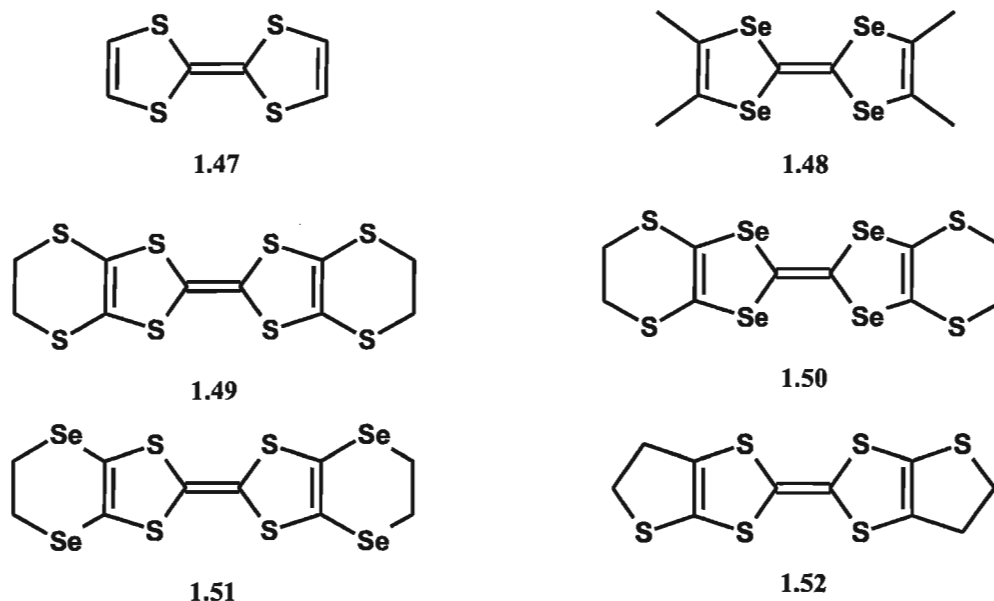


Figure 1.25 Molecular structures of TTF **1.47** and some common derivatives.¹⁰⁰

The structural 1-D character of many TTF-based CT salts makes them susceptible to a Peierls distortion at low temperatures. This means that, upon reaching a certain temperature, the lattice of the 1-D conductor undergoes a periodic distortion resulting from the dimerization of the molecules within a stack that present unpaired electrons. As a consequence, the unpaired electrons become localized and the electrical conductivity is lost.^{98,105} In order to avoid the Peierls distortion, TTF derivatives presenting additional chalcogen atoms were synthesized in order to increase the dimensionality of the lattice of their CT salts. These additional atoms allow the formation of interstack contacts, which enhance the stability of the conducting phases at low temperatures.^{5,107} Some of these derivatives can be seen in Figure 1.25.

In this respect, one of the most extensively explored derivatives is the donor BEDT-TTF (BEDT-TTF = *bis*(ethylenedithio)tetrathiafulvalene, **1.49**) that has been successfully used for the preparation of multifunctional materials presenting metallic conductivity and paramagnetism,¹⁰⁸ superconductivity and paramagnetism,¹⁰⁹ as well as metallic conductivity and ferromagnetism.¹¹⁰ In all of these materials, the electrical conductivity was supplied by stacks of oxidized BEDT-TTF donors, and their magnetic properties are provided by paramagnetic transition metal complexes or networks as the

anionic component. The first account of BEDT-TTF radical cations embedded in oxalate networks was reported by Day and coworkers.¹¹¹ In 1995 they reported three CT salts $(\text{BEDT-TTF})_4\text{AFe}(\text{C}_2\text{O}_4)_3\cdot\text{C}_6\text{H}_5\text{CN}$ ($\text{A} = \text{H}_2\text{O}, \text{K}^+, \text{NH}_4^+$), which displayed dramatically different conductivities depending on the nature of A. The Fe^{3+} oxalate network in the three salts was structurally very similar, but the different charge balance of the network, dictated by the nature of A, conditioned the electronic properties of the BEDT-TTF layers. The crystal structure of the salts with $\text{A} = \text{K}^+, \text{NH}_4^+$, showed the presence of radical cation dimers surrounded by neutral BEDT-TTF molecules. For $\text{A} = \text{H}_2\text{O}$, the organic layer was formed by stacks of evenly spaced BEDT-TTF radical cations. Variable temperature resistivity measurements showed that for $\text{A} = \text{K}^+, \text{NH}_4^+$, the charge transfer salts behaved as semiconductors, whereas for $\text{A} = \text{H}_2\text{O}$ the salt showed a metal to superconductor transition at 7 K, Figure 1.26. This was the first BEDT-TTF-based superconductor presenting paramagnetic transition metal ions in its structure.

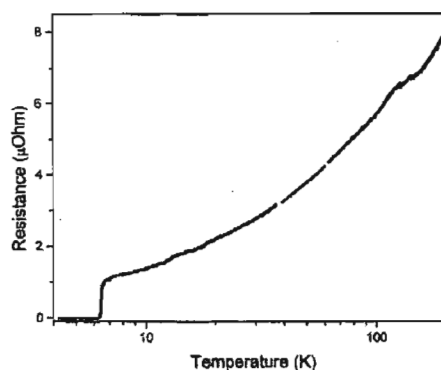


Figure 1.26 Temperature dependence of the resistance of $(\text{BEDT-TTF})_4(\text{H}_2\text{O})\text{Fe}(\text{C}_2\text{O}_4)_3\cdot\text{C}_6\text{H}_5\text{CN}$ for the 5–200 K range. Adapted with permission from 111. Copyright 1995 American Chemical Society.

More recently, Coronado *et al.* reported the coexistence of ferromagnetism and metallic conductivity in the single crystals of $(\text{BEDT-TTF})_3[\text{CrMn}(\text{ox})_3]$ grown *via* electrocrystallization.¹¹⁰ The crystal structure shows honeycomb layers of the bimetallic oxalato complex alternating with layered, slanted stacks of BEDT-TTF radical cations, as shown in Figure 1.27. Magnetic characterization showed that this material exhibited ferromagnetic ordering below 5.5 K, and single crystal resistivity measurements found that this material was a metallic conductor from room temperature to 2 K. The segregation of magnetic and conductive lattices present in this structure is representative

of BEDT-TTF-based multifunctional materials. Although the ferromagnetic interaction was introduced by carefully choosing an oxalate network known to have this behaviour, it is noteworthy that the authors of this study concluded that both conductivity and magnetism were electronically independent, displaying no communication between the two properties. Establishing an interplay between both properties is one of the current challenges preparing this kind of materials, where the segregated nature of the conductive and magnetic sublattices only allows interactions between them to happen *through space*.

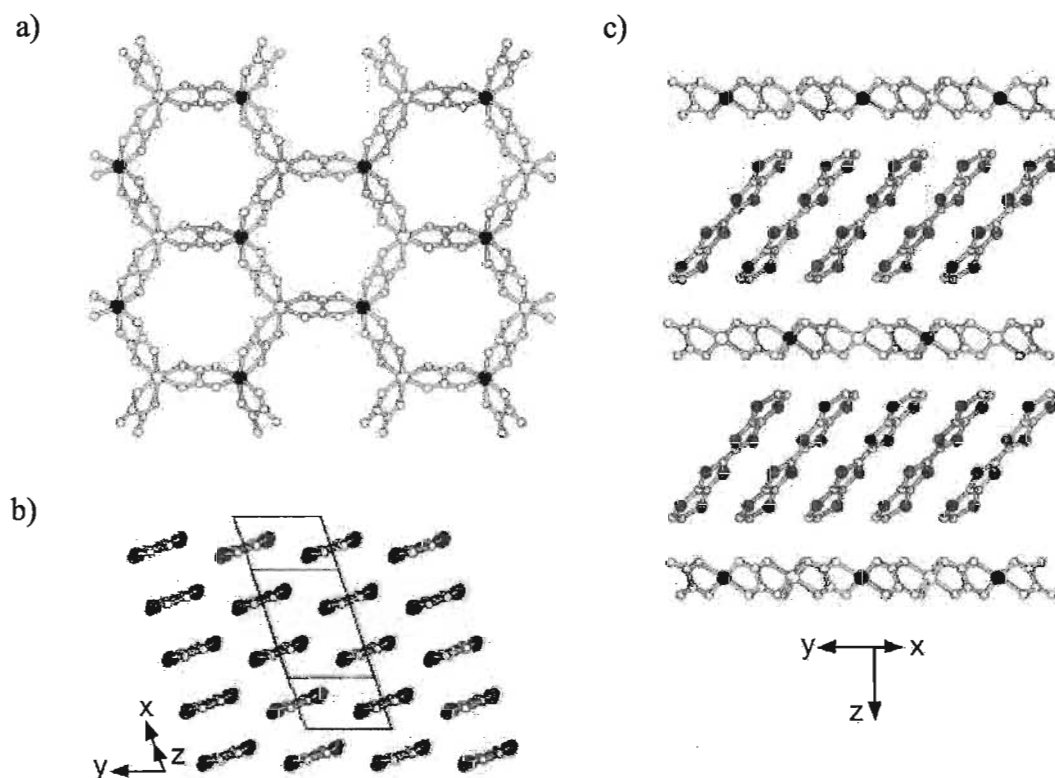


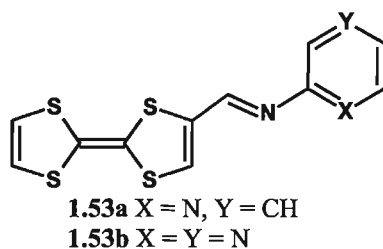
Figure 1.27 Crystal structure of $(\text{BEDT-TTF})_3[\text{CrMn}(\text{ox})_3]$. a) View of the $[\text{CrMn}(\text{ox})_3]^-$ network layers. The filled and open circles represent the two types of metals. b) Slanted stacks of **1.49** forming layers. c) View along the c -axis of the alternating layers. Reprinted with permission from Macmillan Publishers Ltd: Nature 110, copyright 2000.

The interaction between both lattices in these materials may induce exchange coupling between the d electrons through a mechanism similar to the Ruderman-Kittel-Kasuya-Yosida (RKKY) interactions in a metallic medium. In these interactions, the d electrons remain localized and the s - p electrons act as charge carriers, delocalized through the structure. The strong coupling existing between magnetic and conductive

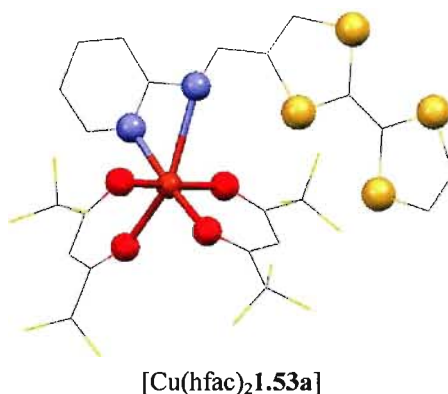
spins generates spin polarization in the electron flow, which in turn mediates the long-range magnetization between localized magnetic spins.^{102,112}

Therefore, in order to promote such π - d interactions between sublattices, there must be a) short *van der Waals* contacts between the molecular components of each sublattice, and b) magnetic spin density and conducting spin density on the atoms presenting short contacts between lattices, otherwise both properties would not interact. Obtaining a structure with two sublattices that meet these conditions is, in principle, possible, albeit difficult given the current limitations in crystal engineering. If the RKKY interactions (or something physically similar) apply, the strength of the *through space* interaction between sublattices is expected to be small, and the coupling between both kinds of spins weak.^{102,112}

This is why a second, *through bond* approach has been explored recently, which consists of joining the conducting and magnetic sublattices *via* covalent bonds. It is then necessary to design spin-polarized systems, in which both π and d spins coexist in the same molecule so that the itinerant electrons are delocalized enough to couple with the magnetic spins. The transformation of TTF and its derivatives into such a class of ligands has been addressed using ligands that include pyridine,¹¹³⁻¹¹⁷ imidazole,¹¹⁸ bipyridine,^{117,119,120} *ter*-pyridine,¹²¹ phenanthroline,¹²² acetylacetonate,¹²³ crown ethers^{119,124} and phosphines.¹²⁵ These ligands can be directly substituted on the TTF molecule or through the use of bridging units such as alkenes,¹¹³⁻¹¹⁵ alkynes,^{120,126} imines,^{114,127,128} hydrazines¹²⁹ and amides.^{117,130} The use of bridging units allows for further modification of the electronic communication between the TTF and ligand moieties. The bridging units can also participate in intermolecular interactions in order to direct the molecular packing in the solid state. Only a small subgroup of the available library of TTF ligands and their complexes will be discussed here.^{131,132}



In 2007, the first report of an imine-bridged pyridyltetrathiafulvalene building block **1.53a** was published by the Pilkington group.¹²⁸ The purpose of imine bridges was twofold: i) to bring the influence of the *d* electrons towards the π electrons of TTF through the conjugated imine and ii) to promote planarity in the coordinated complex, potentially enhancing the through bond π -*d* interactions. This ligand was synthesized *via* the Schiff-base condensation of formyltetrathiafulvalene and 2-aminopyridine, and it was subsequently coordinated to Cu(hfac)₂, affording the complex [Cu(hfac)₂**1.53a**]. The coordination environment of the Cu²⁺ ion can be described as a distorted octahedron formed by the oxygen atoms of two hfac ligands and by one molecule of **1.53a** coordinating with the pyridyl and imino nitrogen atoms. It is worth noting that such coordination gives a less thermodynamically stable four-membered ring. The coordinated ligand is almost planar, and the central C=C bond length is 1.343(3) Å, which is consistent with a neutral TTF. The uncoordinated ligand showed the expected two reversible oxidation potentials for the TTF moiety, at 0.490 and 0.880 V, which were anodically shifted when compared to the unsubstituted TTF molecule (0.380 and 0.770 V). This shift can be attributed to the electron withdrawing nature of the pyridine ring. The cyclic voltammogram of the Cu²⁺ complex showed a greater anodic shift of the oxidation potentials of TTF, 0.530 and 0.900 V, resulting from the enhanced electron withdrawing capability of the coordinated pyridine ring. Magnetic characterization of this complex showed an almost perfect Curie paramagnet behaviour with a very small Weiss constant of $\theta = -0.01$ K). Unfortunately, no radical salts of this complex have been reported to-date.



A couple of years later, the electrocrystallized imino-pyrazine derivative **1.53b** was reported along with Mn²⁺, Co²⁺, Cu²⁺ and Zn²⁺ complexes of the neutral ligand.¹²⁷ In this case, the objective behind introducing a pyrazine moiety was to achieve chelation as in **1.53a** and, at the same time, coordinate through the second N atom of the pyrazine heterocycle. Ligand **1.53b** was successfully electrocrystallized, yielding the radical cation salt (**1.53b**)PF₆. The X-ray structure shows planar ligands forming 1-D stepped chains, forming TTF dimers and pyrazine pairs on each step, Figure 1.28. Conductivity measurements on single crystals at room temperature gave a conductivity of 1.5 kΩ cm⁻¹.

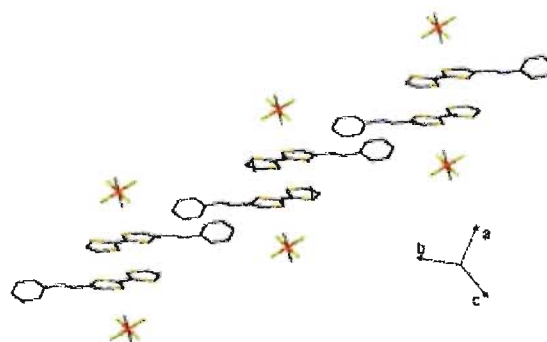
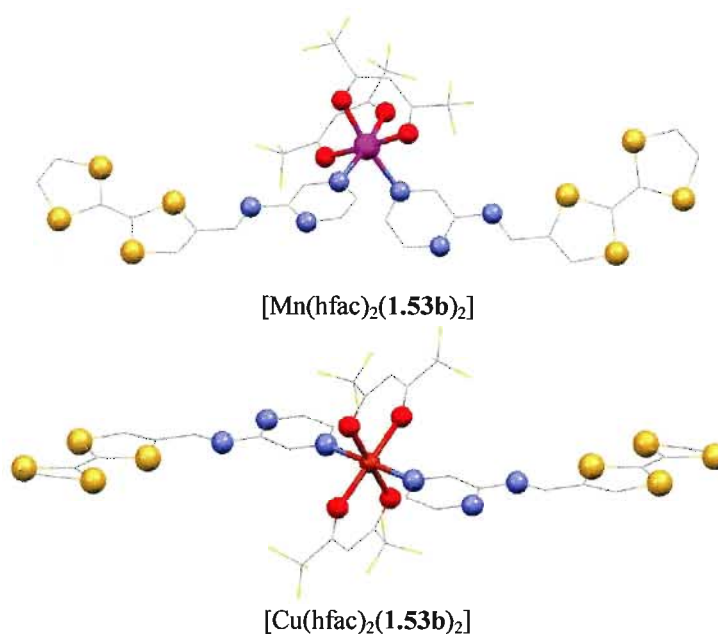


Figure 1.28 Packing diagram of (**1.53b**)PF₆. Figure adapted from reference 127. Reproduced by permission of The Royal Society of Chemistry.

The coordination environment of the Mn²⁺ ion in [Mn(hfac)₂(**1.53b**)₂] can be described as a distorted octahedron formed by the two oxygen atoms of both hfac ligands and by the nitrogen atom of two **1.53b** ligands in a *cis* manner with respect to each other. The ligands do not chelate the metal, but rather act as monodentate ligands coordinating through the N atom farther away from the imino bond. The same coordination mode is

present in the $[\text{Cu}(\text{hfac})_2(\mathbf{1.53b})_2]$ complex, but in this case the TTF ligands are *trans* with respect to each other. In both cases, the crystal structures show long S...S distances, consistent with neutral TTF ligands. The packing diagrams reveal that, in both complexes, the ligand molecules are arranged in a head-to-tail manner. Electrochemical characterization of both complexes showed two reversible oxidations that are anodically shifted when compared to those of the free ligand. This means that the TTF moieties do not interact with each other and the pyridine ring is more electron withdrawing once coordinated to the metal centre. To the best of our knowledge, no radical salts of these complexes have been reported to-date.



The closely related ligand **1.54** has also been coordinated to Mn^{2+} , Cu^{2+} and Co^{2+} salts, forming mononuclear,¹¹³ dinuclear¹³³ as well as homo- and hetero-trinuclear complexes.¹³⁴ The mononuclear complexes of this ligand have the same stoichiometry as the complexes of **1.53b**, with two ligands per metal centre that are coordinated in a *cis* manner for $[\text{Mn}(\text{hfac})_2(\mathbf{1.54})_2]$ and *trans* for $[\text{Cu}(\text{hfac})_2(\mathbf{1.54})_2]$.¹¹³

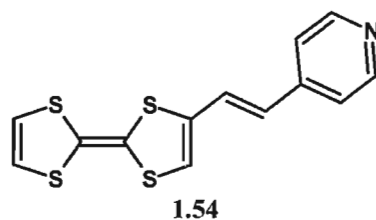
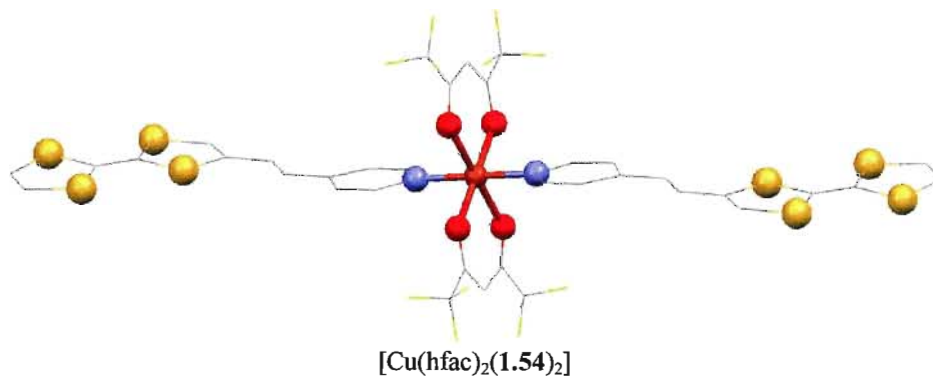


Figure 1.29 Crystal structure of complex $[\text{Mn}(\text{hfac})_2(\mathbf{1.54})_2]$. Reprinted from reference 113 with permission from Elsevier.

The electrochemical characterization of both complexes showed two reversible oxidation bands anodically shifted when compared to those of the free ligand. This means that the TTF moieties do not interact with each other and the pyridine ring is more electron withdrawing once coordinated to a metal centre. SQUID measurements performed between 5 and 300 K determined that the metal centres in $[\text{Mn}(\text{hfac})_2(\mathbf{1.54})_2]$ and $[\text{Cu}(\text{hfac})_2(\mathbf{1.54})_2]$ behave as would be expected for non-interacting paramagnets, with $\chi T = 4.4$ and $0.4 \text{ emu K mol}^{-1}$.



The Cu^{2+} complex $[\text{Cu}(\text{hfac})_2(\mathbf{1.54})_2]$ is one of the very few examples of a coordination complex of a TTF ligand that has been electrocrystallized successfully. The two reported radical cation salts, $[\text{Cu}(\text{hfac})_2(\mathbf{1.54})_2](\text{PF}_6)^{135}$ and $[\text{Cu}(\text{hfac})_2(\mathbf{1.54})_2](\text{BF}_4)^{136}$ share the same 1-D chain motif that can be seen in Figure 1.30. The chains are formed by the π - π stacking of neighbouring TTF molecules into dimers. Although the general structural traits for both salts are similar, ligand **1.54** has a different oxidation state in each salt. In the PF_6^- salt, the shortest S \cdots S intradimer contacts are 3.593(3) Å, and based on the charge balance of the complex, each TTF has a charge of +0.5. EPR characterization of a powdered sample of $[\text{Cu}(\text{hfac})_2(\mathbf{1.54})_2](\text{PF}_6)$ showed a spectrum characteristic for a Cu^{2+} ion with a tetragonally elongated octahedral geometry, but the signal for the TTF radical could only be seen if the sample was dissolved in acetonitrile, indicating the dissociation of the radical pairs. Magnetic susceptibility measurements of the PF_6^- salt performed between 1.9 and 300 K showed weak antiferromagnetic interactions ($\theta = -3.8$ K). The effective moment $\mu_{\text{eff}} = 1.84 \mu_{\text{B}}$ at room-temperature was attributed to the presence of $S = 1/2$ Cu^{2+} ions. The absence of any contribution by the TTF radical cation was attributed to the charge disproportionation of the TTF dimers into neutral dimers and magnetically silent dimers of antiferromagnetically coupled radical cations, as depicted in Figure 1.31.

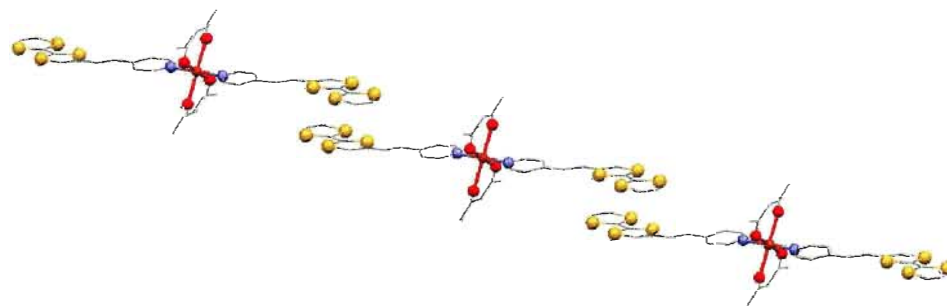


Figure 1.30 1-D chain present in $[\text{Cu}(\text{hfac})_2(\mathbf{1.54})_2](\text{PF}_6)$ and $[\text{Cu}(\text{hfac})_2(\mathbf{1.54})_2](\text{BF}_4)$. Hydrogen and fluorine atoms not shown for simplicity.¹³⁵

In the BF_4^- salt, the shortest S \cdots S intradimer contacts are 3.289(2) Å and, based on the charge balance of the complex, each TTF has a charge of +1. EPR characterization of a powdered sample showed that, as for the PF_6^- salt, only the Cu^{2+} was contributing to the

spectrum and that the signal for the TTF radical was only observable upon dissolution of the powder in DMF. This was again attributed to the charge disproportionation of the TTF dimers into neutral dimers and magnetically silent dimers of antiferromagnetically coupled radical cations (Figure 1.31). No conductivity measurements for either salt have been reported to-date.

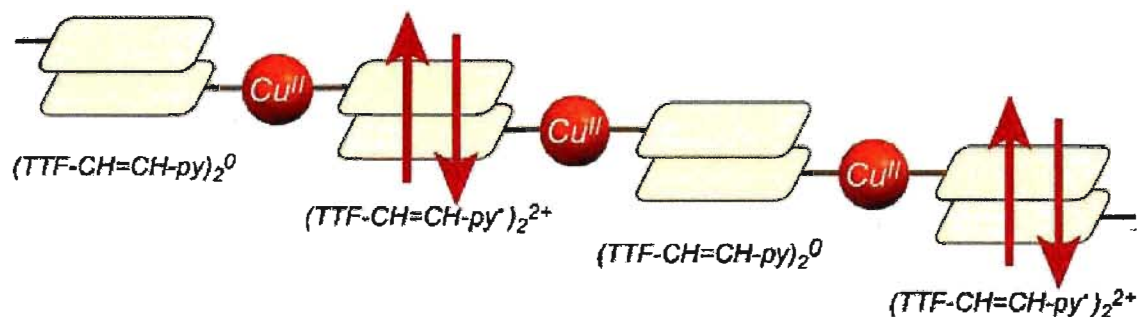
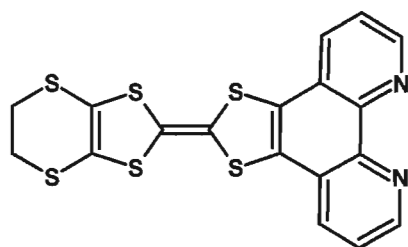
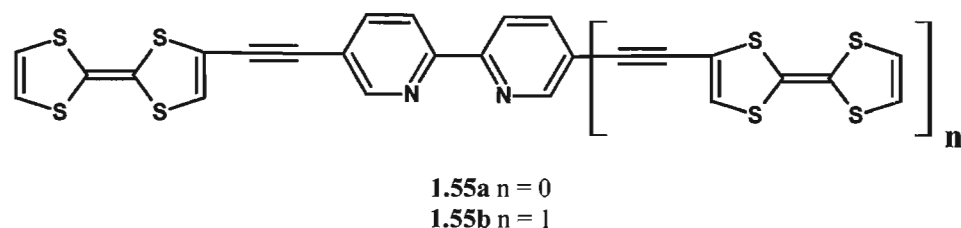
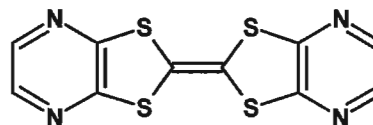


Figure 1.31 Schematic representation of the charge disproportionated chains for $[\text{Cu}(\text{hfac})_2(\mathbf{1.54})_2](\text{PF}_6)$ and $[\text{Cu}(\text{hfac})_2(\mathbf{1.54})_2](\text{BF}_4)_2$. Figure reprinted from reference 137 with kind permission from Springer Science and business Media.

Substitution of a 2,2'-bipyridine moiety on the TTF core has been carried out by different authors in order to achieve a higher degree of coordination predictability and structural control. Ligands **1.55a**¹²⁰ and **1.56**¹²² have been used to study the luminescence of the corresponding Ru^{2+} complexes, rather than for the formation of paramagnetic complexes, but they deserve a comment simply from a structural perspective.



1.56



1.57

Electrochemical characterization of both ligands showed the expected reversible oxidation potentials consistent with the TTF core, and their UV-Vis spectra show bands that could be assigned to intramolecular charge transfer (ICT) bands. The single crystal structure of **1.56** shows that this ligand is flat, which could make the packing of the radical cation salts more predictable and more favourable for electrical conductivity. Although both ligands are suitable candidates for the preparation of magnetic and conducting materials, to the best of our knowledge no such endeavours have been reported to-date.

In TTF-annulated systems such as **1.56**, the coordinating group is always coplanar with the TTF core, a trait that eliminates the possibility of losing communication between conducting and magnetic spins as seen in the organic spin-polarized systems discussed above. Moreover, this feature may even enhance the possibility of an interplay between magnetic and conducting spins. Ligand **1.57** presents two pyrazine rings fused with a TTF core.¹³⁸ The crystal structure of the complex $\text{CuCl}_2(\mathbf{1.57})$ is shown in Figure 1.32. It comprises planar zig-zag chains of the complex, with all the ligand molecules forming slanted stacks that run down the *c*-axis. In this structure, the Cu^{2+} ions adopt a square planar geometry formed by two chloride ions and two pyrazine nitrogen atoms. Variable temperature magnetic susceptibility measurements revealed the presence of antiferromagnetic interactions between neighbouring Cu^{2+} centres ($\theta = -7.4$ K). Based on the crystal structure, the shortest $\text{Cu}^{2+}\cdots\text{Cu}^{2+}$ and $\text{Cu}^{2+}\cdots\text{Cl}\cdots\text{Cu}^{2+}$ distances are about 3.87 and 5.56 Å, respectively, ruling out direct and through-bridge (superexchange) interactions between the paramagnetic centres.

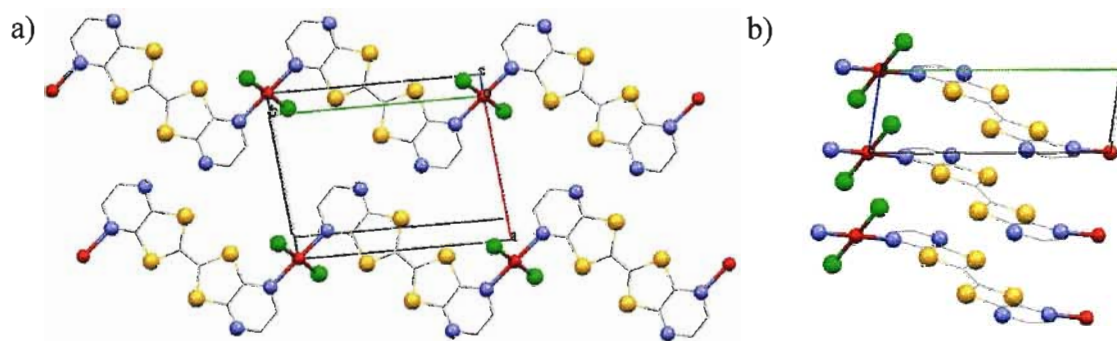


Figure 1.32 a) Planar zig-zag chains of the complex $\text{CuCl}_2(\mathbf{1.57})$, b) stacking of the $\text{CuCl}_2(\mathbf{1.57})$ complexes down the *c*-axis.¹³⁸

The authors of this study concluded that through bond π - d interactions between the magnetic spins and the π system of **1.57** was the mechanism for the antiferromagnetic coupling between Cu^{2+} ions. This explanation is not unreasonable as this coupling has been described previously in the complex $[\text{Cu}(\text{pc})]^{0.33+}[\text{I}_3^-]_{0.33}$ (pc = phthalocyanine).¹³⁹ This compound is formed by one-dimensional columns of $[\text{Cu}(\text{pc})]^{0.33+}$ cations surrounded by the counterions, with an intrastack complex distance of 3.2 Å. Although in this complex the Cu^{2+} ions are too far away from each other to interact, EPR, NMR and magnetic susceptibility studies revealed a coupling between magnetic spins below 6 K. This interaction was attributed to the coupling between Cu^{2+} spins and the conducting electrons of the oxidized pc ligand. To the best of our knowledge, this is the only TTF complex characterized that points at the possibility of TTF-mediated magnetic interactions between paramagnetic centres. No radical cation salts of this complex have been reported to-date.

In order to increase the dimensionality of the interactions between the TTF components of a lattice, TTF derivatives functionalized with hydrogen bonding groups, such as alcohols, acids, phosphonic acids and amides have been extensively researched and recently reviewed.¹⁴⁰ In particular, amide bonds are well known to form hydrogen bond patterns in crystals, and intermolecular hydrogen bonds are useful as an additional tool to direct packing in TTF-based multifunctional materials, where often π - π stacking, and the non-directional electrostatic and *van der Waals* interactions are the only packing forces present in the crystal.¹⁴⁰ This can be seen in the X-ray single crystal structures of the two polymorphs of the DMF solvates of **1.58** presented in Figure 1.33.¹⁴¹ The first polymorph, shown in Figure 1.33 a), displays an uncommon arrangement of TTF ligand molecules roughly perpendicular to each other. In comparison, the polymorph shown in b) and c) displays the molecules of ligand **1.58** forming dimers that are parallel to each other, an arrangement much more common in TTF-based crystals. In both polymorphs, the molecules of **1.58** are approximately planar.

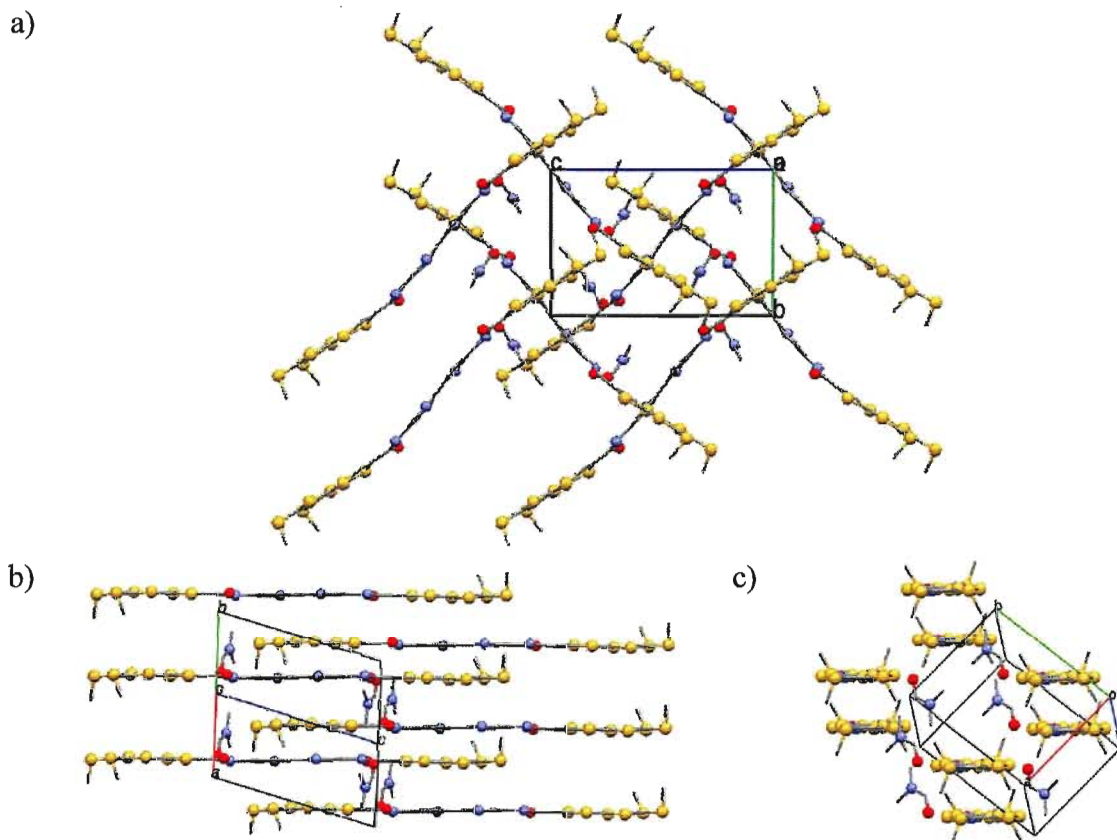
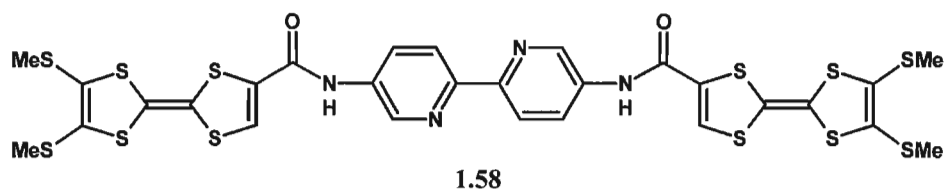
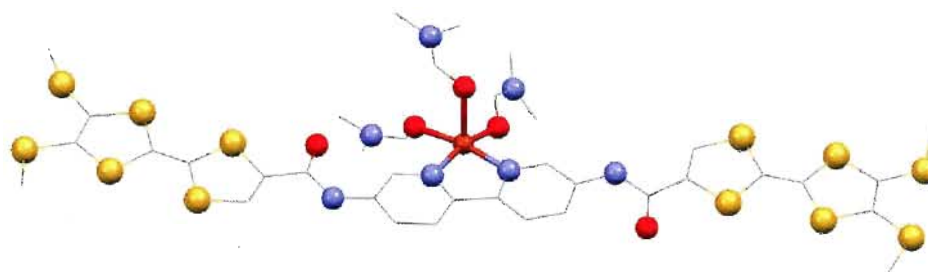


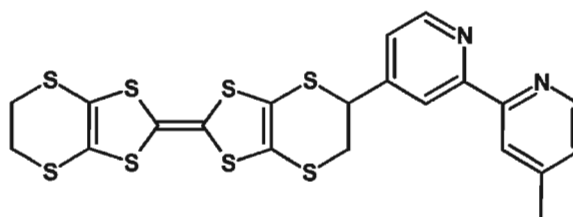
Figure 1.33 a) Arrangement of TTF ligand **1.58** molecules roughly perpendicular to each other, b) stacking arrangement with parallel ligand **1.58**, c) dimers of ligand molecules of the same polymorph as in b).¹⁴¹

The coordination chemistry of **1.58** is limited to the mononuclear Cu^{2+} complex $[\text{Cu}(\mathbf{1.58})](\text{OTf})_2 \cdot 3\text{DMF}$. The Cu^{2+} ion presents a distorted square pyramidal geometry, coordinated by three DMF molecules and one **1.58** ligand. Variable temperature magnetic susceptibility measurements show that the Cu^{2+} ions behave like isolated paramagnets with $S = 1/2$, possibly because of the long distances between the Cu^{2+} ions (*ca.* 7.8 Å).

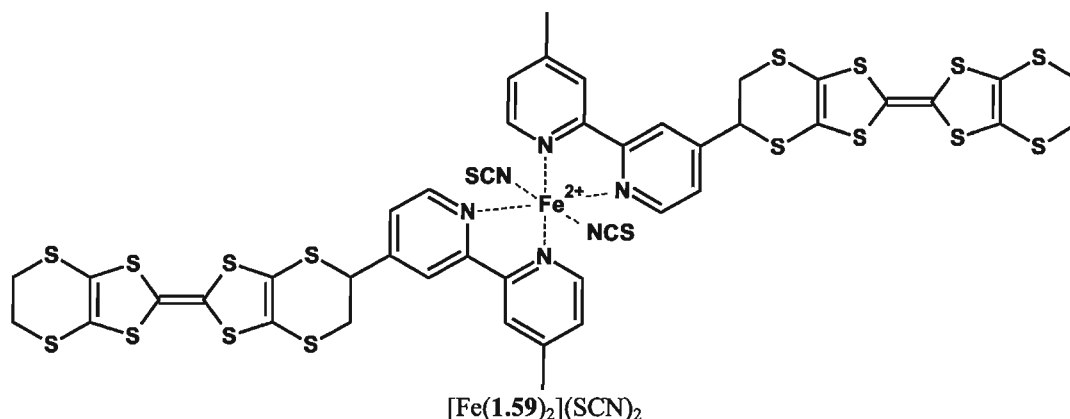


[Cu(1.58)](OTf)₂·3DMF

As previously mentioned, the approach developed by Day and coworkers combining BEDT-TTF and oxalate networks presented this donor as a suitable candidate for the preparation of multifunctional materials.⁵ The additional sulfur atoms in the structure of BEDT-TTF increased the dimensionality of the interactions between donor molecules in the resulting products by establishing additional contacts in the crystal structure. This afforded materials displaying Peierls transition at lower temperatures or no transition at all, and some superconductors at ambient pressure.⁵ These improvements over TTF-based materials prompted the synthesis of BEDT-TTF-based ligands to explore the preparation of multifunctional materials displaying *through bond* π -d interactions.^{121,131,132} In particular, Ouahab *et al.* appended a 2,2'-bipyridine group to BEDT-TTF in order to later form the known SCO complex Fe(bipy)₂(SCN)₂, and therefore prepare a multifunctional complex Fe(1.59)₂(SCN)₂ that could potentially present interplay between electrical conductivity and SCO behaviour.¹⁴²



1.59



With that purpose in mind, they appended a 2,2'-bipyridine to BEDT-TTF, obtaining derivative **1.59**, and finally reacted it with Fe(SCN)₂ to obtain the desired complex [Fe(**1.59**)₂](SCN)₂·CHCl₃. Electrochemical characterization of the ligand and the complex (Table 1.2) showed that for the ligand, the oxidation potential remained almost unchanged from the oxidation potentials of BEDT-TTF, whereas for the Fe²⁺ complex, the first oxidation potential remained the same as that of the ligand but the second oxidation potential decreased.

Table 1.2 Cyclic voltammetric data for **1.49**, **1.59** and [Fe(**1.59**)₂](SCN)₂.¹⁴²

	$E_1^{1/2}$ [V]	$E_2^{1/2}$ [V]
1.49	0.52	0.94
1.59	0.55	0.95
[Fe(1.59) ₂](SCN) ₂	0.55	0.86

Magnetic susceptibility studies of the complex revealed that at room temperature, the value of $\chi T = 1.65 \text{ emu K mol}^{-1}$ is lower than the expected value for a HS Fe²⁺ (ca. $3.7 \text{ emu K mol}^{-1}$) and higher than the expected value for a LS Fe²⁺ (ca. $0.1 \text{ emu K mol}^{-1}$). As the temperature is decreased, χT remained constant until 60 K and then started to decrease. The intermediate value of χT at room temperature was ascribed to a mixture of HS and LS Fe²⁺ species in the ratio of 40:60, and the decrease of χT at low temperatures was assigned to a mixture of zero field splitting and antiferromagnetic interactions. To the best of our knowledge, no study on oxidized complexes of **1.59** has been reported to-date.

1.3.3.1 Examples of spin-polarized systems in the literature

In a spin-polarized TTF-based system, the unpaired electron of an oxidized TTF donor is delocalized through the π -system of the molecule and it couples to the magnetic spins present in the molecule, Figure 1.34 a).⁵ The movement of the conducting electrons through a suitable conduction pathway would then propagate the spin polarization through the material, resulting in the parallel arrangement of all the magnetic spins, Figure 1.34 b).

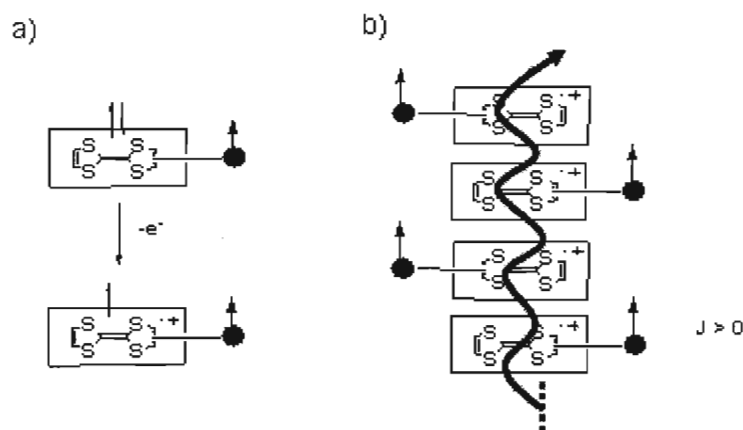
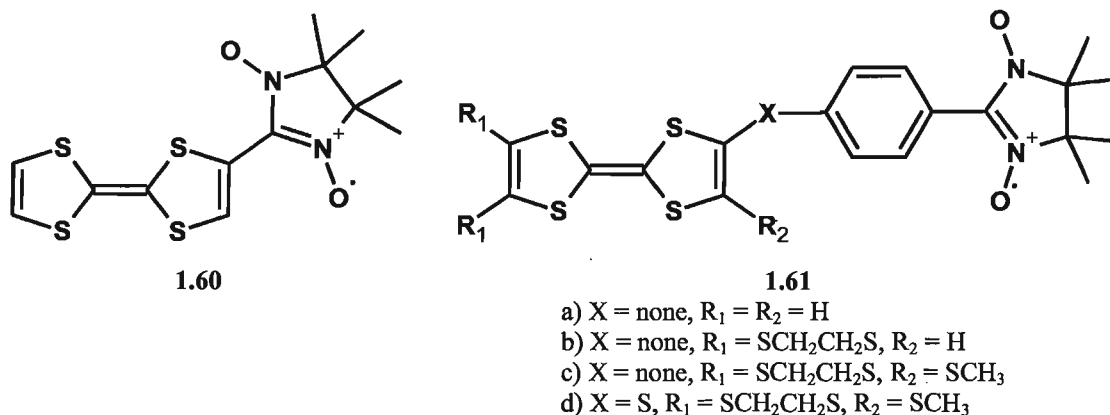


Figure 1.34 Schematic drawing of: (a) oxidation of a TTF ligand bearing paramagnetic centres; (b) stack of oxidized TTF ligands bearing paramagnetic centres, showing itinerant electrons moving through the stack. Adapted from reference 143 with permission.

Sugawara and coworkers used nitronyl nitroxide radicals to prepare the purely organic spin-polarized systems **1.60**¹⁴⁴ and **1.61**.¹⁴⁵ Once the TTF moiety was oxidized **1.60** presented antiferromagnetic coupling, whereas the coupling in **1.61** was ferromagnetic.



At the time, Sugawara postulated that the difference between the ground states of each system, singlet for **1.60** and triplet for **1.61**, is due to the loss of coplanarity between the TTF and the nitronyl nitroxide radical rings as a consequence of steric hindrance. The dependency of the coupling constant J with coplanarity between radicals in these systems was corroborated by Matsuoka *et al.* recently using DFT calculations.¹⁴⁶ The authors showed that the coupling constant changed from ferromagnetic to antiferromagnetic as the dihedral angle θ between the TTF and nitroxide moieties increased, Figure 1.35. A similar dependency has been postulated by Polo *et al.* for π -bridged TTF-verdazyl diradical systems.¹⁴⁷ These results indicate that a planar π system is necessary to establish a favourable polarization pathway between conductive and magnetic spins, and therefore must be present in the building blocks for multifunctional materials displaying cooperativity between magnetism and electrical conductivity.

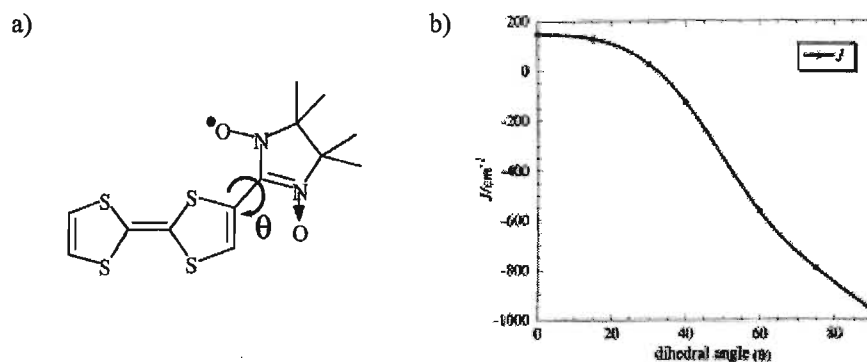
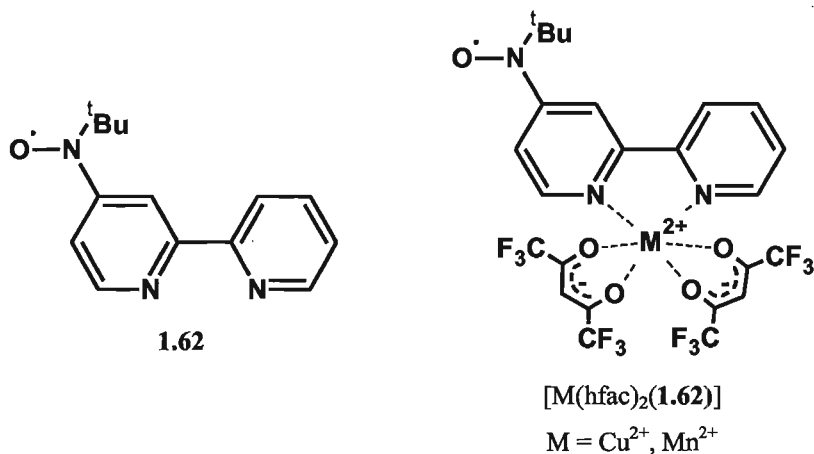


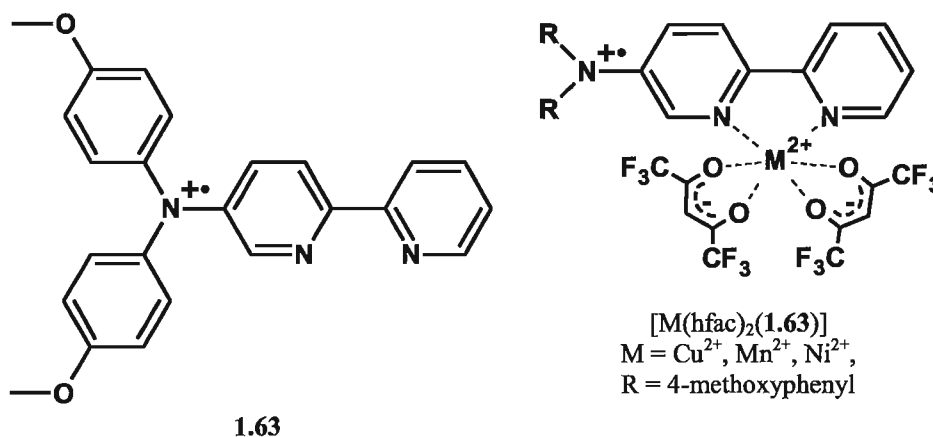
Figure 1.35 a) Molecular structure of **1.60** showing the dihedral angle θ , b) dependency of J with θ . Reprinted from reference 146 with permission from Elsevier.

There are examples in the literature of spin polarized systems that are not TTF-based. In 2000, Iwamura followed up on the spin polarization studies published previously^{148,149} of 3-(*N-ter*-butyl-*N*-oxyamino)pyridine complexes, to investigate spin polarization in Mn^{2+} and Cu^{2+} complexes of 4-(*N-ter*-butyl-*N*-oxylamino)-2,2'-bipyridine, **1.62**.¹⁵⁰ Single crystal X-ray diffraction showed that both complexes were isostructural and that, as expected, the coordination sphere of the metal centres was formed by a chelating ligand **1.62** and two hfac ligands in a distorted octahedron arrangement. Magnetic characterization of the complexes showed that, at 300 K, the values of χT were 4.21 and 0.83 emu K mol^{-1} for the complexes $[\text{Mn}(\text{hfac})_2(\mathbf{1.62})]$ and $[\text{Cu}(\text{hfac})_2(\mathbf{1.62})]$ respectively. These values were different from the calculated spin-only values for the isolated complexes (4.75 and 0.75 emu K mol^{-1} , respectively). Variable temperature magnetic characterization showed that, upon cooling $[\text{Mn}(\text{hfac})_2(\mathbf{1.62})]$ down to 2 K, χT decreased gradually. On the contrary, for $[\text{Cu}(\text{hfac})_2(\mathbf{1.62})]$, the value of χT increased gradually upon cooling. Magnetic modelling of the data showed that the intermolecular exchange couplings were $J/k_B = -20.2$ and 68.7 K respectively, indicating antiferromagnetic and ferromagnetic coupling between the aminoxyl radical and the Mn^{2+} and Cu^{2+} ions within the respective complexes. The same modelling also indicated the presence of small intermolecular ferromagnetic coupling for both complexes.

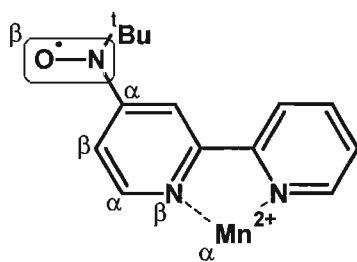


In turn, Lemaire and coworkers reported magnetic studies for Mn^{2+} , Ni^{2+} and Cu^{2+} complexes of a 2,2'-bipyridine substituted triarylamminium radical cation, **1.63**.¹⁵¹ Only the Cu^{2+} complex was characterized by X-ray diffraction. The Cu^{2+} centre adopts a distorted octahedral coordination environment formed by ligand **1.63** and two hfac

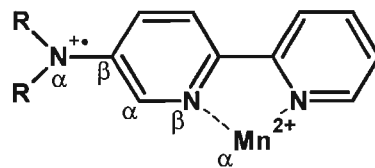
molecules, but it is reasonable to assume that the Mn^{2+} and the Ni^{2+} complexes have the same structure. Oxidation of the tertiary amine with NOPF_6 yielded the radical cation amminium complexes $[\text{M}(\text{hfac})_2(\mathbf{1.63})]$ ($\text{M} = \text{Mn}^{2+}, \text{Ni}^{2+}$) that were magnetically characterized. For $[\text{Mn}(\text{hfac})_2(\mathbf{1.63})]$, the magnetic moment was $6.4 \mu_B$, higher than the theoretical value for a non-interacting high spin Mn^{2+} and a coordinated $S = \frac{1}{2}$ radical ($6.16 \mu_B$). For $[\text{Ni}(\text{hfac})_2(\mathbf{1.63})]$, the magnetic moment was $3.1 \mu_B$, which is lower than the theoretical value for a non-interacting Ni^{2+} ion and a coordinated $S = 1/2$ amminium radical ($3.3 \mu_B$).



The change from antiferromagnetic to ferromagnetic coupling in complexes $[\text{Mn}(\text{hfac})_2(\mathbf{1.62})]$ and $[\text{Mn}(\text{hfac})_2(\mathbf{1.63})]$ can be rationalized based on the different substitution pattern of the radicals on the bipyridine moiety. Phase alternation of the spin density from the radical to the N atom on the bipyridine moiety closer to the radical shows that the $[\text{Mn}(\text{hfac})_2(\mathbf{1.62})]$ complex has positive spin density on that atom. The overlap between the $p\pi$ orbital of this N atom and the d_{xz} and d_{yz} orbitals of Mn^{2+} ion allows the spin polarization to propagate into the metal centre, resulting in antiferromagnetic coupling between the radical and the Mn^{2+} ion (Scheme 1.9). On the other hand, the $[\text{Mn}(\text{hfac})_2(\mathbf{1.63})]$ complex shows negative spin density on the N atom closer to the radical, resulting in ferromagnetic coupling.



[Mn(hfac)₂(1.62)]



[Mn(hfac)₂(1.63)], R = 4-methoxyphenyl

Scheme 1.9 Phase alternation diagram explaining antiferro and ferromagnetic interactions in [Mn(hfac)₂(1.62)] and [Mn(hfac)₂(1.63)].^{150,151}

Figure 1.36 shows the results of the density functional theory calculations at the B3LYP/TZVP level for the [Mn(hfac)₂(1.63)] complex.¹⁵¹ The ammonium nitrogen atom has positive π spin density (+0.26) and the π spin distribution for each atom of the bipyridine ring alternates between positive and negative. The Mn²⁺ ion also features positive spin density (+4.84), which results in the ferromagnetic coupling between the Mn²⁺ ion and the nitrogen radical.

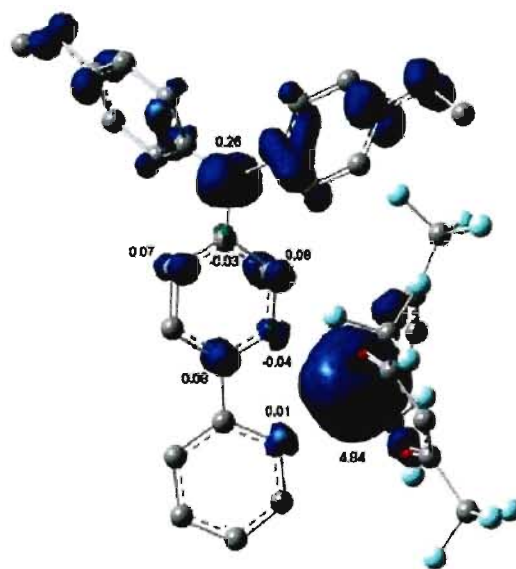


Figure 1.36 Calculated spin density distributions for [Mn(hfac)₂(1.63)]. Spin density shown as dark blue lobes. Reprinted with permission from 151. Copyright 2010 American Chemical Society.

1.4 Organization of this thesis

The work presented in this thesis is divided into three projects, and each project is addressed in its own Chapter. In Chapter 2, the development of novel 3,3'-diamino-2,2'-bipyridine-based *bis*-imine ligands for the preparation of molecular magnets is described. This chapter also reports the coordination chemistry of one of these novel ligands, highlighting the sensitivity of its imine bonds towards hydrolysis. Chapter 3 concerns the synthesis and characterization of a family of π -extended TTF derivatives and their CT salts. In particular, the synthesis of CT salts by means of chemical oxidation and electrocrystallization are described, with emphasis on the experimental conditions required to accomplish the latter. In Chapter 4, the coordination chemistry of a π -extended TTF derivative is presented, detailing both the synthesis and characterization of a new family of coordination complexes. Finally, Chapter 5 contains a summary of the research findings presented in the thesis together with a brief discussion highlighting possible future research directions for all three projects.

CHAPTER 2

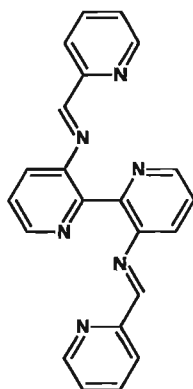
Novel bis-imine ligands for magnetic molecular materials

2.1 Introduction

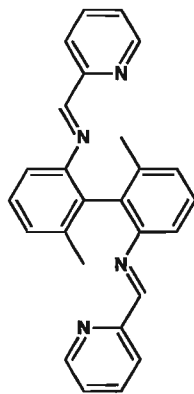
The preparation of molecular materials from small ligands, such as cyanide or oxalate, offers a restricted number of possibilities to derivatize or chemically tune the ligands, leaving the metal ions as the only degree of freedom to control the properties of the material. Additional control over the final product can be attempted by using larger, structurally more complex ligands as building blocks for molecular materials.^{29,42,82,152} This approach offers more possibilities to modify the structure and physical properties of the final product by means of ligand derivatization. More complex ligands can also coordinate more than one paramagnetic transition metal ion, which opens the possibility of changing the arrangement of the coordinated metal cations in the final product by changing the structure of the ligand.^{29,31,59,60}

As outlined in Chapter 1, the ligand 3,3'-diamino-2,2'-bipyridine **1.10** provides a rigid backbone comprised of two pyridine rings with one amino group opposite to each pyridine nitrogen. The coordination chemistry of this ligand has been studied by a number of research groups.⁷²

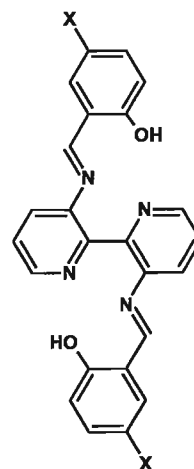
In recent years, the Pilkington group has reported the derivatization of this ligand by converting the amino groups into carboxamide and imine functionalities.^{95,96} The imine ligand **1.40**, however, underwent an extensive rearrangement upon coordination to Co^{2+} . This was a somewhat unexpected result when compared to the related diphenyl analogue **2.1**, which is stable upon coordination to transition metal ions.^{153,154}



1.40



2.1



2.2 X = H

2.3 X = OH

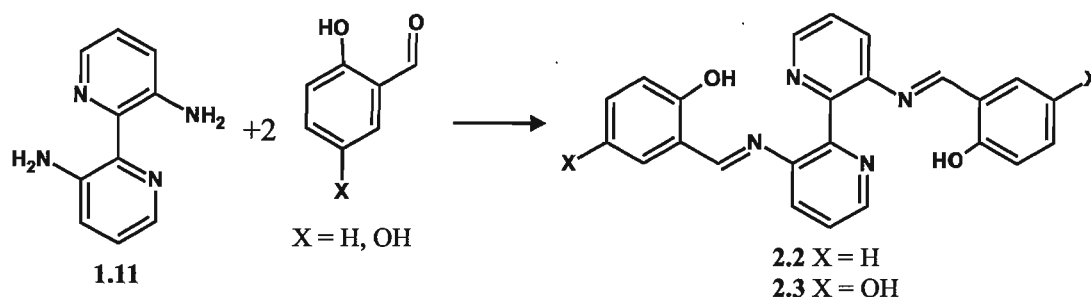
We hypothesized that this difference in ligand stability was caused by the presence of the bipyridine backbone in **1.40**. In **2.1**, the 6,6'-dimethylbiphenyl backbone is electron donating, but the bipyridine backbone in **1.40** is electron withdrawing. The presence of the bipyridine backbone and the pyridine rings in **1.40**, we considered, drains the imine bonds of electron density, making them very susceptible to nucleophilic attack. We proposed that using a less electron withdrawing substituent to replace the pyridine rings on the arms of the ligand might be a good strategy for the preparation of a stable *bis-imine* ligand. In this respect, we chose salicyl aldehyde and 2,5-dihydroxybenzaldehyde for the preparation of two new *bis-imine* ligands **2.2** and **2.3**, given the extensive pool of stable salen-type ligands found in the literature.

2.2 Synthesis and characterization of the *bis-imine* ligands

2.2.1 Synthesis of the *bis-imine* ligands

The previously reported *bis-imine* ligand **1.40** was prepared from 3,3'-diamino-2,2'-bipyridine **1.11** and two equivalents of pyridine-2-carbaldehyde by refluxing the reaction mixture in toluene for five days using a Dean Stark apparatus, following the procedure by Pilkington *et al.*⁹⁵ This ligand can be stored without decomposition in a dry box indefinitely. Two new ligands **2.2** and **2.3** were prepared in 90% yield by the condensation of 3,3'-diamino-2,2'-bipyridine with salicyl aldehyde or 2,5-dihydroxybenzaldehyde in methanol, Scheme 2.1. Both ligands were isolated as yellow

solids and were stable in air. Ligand **2.2** was stable in wet dichloromethane for at least four months according to ^1H NMR studies. Ligand **2.3** can be stored in air for over a year with no decomposition visible by ^1H NMR studies.



Scheme 2.1 Reaction diagram for the synthesis of **2.2** and **2.3**. Reaction conditions: for **2.2**: methanol, r.t. overnight; for **2.3**: methanol, reflux, overnight.

2.2.2 Spectroscopic characterization of ligands **2.2** and **2.3**

The 600 MHz ^1H and ^{13}C NMR spectra of ligand **2.2** show the expected singlet for the imine proton at 8.49 ppm and the imine carbon at 164.71 ppm, corroborating the preparation of this ligand. The singlet corresponding to the OH proton appears at 12.11 ppm, and was identified by the disappearance of this signal due to proton-deuterium exchange after adding deuterium oxide to the NMR solution. The IR spectrum of the ligand shows a band at 1612 cm^{-1} which corresponds to the C=N str of the imine bond. FAB mass spectrometry data shows a peak at $m/z = 394$ consistent with the molecular ion for **2.2**. The ^1H and ^{13}C NMR spectra of ligand **2.3** show the singlet for the imine proton at 8.62 ppm and the imine carbon at 165.63 ppm. The IR spectrum shows a band at 1619 cm^{-1} which corresponds to the C=N str of the imine bond. FAB mass spectrometry data shows a peak at $m/z = 426$ consistent with the molecular ion for **2.3**. The UV-Vis spectra of **2.2** and **2.3** each show three absorption bands between $\lambda = 230$ and 450 nm, Figure 2.1. These bands correspond to the overlapping of $\pi\text{-}\pi^*$ transitions of 3,3'-diamino-2,2'-bipyridine and the phenol or 2,5-dihydroxybenzene rings and the imine bonds.

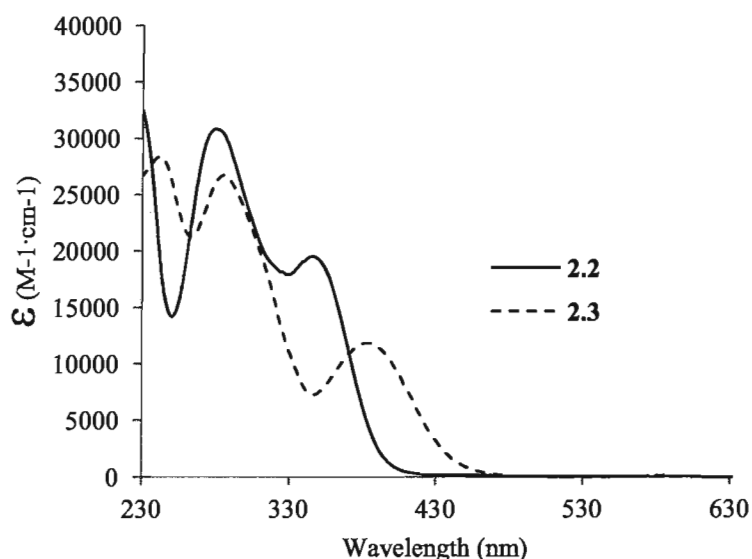


Figure 2.1 UV-Vis spectra of 10^{-5} M solutions of **2.2** and **2.3** in methanol.

2.2.3 X-ray characterization of the *bis*-imine ligands **1.40**, **2.2** and **2.3**

Single crystals suitable for X-ray diffraction of **1.40** were grown at -40°C from THF, and the X-ray crystal structure was determined at 150 K, Figure 2.2. The ligand crystallizes in the monoclinic space group $P2_1/c$, with one crystallographically independent molecule in the unit cell. The two pyridine rings of the bipyridine unit present a torsion angle of $64.4(2)^{\circ}$, which brings the imine arms of the ligand close together. The imine C=N bond lengths are 1.270(2) and 1.274(2) Å and are almost coplanar with their corresponding terminal pyridine rings. The best planes of a terminal pyridine ring and imine bond lie at $51.80(8)^{\circ}$ and $56.59(8)^{\circ}$ from the plane of the bipyridyl pyridine ring to which they are attached. The molecules are packed in centrosymmetric pairs, with a pair of long C17-H17...N5 contacts of 2.53 Å between pyridine N and imine CH groups. Selected bond lengths and angles for ligand **1.40** are summarized in Table 2.1.

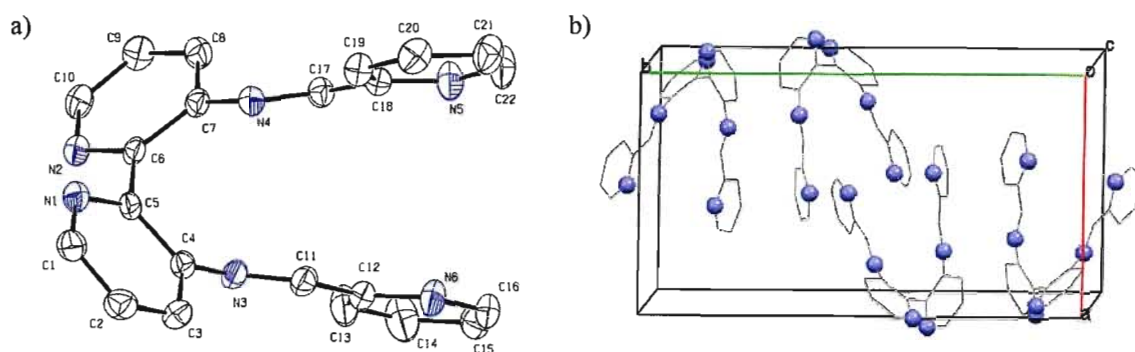


Figure 2.2 a) ORTEP plot of the molecular structure of **1.40** showing the corresponding numbering scheme. Thermal ellipsoids plotted at 50% probability. b) Unit cell of **1.40**. Hydrogen atoms are omitted for clarity.

Table 2.1 Selected bond lengths (Å) and angles (°) for ligand **1.40**.

Bond lengths			
N3-C11	1.270(2)	N5-C18	1.345(2)
N4-C17	1.274(2)	N5-C22	1.339(3)
N3-C4	1.421(2)	N6-C12	1.345(2)
N4-C7	1.415(2)	N6-C16	1.344(3)
N1-C1	1.339(2)	C5-C6	1.490(2)
N1-C5	1.343(2)	C11-C12	1.476(2)
N2-C6	1.340(2)	C17-C18	1.472(2)
N2-C10	1.337(2)		
Bond angles			
N2-C6-C5	116.53(14)	N4-C17-C18	120.68(16)
N1-C5-C6	117.11(14)	N3-C4-C5	118.06(15)
C4-N3-C11	117.95(15)	N4-C7-C6	118.91(15)
C7-N4-C17	119.05(15)	N5-C18-C19	122.96(16)
N3-C11-C12	122.42(16)	N6-C12-C11	114.32(15)
Dihedral angles			
C4-C5-C6-C7	64.4(2)	N3-C11-C12-C13	3.7(3)
C11-N3-C4-C5	130.96(17)	N4-C17-C18-C19	8.2(3)
C17-N4-C7-C6	143.54(17)		

Slow evaporation of a dichloromethane solution of **2.2** afforded yellow needles suitable for X-ray characterization. The ligand crystallizes in the triclinic space group *P*-1, with one crystallographically independent molecule per unit cell, Figure 2.3 a) and b). In contrast to the structure of **1.40**, this ligand crystallizes in an *anti-periplanar* conformation, with the best planes of the bipyridine rings at 71.36(9)° to each other. The phenol rings of each arm are almost coplanar with their corresponding bipyridine ring, showing only small angles of 10.06(9)° and 7.30(9)° between their respective best planes. This coplanar arrangement allows the ligands to pack together with diarylimine units of neighbouring molecules lying face to face; one set of which have shortest interatomic separations of 3.220(3) and 3.272(3), and the other set with shortest separation of 3.283(3) Å.

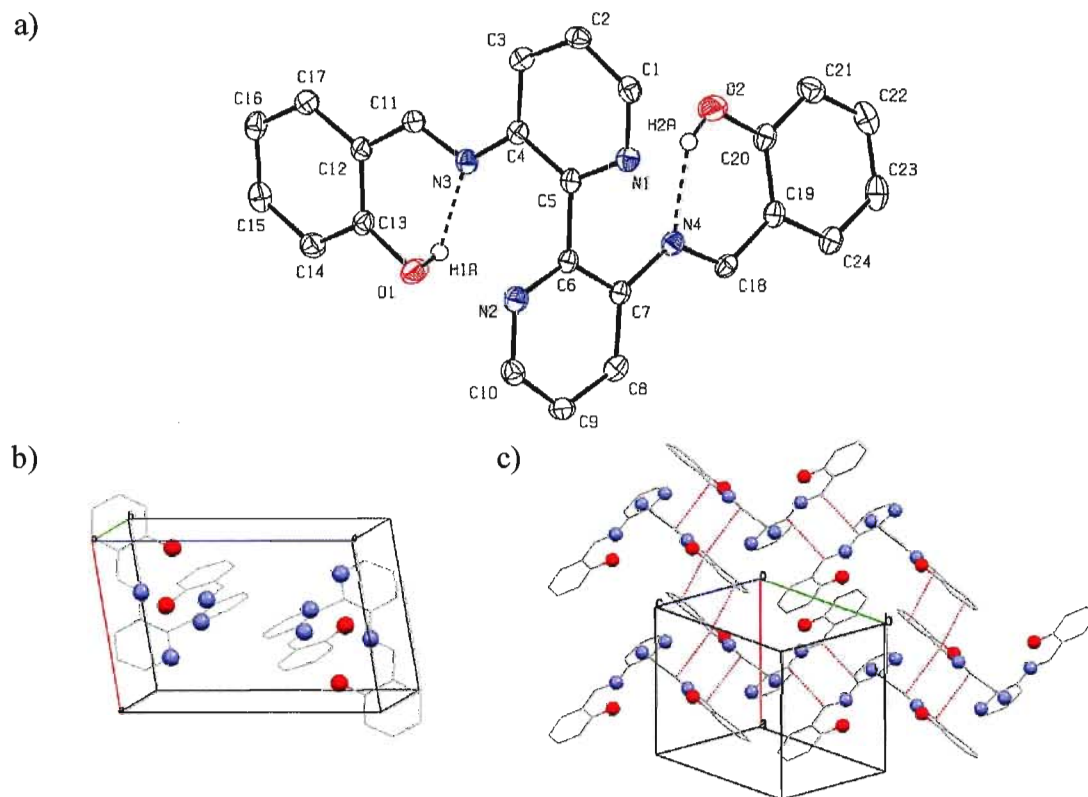


Figure 2.3 a) ORTEP plot of the molecular structure of **2.2** showing the corresponding numbering scheme and the hydrogen bonds between the hydroxyl and imine groups. Thermal ellipsoids plotted at 50% probability. b) Unit cell of **2.2**. c) Short contacts between neighbouring **2.2** molecules shown as dashed red lines. Hydrogen atoms not involved in intramolecular H-bonds are omitted for clarity.

Within each molecule the hydroxyl groups form intramolecular hydrogen bonds to their closest imine nitrogen atoms (OH...N: 1.88 and 1.92 Å). Selected bond lengths and angles for ligand **2.2** are summarized in Table 2.2.

Table 2.2 Selected bond lengths (Å) and angles (°) for ligand **2.2**.

Bond lengths			
N3-C11	1.291(2)	N2-C6	1.346(2)
N4-C18	1.287(2)	N2-C10	1.340(2)
N3-C4	1.418(2)	C5-C6	1.498(2)
N4-C7	1.420(2)	C11-C12	1.448(2)
N1-C1	1.334(2)	C18-C19	1.448(2)
N1-C5	1.347(2)		
Bond angles			
N2-C6-C5	115.91(15)	N3-C11-C12	122.37(15)
N1-C5-C6	115.51(15)	N4-C18-C19	120.80(16)
C4-N3-C11	120.65(15)	N3-C4-C5	116.63(15)
C7-N4-C18	119.05(15)	N4-C7-C6	116.29(15)
Dihedral angles			
C4-C5-C6-C7	110.4(2)	N3-C11-C12-C13	1.3(3)
C11-N3-C4-C5	178.1(2)	N4-C18-C19-C20	2.8(3)
C18-N4-C7-C6	172.8(2)		

It must be pointed out that, during the course of our investigation with **2.2**, two sets of groups reported a different crystal structure for this ligand.^{155,156} The published structure belongs to the monoclinic space group *C2/c*, where only one half of the ligand molecule is crystallographically unique. The symmetry of our polymorph is much lower with one complete ligand that is crystallographically independent. Close inspection of our structure reveals that one contributing factor to the lower symmetry of our structure is the torsion angles between the phenol rings in each arm and their corresponding pyridine ring, which are 2.56° and 8.53°. Due to the higher symmetry, the structure reported in the literature only has one such angle (4.89°). Another difference between both structures is the number of short contacts. In our structure each molecule forms short contacts with

three neighbouring molecules, whereas in the published work each ligand molecule forms short contacts with four neighbours.

Slow cooling of an isopropanol solution of ligand **2.3** afforded yellow needles suitable for X-ray crystallography. The ligand crystallizes in the monoclinic space group *C2/c*, with two ligand molecules and two solvent molecules in the asymmetric unit, Figure 2.3 a). The ligand molecules once again adopt an *anti-periplanar* conformation, with angles of 70° and 75° between the best planes of the bipyridine rings. The phenol rings of each arm are almost coplanar with their corresponding bipyridine ring, showing only small angles of 10° and 15° between their respective best planes. Within each molecule the O1 and O2 hydroxyl groups form an intramolecular hydrogen bond to the imine nitrogen atoms N2 and N4 respectively, Table 2.3.

The *para* O3 and O4 hydroxyl groups of the ligand form intermolecular hydrogen bonds to isopropyl alcohol molecules. Each alcohol molecule is also involved in a second hydrogen bond with a pyridine nitrogen from a second ligand molecule. This series of interactions organizes the ligand molecules into 1D chains that are separated by layers of isopropyl alcohol molecules. This crystal structure does not display the same stacking of diarylimine units as seen for **2.2**. In contrast, there are two short interligand contacts within a chain, namely $C16 \cdots C18 = 3.346(8) \text{ \AA}$ and $C14-H14 \cdots O4 = 2.592(4) \text{ \AA}$. Selected bond lengths and angles for ligand **2.3** are summarized in Table 2.4.

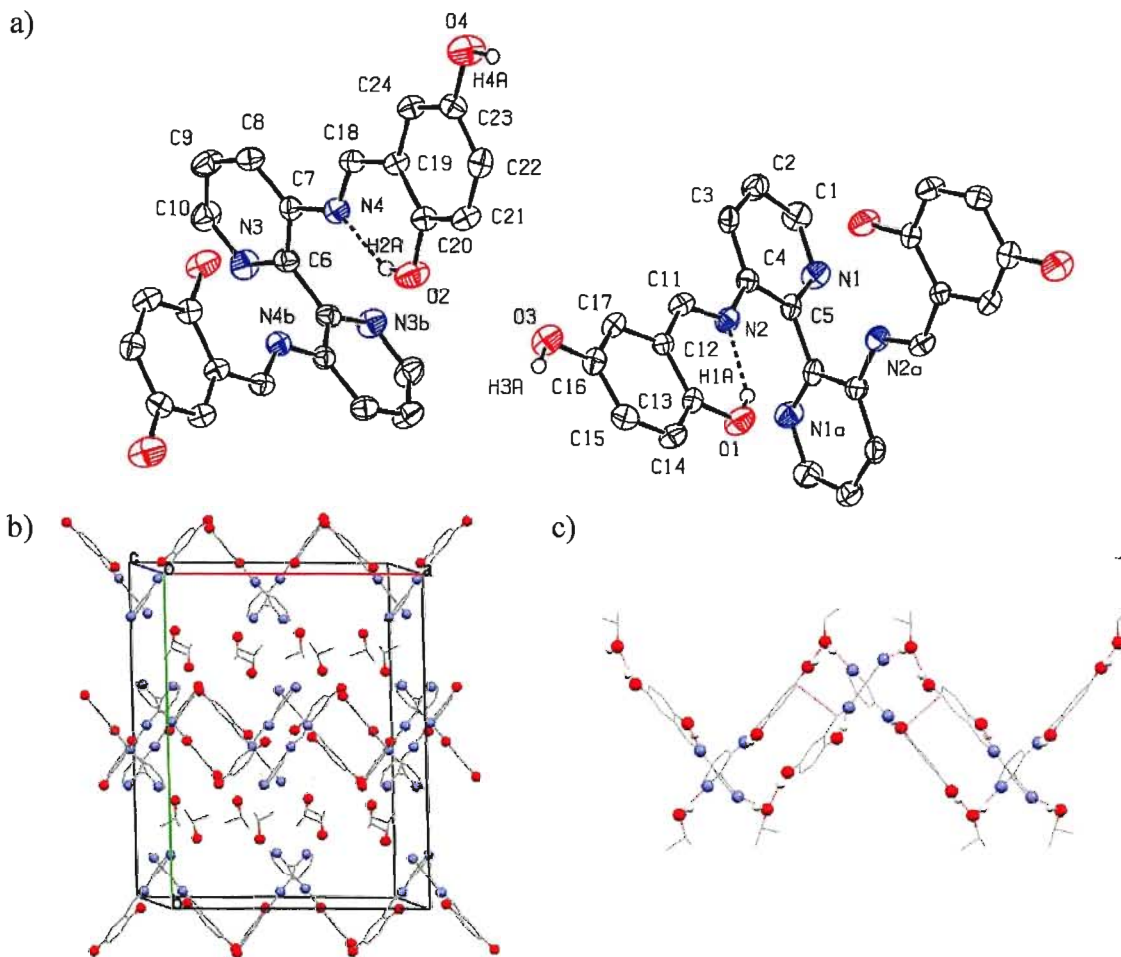


Figure 2.4 a) ORTEP plot of the molecular structure **2.3** showing the corresponding numbering scheme. The hydrogen bonds between the hydroxyl and imine groups are shown as a dotted line. Thermal ellipsoids plotted at 50% probability. b) Unit cell of **2.3**, showing the ligand domains separated by solvent molecules. c) Short contacts and hydrogen bonds are shown as red dotted lines. Some hydrogen atoms and isopropyl alcohol molecules are omitted for clarity.

Table 2.3 Distance d and angle α of the hydrogen bonds for ligand **2.3**.

	d [C-H \cdots N] (\AA)	d [H-C \cdots N] (\AA)	α [C-H \cdots N] ($^\circ$)
O1-H1A \cdots N2	1.85	2.593(5)	147
O2-H2A \cdots N4	1.86	2.605(6)	146
O3-H3A \cdots O5	1.89	2.717(5)	168
O4-H4A \cdots O6	1.86	2.695(6)	178
O5-H5A \cdots N3b	1.98	2.807(5)	169
O6-H6A \cdots N1d	1.94	2.765(7)	168

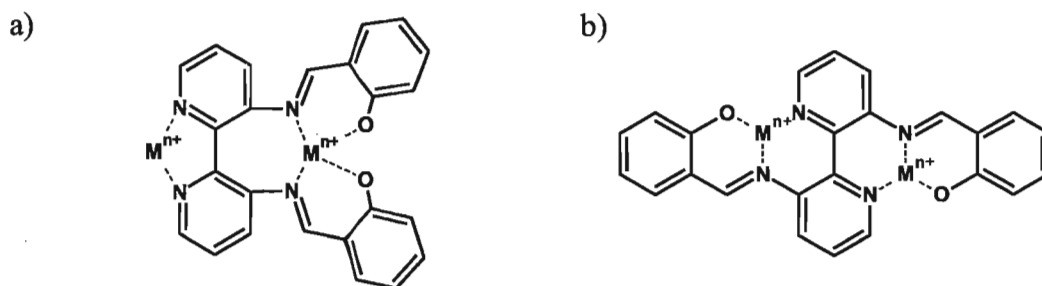
Table 2.4 Selected bond lengths (Å) and angles (°) for ligand **2.3**.

Bond lengths			
N2-C11	1.283(6)	N1-C5	1.345(6)
N4-C18	1.278(6)	N3-C6	1.343(6)
N2-C4	1.421(6)	N3-C10	1.335(6)
N4-C7	1.416(6)	C5-C5a ⁱ	1.490(9)
N1-C1	1.337(6)	C6-C6b ⁱⁱ	1.492(10)
Bond angles			
N1-C5-C5a ⁱ	116.0(4)	C7-N4-C18	121.0(4)
N3-C6-C6b ⁱⁱ	115.3(4)	N2-C4-C5	115.8(4)
C4-N2-C11	122.4(4)	N4-C7-C6	116.4(4)
Dihedral angles			
C4-C5-C5a-C4a ⁱ	75.9(8)	C18-N4-C7-C6	165.8(5)
C7-C6-C6b-C7b ⁱⁱ	70.6(8)	N2-C11-C12-C13	1.7(9)
C11-N2-C4-C5	170.9(5)	N4-C18-C19-C20	0.9(9)

Symmetry transformation: ⁱ-x,y,-z+3/2, ⁱⁱ-x+1,y,-z+3/2

2.3 Coordination chemistry of the *bis*-imine ligand **2.2**

Ligand **2.2** has two potential binding modes, shown in Scheme 2.2. The asymmetric binding mode a) could coordinate metal ions M^{n+} through the N lone pairs of the bipyridine backbone and/or using the tetradentate N_2O_2 binding site formed by both imine nitrogen and phenol oxygen atoms of the arms of the ligand, much in the same manner as biphenyl *bis*-imine ligands reported in the literature.¹⁵³ On the other hand, the symmetric binding mode b) could coordinate to metal ions M^{n+} via two tridentate N_2O binding pockets when the ligand is in a *trans*-coplanar conformation of **2.2**.

**Scheme 2.2** Potential binding modes of ligands **2.2**.

2.3.1 Synthesis and characterization of complex 2.4

Although the objective of this project was the preparation of molecular magnets, we decided to make a quick diversion into the coordination chemistry of Sn^{2+} . Tin complexes have been used in organic synthesis¹⁵⁷ and catalysis,^{158,159} and there are examples in the literature of tin complexes formed with salen-type ligands^{160-162,163}. Reaction of SnCl_2 with **2.2** in the absence of base afforded dark orange needles of complex **2.4** suitable for X-ray diffraction. As expected, the IR spectrum does not show a C=N imine str and presents overlapped OH and secondary amine strs around 3300 cm^{-1} . FAB mass spectrometry data shows a peak at $m/z = 515$ consistent with the $[\text{M-Cl}]^+$ ion. The UV-Vis spectrum of the complex shows an intense band at $\lambda = 430\text{ nm}$ corresponding to the $\pi\text{-}\pi^*$ transition of the phenol ring of the diazepine ligand, Figure 2.5. The bands at higher energies correspond to the $\pi\text{-}\pi^*$ transitions of the bipyridine backbone.

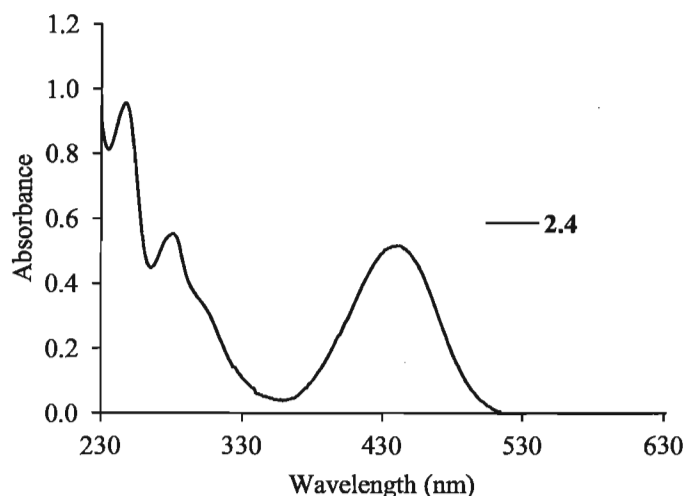


Figure 2.5 UV-Vis spectrum of an approximately 10^{-5}M solution of complex **2.4** in methanol.

Single crystals of complex **2.4** were characterized by X-ray diffraction. This complex crystallizes in the monoclinic space group $P2_1/c$ with one complex and two ethanol molecules that are crystallographically independent in the unit cell, Figure 2.6. The complex is comprised of the diazepine ligand **2.5** that is coordinated to a Sn^{4+} ion *via* the lone pairs on the pyridyl N atoms. Four Cl^- ions complete the distorted octahedral geometry around the metal centre.

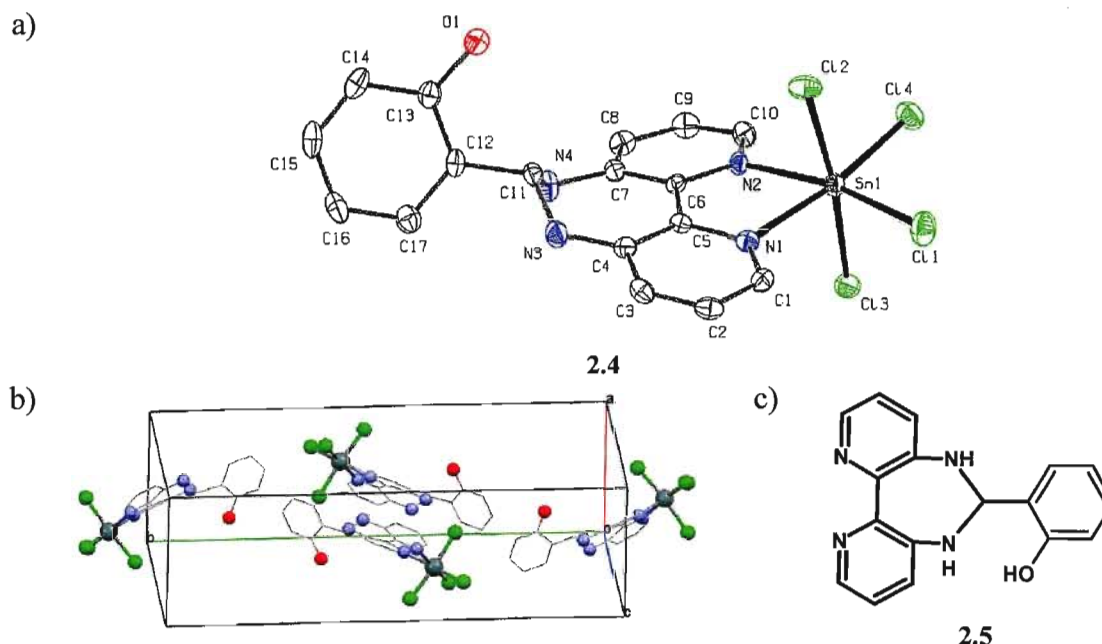


Figure 2.6 a) ORTEP plot of the molecular structure of the Sn^{4+} complex **2.4** showing the corresponding numbering scheme. Thermal ellipsoids plotted at 50% probability. b) Unit cell of **2.4**. Ethanol molecules and hydrogen atoms are omitted for clarity. c) diazepine ligand **2.5** resulting from the intramolecular cyclization of **2.2**.

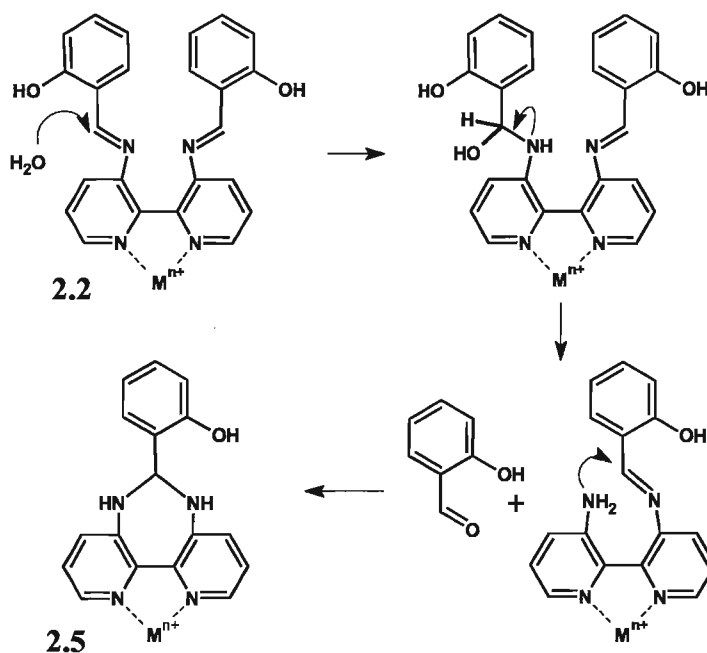
Based on the charge balance of the complex, it is apparent that the Sn ion has been oxidized from Sn^{2+} to Sn^{4+} . The axial Sn-Cl distances are slightly longer than the equatorial distances, with bond lengths of 2.4021(15) and 2.4316(16) Å for the former and 2.3721(17) and 2.3771(15) Å for the latter. The axial chloride ligands form a Cl-Mn-Cl angle of 172.93(5)° tilted away from the bipyridine ligand. The hydroxyphenyl substituent adopts the equatorial position of the diazepine ring, with an angle of 64.1(2)° with respect to the bipyridine best plane. The crystal packing shows alternating stepped stacks of molecules that run down the *c*-axis, with pairs of steps related by an inversion centre. Two ethanol molecules bridge the steps in these centrosymmetric pairs with long hydrogen bonds between N4-H...O2 and O2-H...Cl4, with bond lengths of 2.23 and 2.42 Å respectively. A view down the *b*-axis of the unit cell reveals that the molecules of the complex are arranged in a head-to-tail fashion, forming corrugated sheets with ethanol molecules hydrogen-bonded to the hydroxyphenyl substituents of the diazepine ligand (O1-H...O3, bond length 1.85 Å). See Table 2.5 for selected bond lengths and angles.

Table 2.5 Selected bond lengths (Å) and angles (°) for complex **2.4**.

Bond lengths			
Sn1-Cl1	2.3721(17)	C6-C7	1.416(7)
Sn1-Cl2	2.4021(15)	C7-C8	1.409(8)
Sn1-Cl3	2.4316(16)	C8-C9	1.355(8)
Sn1-Cl4	2.3771(15)	C9-C10	1.382(8)
Sn1-N1	2.205(4)	C11-C12	1.515(7)
Sn1-N2	2.191(4)	N3-C11	1.436(7)
N4-C11	1.450(7)		
Bond angles			
Cl1-Sn1-Cl2	94.44(5)	Cl1-Sn1-Cl3	91.56(5)
Cl1-Sn1-Cl4	95.46(5)	Cl2-Sn1-Cl3	172.93(5)
Cl1-Sn1-N1	95.00(12)	Cl2-Sn1-Cl4	91.87(5)
Cl1-Sn1-N2	168.56(12)	Cl2-Sn1-N1	86.00(12)
Cl2-Sn1-N2	88.10(12)	Cl4-Sn1-N1	169.47(12)
Cl3-Sn1-Cl4	91.27(5)	Cl4-Sn1-N2	95.61(12)
Cl3-Sn1-N1	89.77(12)	N1-Sn1-N2	74.02(16)
Cl3-Sn1-N2	85.29(12)	N4-C11-C12	108.7(4)
N3-C11-C12	111.0(4)	N3-C11-N4	111.1(4)
C6-N2-C10	122.7(4)		
Dihedral angle			
C4-C5-C6-C7	-9.2(8)		

The formation of the diazepine ligand **2.5** can be explained by the initial hydrolysis of one imine group of ligand **2.2**, releasing an amino group which then adds to the remaining imine group to form the dihydro-1,3-diazepine **2.5** as shown in Scheme 2.3. Once the imine bond has been hydrolyzed, the substituents in the 3 and 3' positions must be in close proximity for the amino group to carry out the nucleophilic addition on the remaining iminic carbon. While a foreseeable conformational rotation around the C5-C6 bond may allow this to happen for free **2.2** in solution, it is also possible that metal coordination to the bipyridine backbone templates both positions in close proximity and increases the speed of the cyclization reaction. ¹H NMR characterization of a solution of

ligand **2.2** over a period of months showed that, unlike the structurally related ligand *bis*-imine **1.40**, the imine bonds are stable in CD₂Cl₂ solution. It is then reasonable to assume that, as initially proposed, the Lewis acidic metal cations catalyze the hydrolysis reaction in solution, facilitating the formation of the diazepine derivative **2.5**.



Scheme 2.3 Proposed mechanism for the intramolecular cyclization of ligand **2.2** to form ligand **2.5**.

In this respect, Rebek *et al.* showed that the rate of intramolecular cyclization of a model system consisting of a 3,3'-disubstituted-2,2'-bipyridine with an electrophilic ester moiety on one ring and a nucleophilic amide on the other as substituents could be enhanced by coordination of the bipyridine backbone to NiCl₂.⁹² Hydrolysis of an imine bond into an amine group could happen before or after coordination to a metal cation without affecting the outcome of the cyclization.

2.3.2 Synthesis and characterization of complex **2.6**

Reaction of ligand **2.2** with MnCl₂ afforded rhombohedral shaped single crystals of complex **2.6** suitable for X-ray diffraction. The IR spectrum of complex **2.6** does not show an imine C=N str and presents overlapped OH and secondary amine strs around

3300 cm^{-1} . FAB mass spectrometry data shows a peak at $m/z = 634$, consistent with $[\text{M-L}]^+$ where L is once again the diazepine ligand **2.5**. The UV-Vis spectrum of the complex shows a band at 400 nm corresponding to the $\pi\text{-}\pi^*$ transition of the phenol ring overlapped with metal to ligand charge transfer (MLCT) band, Figure 2.7. The bands at higher energies correspond to the $\pi\text{-}\pi^*$ transition of the bipyridine backbone.^{164,165} Given that Mn^{2+} is d^5 , all the $d\text{-}d$ transitions are spin forbidden and, as a consequence, no such transitions are visible due to their overlap with much more intense ligand-related bands.¹⁶⁶

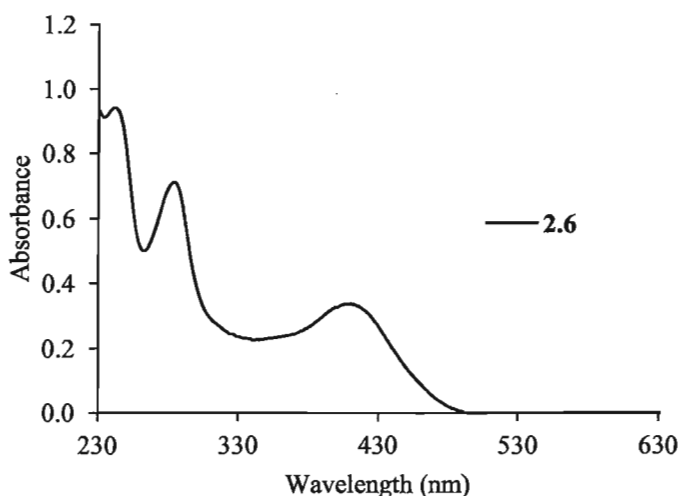


Figure 2.7 UV-Vis spectrum of an approximately 10^{-5}M solution of complex **2.6** in methanol.

Single crystals of complex **2.6** were characterized by X-ray diffraction. The reaction product is a centrosymmetric dinuclear Mn^{2+} complex comprising two diazapene **2.5** ligands that crystallises in the triclinic space group $P\bar{1}$, Figure 2.8. The coordination environment of each Mn^{2+} ion is comprised of a diazepine ligand **2.5** that is coordinated to a Mn^{2+} ion *via* the lone pairs on the pyridyl N atoms. Three Cl^- ions and one ethanol solvent molecule complete the distorted octahedral geometry around the metal centre. Two of the Cl^- ions act as μ -bridges between two Mn^{2+} ions, with intradimer $\text{Mn}\cdots\text{Mn}$ distances of 3.4935(5) Å. All Mn-Cl distances are similar, with $\text{Mn-Cl}_{\text{bridge}}$ bond lengths of 2.5359(6) and 2.5218(5) Å, and 2.5218(5) Å for the $\text{Mn-Cl}_{\text{axial}}$ bonds. The ethanol molecule coordinated to the Mn^{2+} ion appears to be protonated based on the charge balance and on the presence of electron density in the difference map that indicates the presence of a hydrogen atom bonded to the O atom of the ethanol molecule. There are

interdimer short contacts between each diazepine amine to one Cl^- ion of a neighbouring dimer, with $\text{N4-H}\cdots\text{Cl}_{\text{bridge}}$ distances of 2.750(2) Å and $\text{N3-H}\cdots\text{Cl}_{\text{axial}}$ distances of 2.603(9) Å. The same axial Cl^- anion also makes a short contact with a hydroxyl group from a neighbouring dimer, with a $\text{OH}\cdots\text{Cl}_{\text{axial}}$ distance of 2.360(2) Å. There are also π -stacking interactions between bipyridine rings in the range of 3.2306(8) - 3.2537(8) Å between the best planes of partially overlapped dimers. The shortest interdimer $\text{Mn}\cdots\text{Mn}$ distance is 8.4841(6) Å, which renders the dimers magnetically isolated from each other (see below). See Table 2.6 for selected bond lengths and angles for this complex.

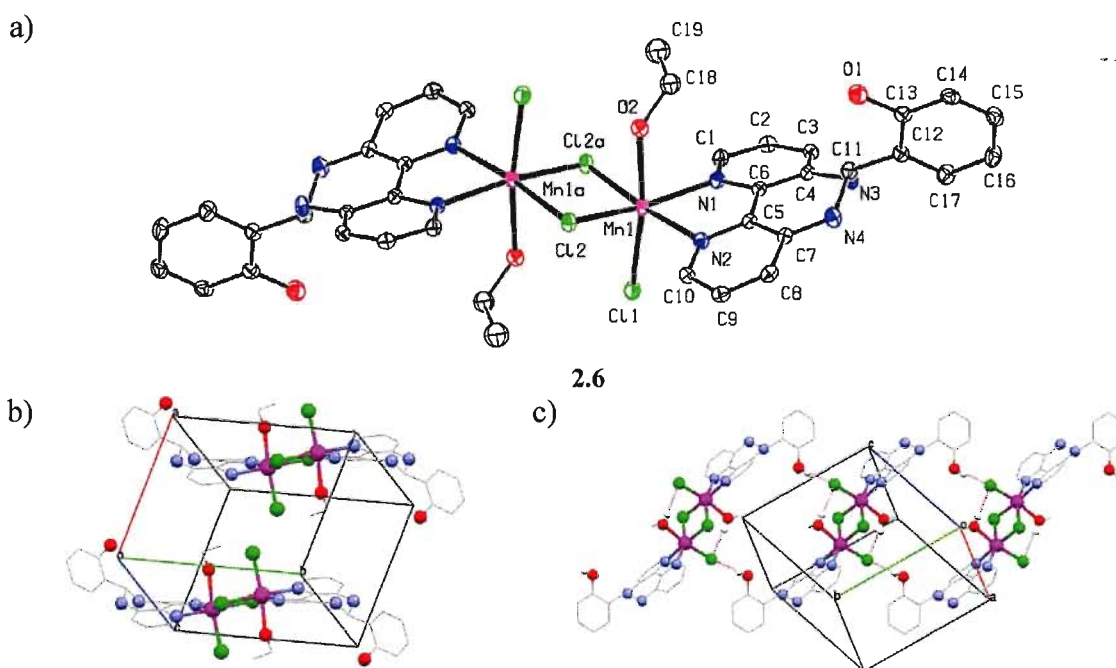


Figure 2.8 a) ORTEP plot of the molecular structure **2.6** showing the corresponding numbering scheme. Thermal ellipsoids plotted at 50% probability. b) Unit cell of **2.6**. c) Hydrogen bonding interactions between hydroxyl groups and axial chloride ions show as red dotted lines. Hydrogen atoms are omitted for clarity except where necessary.

Table 2.6 Selected bond lengths (Å) and angles (°) for complex **2.6**.

Bond length			
Mn1-Cl1	2.5344(6)	Mn1-N2	2.2178(18)
Mn1-Cl2	2.5218(5)	Mn1-Cl2a ⁱ	2.5359(6)
Mn1-O2	2.3427(16)	N3-C11	1.454(3)
Mn1-N1	2.1999(16)	N4-C11	1.446(3)
Bond angle			
Cl1-Mn1-Cl2	95.06(2)	Cl2a-Mn1-O3 ⁱ	85.61(4)
Cl1-Mn1-O2	172.11(4)	Cl2a-Mn1-N1 ⁱ	99.41(5)
Cl1-Mn1-N1	101.95(5)	Cl2a-Mn1-N2 ⁱ	171.41(4)
Cl1-Mn1-N2	91.20(5)	O2-Mn1-N1	84.83(6)
Cl1-Mn1-Cl2a ⁱ	89.25(2)	O2-Mn1-N2	94.77(6)
Cl2-Mn1-O2	79.22(4)	N1-Mn1-N2	72.11(6)
Cl2-Mn1-N1	159.21(5)	N3-C11-N4	109.86(17)
Cl2-Mn1-N2	95.88(4)	N3-C11-C12	110.47(15)
Cl2-Mn1-Cl3a ⁱ	92.63(2)	N4-C11-C12	110.51(17)
Dihedral angle			
C4-C5-C6-C7	9.4(3)		

Symmetry transformation: ⁱ2-x, -1-y, 1-z.

2.3.2.1 Magnetic characterization of **2.6**

Magnetic susceptibility measurements on a polycrystalline sample of **2.6** were carried out in an applied field of 1000 Oe between 2-300 K. Figure 2.9 shows that $1/\chi$ decreases monotonically as the temperature decreases until reaching 50 K. Below this temperature the data deviates from the expected linear behaviour. An appropriate fit for the data above 50 K was obtained applying the Curie-Weiss law to the magnetic data. The fit afforded a Curie constant of 8.74 emu K/Oe mol (expected 8.75 for two $S=5/2$ with $g=2$), indicating the presence of two high spin Mn^{2+} ions per molecule and the value of the Weiss constant of $\theta = -19.37$ K.

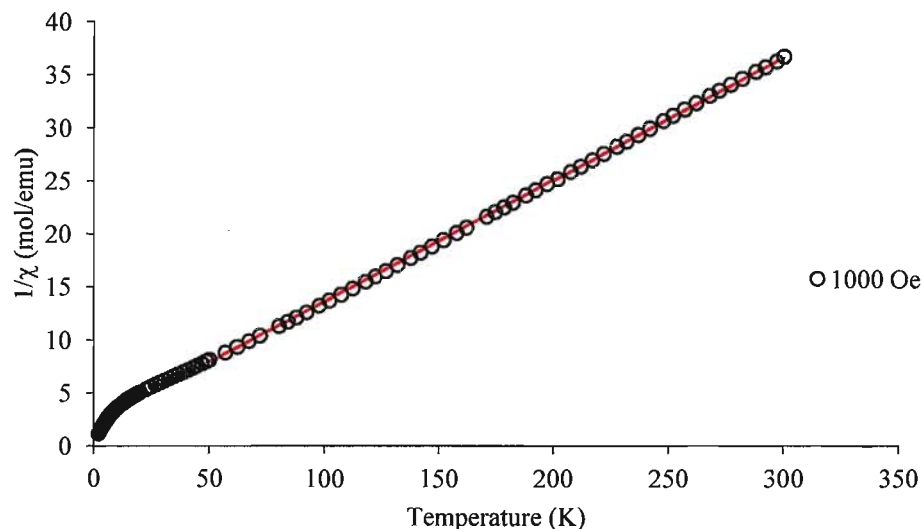


Figure 2.9 Variation of $1/\chi$ versus temperature for **2.6**. The fit to the Curie-Weiss law is shown as a red line.

The room temperature value of χT is 8.17 emu K/mol, a bit lower than the expected 8.75 emu K/mol for two non-interacting $S = 5/2$ Mn^{2+} cations. This result agrees with the fit using the Curie-Weiss law, indicating the presence of antiferromagnetic interactions in the compound. Given that the dimers seem well isolated (shortest interdimer $\text{Mn}\cdots\text{Mn}$ distance of 8.4841(6) Å), the lower χT can be attributed to an intradimer antiferromagnetic coupling between the Mn^{2+} ions. Figure 2.10 shows that χT remains fairly constant down to 100 K and then it starts decreasing, reaching a value of 1.7 emu K/mol at 2 K. In order to model this data we assumed isotropic interactions between the coordinated Mn^{2+} cations due to the high symmetry of the complex and that there is no orbital contribution to the magnetic moment for these ions. The appropriate spin Hamiltonian for this dinuclear complex is then defined by equation (2.1)

$$H = -JS_{\text{Mn}_A} \cdot S_{\text{Mn}_B} \quad (2.1)$$

and using the van Vleck equation the corresponding expression for the magnetic susceptibility of a homodinuclear d^5 - d^5 complex is

$$\chi = \frac{Ng^2\beta^2}{k_B(T-\theta)} \frac{2\exp(x) + 10\exp(3x) + 28\exp(6x) + 60\exp(10x) + 110\exp(15x)}{1 + 3\exp(x) + 5\exp(3x) + 7\exp(6x) + 9\exp(10x) + 11\exp(15x)} \quad (2.2)$$

where

$$x = \frac{J}{k_B T}$$

Figure 2.10 shows the fit (red line) to the experimental data (empty circles) using equation (2.2). The simulated data fits the experimental data all the way down to 50 K, where the fit deviates from the experimental data and tends towards a χT of zero. A single parameter curve fit to the expression for χT between 40-300 K afforded $J = -3.59$ K with $g = 1.99$ and $\theta = -0.1$ K ($R = 9.3 \cdot 10^{-4}$, where $R = [\Sigma(\chi_{\text{obs}} - \chi_{\text{calc}})^2 / \Sigma(\chi_{\text{obs}})^2]$). With an intradimer Mn...Mn distance of 3.4935(5) Å, direct interaction between magnetic centres can be ruled out, which points at the chloro bridges as the mediators of the exchange coupling.

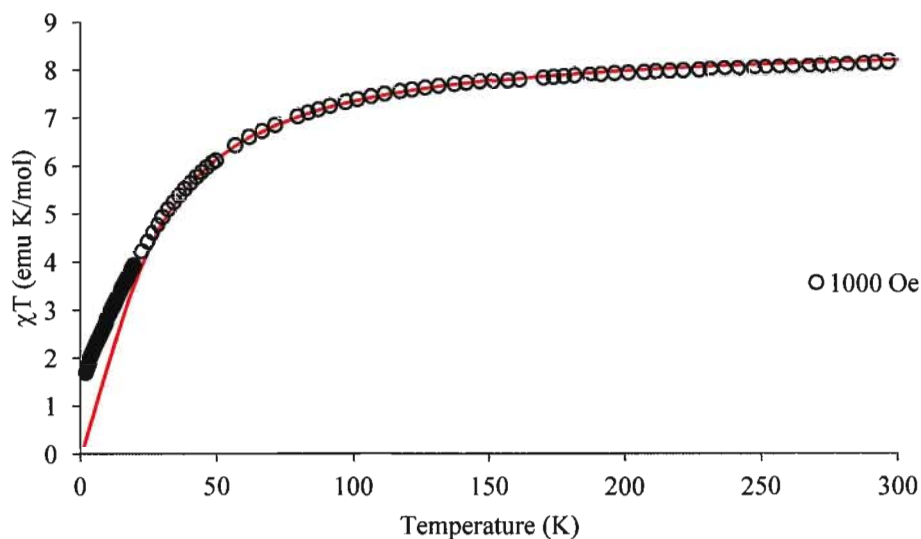


Figure 2.10 Variation of χT versus temperature for complex **2.6**. The fit to the van Vleck equation is shown as a red line.

The examples of chloro-bridged Mn^{2+} dimers available in the literature show that the strength and nature of the magnetic coupling depends on the topology and geometry of the Mn-Cl-Mn fragment. Magnetic coupling J and structural parameters for some representative complexes containing the $[\text{Mn}_2(\mu\text{-Cl})_2]^{2+}$ structural unit are summarized in Table 2.7. The coupling constant J for **2.6** is reasonable as compared with the literature values in the table, but the Mn...Mn distance and the Mn-Cl-Mn angle are small as compared with the tabulated data. A model explaining the influence of the structural parameters for chloro-bridged octahedral Mn^{2+} complexes on the magnitude and nature of the magnetic coupling has not been reported to-date. Although it would be tempting to correlate the coupling constant J with the Mn...Mn distance, the data presented in Table 2.7 shows exceptions, and our Mn^{2+} complex **2.6** is one of them. More detailed magnetostructural and theoretical studies for this kind of complexes are necessary before an accurate description of the magnetic interactions can be provided.

Table 2.7 Magnetic coupling J and structural parameters for chloro-bridged octahedral Mn^{2+} complexes.

Compound	$J (\text{cm}^{-1})$	$d_{\text{Mn}\cdots\text{Mn}} (\text{\AA})$	$\alpha_{\text{Mn-Cl-Mn}} (^{\circ})$	$d_{\text{Mn}(\mu\text{-Cl})} (\text{\AA})$	Ref.
^a $[\text{Mn}_2(\text{tpa})_2(\mu\text{-Cl})_2]^{2+}$	-8.8	3.521	88.6	2.63, 2.41	167
^b $\text{Mn}_2(\text{NIT2-thz})_2(\mu\text{-Cl})_2\text{Cl}_2(\text{H}_2\text{O})_2$	-8.4	3.514	88.5	2.52, 2.51	168
2.6	-3.59	3.493	87.3	2.52, 2.53	This work
^c $[\text{Mn}_2(\text{tacud})_2(\mu\text{-Cl})_2\text{Cl}_2]$	-1.81	3.655	90.2	2.60, 2.56	169
^d $[\text{Mn}_2(\text{pol})_2(\text{H}_2\text{O})_2(\mu\text{-Cl})_2\text{Cl}_2]$	-0.14	3.752	94.3	2.59, 2.52	170
^e $[\text{Mn}_2(\text{biz})_2(\mu\text{-Cl})_2]^{2+}$	+0.33	3.740	93.5	2.58, 2.56	171
^f $[\text{Mn}(\text{mymol})_2(\mu\text{-Cl})_2\text{Cl}_2]$	+0.94	3.694	93.8	2.61, 2.45	164

^a tpa = tris(2-pyridylmethyl)amine, ^b NIT2-thz = 2-(2'-thiazole)-4,4,5,5-tetramethylimidazoline-1-oxyl-3-oxide, ^c tacud = 1,4,8-triazacycloundecane, ^d pol = 2-pyridinemethanol, ^e biz = 2,2'-bi-imidazoline, ^f mymol = 2-methyl-6-[(pyridine-2-ylmethylene)amino]phenol

A reasonable explanation for the difference between simulated and experimental data below 50 K would be a paramagnetic impurity. Including simply a MnCl_2 impurity was attempted, but it did not improve the model. The formation of **2.5** and the excess of MnCl_2 present in the reaction solution may very well result in the formation of a mixture of chloride/salicylate Mn^{2+} complexes as a source of this impurity. Given the unknown and complex nature of the impurity no further attempts were made to model the data at low temperatures. It is worth noting that, during the modelling of the data, the effect of J

and θ on the final model were very close, possibly because both parameters have similar values. Based on the inter- and intramolecular Mn...Mn distances observed in the crystal structure, we decided to give the larger value to the exchange coupling constant J . Our rationale was that a larger coupling between two μ -chloro-bridged Mn^{2+} ions makes more sense than a strong through-space exchange coupling over a distance of 8.4 Å.

2.3.3 Synthesis and characterization of complex 2.7

Reaction of **2.2** with $\text{Cu}(\text{ClO}_4)_2$ in methanol afforded deep green blocks of the centrosymmetric complex **2.7** suitable for single crystal X-ray diffraction. The IR spectrum of complex **2.7** does not show a C=N imine str and presents a strong band at 1096 cm^{-1} indicative of a free perchlorate counterion.¹⁷² The phenol OH and secondary amine strs appear overlapped at 3300 cm^{-1} . FAB mass spectrometry data shows a peak at $m/z = 695$, consistent with the molecular ion $[\text{M-L}]^+$, where L is once again the diazepene ligand **2.5**. The UV-Vis spectrum of the complex shows a band at $\lambda = 400\text{ nm}$ formed by the overlapping $\pi\text{-}\pi^*$ transitions of the phenol ring of the diazepene ligand and the MLCT transitions, Figure 2.11.^{173,174} The bands at higher energies correspond to the $\pi\text{-}\pi^*$ transition of the bipyridine backbone. No $d\text{-}d$ bands are visible due to their overlap with much more intense ligand-related bands.¹⁶⁶

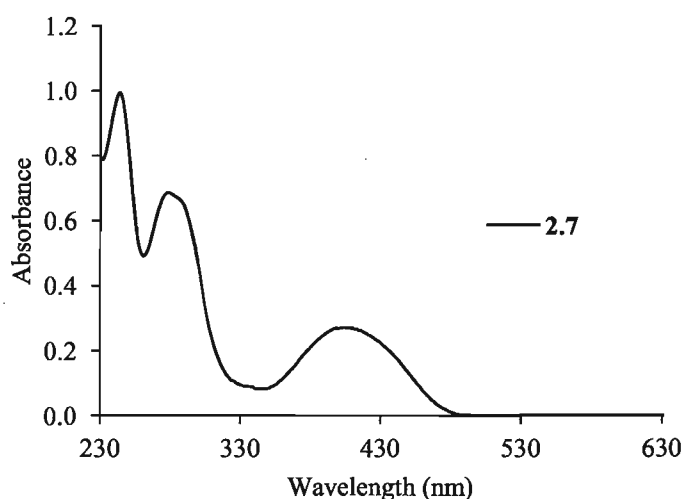


Figure 2.11 UV-Vis spectrum of a 10^{-5}M solution of complex **2.7** in methanol.

Single crystals of complex **2.7** were characterized by X-ray diffraction. The complex crystallizes in the orthorhombic space group *Pnna*. In this case, the complex is also a dinuclear molecule, but the Cu^{2+} ions have a distorted square base pyramidal coordination geometry, forcing **2.5** to form a ‘double-decker’ dimer instead of a linear dimer as in complex **2.6**. Another difference between complexes **2.6** and **2.7** is the presence of the salicylaldehyde anion in the coordination environment of Cu^{2+} ion. This can be rationalized based on the poor coordinating ability of a perchlorate ion as compared to that of the salicylaldehyde anion generated from the hydrolysis of **2.2**.

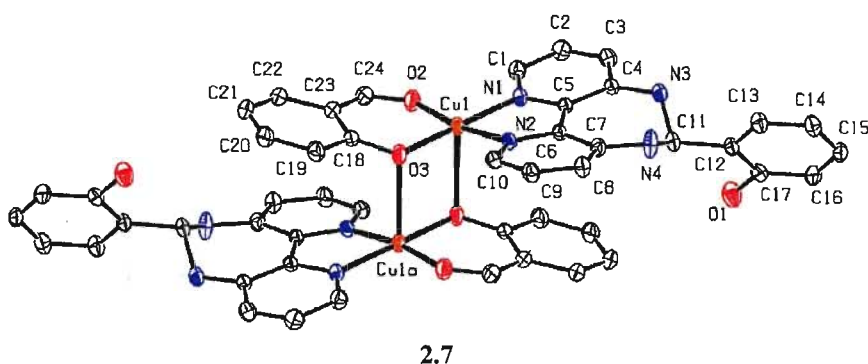


Figure 2.12 ORTEP plot of the molecular structure of Cu^{2+} complex **2.7** showing the corresponding numbering scheme. Thermal ellipsoids plotted at 50% probability. The hydrogen atoms and perchlorate counterions are omitted for clarity.

The bipyridine ring and the salicylaldehyde anion form the base of the square base pyramid, with bond lengths ranging from 1.9142(18) to 1.977(2) Å. The axial position is occupied by the deprotonated hydroxyl group of the symmetrically equivalent salicylaldehyde anion, with a long O3b-Cu bond distance of 2.4949(19) Å. This bridging mode has been observed for other perchlorate salts of various complexes.^{175,176} The asymmetric unit contains two disordered perchlorate anions, necessary to balance the overall charges of the dimer (Figure 2.13). The umbrella-like shape of the perchlorate anion type A comes from the two components of positional disorder about the C11-O4 bond along a two-fold axis.

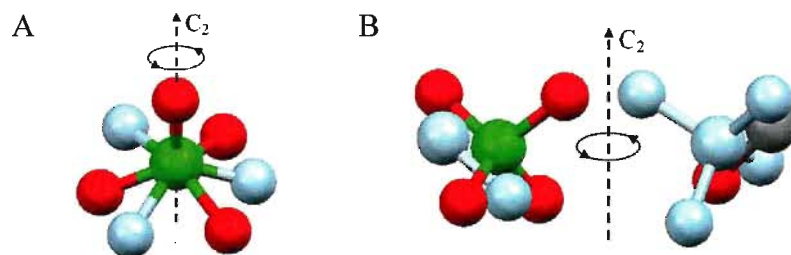


Figure 2.13 Perchlorate disorder types A and B. Chlorine and oxygen atoms are shown in green and red respectively. The atoms belonging to the second component of the disorder are shown in light blue.

These disordered O atoms refine nicely to an occupation factor close to 0.5, indicative of about a 50% distribution of perchlorate anions type A between two orientations in the same position in the unit cell, rotated 180° from each position. The disorder of type B perchlorate anions is somewhat more complicated. Careful analysis of the electron density map revealed a methanol molecule overlapped with a type B perchlorate anion. Refinement of the occupancy factor of the atoms in each molecule showed that each molecule exchange places 50% of the time across the two-fold axis, so in each position we can find either a methanol or perchlorate molecule in the crystal structure.

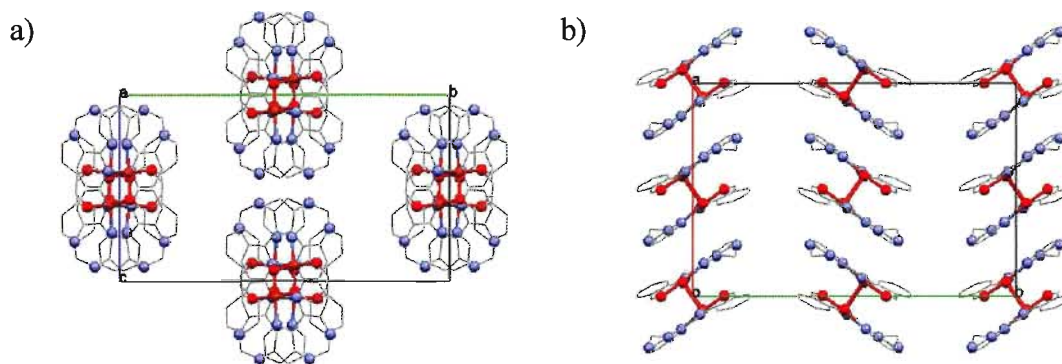


Figure 2.14 a) View of the unit cell of 2.7 down the *a*-axis, c) view of the unit cell down the *c*-axis. The hydrogen atoms and perchlorate counterions are omitted for clarity.

The crystal packing shows alternating, tilted stacks of dimers running down the *a*-axis. There is an extensive network of interactions between stacks and perchlorate anions of both types. One of the perchlorate ions bridges a total of four neighbouring dimers. This perchlorate participates in hydrogen bonding interactions involving the disordered

oxygen atoms in the anion and the hydroxyphenyl protons of two neighbouring dimers, with bond lengths of 2.14 and 2.04 Å for O1-H \cdots O7 and O1-H \cdots O5 respectively. The perchlorate O atom sitting on the two-fold axis forms two hydrogen bonds with the secondary amines of two neighbouring dimers related by the same axis, with a N4-H \cdots O4 bond length of 2.28(2) Å. Two O atoms of the other perchlorate ion in the asymmetric unit interacts with one complex dimer *via* a bifurcated hydrogen bond with a secondary imine, with bond distances N3-H \cdots O10 of 2.47(1) Å and N3-H \cdots O11 of 2.21(2) Å. This amine also forms hydrogen bonds with the disordered methanol molecule, with a hydrogen bond length N3-H \cdots O30 equal to 2.19(9) Å. See Table 2.8 for selected bond lengths and angles for this complex.

Table 2.8 Selected bond lengths (Å) and angles (°) for complex **2.7**.

Bond lengths			
Cu1-O2	1.946(2)	Cu1-O3b ⁱ	2.4949(19)
Cu1-O3	1.9142(18)	N3-C11	1.452(3)
Cu1-N1	1.964(2)	N4-C11	1.451(3)
Cu1-N2	1.977(2)		
Bond angles			
O2-Cu1-O3	91.43(8)	O3-Cu1-N2	95.20(8)
O2-Cu1-N1	92.52(8)	O3-Cu1-O3b ⁱ	80.90(7)
O2-Cu1-N2	170.67(8)	O3b-Cu1-N1 ⁱ	101.07(8)
O2-Cu1-O3b ⁱ	91.20(7)	O3b-Cu1-N2 ⁱ	96.32(8)
O3-Cu1-N1	175.55(8)	N1-Cu1-N2	80.65(8)
N4-C11-C12	109.7(2)	N3-C11-N4	110.3(2)
N3-C11-C12	109.4(2)		
Dihedral angle			
C4-C5-C6-C7	-4.3(4)		

Symmetry transformation: ⁱ-x,1-y,2-z.

2.3.3.1 Magnetic characterization of complex 2.7

Magnetic susceptibility measurements on a polycrystalline sample of **2.7** were carried out in an applied field of 1000 Oe between 2-300 K. The room temperature value of χT is 0.78 emu K/mol, which is a little bit higher than the theoretical value 0.75 cm³ K/mol for two non-interacting Cu²⁺ ions ($S = 1/2$, $g = 2$, $\chi T = 0.375$ cm³ K/mol). Figure 2.15 shows that χT remains fairly constant down to 20 K where it starts decreasing, reaching a value of 0.45 cm³ K/mol at 2 K.

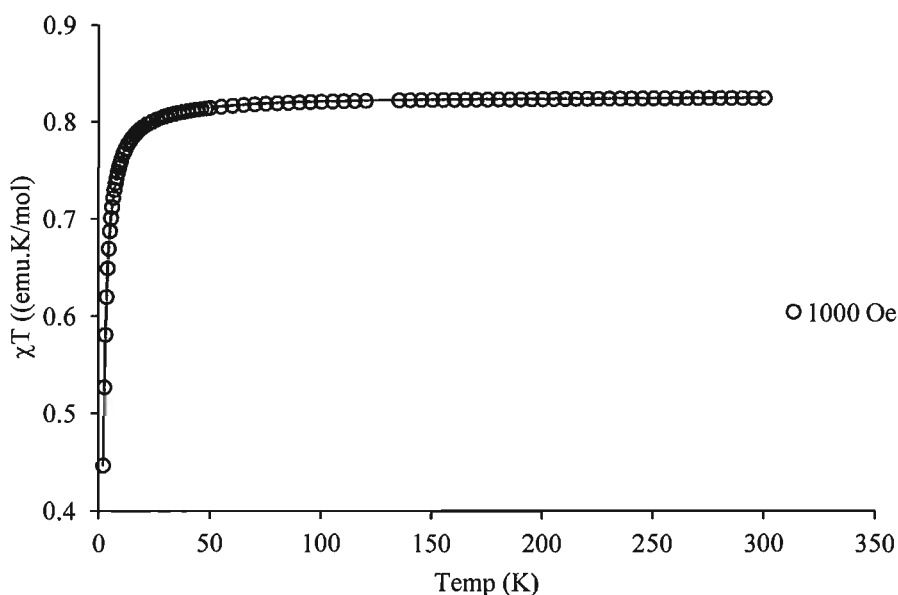


Figure 2.15 Variation of χT versus temperature for complex **2.7**. The fit to the van Vleck equation is shown as a red line.

In order to model this data, we assumed isotropic interactions between the coordinated Cu²⁺ cations due to the high symmetry of the complex and that there is no orbital contribution to the magnetic moment for this ions. The appropriate spin Hamiltonian for this dinuclear complex is then defined by equation (2.3)

$$H = -JS_{Cu_A} \cdot S_{Cu_B} \quad (2.3)$$

and from the van Vleck equation we can derive the Bleaney-Bowers equation (2.4) for the magnetic susceptibility of a homodinuclear d^9 - d^9 system:

$$\chi = \frac{2Ng^2\beta^2}{k_B(T - \theta)[3 + \exp\left(\frac{-J}{k_BT}\right)]} \quad (2.4)$$

Figure 2.15 shows the fit (red line) to the experimental data (empty circles) using equation (2.4). The simulated data fits the experimental data across the complete experimental temperature range. A single parameter curve fit to the expression for χT between 2-300 K afforded $J = -2.23$ K with $g = 2.1$, $\theta = -0.01$ K ($R = 9.3 \cdot 10^{-5}$). This indicates that the dimers are magnetically well isolated and, that within a dimer, the two Cu^{2+} ions are antiferromagnetically coupled to each other. This behaviour agrees with that of other Cu dimers from the literature that display a μ -oxo group from a salicyl moiety that bridges the two metal centres. The magnetic orbitals $d_{x^2-y^2}$ in the dimer are parallel to each other, and the bridging O atoms overlap with the $d_{x^2-y^2}$ orbital of one Cu^{2+} ion and with the d_z^2 orbital of the other. This hampers any kind of coupling between the spin on each metal centre except if orbital orthogonality is lost due to lattice effects.^{177,178}

2.3.4 Synthesis and characterization of complex 2.8

In order to promote the coordination of **2.2** in a symmetrical conformation similar to the one shown in Scheme 2.2 b), the ligand was deprotonated with triethylamine and subsequently reacted with FeCl_3 in dry acetonitrile. Slow evaporation in air of the resulting red reaction solution afforded red needles suitable for X-ray diffraction. MALDI-TOF mass spectrometry data for the single crystals shows a peak at $m/z = 634.1036$, consistent with the molecular ion of complex **2.8**. The homoleptic complex **2.8** shows that our objective is partially accomplished, Figure 2.16 a). This complex crystallizes in the centrosymmetric space group $C2/c$, with the Fe^{3+} ion located on an inversion centre. Two molecules of ligand **2.9** related by the inversion centre coordinate in a facial manner to the Fe^{3+} ion, forming a distorted octahedral geometry around the metal centre. The crystal structure reveals that the ligand has been partially hydrolyzed, essentially losing one of its arms, but it is still able to coordinate in a tridentate manner *via* its deprotonated hydroxyphenyl group, one pyridine N atom and the remaining imine N lone pair. See Table 2.9 for selected bond lengths and angles.

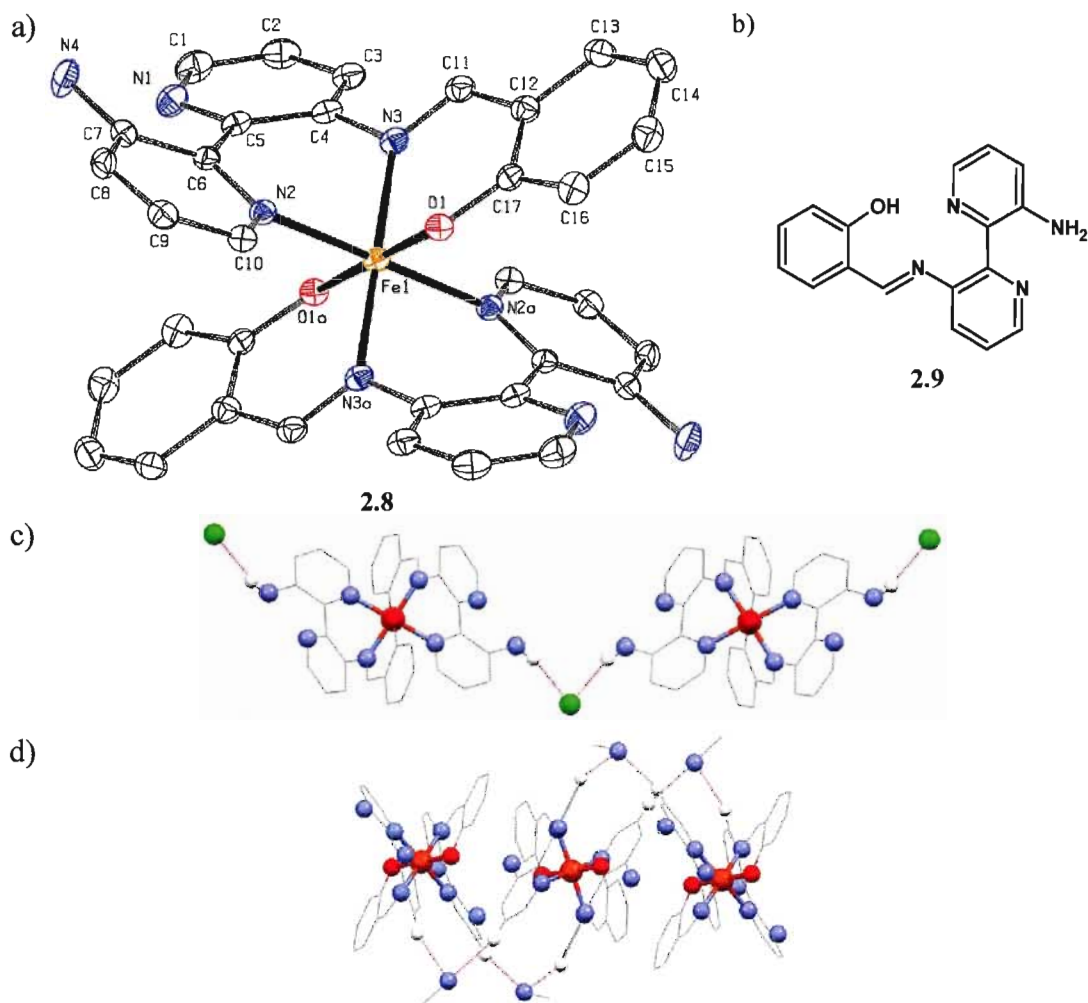


Figure 2.16 a) ORTEP plot of the molecular structure of **2.8** showing the corresponding numbering scheme. Thermal ellipsoids are plotted at 50% probability. b) Schematic representation of the molecular structure of ligand **2.9**. c) Hydrogen bonding interactions between amino groups and chloride counterions shown as red dashed lines. d) Intrastack acetonitrile short contacts between neighbouring complex molecules. The hydrogen atoms, chloride counterion and acetonitrile molecules are omitted for clarity where necessary.

In order to coordinate in this manner the bipyridine unit adopts the anti-periplanar configuration, expected for a symmetrical coordination mode as shown in Scheme 2.2, with an angle of $26.72(8)^\circ$ between the best planes of the amino-pyridine rings. The imine group is conjugated with the hydroxyphenyl ring, with a torsion angle of just 10° between the C=N and the (aryl)C-O bonds, while the hydroxyphenyl ring is twisted away from the bipyridine ring by an angle of $35.00(10)^\circ$. The Fe-N_{imine} bond lengths are in the range of 1.92-1.98 Å, consistent with a low spin Fe³⁺ complex.³⁰

There is a hydrogen bond between the free amino group and a pyridine N atom, N4-H4 \cdots N1 of 2.04 Å, which is slightly longer than the equivalent interaction reported in the structure of 3,3'-diamino-2,2'-bipyridine. This same amine forms a second hydrogen bond with a Cl⁻ counterion, presenting a bond distance of 2.43 Å, as shown by dashed lines in Figure 2.16. Each complex **2.8** forms two such hydrogen bonds that give rise to a 1D arrangement of chloride-bridged complexes that propagate along the [1,0,2] direction, Figure 2.16 c). The complexes stack down the *c*-axis, with four molecules forming short intra-track contacts C3-H3 \cdots N5 and C9-H9 \cdots N5 of 2.59 and 2.73 Å respectively, Figure 2.16 d). The shortest Fe \cdots Fe distance is 6.6340(17) Å and occurs within a stack.

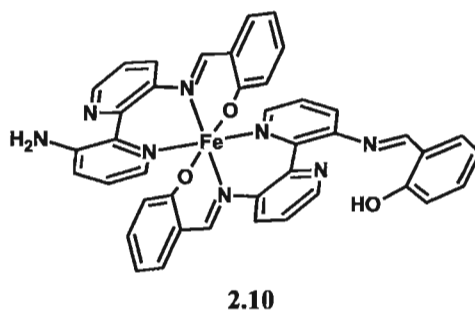
Table 2.9 Selected bond lengths (Å) and angles (°) for complex **2.8**.

Bond lengths			
Fe1-O1	1.8704(14)	Fe1-O1a ⁱ	1.8704(14)
Fe1-N2	1.9866(18)	Fe1-N2a ⁱ	1.9866(18)
Fe1-N3	1.9279(18)	Fe1-N3a ⁱ	1.9279(18)
N3-C11	1.295(3)		
Bond angles			
O1-Fe1-N2	91.01(6)	N2-Fe1-N3a ⁱ	94.12(7)
O1-Fe1-N3	89.83(7)	O1a-Fe1-N3 ⁱ	90.17(7)
O1-Fe1-O1a ⁱ	180	N2a-Fe1-N3 ⁱ	94.12(7)
O1-Fe1-N2a ⁱ	88.99(6)	N3-Fe1-N3a ⁱ	180
O1-Fe1-N3a ⁱ	90.17(7)	O1a-Fe1-N2a ⁱ	91.01(6)
N2-Fe1-N3 ⁱ	85.88(7)	O1a-Fe1-N3a ⁱ	89.83(7)
O1a-Fe1-N2 ⁱ	88.99(6)	N2a-Fe1-N3a ⁱ	85.88(7)
N2-Fe1-N2a ⁱ	180		
Dihedral angle			
C4-C5-C6-C7	150.6(2)		

Symmetry transformation: ⁱ2-x,-y,-z

As briefly mentioned, the formation of ligand **2.9** requires the hydrolysis of one imine bond of ligand **2.2** without any cyclization. A feasible mechanism for the formation of complex **2.8** is the coordination of a metal ion by two molecules of ligand **2.2** *via* the

deprotonated phenol ring, the imine nitrogen and a pyridine nitrogen in a tridentate manner (symmetric binding mode b) in Scheme 2.2. Subsequent hydrolysis of the uncoordinated imine bonds would yield complex **2.9**. This scenario is not unlikely given the fragment ion at $m/z = 738.16$ present in the MALDI-TOF mass spectrum of (unwashed) single crystals of complex **2.8**. The mass of this fragment matches the expected mass of complex **2.10**.



2.3.4.1 Magnetic characterization of complex **2.8**

Magnetic susceptibility measurements were carried out on a polycrystalline sample of **2.8** in an applied field of 1000 Oe between 2–300 K. Figure 2.17 shows that $1/\chi$ decreases monotonically as the temperature decreases following the Curie-Weiss law. A one parameter fit to the data afforded a Curie constant of 0.377 emu K/Oe mol (expected 0.375 for one $S = 1/2$ and $g = 2$), indicating the presence of one low spin Fe^{3+} cation. The fit also afforded a Weiss constant of $\theta = -1.3$ K, indicating that the magnetic centres are fairly well isolated from each other with only weak antiferromagnetic interactions present between Fe^{3+} cations. Figure 2.18 shows that, as expected for a weak antiferromagnetic coupling, χT remains fairly constant down to 20 K and then it starts decreasing until it reaches a value of $0.22 \text{ cm}^3 \text{ K/mol}$ at 2 K.

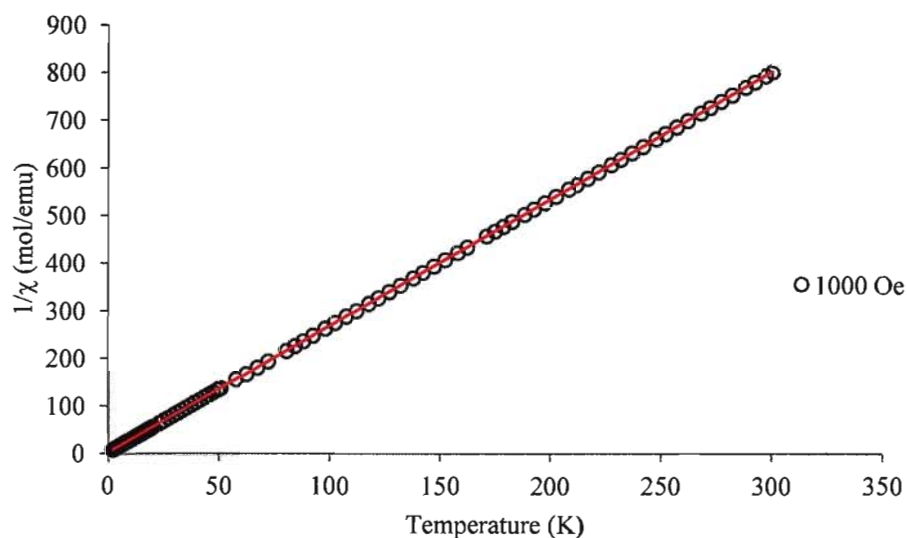


Figure 2.17 Variation of the $1/\chi$ product versus temperature for complex **2.8**. The fit to the Curie-Weiss law is shown as a red line.

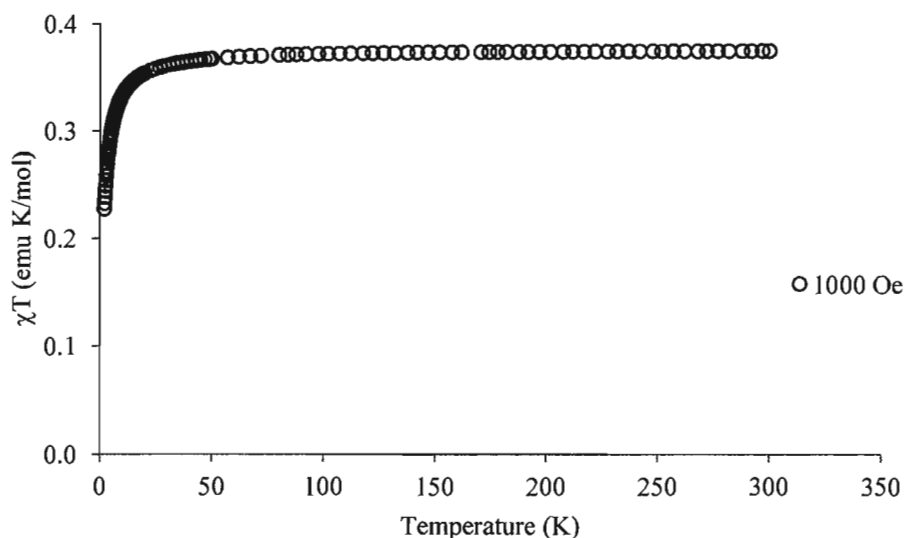


Figure 2.18 Variation of the χT product versus temperature for complex **2.8**.

2.3.5 Synthesis and characterization of complex **2.11**

The preparation of complex **2.11** was carried out under similar conditions as the preparation of complex **2.8**. In this case, however, the reaction solution was cooled to 4°C, and red single crystals suitable for single crystal X-ray diffraction were obtained after two weeks. This complex is comprised of two Fe^{3+} centres coordinated by two molecules of **2.2** and one μ -oxo bridge. The IR spectrum of the single crystals shows a

band at 1610 cm^{-1} which corresponds to the C=N str in the ligand. The frequency for this band is very close to the band corresponding to the C=N str for the free ligand, observed at 1612 cm^{-1} . This is indicative of weak bonding of the lone pairs of the imine N atom to the Fe^{3+} centres. The UV-Vis spectrum of the complex is shown in Figure 2.19. The absorption bands between 230 and 300 nm correspond to the $\pi\text{-}\pi^*$ transitions of the ligand. At lower energies, the spectrum shows three more bands, at $\lambda = 348, 426$ and 492 nm. The band at $\lambda = 348$ nm can be tentatively assigned to the overlapping contributions of the imine-Fe and phenolate-Fe ligand to metal charge transfer (LMCT) bands.^{179,180} The smaller bands at $\lambda = 426$ and 492 nm can be tentatively assigned to the Fe-O-Fe LMCT band and to an additional band due to phenolate-Fe LMCT,^{179,181} but further studies will be necessary to fully assign each of the LMCT process. Given that a high spin Fe^{3+} complex is a d^5 system, all the $d\text{-}d$ bands are forbidden and, as a consequence, these bands are not visible due to their overlap with much more intense ligand-related bands.¹⁶⁶

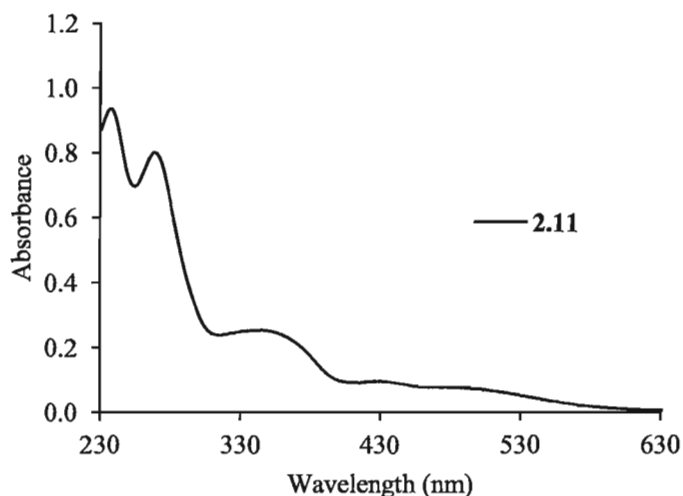


Figure 2.19 UV-Vis spectrum of a 10^{-5}M solution of complex **2.11** in methanol.

X-ray diffraction experiments on the single crystals of **2.11** revealed that this complex crystallizes in the space group $P\text{-}1$, with one crystallographically independent dimer per unit cell. The coordination complex comprises two molecules of **2.2** coordinating two pentacoordinated Fe^{3+} ions, Figure 2.20 a) and b). Both metal centres present distorted coordination environments that could be described as being intermediate between square pyramidal and trigonal bipyramidal. The trigonality index τ proposed by

Addison *et al.*¹⁸² can be used to determine how close a pentacoordinated centre is to these two geometries. This index has the value $\tau = 0$ for a perfect tetragonal geometry, and it is $\tau = 1$ for a perfect trigonal bipyramidal geometry. For complex **2.11** $\tau_{\text{Fe1}} = 0.76$ and $\tau_{\text{Fe2}} = 0.6$, so the coordination sphere of both Fe^{3+} ions can be described as being closer to that of a distorted trigonal bipyramidal geometry.

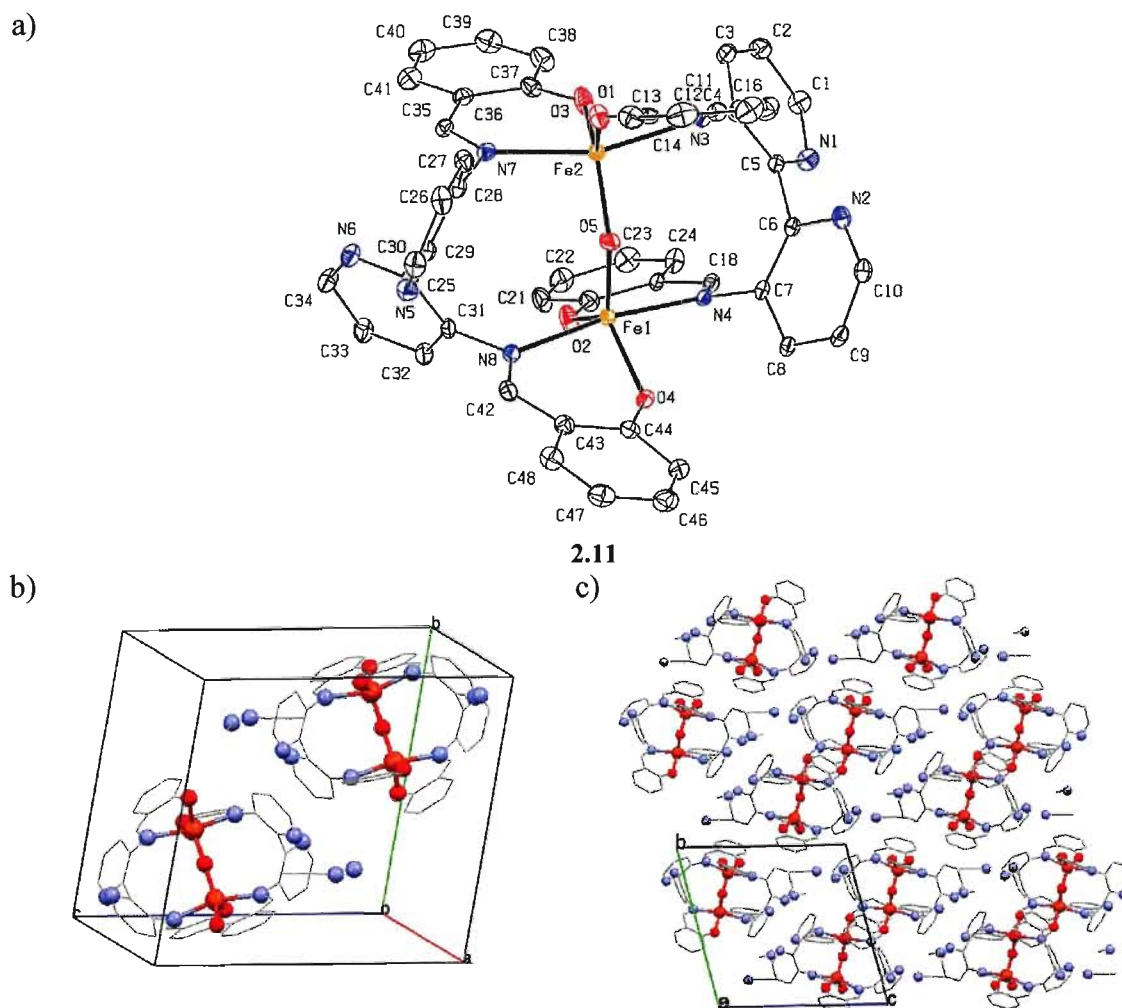


Figure 2.20 a) ORTEP plot of the molecular structure of **2.11** showing the corresponding numbering scheme. Thermal ellipsoids are plotted at 50% probability. b) Unit cell of **2.11**. c) View of the packing diagram of **2.11** on the *bc* plane. The hydrogen atoms and acetonitrile molecules are omitted for clarity when necessary.

The equatorial plane of the coordination environment of both metal atoms comprises two oxo groups from the deprotonated phenol rings and the μ -oxo group that bridges both metal centres, and the axial positions are occupied by two imine nitrogen atoms. In this complex, the coordination mode of **2.2** is similar to the symmetric mode

shown in Scheme 2.2 b), but the bipyridine ring is not involved in the coordination of the metal centres. This is caused by the bridging oxygen atom, which keeps both Fe³⁺ ions in close proximity and forces the ligand molecules to bring their imine arms close together, leaving the pyridine nitrogen atoms uncoordinated with an angles of 80.8(2)° and 83.1(2)° between their respective best planes. The Fe-N_{imine} bond lengths are in the range 2.162-2.171 Å, which indicates that both Fe³⁺ ions are high spin.³⁰ The C=N bonds of the complex are not noticeably longer than those of the free ligand (C=N_{ligand} = 1.287-1.291 Å vs. C=N_{complex} = 1.292-1.299 Å). This is probably a consequence of the weak bonding of the imine N lone pairs to the Fe³⁺ ions due to the electronic population of the antibonding, orbitals. See Table 2.10 for selected bond lengths and angles for this complex.

Table 2.10 Selected bond lengths (Å) and angles (°) for complex **2.11**.

Bond lengths			
N3-C11	1.292(5)	Fe1-N4	2.162(3)
N4-C18	1.299(5)	Fe1-N8	2.167(3)
N7-C35	1.289(5)	Fe2-O5	1.779(3)
N8-C42	1.289(4)	Fe2-O1	1.909(3)
Fe1-O4	1.909(2)	Fe2-O3	1.891(2)
Fe1O5	1.795(3)	Fe2-N3	2.171(3)
Fe1-O2	1.887(3)	Fe2-N7	2.167(3)
Bond angles			
C4-N3-C11	116.0(3)	O5-Fe1-N4	95.0(1)
C7-N4-C18	117.4(3)	O4-Fe1-N8	85.5(1)
C31-N8-C42	117.0(3)	O2-Fe1-N8	88.3(1)
C35-N7-C28	117.1(3)	O5-Fe1-N8	95.0(1)
O4-Fe1-O2	119.0(1)	O1-Fe2-N3	84.7(1)
O2-Fe1-O5	123.3(1)	O3-Fe2-N3	84.7(1)
O5-Fe1-O4	117.6(1)	O5-Fe2-N3	98.8(1)
O5-Fe2-O1	114.5(1)	O1-Fe2-N7	86.6(1)
O5-Fe2-O3	118.7(1)	O3-Fe2-N7	86.5(1)
O3-Fe2-O1	126.8(1)	O5-Fe2-N7	99.2(1)
O4-Fe1-N4	89.2(1)	Fe1-O5-Fe2	148.0(2)

Table 2.10 Continued.

Bond angles			
O2-Fe1-N4	86.8(1)		
Dihedral angles			
C4-C5-C6-C7	102.8(5)	C28-C29-C30-C31	101.7(5)
C11-N3-C4-C5	64.25(5)	C35-N7C28-C29	69.1(5)
C18-N4-C7-C6	76.5(5)	C42-N8-C31-C30	70.2(5)

The molecules pack on the *bc* plane with their non-crystallographic C_2 axis parallel to the *a*-axis of the unit cell, Figure 2.20 c). The structure presents intermolecular $CH\cdots\pi$ interactions within the range 2.81–2.89 Å, and weak $C-H\cdots X$ interactions between pyridine/imine hydrogen atoms and phenol O atoms or pyridine N atoms, Table 2.11.

Table 2.11 Distance *d* and angle α of the $C-H\cdots X$ short contacts in 2.11 .

	<i>d</i> [C-H \cdots X] (Å)	<i>d</i> [H-C \cdots X] (Å)	α [C-H \cdots X] (°)
C8-H8 \cdots O4	2.47	2.988(5)	114
C27-H27 \cdots O1	2.48	2.905(5)	107
C18-H18 \cdots N1	2.52	3.097(6)	119
C42-H42 \cdots N5	2.62	3.173(6)	118
C35-H35 \cdots N6	2.61	3.106(6)	113
C3-H3 \cdots O3 ⁱ	2.54	3.311(6)	138
C35-H35 \cdots N6 ⁱⁱ	2.59	3.381(6)	142

Symmetry transformation: ⁱ1-*x*,2-*y*,1-*z*, ⁱⁱ1-*x*,2-*y*,-*z*.

2.4 Conclusions

Two new *bis*-imine ligands **2.2** and **2.3** have been synthesized and fully characterized. The free ligands **2.2** and **2.3** are more stable versus hydrolysis than ligand **1.40**, as expected from replacing the pyridine rings on the arms of the ligand by phenol rings. The coordination of **2.2** to a series of metal salts has been carried out, and the characterization of the products has revealed that its coordination chemistry strongly influences the susceptibility of the imine bonds towards nucleophilic attack. While the formation of the diazepine ligand **2.5** seems to be the dominant reaction in the presence of no base,

deprotonation of the phenol ring yielded the desired tridentate molecular coordination albeit with a reminder of the sensitivity of imines to hydrolysis. The metal-catalyzed formation of the diazepine **2.5** illustrates a potential protection-deprotection-cyclization strategy for the synthesis of novel dipyridyl 1,3-diazepine derivatives in mild conditions. The complexes prepared with the diazepine ligand **2.5** showed intramolecular antiferromagnetic coupling and weak magnetic interactions with their neighbours. Complex **2.8** presents the targeted symmetric coordination mode of ligand **2.2**, even though one of the imine bonds is hydrolyzed. The behaviour of the Fe^{3+} centres in this complex is very close to that of a Curie paramagnet, presenting a very small antiferromagnetic interaction at low temperatures. The preparation of complex **2.11** highlights the suitability of ligand **2.2** for the preparation of polynuclear paramagnetic metal complexes using the ligand as a framework for templating the metal centres. Although the coordination chemistry of 3,3'-diamino-2,2'-bipyridine is dominated by the chelation of the bipyridine ring, complexes **2.8** and **2.11** prove that our strategy to enhance and control its coordination chemistry through rational ligand design is successful.

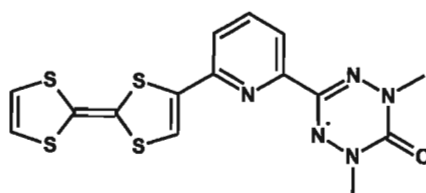
CHAPTER 3

Preparation and characterization of a family of π -extended TTF derivatives and their CT salts

3.1 Introduction

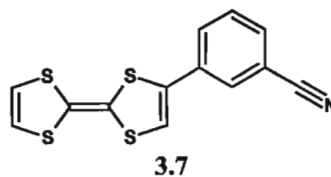
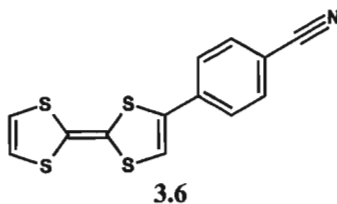
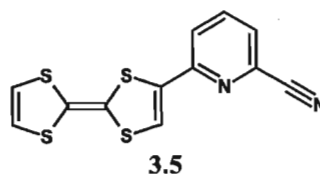
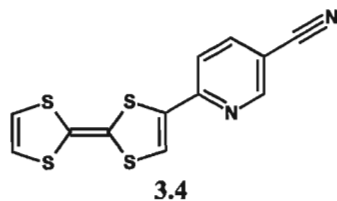
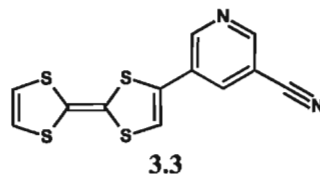
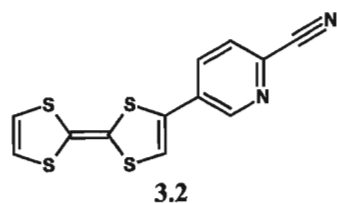
As presented in Chapter 1, two strategies have been adopted for the preparation of multifunctional materials that present interplay between their magnetic and conducting sublattices, referred to as the *through space* and *through bond* approaches. In the latter approach, the introduction of d spins on a TTF-based ligand can be easily achieved by coordinating the ligand to paramagnetic transition metals, but the challenge here is that there must exist a suitable conduction pathway in the solid state so the TTF π electrons can give rise to electrical conductivity. This step is not so straightforward, as the TTF moiety must present the appropriate oxidation state to facilitate electrical conductivity and the oxidized complex must be stable. Furthermore, it is very difficult to control the molecular arrangement of the desired complex in the solid state so that the desired conduction pathway is achieved. The difficulties, of course, don't end here. The loss of coplanarity of the π system due to packing forces may also impede the communication between π and d spins.^{146,147}

In 2005 the Pilkington group published the bidentate chelating TTF-verdazyl ligand **3.1** as a suitable candidate for the preparation of this kind of materials.¹⁸³ The pyridyl-verdazyl moiety was designed as a spin-bearing bidentate chelating unit capable of coordinating paramagnetic transition metals. The results discussed in this Chapter follow on from these studies, where the pyridyl-verdazyl groups have been substituted by cyanopyridyl and *bis*-aryl moieties.

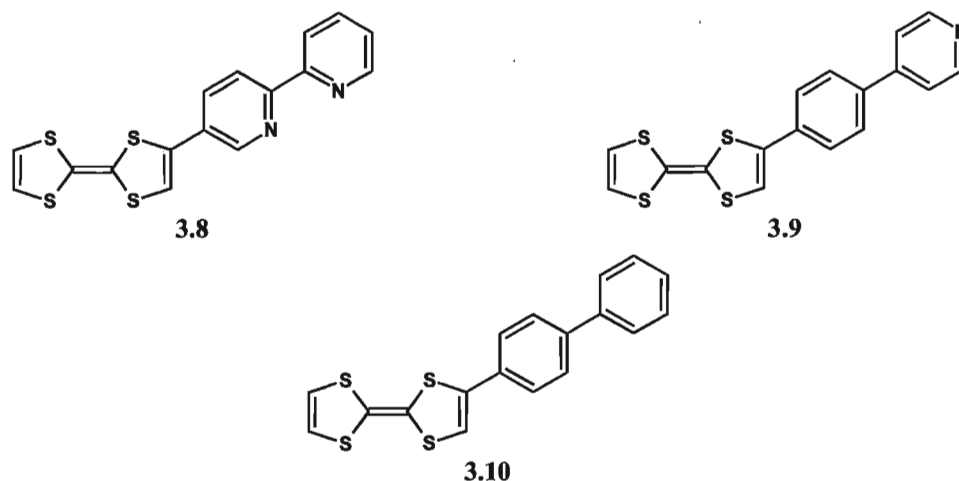


3.1

Pyridine is by far the ligand of choice when it comes to adding binding sites to TTF, and the resulting ligands have been reviewed recently.^{131,132} Organic nitriles can engage in intermolecular interactions such as halogen bonding or hydrogen bonds,^{140,184} but the nitrile derivatives of TTF have been scarcely researched.¹⁸⁵⁻¹⁹⁰ The objectives of this project are: i) explore the synthesis and characterization of a new family of cyanopyridyl TTF derivatives **3.2-3.5** and their charge transfer (CT) salts, ii) study the effect of the electron-withdrawing cyanopyridyl group on the electrochemical properties of TTF, iii) determine what effect this functionality would have on directing the packing of the donors in their neutral state as well as in their CT salts. The long term objectives are to take advantage of the nitrile functionality in order to form a second heterocycle such as imidazole and tetrazole rings. The electrochemical properties of the resulting bidentate chelating ligands and the magnetic properties of their corresponding complexes could in turn be studied, along with their CT salts. Cyanobenzyl derivatives **3.6**¹⁹¹ and **3.7** were also prepared and characterized as a comparison to the pyridyl family of systems that will enable us to study the effect of changing the aromatic ring spacer has on the electrochemical properties of TTF.



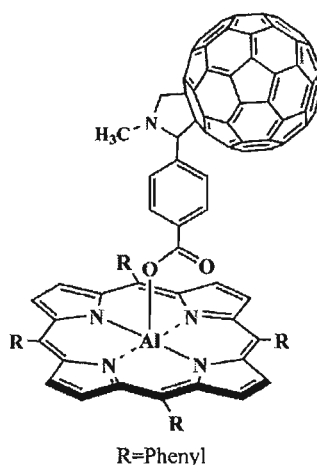
Substitution of TTF with *bis*-aryl moieties targeted the addition of three specific fragments to the TTF molecule: 2,2'-bipyridyl **3.8**, phenyl-4-pyridyl **3.9** and biphenyl **3.10**.



2,2'-Bipyridine derivatives of TTF are reported in the chemical literature, but in all cases there was either a functional group bridging both moieties or the bipyridine ring was fused directly to the 1,3-dithiole ring(s) of the TTF molecule.^{120,122,141} We proposed to take full advantage of the versatile mono-substitution chemistry reported for TTF molecules⁹⁷ in order to attach the 2,2'-bipyridyl ligand directly onto one of the 1,3-dithiole rings of parent TTF.

The first donor ligand **3.8** should be capable of binding transition metal ions and as such, after oxidation, might form an extended π system that could potentially allow communication between coordinated metal *d* spins and the TTF π electrons, possibly forming the desired conduction pathway to allow electrical conductivity. In this Chapter we present the synthesis of this system together with the preparation and characterization of thirteen novel CT salts. The coordination chemistry of this ligand is presented in Chapter 4. The 4-phenyl pyridyl derivative **3.9** was prepared as part of a collaboration with the van der Est group at Brock University for a project aimed towards the optimization of the charge separation time for the development of biomimetic models for artificial photosynthesis.¹⁹² Light irradiation of the supramolecular diad shown in Scheme 3.1 would cause the transfer of an electron from the Al(III) porphyrin (AlPor) to the

acceptor fullerene (C_{60}), $AlPor-C_{60} \rightarrow AlPor^{+} \cdot C_{60}^{-\cdot}$. Axial coordination of **3.9** to $AlPor-C_{60}$ would result in the realization of the novel diad **3.9- $AlPor-C_{60}$** that will allow a secondary electron transfer to take place upon irradiation, **3.9- $AlPor-C_{60}$** \rightarrow **3.9 $^{+}$ - $AlPor-C_{60}^{-\cdot}$** and the charge separation would be more stabilized than without **3.9**. Optimization of the charge separation is important to develop systems suitable for the application of artificial photosynthesis as renewable energy sources.¹⁹³



Scheme 3.1 Scheme of the supramolecular diad $AlPor-C_{60}$. Adapted with permission from 192. Copyright 2011 American Chemical Society.

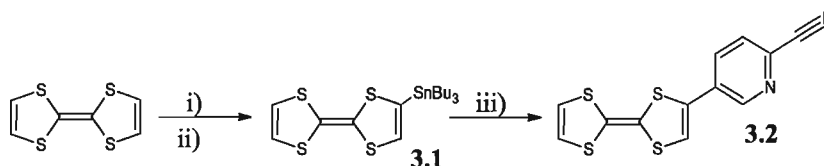
Finally, in the literature there are reports of phenyl- polyphenyl- or *bis*-biphenyl substituted TTF derivatives.^{194-196,197} The published *bis*-biphenyl derivatives are mixtures of *cis* and *trans* isomers generated by the homocoupling of the corresponding biphenyldithiolium salt. These molecules have been demonstrated to be suitable candidates for the preparation of field-effect transistors. As previously mentioned, we targeted the preparation of the monosubstituted biphenyl TTF derivative **3.10** as a model for comparison to the bipyridine and phenyl pyridine donor ligands **3.8** and **3.9**, respectively.

3.2 Preparation and characterization of novel cyanoaryl derivatives of TTF

3.2.1 Synthesis of 3.2-3.5

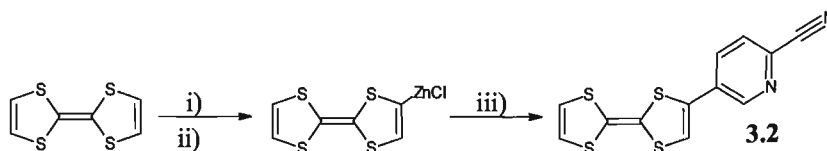
Two of the approaches described in the chemical literature for the preparation of monosubstituted derivatives of TTF are Stille and Negishi coupling reactions. The Stille

coupling involves a two-step synthetic strategy, with the initial preparation and purification of a stannyl-tetrathiafulvalene intermediate that is reacted with aryl halides *via* a Pd-catalyzed coupling reaction, Scheme 3.2.^{37,115}



Scheme 3.2 Reagents and conditions: i) 1.2 eq. LDA, THF, -82°C, 1 h, ii) 1.2 eq. Bu₃SnCl, THF, -82°C, 1 h, iii) 1.2 eq. Bromo-cyanopyridine, 0.1 eq. Pd(PPh₃)₄, THF, -82°C to r.t., overnight.

On the other hand, adopting the Negishi coupling strategy involves the *in situ* preparation of a TTF zincate complex and its subsequent Pd-catalyzed coupling with aryl halides, as a one-pot synthesis, Scheme 3.3.¹⁹⁸



Scheme 3.3 Reagents and conditions: i) 1.2 eq. LDA, THF, -82°C, 1 h, ii) 1.2 eq. ZnCl₂, THF, -82°C, 1 h, iii) 1.2 eq. Bromo-cyanopyridine, 0.1 eq. Pd(PPh₃)₄, THF, -82°C to r.t., overnight.

In this respect, our first approach to preparing the cyanoaryl derivatives **3.2-3.5** consisted of the Stille coupling between stannyl-tetrathiafulvalene and the appropriately substituted commercially available bromocyanopyridine. In our hands, this approach afforded all four isomers **3.2-3.5** in reproducibly low yields (5-15%). As a consequence, a second strategy was followed and all four derivatives were successfully prepared *via* the Negishi coupling of TTF zincate with the appropriate aryl halide. All four compounds were isolated as red/orange microcrystalline powders after purification of the crude products *via* column chromatography on neutral alumina. The yield of this reaction was good for derivatives **3.2** and **3.4** (ca. 80%), but lower (ca. 25%) for **3.3** and **3.5**.

The cyanobenzyl derivatives **3.6** and **3.7** were prepared following a modification of the published procedure for **3.6**.¹⁹¹ Purification of the crude products was achieved by chromatography on neutral alumina, affording the desired compounds in *ca.* 60% yield

The cyanopyridyl derivatives **3.2-3.5** were also characterized by single crystal X-ray diffraction. In all cases, single crystals suitable for X-ray diffraction were obtained *via* the slow evaporation of saturated solutions of acetonitrile, affording needles. These compounds showed a high tendency to crystallize as twins. Nevertheless, suitable single crystals could be grown for all four cyanopyridyl derivatives.

3.2.2 Single-crystal X-ray characterization of cyanopyridyl derivatives

The single crystal structure of **3.2** was determined from X-ray studies at 220 K, Figure 3.1. This derivative crystallizes in the monoclinic space group $P2_1/c$, with one crystallographically independent molecule in the unit cell, Figure 3.2, a). The TTF is almost planar, with swivel angles at the S atoms smaller than 4° for each ring. The pyridine ring is almost coplanar with the TTF donor, presenting a torsion angle of about 5° . See Table 3.1 for selected bond lengths and bond angles for **3.2**.

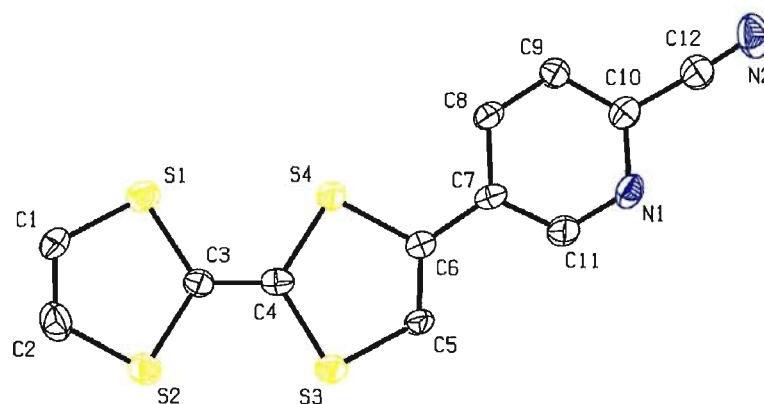


Figure 3.1 ORTEP plot of the molecular structure of **3.2** showing the corresponding numbering scheme. Thermal ellipsoids plotted at 50% probability. Hydrogen atoms are omitted for clarity.

Table 3.1 Selected bond lengths (Å) and angles (°) for **3.2**.

Bond lengths			
S1-C1	1.747(19)	S4-C6	1.766(17)
S1-C3	1.758(17)	C1-C2	1.34(3)
S2-C3	1.751(17)	C3-C4	1.38(2)
S2-C2	1.753(19)	C5-C6	1.32(2)
S3-C5	1.743(17)	C6-C7	1.49(2)
S3-C4	1.758(17)	N2-C12	1.16(2)
S4-C4	1.740(16)		
Bond angles			
C1-S1-C3	95.1(9)	C4-S4-C6	93.8(8)
C3-S2-C2	94.3(9)	S2-C3-S1	115.3(9)
C5-S3-C4	93.5(8)	S4-C4-S3	116.5(9)
Dihedral angles			
C5-C6-C7-C11	5(3)		

Close examination of the crystal packing reveals that this derivative crystallizes in slanted stacks of TTF donors arranged in a head-to-tail fashion along the *c*-axis. Within one stack, the TTF and cyanopyridyl rings are arranged in a parallel manner. The shortest intrastack distance between neighbouring molecules is 3.93 Å, revealing that this packing arrangement is stabilized by weak π - π interactions. Furthermore, there are short interstack contacts between the nitrogen and sulfur atoms of neighbouring molecules across steps of stacks aligned along the *c*-axis, Figure 3.3 a).

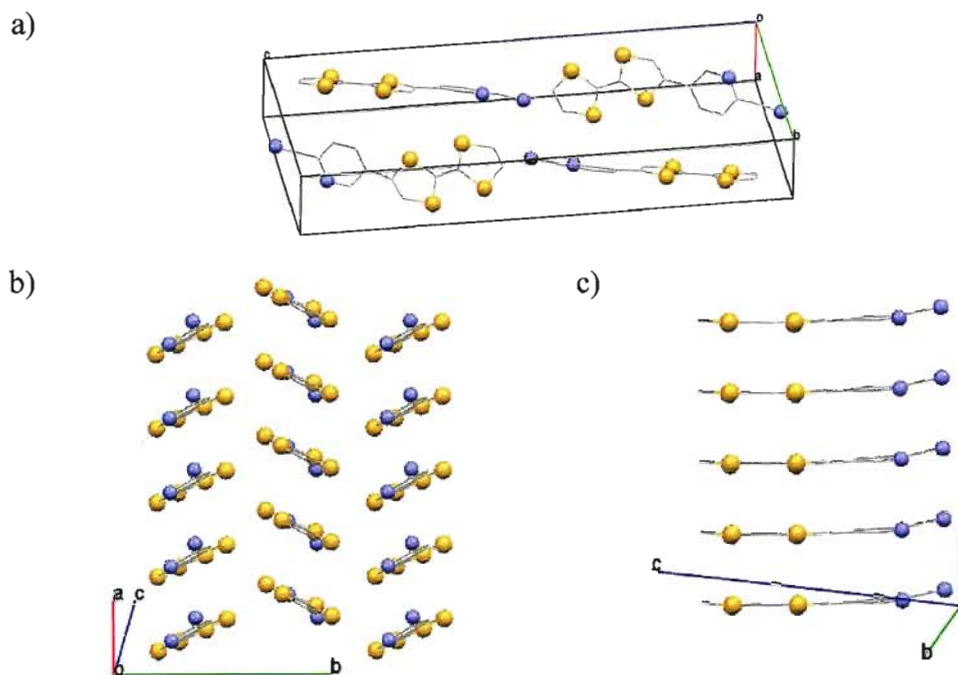


Figure 3.2 a) Unit cell of **3.2**, b) view of the stacks along the *b*-axis, c) side view of one stack. Hydrogen atoms are omitted for clarity.

All S...S distances in the crystal structure of this derivative are fairly long, consistent with the presence of neutral TTF molecules. In this respect, the intrastack S...S distances are 3.932(5) Å, and there are shorter interstack S...S contacts of 3.592(6) Å across steps of neighbouring stacks that run along the *b*-axis of the unit cell, just slightly less than the sum of the *van der Waals* radii for two sulphur atoms, Figure 3.3, b).

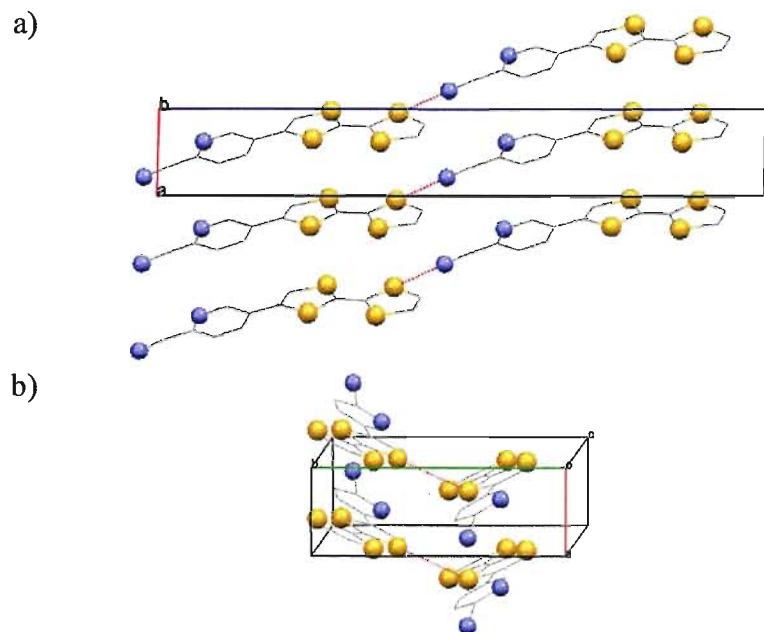


Figure 3.3 a) Interstack short contacts of **3.2** shown as red dotted lines, along the *c*-axis between atoms N2-S2a, and b) along the *b*-axis between atoms S4-S3b. Hydrogen atoms are omitted for clarity.

The molecular structure of **3.3** was determined from single crystal X-ray studies at room temperature, Figure 3.4. This derivative crystallizes in the monoclinic space group *Pbca*, with one crystallographically independent molecule in the unit cell, as shown in Figure 3.5 a). Like the previous derivative, the TTF molecule is almost planar, with swivel angles at the S atoms smaller than 5° for each ring. The pyridine ring is coplanar with the dithiolene rings of the TTF molecule. See Table 3.2 for selected bond lengths and bond angles.

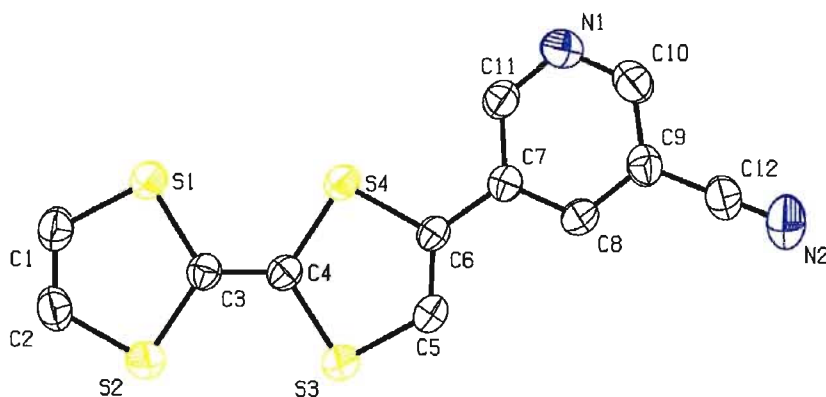


Figure 3.4 ORTEP plot of the molecular structure of **3.3** showing the corresponding numbering scheme. Thermal ellipsoids plotted at 50% probability. Hydrogen atoms are omitted for clarity.

Molecules of **3.3** pack in slanted stacks that run along the *b*-axis of the unit cell. Once again molecules within a stack are arranged in a head-to-tail fashion, Figure 3.5, c). The shortest intrastack distance between neighbouring molecules is 3.76 Å, revealing that this packing arrangement is also stabilized by weak π - π interactions.

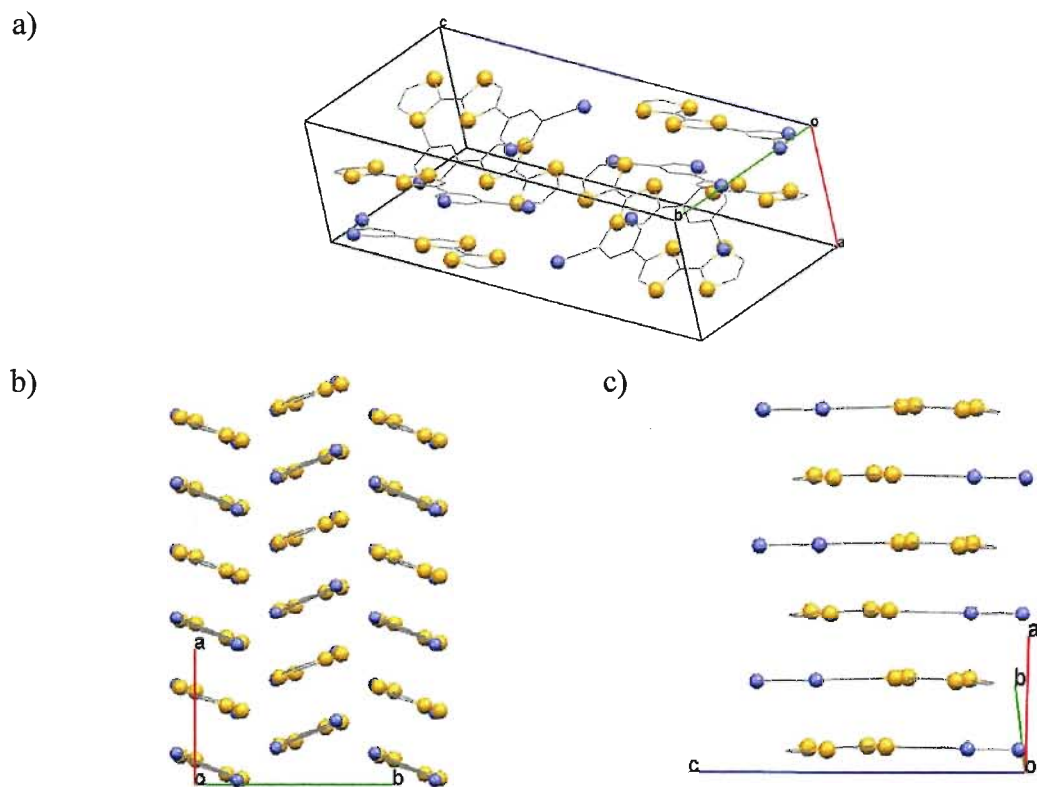


Figure 3.5 a) Unit cell of **3.3**, b) view of the stacks along the *b*-axis, c) view of one stack along the *c*-axis.

Table 3.2 Selected bond lengths (Å) and angles (°) for **3.3**.

Bond lengths			
S1-C1	1.739(2)	S4-C6	1.7650(18)
S1-C3	1.7611(18)	C1-C2	1.320(3)
S2-C3	1.7603(19)	C3-C4	1.349(3)
S2-C2	1.739(2)	C5-C6	1.333(3)
S3-C5	1.730(2)	C6-C7	1.474(3)
S3-C4	1.7603(19)	N2-C12	1.140(3)
S4-C4	1.7616(19)		
Bond angles			
C1-S1-C3	94.76(10)	C4-S4-C6	95.29(9)
C3-S2-C2	94.42(10)	S2-C3-S1	114.42(10)
C5-S3-C4	94.79(9)	S4-C4-S3	114.25(10)
Dihedral angles			
C5-C6-C7-C8	-0.3(3)		

Close inspection of the packing diagram of **3.3** shows a weak H-bonding interaction between a dithiolate ring proton of a TTF molecule and the nitrogen atom of a nitrile group from a derivative molecule in an adjacent stack such that C2a-H \cdots N2 of 2.74 Å, Figure 3.6 a). All the intermolecular S \cdots S distances in this crystal structure are fairly long, once again consistent with the presence of neutral TTF molecules. In comparison with the previous structure, the shortest S \cdots S distances are 3.5340(8) Å involving the edge to-edge interactions between sulfur atoms of adjacent stacks, Figure 3.7 b). Due to the head-to-tail stacking, the shortest intrastack S \cdots S distances are 3.8847(3) and 4.3627(8) Å, indicating no interactions between S atoms within a stack.

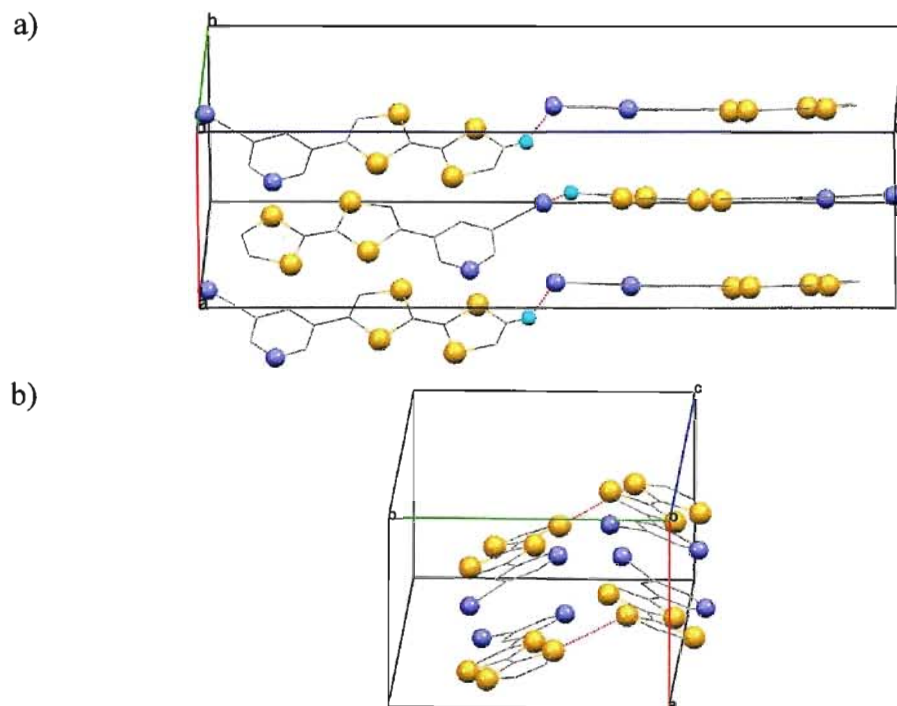


Figure 3.6 Interstack short contacts of **3.3** shown as red dotted lines, a) along the *c*-axis between atoms C2a-H2a...N2 ($x, 1/2-y, -1/2+z$), and b) along the *b*-axis between atoms S2-S1b. Hydrogen atoms shown when necessary, otherwise they are omitted for clarity.

The crystal structure of **3.4** was determined from X-ray diffraction studies at 150 K, Figure 3.7. This derivative also crystallizes in the monoclinic space group $P2_1/c$, with one crystallographically independent molecule in the unit cell, as seen in Figure 3.8 a). The two rings of the TTF molecule are almost planar, with swivel angles at the S atoms smaller than 9° for each ring. The pyridine ring is coplanar with the dithiole rings of the TTF molecule. See Table 3.3 for selected bond lengths and bond angles.

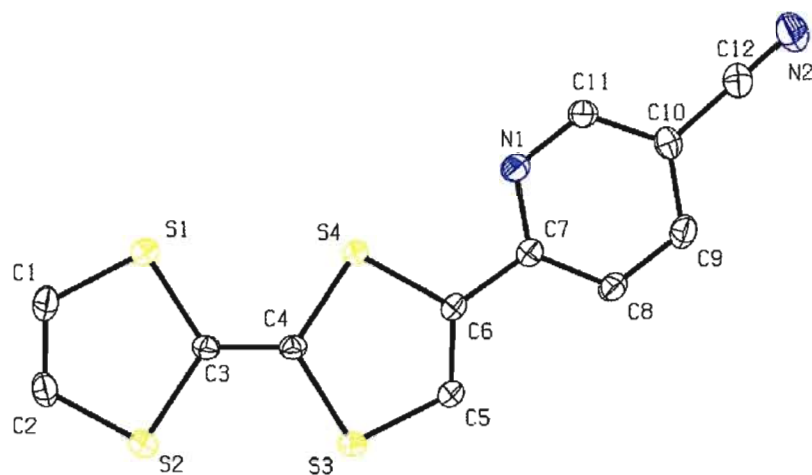


Figure 3.7 ORTEP plot of **3.4** showing the corresponding numbering scheme. Thermal ellipsoids plotted at 50% probability. Hydrogen atoms are omitted for clarity.

This product crystallizes as slanted stacks of donors that run down the *b*-axis. Within one stack the molecules are arranged in a head-to-tail fashion as shown in Figure 3.8 c), with one TTF donor ring overlapping partially with the cyanopyridyl ring from a neighbouring molecule within the stack. The shortest intra-track distances between molecules is 3.52 Å, indicative of π - π stacking interactions. The shortest intrastack S...S distance is 3.6426(6) Å, slightly longer than the sum of the *van der Waal* radii for two sulfur atoms.

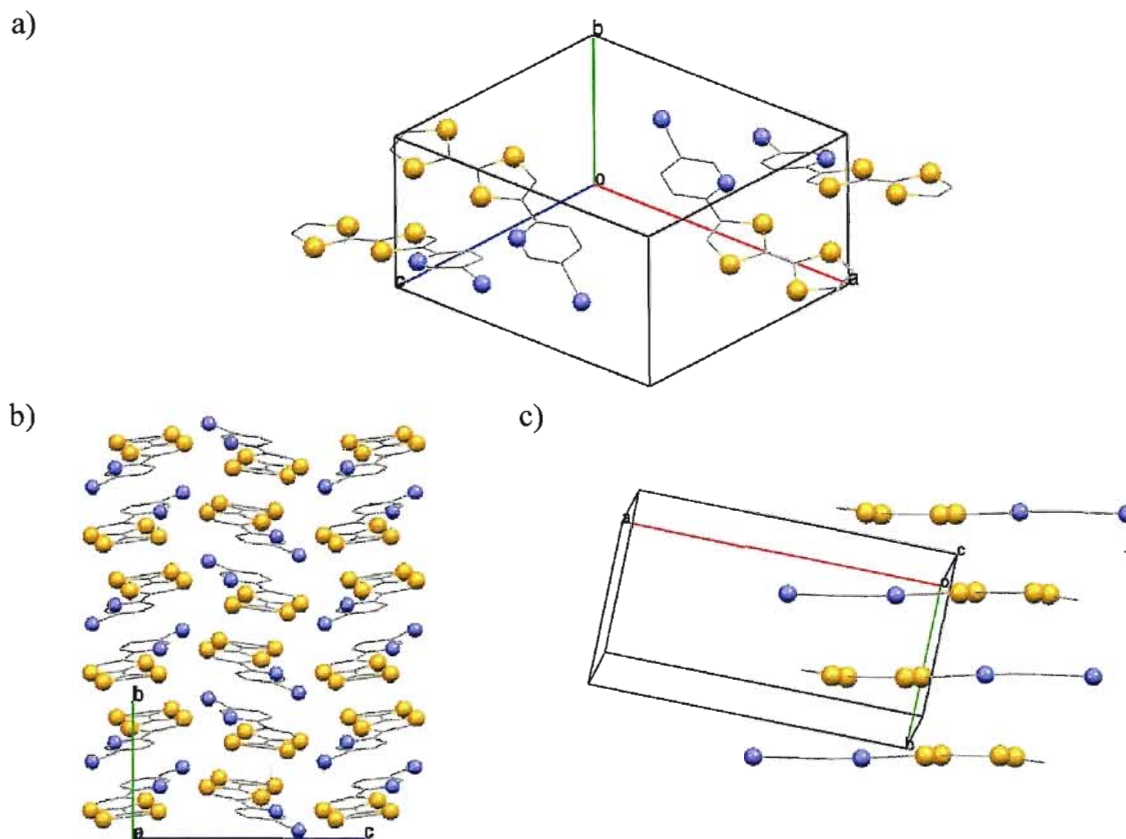


Figure 3.8 a) Unit cell of **3.4**, b) view along the *c*-axis of the stacks, c) view of one stack along its long side, showing the head-to-tail arrangement of the stack. Hydrogen atoms are omitted for clarity.

The crystal packing reveals non-classical H-bonds between the N atom of a nitrile functional group and a pyridyl H-atom from a neighbouring derivative pyridine. The shortest S...S contacts are S3-S4a of 3.4408(6) Å and S3-S1a of 3.5820(6) Å.

Table 3.3 Selected bond lengths (Å) and angles (°) for **3.4**.

Bond lengths			
S1-C1	1.7406(15)	S4-C6	1.7613(14)
S1-C3	1.7583(14)	C1-C2	1.334(2)
S2-C3	1.7675(14)	C3-C4	1.3468(19)
S2-C2	1.7438(16)	C5-C6	1.3452(19)
S3-C5	1.7255(14)	C6-C7	1.4560(19)
S3-C4	1.7560(13)	N2-C12	1.144(2)
S4-C4	1.7586(14)		
Bond angles			
C1-S1-C3	94.64(7)	C4-S4-C6	95.33(6)
C3-S2-C2	94.34(7)	S2-C3-S1	114.55(8)
C5-S3-C4	94.79(9)	S4-C4-S3	114.74(7)
Dihedral angles			
C5-C6-C7-C8	1.1(2)		

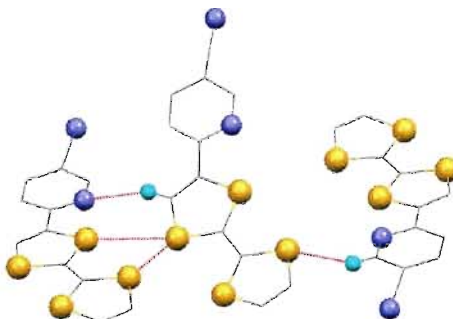


Figure 3.9 Interstack short contacts of **3.4** shown as red dotted lines. a) N...H and bifurcated S...S interactions. Hydrogen atoms shown when necessary, otherwise they are omitted for clarity.

The only difference between the molecular structures of derivatives **3.2** and **3.4** is the location of the pyridine nitrogen atom with respect to the TTF moiety. Placing the pyridine nitrogen atom *ortho* with respect to the TTF results in a hydrogen atom in the *para* position to this pyridyl nitrogen, Figure 3.10 b). The acidity of this hydrogen atom may enhance the electronic interactions with neighbouring nitrile groups to form short

contacts similar to the hydrogen bonds between aldehydes in the solid state, Figure 3.10 a).¹¹⁵ These non classical CN \cdots H interactions are not present in the crystal structure of **3.2**.

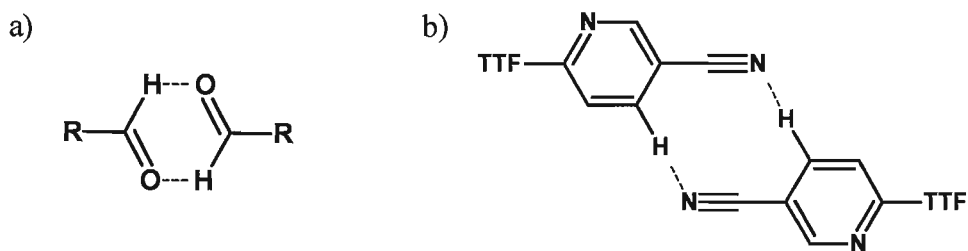


Figure 3.10 a) Hydrogen bonding interactions of aldehydes in the solid state and b) CN \cdots H contacts in **3.4**.

The single crystal structure of **3.5** was determined from X-ray studies at 150 K, Figure 3.11. As shown in Figure 3.12 a), this derivative crystallizes in the monoclinic space group $P2_1/n$, with one crystallographically independent molecule in the unit cell. The TTF moiety is almost planar, with swivel angles at the S atoms smaller than 8° for each ring. The pyridine ring is almost coplanar with the TTF moiety, presenting a torsion angle of about -7.5°. See Table 3.4 for selected bond lengths and bond angles.

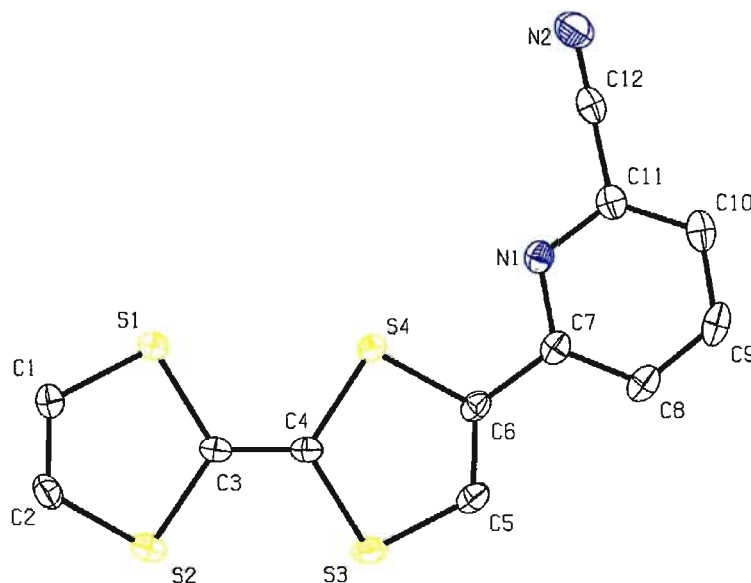


Figure 3.11 ORTEP plot of the molecular structure of **3.5** showing the corresponding numbering scheme. Thermal ellipsoids plotted at 50% probability. Hydrogen atoms are omitted for clarity.

Table 3.4 Selected bond lengths (Å) and angles (°) for **3.5**.

Bond lengths			
S1-C1	1.7380(17)	S4-C6	1.7590(16)
S1-C3	1.7570(16)	C1-C2	1.329(2)
S2-C3	1.7601(16)	C3-C4	1.347(2)
S2-C2	1.7416(18)	C5-C6	1.345(2)
S3-C5	1.7294(18)	C6-C7	1.461(2)
S3-C4	1.7567(16)	N2-C12	1.139(2)
S4-C4	1.7591(16)		
Bond angles			
C1-S1-C3	94.80(8)	C4-S4-C6	94.74(8)
C3-S2-C2	94.49(8)	S2-C3-S1	114.42(9)
C5-S3-C4	94.86(8)	S4-C4-S3	115.01(9)
Dihedral angles			
C5-C6-C7-C8	-7.5(2)		

The TTF donor moieties of the molecule stack on top of the cyanopyridyl acceptor moieties of adjacent molecules as shown in Figure 3.12 b). The crystal structure can be best described as stacks of molecular chains, which propagate along the *c*-axis of the unit cell, connected *via* CH \cdots N2 hydrogen bonds, Figure 3.12, c).

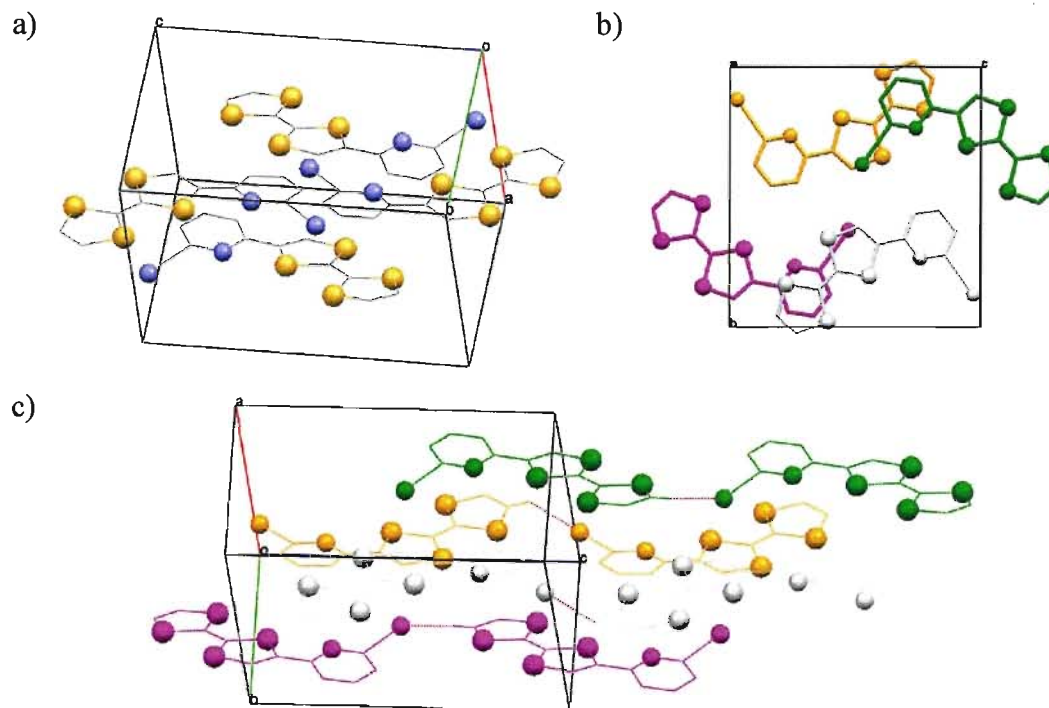


Figure 3.12 a) Unit cell of **3.5**, b) unit cell down the *a*-axis showing the green and white molecules over the pink and yellow molecules, c) four chains in different colours showing the C-H \cdots N hydrogen bond along the *c*-axis in dotted red lines. Hydrogen atoms shown when necessary as coloured sticks, otherwise they are omitted for clarity.

The shortest intra-track distances between molecules is 3.54 Å, indicative of π - π stacking interactions. All the S \cdots S distances in this structure are longer than the sum of the *van der Waal* radii for two sulfur atoms. The non-classical hydrogen bonding interactions present in this structure are summarized in Table 3.5. In both cases the bonds involve the nitrogen atoms of the nitrile groups.

Table 3.5 Distance *d* and angle θ of the CN \cdots HC short contacts of derivative **3.5**.

	<i>d</i> [C-H \cdots N] (Å)	<i>d</i> [H-C \cdots N] (Å)	θ [C-H \cdots N] (°)
C2a-H2a \cdots N2 ⁱ	2.62	3.277(2)	126
C5b-H5b \cdots N2 ⁱⁱ	2.59	3.467(2)	154

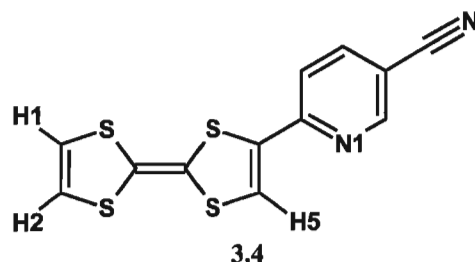
Symmetry transformation: ⁱ*x*,*y*,-1+*z*, ⁱⁱ3/2-*x*,-1/2+*y*,3/2-*z*.

In summary, the crystal structures of derivatives **3.2-3.5** show the presence of weak π - π interactions directing the stacking of the derivatives. Derivatives **3.2-3.4** form discrete stacks, displaying a parallel stacking arrangement molecules for **3.2** and a head-to-tail arrangement for **3.3** and **3.4**. Derivative **3.5** does not form discrete stacks, but

rather each derivative molecule overlaps with four neighbouring molecules in a head-to-tail manner.

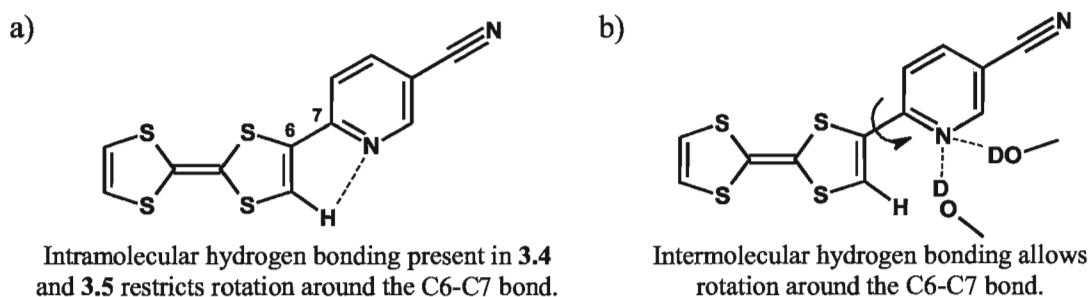
3.2.3 Spectroscopic characterization

All nitrile derivatives **3.2-3.7** were fully characterized by 600 MHz ^1H and ^{13}C NMR, UV-Vis, MS and IR spectroscopy as well as CV, elemental analysis and melting point determination. The ^1H and ^{13}C NMR spectra of all the cyanopyridyl derivatives have been fully assigned using 1-D and 2-D NMR (COSY, HSQC, HMBC). In these derivatives, the TTF protons appear between 7.26 and 6.38 ppm, and the pyridyl protons appear between 8.88 and 7.56 ppm. Protons H1 and H2, Scheme 3.4, appear overlapped as one singlet at 6.39 ppm for **3.2** and **3.3** in the ^1H NMR in CDCl_3 , due to their similar electronic environments. For **3.4** and **3.5**, however, these two protons appear as two differentiated doublets.



Scheme 3.4 Numbering scheme for the TTF hydrogen atoms and the pyridine nitrogen atom of the cyanopyridyl derivatives **3.2-3.5**.

The different signals for protons H1 and H2 in the ^1H NMR spectra in CDCl_3 for derivatives **3.4** and **3.5** seems to indicate the presence of different electronic environments for these two protons. This could be explained by the formation of an intramolecular hydrogen bond between the pyridine N1 and the H5 proton on the dithiole ring in CDCl_3 . The formation of this bond could lead to different electronic environments for H1 and H2 by locking in position the pyridine ring. If the spectra are recorded in MeOD protons H1 and H2 appear as a singlet as in derivatives **3.2** and **3.3**. The competition between the MeOD solvent molecules and the H5 proton to interact with N1 most likely hinders the formation of this intramolecular hydrogen bond, allowing the TTF moiety in **3.4** and **3.5** to rotate freely, Scheme 3.5.



Scheme 3.5 a) Intramolecular H5...N1 hydrogen bond in CDCl₃. b) Intramolecular hydrogen bonding between N1 and surrounding MeOD molecules.

The ¹H NMR and ¹³C NMR spectra of the cyanobenzyl derivatives **3.6** and **3.7** have been fully assigned by 1-D and 2-D experiments (COSY, HSQC, HMBC). In these derivatives, the protons of the dithiole rings of the TTF molecules are observed as sharp singlets between 6.72-6.37 ppm. The aromatic pyridyl protons are visible between 8.70 and 7.50 ppm.

The UV-Vis spectra of the acetonitrile solution of compounds **3.2-3.7** are presented in Figure 3.13. All derivatives show two distinct absorption bands, the first centred at about $\lambda = 310$ nm and a second broader band at $\lambda = 415-510$ nm, Table 3.8. The band at higher energy together with its neighbouring shoulders can be assigned to the overlap of the transitions within the TTF and cyanopyridyl moieties based on the spectra of TTF, bromocyanopyridyl precursors and TTF derivatives present in the literature.^{120,126,199} The broad band at lower energy is not present in solutions containing a mixture of unsubstituted TTF and the corresponding bromocyanopyridine. This indicates that the absorption maxima corresponds to an intramolecular charge transfer (ICT) band and highlights the electronic communication between the donor TTF and acceptor cyanopyridyl moieties within these derivatives.^{126,199-201}

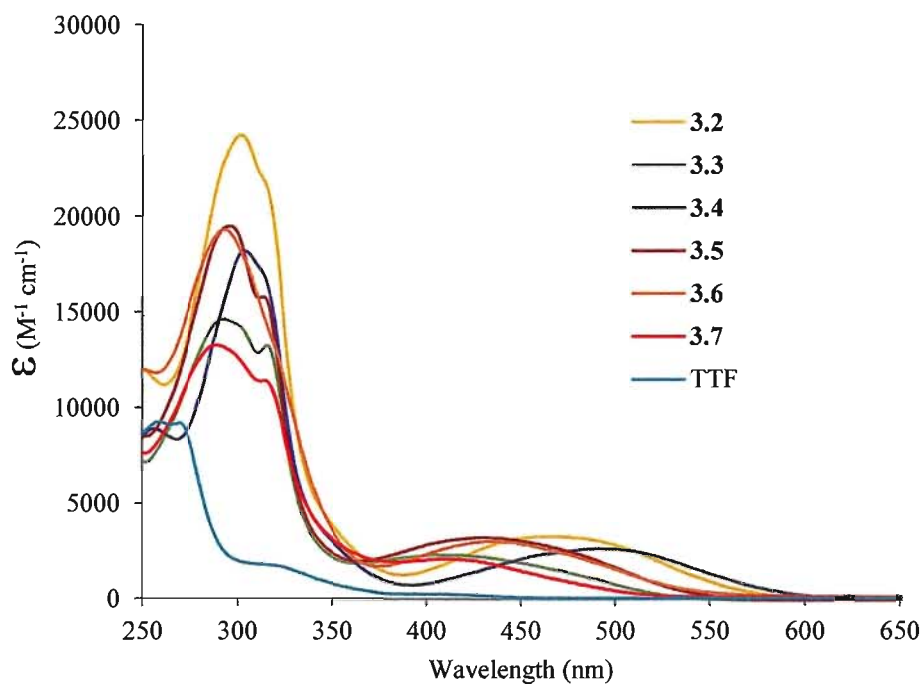


Figure 3.13 UV-Vis spectra of 10^{-5}M solutions of derivatives **3.2-3.7** and TTF in acetonitrile.

Table 3.6 presents the absorbance maxima λ_{max} of the band at lower energy for solutions of derivatives **3.2-3.7** in solvents with different polarities. The absorbance maxima for these compounds are red shifted as the solvent polarity increases, confirming their assignment as intramolecular charge transfer (ICT) bands. This shift is similar to the shift obtained for 4-alkynylpyridine-substituted TTF derivatives.¹²⁶ The energy difference of the HOMO-LUMO gap increases following **3.4** < **3.2** < **3.6** < **3.5** < **3.7** < **3.3**. This trend can be rationalized based on the electron-withdrawing nature of the substituents (nitrile and pyridine nitrogen atom) of the ring and their relative substitution pattern with respect to the TTF moiety. In order to enhance the electron-accepting nature of the ring, the TTF moiety has to be *ortho* or *para* with respect to the substituents. This results in an ICT band at longer wavelengths for **3.6** as compared to for **3.7**, where formally the TTF moiety is not affected by the effect of the nitrile.

Table 3.6 UV-Vis ICT λ_{max} (nm) in different solvents for derivatives **3.2-3.7**

	3.2	3.3	3.4	3.5	3.6	3.7
Benzene	479	417	513	439	451	425
DCM	475	415	505	437	448	422
MeOH	470	410	500	435	444	421
Acetonitrile	467	406	493	432	438	414

The effect of the position of the substituents in the cyanopyridyl derivatives is summarized in Table 3.7. At one end, both substituents in derivative **3.4** are ideally positioned to withdraw electron density from the TTF moiety, and as a result, this derivative has the ICT band at the longest wavelength. On the other end, derivative **3.3** has both substituents placed so no net influence would be expected, which gives the ICT band at the shortest wavelength. For **3.2** and **3.5**, only one of the substituents influences the TTF moiety and, based on these results the substituent with the largest electron-withdrawing capability is the nitrile group, which causes a blue shift of the ICT band to lower energies relative to **3.5**. A similar trend can be seen in the benzonitrile derivatives, where the influence of the CN group drives the ICT band to longer wavelengths.

Table 3.7 Influence of heterocycle substituents on TTF for derivatives **3.2-3.7**. Y = 'yes', N = 'no'.

	3.4	3.2	3.5	3.3	3.6	3.7
CN influence	Y	Y	N	N	Y	N
N _{pyridine} influence	Y	N	Y	N	—	—
ICT λ_{max} (nm)	493	467	432	406	438	414

Given the influence of the nitrile group on the position of the ICT band, we decided to study if there was any correlation between the nitrile str of derivatives **3.2-3.7** and the ICT band. The IR spectra of the nitrile derivatives show that the CN str peak of all derivatives falls within the range 2220-2231 cm^{-1} , which is in agreement with the CN str frequencies reported in the literature for conjugated imines.²⁰² Comparison with the nitrile str frequencies of the corresponding bromocyanopyridyl starting materials shows little to no frequency change after the coupling. Comparison of the CN str frequency with the ICT λ_{max} reveals that, as the ICT band shifts to shorter wavelengths, the CN str seems

to move to higher frequencies following the trend $3.4 < 3.2 \approx 3.5 < 3.3$. The benzonitrile derivatives **3.6** and **3.7** do not present any such correlation.

Table 3.8 FT-IR nitrile stretching frequencies (cm^{-1}) and UV-Vis ICT λ_{max} (nm) for derivatives **3.2-3.7**.

	CN _{str} ^a	ICT λ_{max} ^b
3.4	2220	493
3.2	2228	467
3.5	2227	432
3.3	2231	406
3.6	2223	438
3.7	2224	414

Experimental conditions: ^a pressed KBr pellet, ^b 1 mM solution in acetonitrile.

3.2.4 Electrochemical characterization

Cyclic voltammetry measurements of acetonitrile solutions of derivatives **3.2-3.7** show the expected two-step reversible oxidation potentials for the TTF moiety, corresponding to the sequential formation of the radical cation and dication species respectively, Table 3.9. All oxidation potentials for the derivatives are higher than the potentials necessary to oxidize unsubstituted TTF. This shift is due to the extended delocalization of electron density over the aromatic ring and the presence of the electron-withdrawing nitrile substituents.^{126,200} Derivatives **3.2** and **3.3** have the highest oxidation potentials, whereas derivatives **3.5-3.7** have the lowest oxidation potentials. Comparison of the ICT bands with the oxidation potentials shows no obvious trend.

Table 3.9 Cyclic voltammetry oxidation potentials (V) for derivatives **3.2-3.7**.

	$E_{1/2}^1$ ^a	$E_{1/2}^2$ ^a
TTF	0.37	0.76
3.2	0.48	0.85
3.3	0.48	0.85
3.4	0.46	0.84
3.5	0.45	0.83
3.6	0.45	0.82
3.7	0.45	0.82

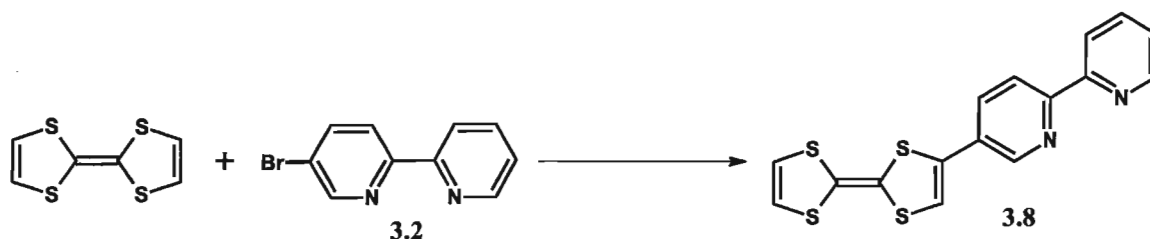
Experimental conditions: ^a 0.1 M solution in acetonitrile, 0.1 mM TBAPF₆.

3.3 Novel π -extended *bis*-aryl TTF systems: rational ligand design for the preparation of magnetic hybrid electrical conductors.

3.3.1 Synthesis of 3.8-3.10

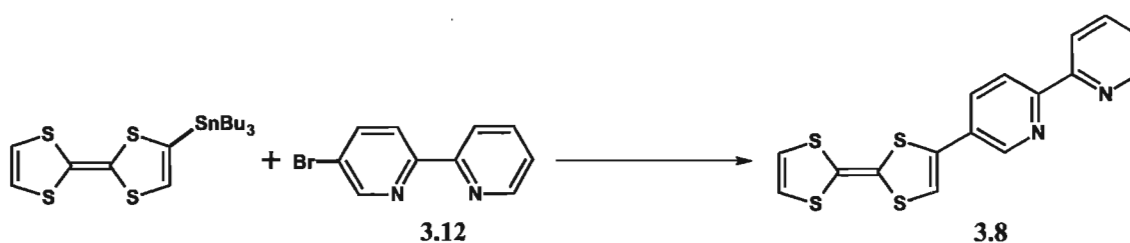
The synthesis of **3.8-3.10** was accomplished by coupling the stannyl or zincate TTF species with the appropriate *bis*-aryl halide, following the strategy previously described for the synthesis of the cyanopyridyl derivatives discussed previously above. The preparation of derivatives **3.8** and **3.9** also required the synthesis of the corresponding *bis*-aryl halides, which was carried out following literature procedures.^{203,204}

The initial approach for preparing **3.8** involved the Negishi coupling of TTF and 4-bromo-2,2'-bipyridine **3.12**, Scheme 3.6. In the first step, the TTF zincate was prepared as for the cyanopyridyl derivatives and then **3.12** and the catalyst were added at -82°C. After allowing the reaction to warm up to room temperature overnight, a pale yellow solid was visible in solution. After workup and purification *via* column chromatography, unreacted **3.12** could be separated from the desired product **3.8**. The large amount of **3.12** isolated after workup could be reused in subsequent reactions after purification. Unfortunately the overall yield of **3.8** for this reaction was only about 10%.



Scheme 3.6 Reagents and conditions: i) 1.2 eq. LDA, THF, -82°C, 1 h, ii) 1.2 eq. ZnCl₂, THF, -82°C, 1 h, iii) 1.2 eq. **3.12**, 0.1 eq. Pd(PPh₃)₄, THF, -82°C to r.t., overnight.

A Negishi coupling was initially attempted even though the coordination of **3.12** to the Zn²⁺ ion in TTF zincate was anticipated to cause low yields by hindering the desired Pd catalyzed C-C coupling. This reaction choice may not make much sense now to the reader, but chronologically makes perfect sense. The *bis*-aryl **3.8** was the first synthetic target pursued right after the preparation of the cyanopyridyl derivatives. In that instance, Stille coupling had failed to give good yields for the coupling of bromocyanopyridines to stannyl-tetrathiafulvalene even though there are literature precedents for this coupling.^{37,115} Once Negishi coupling failed, Stille coupling was successfully carried out. In this respect, reaction of stannyl-tetrathiafulvalene with **3.12** in dry toluene yielded the bipyridyl substituted TTF derivative **3.8** in moderate yields, Scheme 3.7. Cooling of the reaction solution to room temperature and then overnight in the freezer caused the precipitation of **3.8** as a dark red powder. This powder was isolated by filtration and washed repeatedly with petroleum ether to remove unreacted stannyl-tetrathiafulvalene and 4-bromo-2,2'-bipyridine.



Scheme 3.7 Reagents and conditions: 1.0 eq. TTFSnBu₃, 1.4 eq. **3.12**, 0.1 eq. Pd(PPh₃)₄, toluene, reflux, 24h.

Sublimation of **3.8** at 100°C for 24 h gave orange needles suitable for single crystal X-ray diffraction. The molecular structure of **3.8** measured at 150 K is presented

in Figure 3.14. The molecule crystallizes in the monoclinic space group $P2_1/n$, with one crystallographically independent molecule in the unit cell, Figure 3.15 a). The dithiolene rings of the TTF are almost planar, with swivel angles at the S atoms of 8° or smaller for each ring. Both bipyridine rings adopt an *anti* conformation and are coplanar. The TTF and bipyridine moieties are not coplanar with respect to each other. The bipyridine ring is twisted out of the best plane of the TTF molecule by a dihedral angle of 14.8° . See Table 3.10 for selected bond lengths and angles.

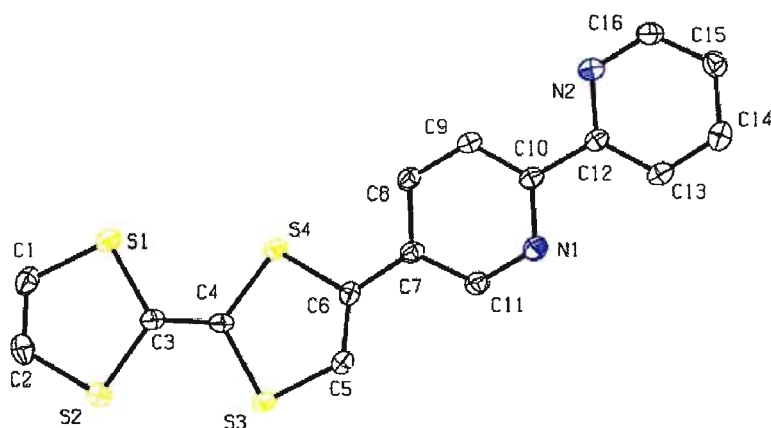


Figure 3.14 ORTEP plot of the molecular structure of **3.8** showing the corresponding numbering scheme. Thermal ellipsoids plotted at 50% probability. Hydrogen atoms are omitted for clarity.

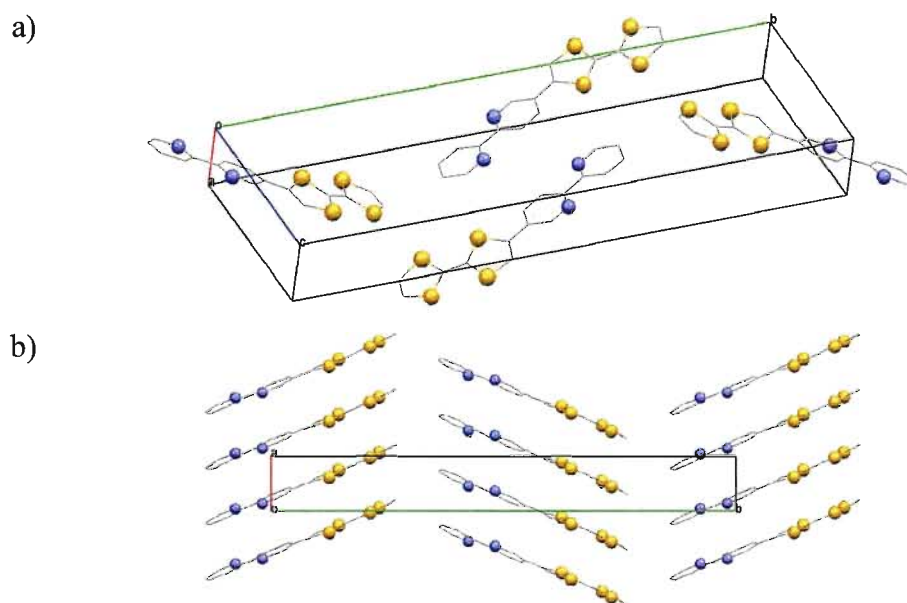


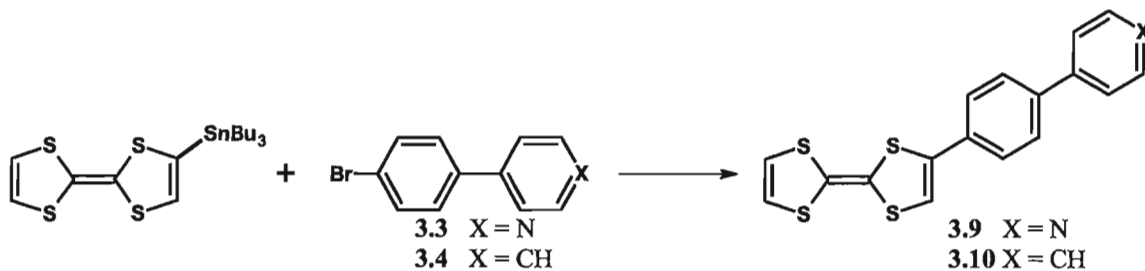
Figure 3.15 a) Unit cell of **3.8**, b) view of the stacks along the *b*-axis. Hydrogen atoms are omitted for clarity.

Derivative **3.8** crystallizes forming slanted stacks running along the *a*-axis, Figure 3.15 b). The molecules stack in a parallel manner, and the stacks are organized in a head-to-tail fashion forming corrugated sheets along the *b*-axis. The shortest intrastack distance between neighbouring molecules is 3.88 Å, revealing that this packing arrangement is stabilized by weak π - π interactions. The shortest intra and interstack S...S distances are of 3.884(2) and 3.632(1) Å respectively, indicating no S...S distances shorter than the sum of their *van der Waals* radii.

Table 3.10 Selected bond lengths (Å) and angles (°) for **3.8**.

Bond lengths			
S1-C1	1.740(4)	S4-C4	1.750(4)
S1-C3	1.761(4)	S4-C6	1.769(4)
S2-C3	1.762(4)	C1-C2	1.321(6)
S2-C2	1.747(4)	C3-C4	1.346(5)
S3-C5	1.746(4)	C5-C6	1.336(5)
S3-C4	1.761(4)	C6-C7	1.470(5)
Bond angles			
C1-S1-C3	94.56(19)	C4-S4-C6	95.84(18)
C3-S2-C2	94.68(19)	S2-C3-S1	114.5(2)
C5-S3-C4	94.87(18)	S4-C4-S3	114.2(2)
Dihedral angles			
C5-C6-C7-C11	14.8(6)	N1-C10-C12-C13	0.6(5)

Stille coupling was also used for the preparation of TTF-phenyl analogues **3.9** and **3.10**, Scheme 3.8. Reaction of stannyl-tetrathiafulvalene in refluxing toluene with the corresponding *bis*-aryl halide gave the desired products in medium to low yields after purification by flash chromatography.



Scheme 3.8 Reagents and conditions for: a) **3.9**: 1.2 eq. **3.13**, 0.1 eq. Pd(PPh₃)₄, toluene, reflux, 24h, b) **3.10**: 0.86 eq. **3.14**, 0.1 eq. Pd(PPh₃)₄, toluene, reflux, 12h.

3.3.2 Spectroscopic characterization

The ¹H-NMR characterization of derivatives **3.8-3.10** shows the expected singlets for the 1,3-dithiole TTF protons between 6.72 and 6.37 ppm. The signals corresponding to the aromatic protons appear between 8.76 and 7.39 ppm.

The UV-Vis spectra of these derivatives were recorded in acetonitrile, Figure 3.16. All derivatives present two absorption bands, one at $\lambda = 305$ nm and a second broad band within the $\lambda = 400$ -440 nm range. The band at highest energy is once again assigned to local transitions within the TTF and *bis*-aryl moieties based on the spectra of related TTF derivatives present in the literature.^{120,183} The broad band at lower energy is not present in a solution containing a mixture of unsubstituted TTF and the corresponding bromo-bisaryl. This indicates that this band is an ICT band, and points at the electronic communication between the donor and acceptor moieties in these derivatives.

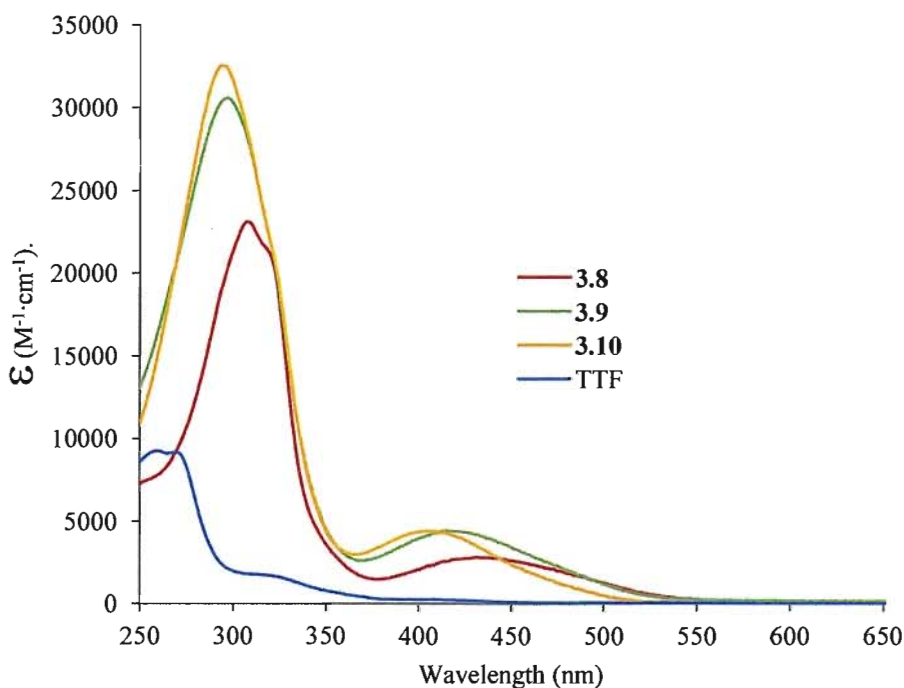


Figure 3.16 UV-Vis spectra of 10^{-5} M solutions of derivatives **3.8-3.10** and TTF in acetonitrile.

The absorbance maximum λ_{max} ICT for derivatives **3.8-3.10** in solvents with different polarities are presented in Table 3.11. The absorbance maximum is red shifted by 14-18 nm as the solvent polarity increases, corroborating the occurrence of an intramolecular charge transfer.^{126,200}

Table 3.11 UV-Vis ICT λ_{max} (nm) in different solvents for derivatives **3.8-3.10**.

Solvent	3.8	3.9	3.10
Benzene	445	434	416
DCM	442	425	411
MeOH	434	421	404
Acetonitrile	427	417	402

3.3.3 Electrochemical characterization

Derivatives **3.8-3.10** show the expected two-step reversible one electron oxidation of the TTF molecule. All oxidation potentials for the derivatives are higher than the potentials necessary to oxidize unsubstituted TTF. They span a potential range similar to

the cyanopyridyl derivatives discussed above. This shift is due to the extended delocalization of electron density over the aromatic rings and the electron-withdrawing character of pyridine rings.^{126,200} The potential decrease following the trend **3.8** > **3.9** > **3.10** matches the decreasing trend of ICT λ_{max} .

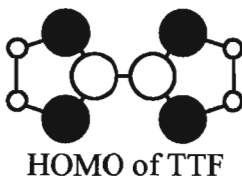
Table 3.12 Uv-Vis ICT λ_{max} (nm) and cyclic voltammetry oxidation potentials (V) for derivatives **3.8-3.10**.

	ICT λ_{max} ^a	$E_{1/2}^1$ ^b	$E_{1/2}^2$ ^b
TTF	NA	0.37	0.76
3.8	427	0.45	0.82
3.9	417	0.42	0.80
3.10	402	0.40	0.78

Experimental conditions: a) 10^{-5} M solutions in acetonitrile, b) 0.1 mM solution in acetonitrile, 0.1 mM TBAPF₆.

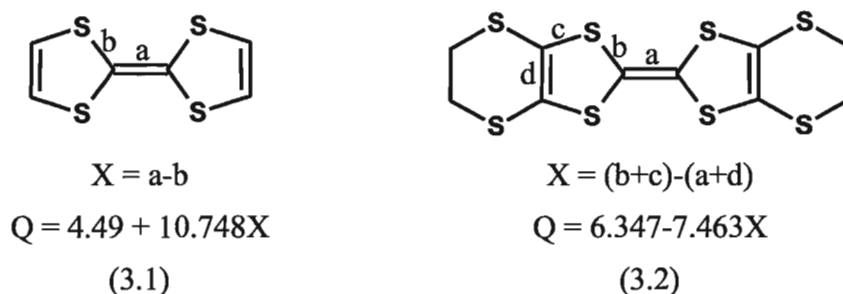
3.4 Synthesis and characterization of charge transfer salts

The preparation of the CT salts of derivatives **3.2-3.4**, **3.8** and **3.10** was carried out by reaction with iodine and/or using electrochemical methods. Oxidation of derivative **3.5** was not attempted because of the poor preparation yield of the derivative and purification difficulties. The composition of the CT salts below was determined by elemental analysis and/or X-ray diffraction if single crystals were obtained. In particular, the bond lengths of the TTF donors in the single crystal structures below have been closely inspected in order to evaluate their oxidation state. Upon oxidation, the bond lengths of TTF change due to the variation of the electronic population of its highest occupied molecular orbital (HOMO). The bonds that display the largest change are the central C=C and C-S bonds, as their contribution to the HOMO is the largest, Scheme 3.9.¹⁴⁰



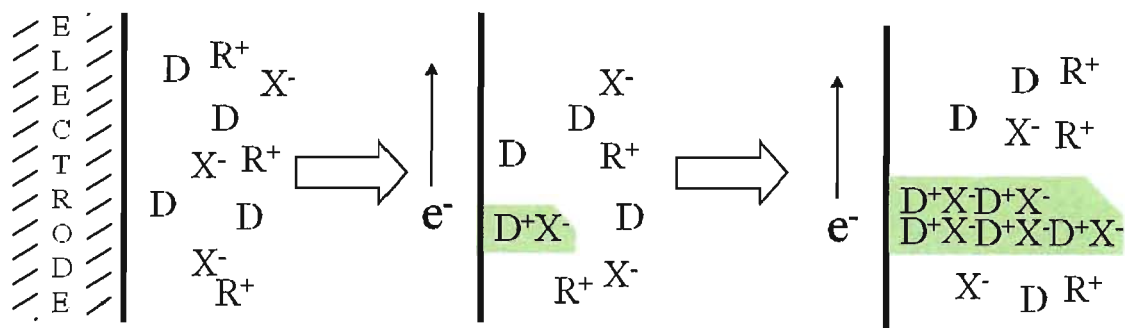
Scheme 3.9 Scheme showing the HOMO of TTF. The black and white circles indicate the atomic orbital contribution to the HOMO. The colour of the circle indicates the sign of the contribution.¹⁴⁰

Equations (3.1)²⁰⁵ and (3.2)²⁰⁶ have been used in the literature to calculate the charge Q of TTF donors in CT salts as a function of their bond lengths. These empirical equations were determined by a least square fit of the parameter X from data sets of TTF and BEDT-TTF CT salts of known stoichiometry. As shown in Scheme 3.10, equation (3.1) uses the central C=C and C-S bonds in order to calculate the charge, whereas equation (3.2) uses these bonds plus the outer C=C bonds. Given that equations (3.1) and (3.2) were determined based on TTF and BEDT-TTF CT series of salts respectively, we decided to evaluate the suitability of these two equations for calculating the charge of our unsymmetrical TTF derivatives.



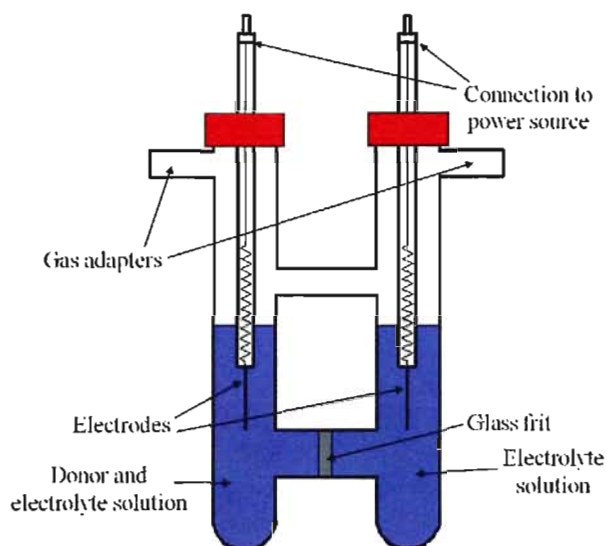
Scheme 3.10 Schematic representation of the bonds used for the CT calculations.

The synthesis of the PF_6^- CT salts of derivatives **3.2**, **3.4**, **3.8** and **3.10** was carried out using the electrocrystallization technique. Electrocrystallization is an electrochemical method for the electrolysis of electroactive species in solution in order to obtain a solid. During an electrocrystallization experiment, the electroactive species is oxidized or reduced to form an ion. Association of this ion with a suitable counterion in solution leads to the precipitation of the corresponding salt. This method was used for the preparation of the first superconducting organic CT salts of TMTSF,¹⁰⁶ and has been extensively used for the preparation of magnetic conducting CT salts of TTF and its derivatives.^{5,207,208} Scheme 3.11 shows that, in a typical experiment, the electroactive donor D is dissolved in an organic solvent along with the electrolyte RX . The slow oxidation of D into the radical cation results in the slow increase of its concentration in solution. Under the appropriate experimental conditions, the CT salt DX crystallizes forming single crystals on the electrode. If the CT salt is conducting the crystal becomes part of the electrode and this promotes further crystal growth.²⁰⁷



Scheme 3.11 Diagram showing the electrocrystallization process of the electroactive donor D into the CT salt DX in the presence of the electrolyte RX. The single crystal is represented as a green shape.

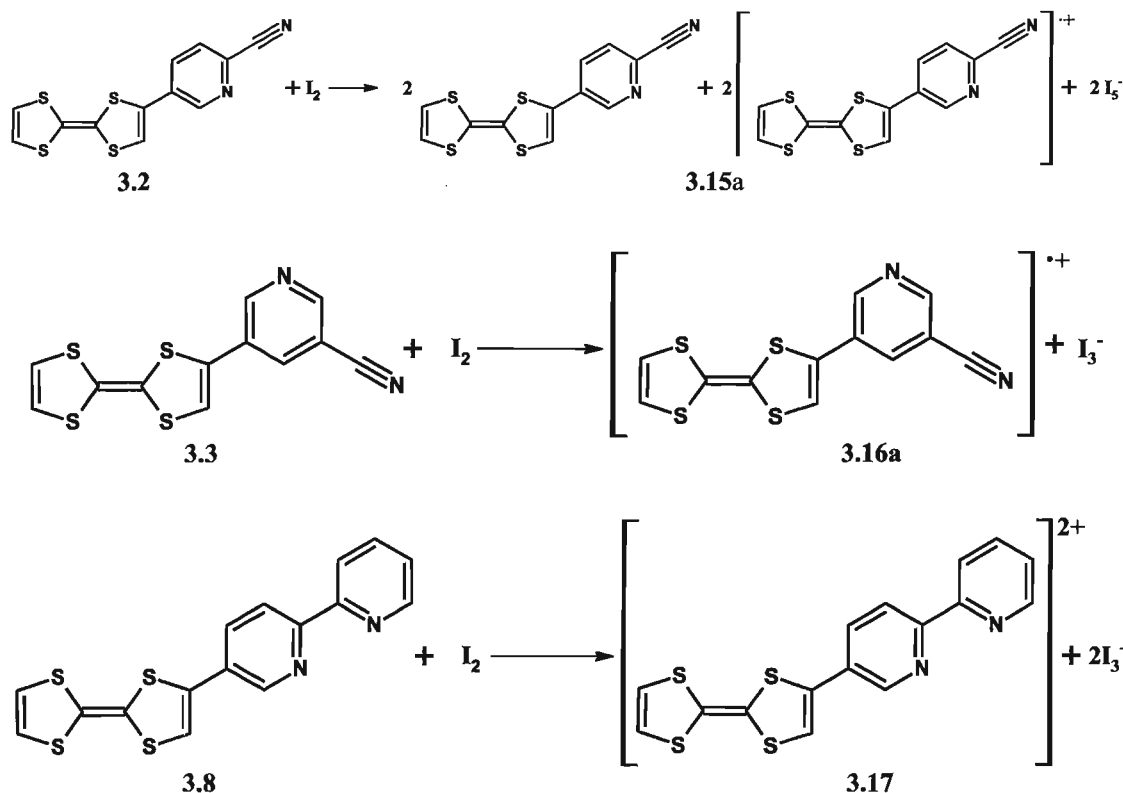
Scheme 3.12 shows the schematic representation for a typical electrocrystallization H-cell set up used in this thesis. In this method the voltage, current intensity, solvent, electrolyte, temperature and electrode surface are parameters to optimize in order to establish the appropriate conditions for the growth of single crystals. The electrocrystallization experiments in this thesis were carried out under galvanostatic conditions, which sets the current intensity but allow the voltage to change as needed by the electrochemical reaction. In this manner the CT salts were generated slowly in solution, increasing the chances of obtaining single crystals. The electrodes used consisted of 1mm of diameter Pt wire with 10% Ir.²⁰⁷ All the experiments were carried out at room temperature, in the dark, and with the H cell placed in a sand bath in order to minimize vibrations of the experimental setup. The electrolyte used was TBAPF₆ (TBA = tetrabutylammonium) as it has been used in the literature with good results for the preparation of TTF-based CT salts.^{5,106,127,135,207}



Scheme 3.12 Schematic representation of the electrocrystallization H-cell used in this work.

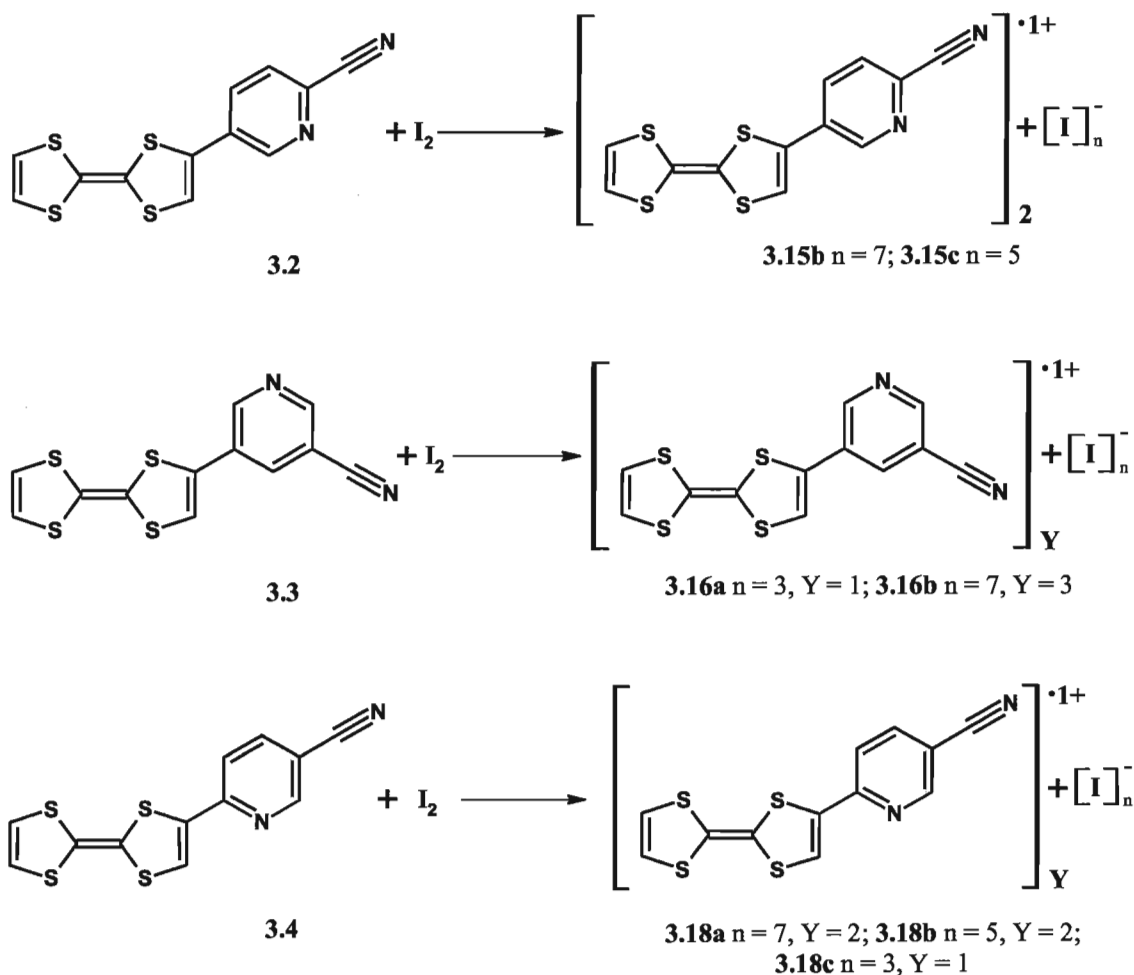
3.4.1 Oxidation of 3.2, 3.3 and 3.8 with I_2

The chemical oxidation of TTF derivatives with I_2 is also a common method employed for the preparation of radical cation salts.^{209,210} In our case, the two methods used to carry out these reactions were slow diffusion and direct reaction, Scheme 3.13 and Scheme 3.14 respectively. In the slow diffusion method, a solution of I_2 in acetone was carefully layered over a DCM solution of the corresponding functionalized TTF donor in a test tube. The tubes were then capped and left undisturbed for two weeks, after which time small black blocks suitable for single crystal X-ray diffraction had formed at the interface between both solutions. Although this method was carried out for derivatives **3.2-3.4** and **3.8**, only single crystals of the CT salts **3.15a**, **3.16a** and **3.17** were obtained. The yield of single crystals for this method was of the order of a few very tiny crystals with very low reproducibilities. The crystals were always shaped like blocks, and were too small for resistivity measurements.



Scheme 3.13 Reaction scheme for the formation of radical cation salts *via* the slow diffusion of the TTF derivative and the iodine solutions.

The direct reaction method was adopted to attempt to prepare the radical cation salts **3.15a**, **3.16a** and **3.17** on a larger scale, Scheme 3.14. All reactions were carried out by adding I₂, in solution or as a solid, to a stirring solution of the corresponding TTF derivative in DCM under nitrogen. The stoichiometry of all of the reaction products was established by elemental analysis, and the structures of the polyiodide anions were assigned based on structural parameters and literature precedents. Product **3.15c** was obtained in two different ways: from **3.15b** after leaving the product under vacuum overnight, and by reacting a solution of **3.2** with solid I₂. The loss of I₂ is indicative of the weak binding of this molecule in the crystal lattice.

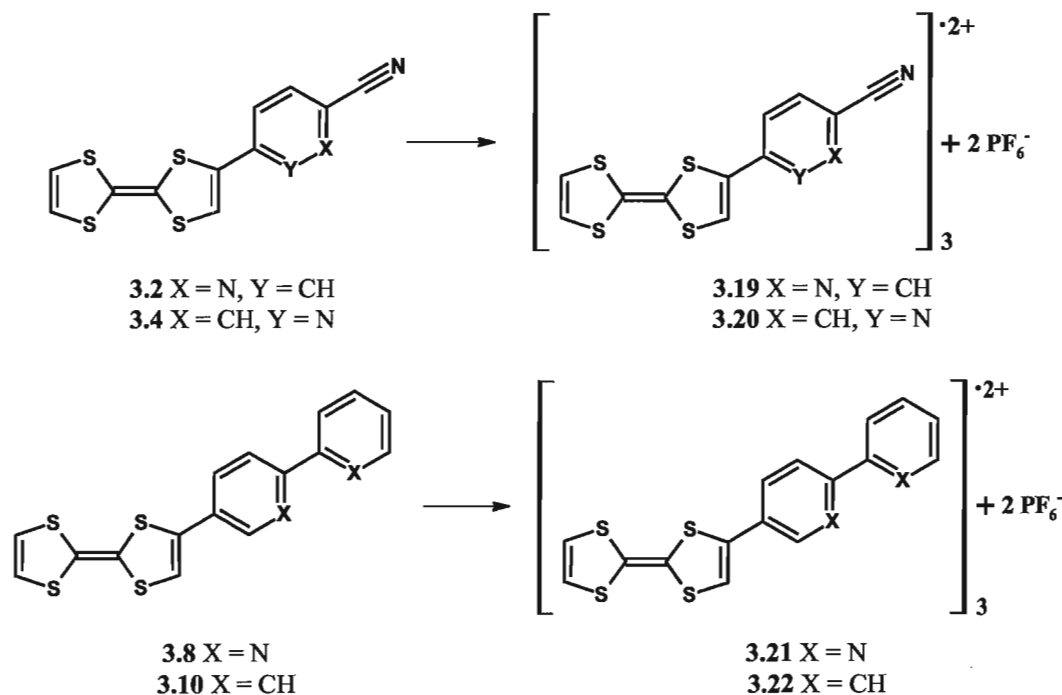


Scheme 3.14 Reaction scheme for the formation of radical cation salts *via* the second method namely direct reactions between the TTF derivative and iodine.

3.4.2 Electrochemical synthesis of CT salts

The electrocrystallization of derivatives **3.2**, **3.4**, **3.8** and **3.10** was carried out in a glass H cell with a medium porosity frit separating the anodic and cathodic arms. In both cases, an excess of TBAPF₆ was used in order to provide a counterion and decrease the resistance of the solution in the cell. Chloroform solutions containing the derivatives and the electrolyte were prepared and filtered inside the corresponding H cell arm. In all the experiments the H cells were allowed to stand at room temperature for 10 minutes after preparation before applying a 0.1 μ A DC. The charge transfer salts **3.19** and **3.20** grew on the anode as polycrystalline powders, and their composition was established by elemental analysis. The charge transfer salts **3.21** and **3.22** grew on the anode as clusters of small

black needles after a few weeks, and were isolated and washed with chloroform. These crystals were found suitable for X-ray diffraction. The four salts obtained by electrocrystallization have the stoichiometry $T_3(PF_6)_2$ where T is the corresponding TTF derivative.



Scheme 3.15 Reaction scheme for the preparation of CT salts **3.19-3.22** via electrocrystallization.

3.4.3 X-ray characterization of CT salts **3.15** and **3.16**

3.4.3.1 X-ray characterization of the CT salt **3.15**

The single crystal structure of the CT salt **3.15** was determined from single crystal X-ray diffraction studies at 173 K, Figure 3.17. This derivative crystallizes in the triclinic space group $P-1$, with four crystallographically independent **3.2** molecules and two I_5^- in the unit cell as shown in Figure 3.18 a). The four TTF derivatives are almost planar, with swivel angles at the S atoms in the range 0.5-7.4°. The torsion angles between the pyridine rings and the TTF moiety are in the range 24-28°. See Table 3.13 for selected bond lengths and bond angles.

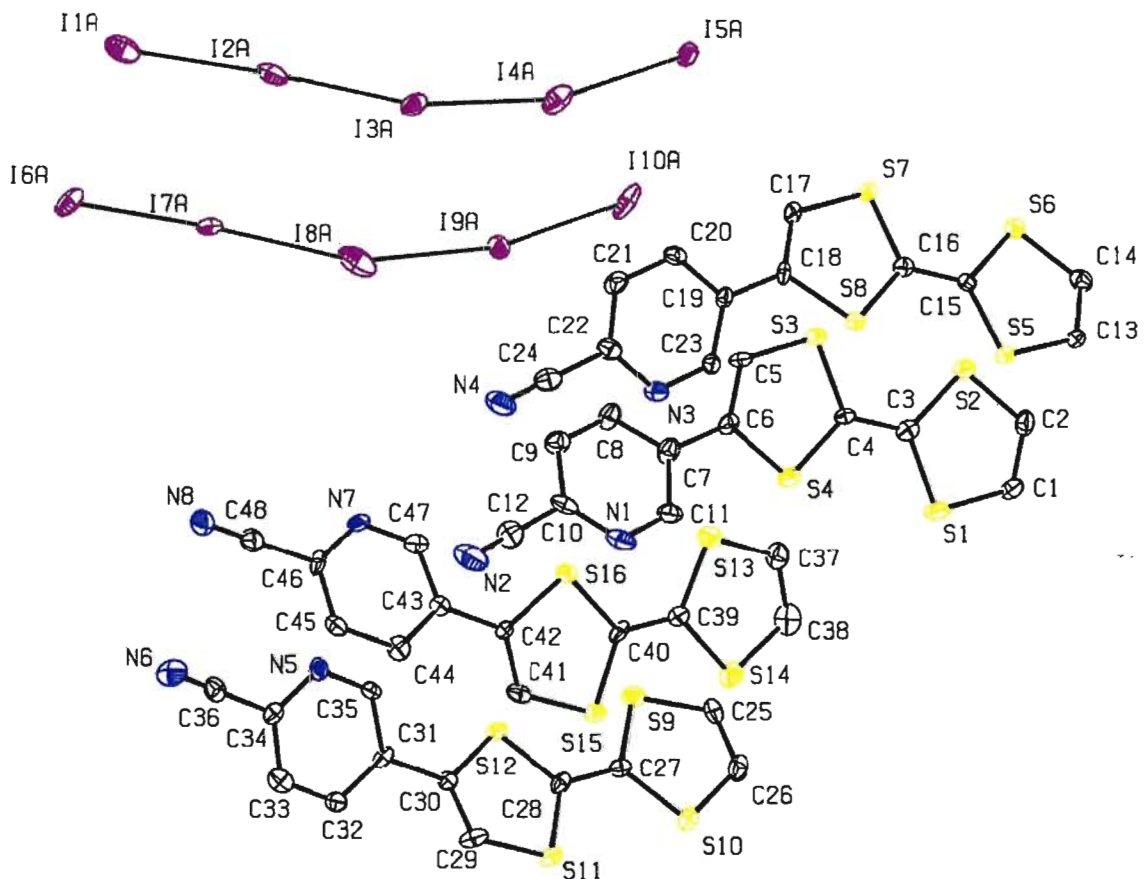


Figure 3.17 ORTEP plot of the asymmetric unit of **3.15a**, showing the corresponding numbering scheme. Thermal ellipsoids plotted at 50% probability. Hydrogen atoms are omitted for clarity.

All the TTF derivatives form dimers in which only the TTF moieties are overlapped. The derivative molecules are arranged in an antiparallel manner within each dimer and they display short intradimer S...S contacts in the range 3.24–3.51 Å. As shown in Figure 3.18 b), the dimers stack at an angle in the range of 22–32° from each other. The interdimer S...S contacts are longer than the sum of their *van der Waals* radii, but the distances between the centroid of the thiolene ring and the closest S atoms of the neighbouring TTF derivative are in the range 3.30–3.50 Å. This indicates interactions between the lone pairs of the S atom and the π system of the thiolene ring. The angle between TTF dimers is caused by the presence of two I_5^- anions (see below) inserted between the stacks, Figure 3.18 c). The structure presents C–H...N short contacts, Table 3.14. There are no short CN...I contacts in the structure.

Table 3.13 Selected bond lengths (Å) and angles (°) for **3.15a**.

Bond lengths			
S1-C3	1.742(13)	S16-C40	1.729(12)
S2-C3	1.739(14)	C39-C40	1.370(19)
S3-C4	1.731(12)	I1A-I2A	3.245(16)
S4-C4	1.738(13)	I2A-I3A	3.064(15)
C3-C4	1.406(5)	I3A-I4A	3.184(7)
S5-C15	1.723(12)	I4A-I5A	3.129(7)
S6-C15	1.728(13)	I1B-I2B	2.97(3)
S7-C16	1.713(12)	I2B-I3B	3.42(3)
S8-C16	1.719(13)	I3B-I4B	3.098(12)
C15-C16	1.394(18)	I4B-I5B	3.245(16)
S9-C27	1.715(13)	I6A-I7A	3.071(11)
S10-C27	1.731(13)	I7A-I8A	3.237(12)
S11-C28	1.722(14)	I8A-I9A	3.147(6)
S12-C28	1.725(12)	I9A-I10A	3.088(7)
C27-C28	1.388(19)	I6B-I7B	3.33(2)
S13-C39	1.738(14)	I7B-I8B	3.116(19)
S14-C39	1.726(14)	I8B-I9B	3.112(11)
S15-C40	1.735(14)	I9B-I10B	3.321(19)
Bond angles			
S1-C3-S2	114.9(7)	I3A-I4A-I5A	164.8(3)
S3-C4-S4	115.5(7)	I1B-I2B-I3B	174.8(7)
S5-C15-S6	114.9(7)	I2B-I3B-I4B	150.6(7)
S7-C16-S8	116.4(7)	I3B-I4B-I5B	172.8(5)
S9-C27-S10	115.2(8)	I6A-I7A-I8A	175.3(4)
S11-C28-S12	115.9(8)	I7A-I8A-I9A	160.6(4)
S13-C39-S14	114.7(8)	I8A-I9A-I10A	167.5(2)
S15-C40-S16	115.5(8)	I6B-I7B-I8B	170.6(8)
I1A-I2A-I3A	174.2(3)	I7B-I8B-I9B	168.0(6)
I2A-I3A-I4A	163.2(3)	I8B-I9B-I10B	157.4(5)
Dihedral angles			
C5-C6-C7-C8	25(2)	C29-C30-C31-C32	-28(2)
C17-C18-C19-C20	-26(2)	C29-C30-C31-C32	-28(2)

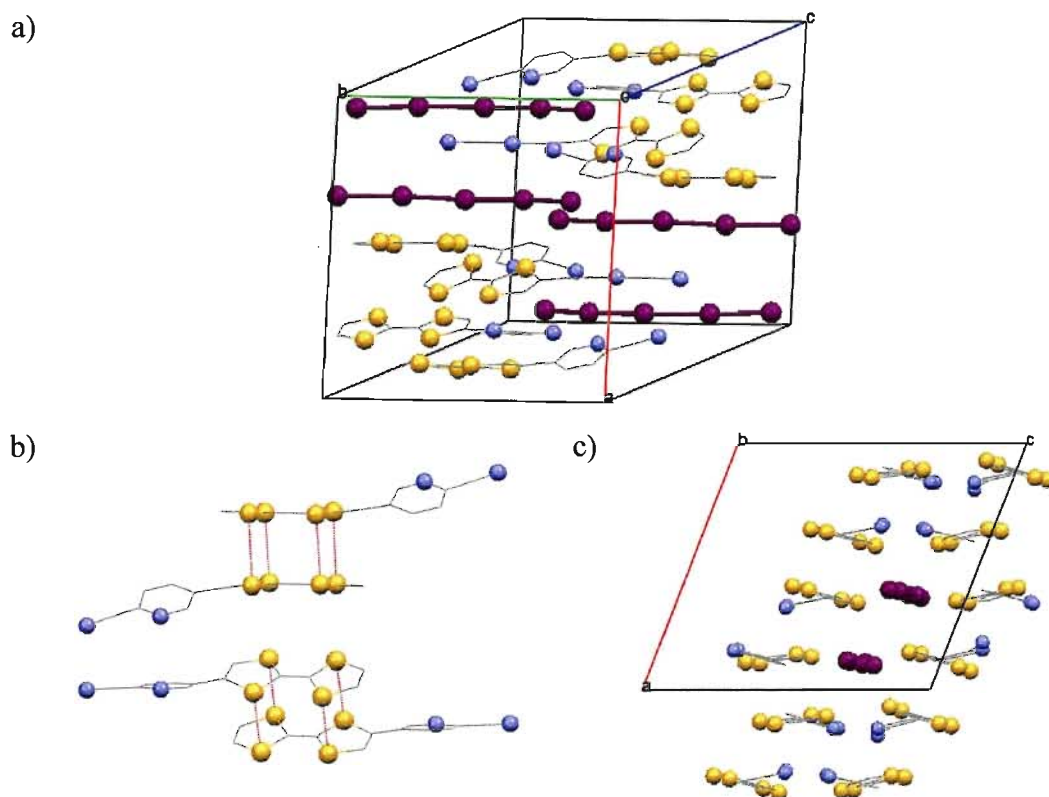


Figure 3.18 a) Unit cell of **3.15a**, b) Stack of dimers of **3.15a** showing the S...S short contacts between TTF moieties as dashed red lines. c) I₅⁻ anions between stacks of derivatives.

Table 3.14 Distance *d* and angle α of the CH...N short contacts in **3.15a**.

	<i>d</i> [C-H...N] (Å)	<i>d</i> [H-C...N] (Å)	α [C-H...N] (°)
C37a-H37a...N8 ⁱ	2.43	3.260(19)	146
C1b-H1b...N2 ⁱ	2.50	3.280(2)	139
C35c-H35c...N2	2.59	3.530(2)	169

Symmetry transformation: ⁱ*x*, -1+*y*, *z*.

The crystal structure presents two groups of five iodine atoms each in a linear arrangement. These two groups could be considered as I₅⁻ anions or as two I₃⁻ anions plus two I₂ molecules. The I-I bond lengths in the structure are in the range 2.97-3.24 Å, longer than the 2.71 Å expected for I₂ but a reasonable fit for two I₅⁻ anions.^{209,211} The presence of positional disorder in the I₅⁻ anions made it necessary to refine the occupancy factor for each disordered anion, to a final occupancy of about 65% for each polyiodide, Figure 3.19. These anions are arranged roughly parallel to the TTF derivatives, with short

I...I contacts of about 3.20 Å between the terminal iodine atoms of I_5^- anions in neighbouring unit cells. This distance falls within the 2.97-3.24 Å bond length in the I_5^- anions in this structure. This is a common feature in polyiodide salts, which results in channels occupied by polyiodide anions that run through the crystal structure.²¹¹

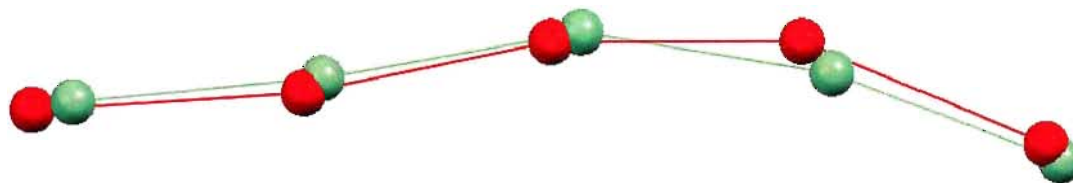


Figure 3.19 Molecular structure showing in different colours the overlapped components of the positional disorder of an I_5^- counterion.

If each polyiodide has a charge of -1, based on the charge neutrality principle, it would be expected that two of the four TTF derivatives in the asymmetric unit would be oxidized. Interestingly, all the TTF moieties in this structure form dimers with S...S distances shorter than the sum of their *van der Waals* radii, a structural trait normally only common for TTF radical cations. Based on the central C=C bond length we can divide the four dimers into two groups: in group A the TTF molecules have a C=C bond length of ca. 1.37 Å, and in group B the C=C bond lengths are longer than 1.38 Å. The range of the S...S contacts for the TTF molecules within the two groups is different, with group A showing the widest S...S contact range. The estimation of the amount of charge transfer according to equations (3.1) and (3.2) for each dimer (Table 3.16), surprisingly, does not give a conclusive answer, particularly when compared with the CT calculations of neutral **3.2**.

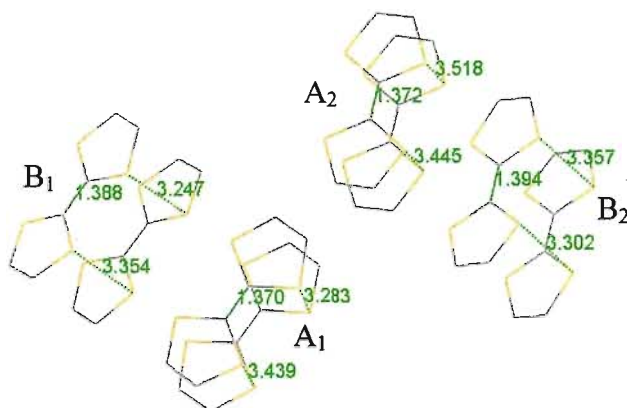


Figure 3.20 TTF dimers in **3.15a**. Cyanopyridyl moieties and counterions are omitted for clarity. The C=C bond lengths and S...S contacts for the TTF molecules are shown in Å.

The CT calculations using equation (3.1) for neutral **3.2-3.5** give values close to zero charge for all the derivatives except for **3.2**, which has a charge of +0.48, Table 3.15. The CT calculations using equation (3.2) give a similarly high value for **3.2** and the rest of derivatives have charges ranging +0.16 and +0.26. Equation (3.2) was obtained from a set of BEDT crystal structures, so it may not be applicable to a TTF system, although it has been applied by several research groups to account for the oxidation state of TTF derivatives other than BEDT-TTF.¹²⁷ Still, the CT calculation for **3.2** using equation (3.1) is quite unexpected.

Table 3.15 CT calculations for the neutral derivatives **3.2-3.5**.

	Eq. (3.1)	Eq. (3.2)
3.2	+0.48	+0.44
3.3	+0.05	+0.16
3.4	+0.07	+0.25
3.5	+0.06	+0.26

The ICT observed by UV-Vis for **3.2** doesn't support these calculations as the ICT band appears at a similar wavelength as the ICT bands of the other cyanopyridyl derivatives. In solution, the ICT band results from the average of the conformations due to the rotation of the C_{TTF}-C_{pyridine} bond, whereas equations (3.1) and (3.2) give CT values for a fixed conformation. The reason for the large CT value could be intermolecular

interactions present only in the crystal structure of **3.2**. This derivative forms stacks with all the molecules oriented parallel to each other within a stack, an arrangement we don't see in derivatives **3.3-3.5**. Moreover, the crystal structure presents interstack CN2-S2a short contacts that could result in additional electron density being removed from the TTF moiety, resulting in longer bond lengths.

The larger standard deviation of the bond lengths in the crystal structure of **3.2** as compared to those of the rest of the neutral cyanopyridine derivatives may also be an explanation for the large CT value for **3.2**. The preparation of better crystals of **3.2** was attempted several times, but no single crystals suitable for X-ray diffraction studies were obtained. Further experimentation is necessary in order to account for the anomalous CT value for derivative **3.2**.

The calculation for the CT in A dimers with equations (3.1) and (3.2) affords, again, unexpected results as shown in Table 3.16. The CT for A dimers is within the range +0.57-0.89 depending on the equation used. The charge for the B dimers is close to +1, which is expected for two **3.2**⁺⁺. A possible explanation for the unexpected CT calculations may be the positional disorder present in the I₅⁻ anions. This may have an impact on the accuracy of the bond lengths in the crystal structure, resulting in erroneous CT calculations.

Table 3.16 CT calculations for **3.2** and **3.15**.

	Eq. (3.1)	Eq. (3.2)
3.2	+0.48	+0.44
A ₁	+0.60	+0.89
A ₂	+0.57	+0.71
B ₁	+0.88	+0.84
B ₂	+0.98	+1.10

In conclusion, the charge balance based on the presence of two I₅⁻ anions in the asymmetric unit suggests that two of the four unique TTF derivatives are in the radical cation form. The CT calculations indicate the presence of two **3.2**⁺⁺ (B dimers) and two derivatives with a CT similar the neutral **3.2** (A dimers). Analysis of the crystal structure

reveals that the four unique TTF derivatives form dimers, displaying short S...S contacts consistent with the distances expected for TTF radical cations. We consider that this CT salt is formed by two **3.2**^{•+} with the corresponding I₅⁻ anions, and that the short S...S contacts formed by the A dimers are due to packing effects. Further studies will be necessary in order to corroborate this conclusion.

3.4.3.2 X-ray characterization of the CT salt 3.16a

The molecular structure of **3.16a** was determined from single crystal X-ray diffraction studies at 273 K, Figure 3.21 a). This derivative crystallizes in the monoclinic space group *P2₁/n*, with two crystallographically independent TTF radical cations **3.3**^{•+} and two unique I₃⁻ anions. The two dithiole rings of the TTF moiety are almost planar, with swivel angles at the S atoms of about 6° for each ring. There is a slight torsion angle in the range of 15-19° between the pyridine ring and the TTF moiety for both independent molecules. In this case, the cyanopyridyl moiety has rotated 180° with respect to the TTF moiety compared to the structure of the neutral donor **3.3**. A view of the unit cell is shown in Figure 3.23 b).

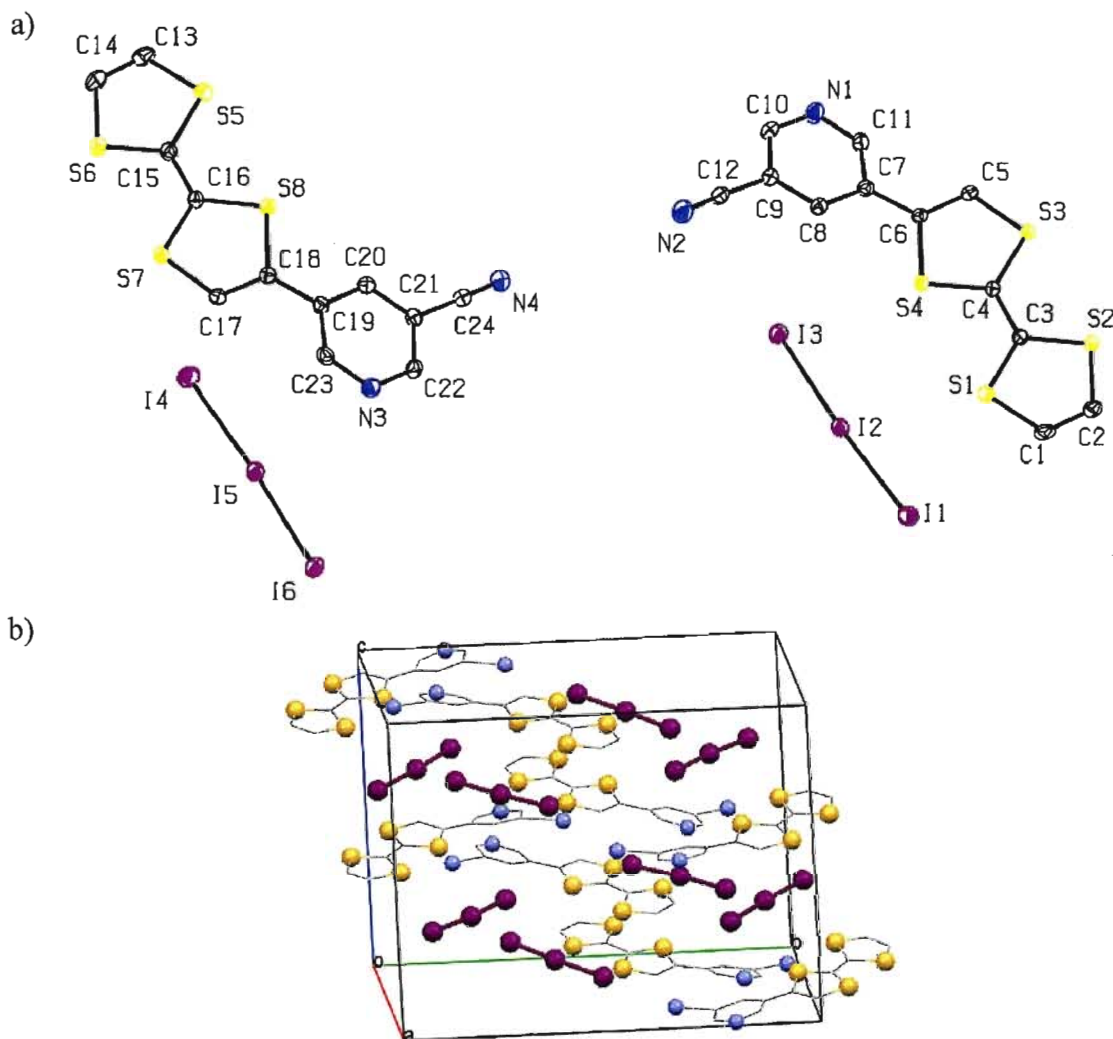


Figure 3.21 a) ORTEP plot of molecular structure of the asymmetric unit of **3.16a**, showing the corresponding numbering scheme. Thermal ellipsoids plotted at 50% probability. Hydrogen atoms are omitted for clarity. b) Unit cell of **3.16a**.

The radical cations of **3.3**^{•+} pack as dimers, displaying short S...S contacts in the range 3.20-3.36 Å (Figure 3.22). There are also lateral short S...S contacts between dimers of about 3.55 Å. From the molecular structure of the complex we can determine that the donor and anion are in a 1:1 ratio, which suggests that each TTF donor molecule is oxidised in the form of a radical cation. The full oxidation and the lack of a clear conducting pathway make it reasonable to conclude that this salt would be a poor conductor or an insulator.

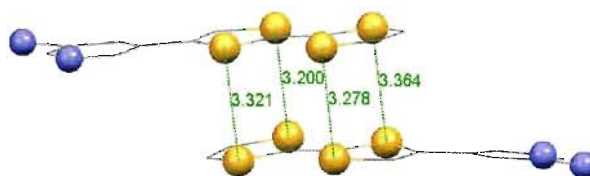


Figure 3.22 Dimer of 3.3^{++} in **3.16a**.

Inspection of the packing diagram reveals that the structure of this CT salt is comprised a herringbone-like arrangement of segregated chains of radical cation donors and I_3^- anions that run along the *b*-axis of the unit cell, Figure 3.23. There are no short $S\cdots S$ contacts involving TTF donors within a chain but each TTF donor participates in two H-bonding interactions involving the nitrile and pyridine N atoms, Table 3.18. These H-bonding interactions propagate through the chains of donors, Figure 3.23. Each TTF donor is roughly parallel to an I_3^- anion such that there are short $S\cdots I$ contacts in the range 3.54-3.75 Å, Figure 3.23. See Table 3.17 for selected distances and angles.

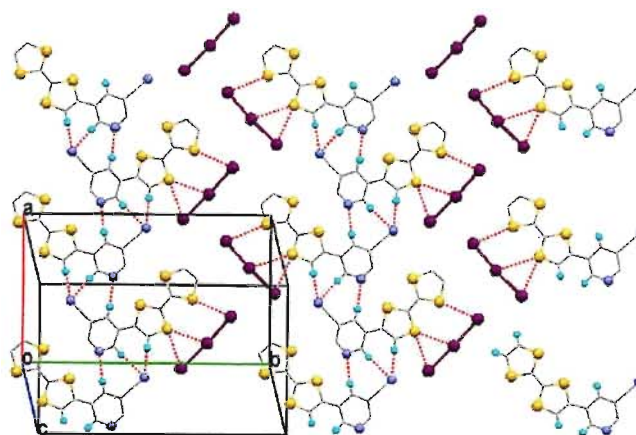


Figure 3.23 Layers of molecules of **3.16a** that run along the *b*-axis of the unit cell.

Table 3.17 Selected bond lengths (Å) and angles (°) for **3.16a**.

Bond lengths			
S1-C1	1.725(4)	S5-C13	1.728(4)
S1-C3	1.712(3)	S6-C14	1.729(4)
S2-C3	1.724(3)	S7-C17	1.719(4)
S2-C2	1.720(4)	S8-C18	1.754(4)
S3-C5	1.715(3)	C13-C14	1.333(6)
S3-C4	1.715(4)	C15-C16	1.386(5)
S4-C4	1.719(3)	C17-C18	1.358(5)
S4-C6	1.746(3)	C18-C19	1.475(5)
C1-C2	1.343(5)	N4-C24	1.141(5)
C3-C4	1.406(5)	I1-I2	2.9429(4)
C5-C6	1.345(2)	I2-I3	2.9224(4)
C6-C7	1.354(5)	I4-I5	2.9544(4)
N2-C12	1.141(5)	I5-I6	2.9048(4)
Bond angles			
C1-S1-C3	95.28(18)	C16-S8-C18	95.47(17)
C3-S2-C2	95.06(18)	S2-C3-S1	115.52(19)
C5-S3-C4	95.29(17)	S4-C4-S3	115.74(19)
C4-S4-C6	95.47(16)	S6-C15-S5	115.3(2)
C13-S5-C15	94.95(19)	S8-C16-S7	115.6(2)
C14-S6-C15	94.80(19)	I1-I2-I3	175.860(11)
C16-S7-C17	95.07(17)	I4-I5-I6	175.761(11)
Dihedral angles			
C5-C6-C7-C8	19.7(5)	C17-C18-C19-C23	-15.6(5)

Table 3.18 Distance *d* and angle *θ* for the CH...N short contacts in **3.16a**.

	<i>d</i> [C-H...N] (Å)	<i>d</i> [H-C...N] (Å)	<i>θ</i> [C-H...N] (°)
C5-H5...N4 ⁱ	2.43	3.360(6)	177
C8a-H8a...N3 ⁱⁱ	2.47	3.391(6)	172
C17b-H17b...N2 ⁱⁱⁱ	2.53	3.453(6)	177
C20c-H20c...N1 ^{iv}	2.47	3.388(6)	171

Symmetry transformation: ⁱ 5/2-x, 1/2+y, 3/2-z, ⁱⁱ 3/2-x, 1/2+y, 3/2-z, ⁱⁱⁱ 3/2-x, -1/2+y, 3/2-z, ^{iv} 5/2-x, -1/2+y, 3/2-z.

The results of the charge transfer calculation for each crystallographically independent radical cation in this salt are shown on Table 3.19. In this case, both equations give similar results and are consistent with the donor having a charge close to zero in the neutral molecule and a charge close to +1 in the CT complex.

Table 3.19 CT calculations for the neutral **3.3** and **3.3⁺**

	Eq. (3.1)	Eq. (3.2)
3.3	+0.05	+0.16
3.3⁺ (1)	+1.14	+1.20
3.3⁺ (2)	+0.81	+0.90

3.4.4 Additional characterization of CT salts of cyanopyridyl donors

The nitrile str frequencies of the CT salts **3.15b**, **3.15c**, **3.16a**, **3.16b**, **3.18a-c**, **3.19** and **3.20** obtained from FT-IR spectroscopy are listed in Table 3.20 along with the CT salt stoichiometry and the CN str frequencies of the neutral donors. The table shows only minor differences in the CN str between the neutral donors and the CT salts. The CT salts of derivative **3.4** display the largest frequency change of all the CT salts listed in the table. Only one CN str was present in the IR spectra for all of the CT salts. This could mean that either there is only one type of TTF derivative present in the CT salt or that the IR frequency of the nitrile functional group is not sensitive to the oxidation state of the TTF moiety. Comparison of the stoichiometry of the CT salts **3.19** and **3.20** with CT salts **3.21** and **3.22** (see below) indicates the possibility of having TTF derivatives with two

different oxidation states. If this is the case for **3.19** and **3.20**, then we can conclude that, for this system, the CN str frequency is not an accurate indicator of the oxidation state of the TTF derivatives in a CT salt. This contrasts with the observed correlation between the CN str and oxidation state of TCNQ in CT salts.²¹²

Table 3.20 IR nitrile stretching frequencies (cm⁻¹) for the corresponding neutral donor and CT salts **3.15b**, **3.15c**, **3.16a**, **3.16b**, **3.18a-c**, **3.19** and **3.20** and the stoichiometry of their CT salts.

	Neutral donor	CT salt	Stoichiometry ^a
3.15b	2228 (3.2)	2229	(3.2) ₂ I ₇
3.15c	2228 (3.2)	2229	(3.2) ₂ I ₅
3.16a	2231 (3.3)	2226	(3.3)I ₃
3.16b	2231 (3.3)	2233	(3.3) ₂ I ₇
3.18a	2220 (3.4)	2233	(3.4) ₂ I ₇
3.18b	2220 (3.4)	2232	(3.4) ₂ I ₅
3.18c	2220 (3.4)	2233	(3.4)I ₃
3.19	2228 (3.2)	2225	(3.2) ₃ (PF ₆) ₂
3.20	2220 (3.4)	2231	(3.4) ₃ (PF ₆) ₂

^aObtained from elemental analysis.

Experimental conditions: pressed KBr pellet.

The UV-Vis spectra of acetonitrile solutions of the CT salts **3.15c**, **3.16a**, **3.18b** and **3.18c** are shown in Figure 3.24. All spectra present four general features: i) a band at high energy centered at $\lambda = 275$ nm, resulting from the overlapped local transitions of TTF (neutral and radical) and the corresponding cyanopyridyl group, ii) a polyiodide band at ca. $\lambda = 365$ nm, iii) a sharp band centered at $\lambda = 450$ nm, and iv) a broad band at $\lambda = 580$ nm, corresponding to the presence of the TTF moiety radical cation state.^{213,214} In the case of **3.15c** and **3.18b**, the spectra are the result of the overlap of neutral and oxidized TTF moieties, and for all of the CT salts the ICT band is centered at $\lambda = 450$ nm.

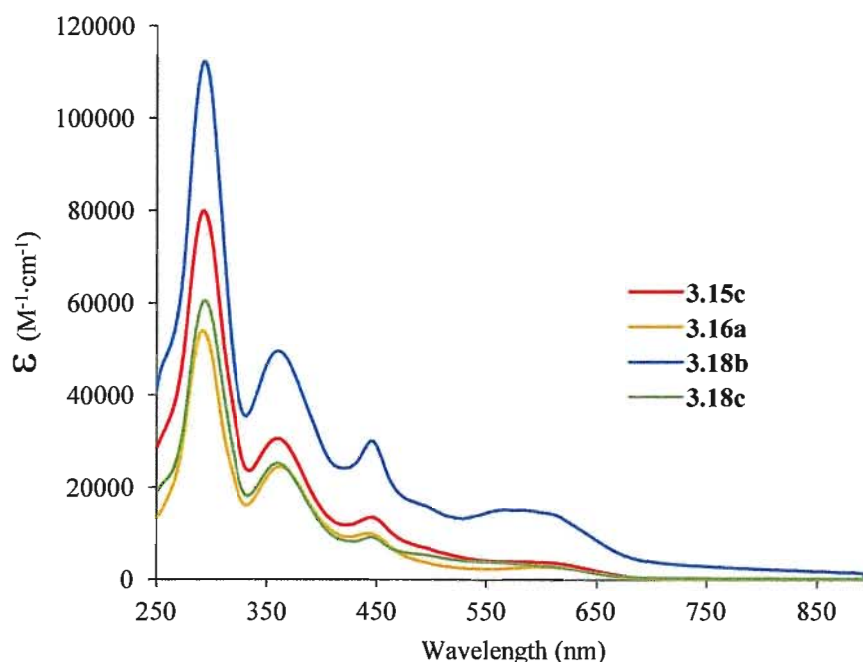


Figure 3.24 UV-Vis spectra of 10^{-5} M solutions of polyiodine CT salts **3.15c**, **3.16a**, **3.18b**, **3.18c** in acetonitrile.

Variable temperature conductivity measurements between 77 and 293 K were carried out on pressed pellets of the CT salts **3.15c**, **3.16a**, **3.18b** and **3.18c**. These measurements revealed that the salts displayed semiconducting behaviour with conductivities ranging from 1.852×10^{-7} to $9.620 \times 10^{-3} \text{ S cm}^{-1}$ at room temperature, Table 3.21. The low conductivity of **3.16a** can be attributed to the absence of stacks of TTF dimers in the solid state, making it difficult for conducting electrons to move through the material due to the lack of a good conduction pathway. No crystal structures are available for the remainder of the CT salts in Table 3.21, so without information regarding the packing of these CT salts in the solid state no further analysis is possible.

Table 3.21 Electrical conductivity measurements (S cm^{-1}) at room temperature of pressed pellets of the CT salts **3.15c**, **3.16a**, **3.18b** and **3.18c**.

	Conductivity
3.15c	5.460×10^{-3}
3.16a	1.852×10^{-7}
3.18b	9.620×10^{-3}
3.18c	4.740×10^{-3}

3.4.5 X-ray characterization of CT salts 3.17, 3.21, 3.22

3.4.5.1 X-ray characterization of the CT salt 3.17

The single crystal structure of the CT salt **3.17** (Figure 3.25) was determined from X-ray diffraction studies at 150 K. The CT salt crystallizes in the triclinic space group $P\bar{1}$, with one crystallographically unique and two disordered I_3^- anions in the unit cell, Figure 3.26 a).

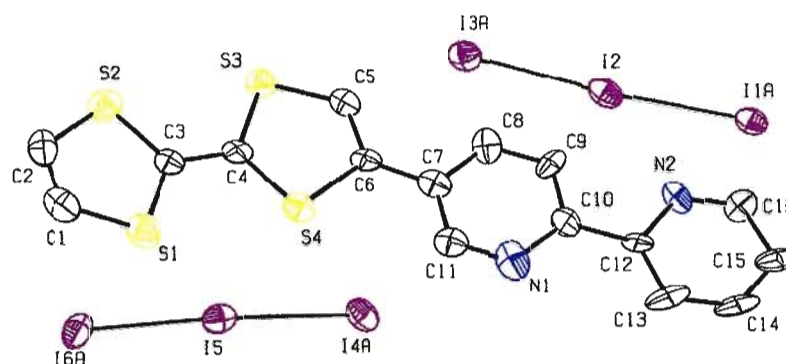


Figure 3.25 ORTEP plot of the asymmetric unit of **3.17**, showing the appropriate numbering scheme. Thermal ellipsoids are plotted at 50% probability. Hydrogen atoms and iodine disorder are omitted for clarity.

The TTF moiety is almost planar, with swivel angles at the S atoms smaller than 6° . The TTF and bipyridine rings are coplanar, displaying a small dihedral angle of 4.0° between their respective best planes. See Table 3.22 for selected bond lengths and bond angles.

Table 3.22 Selected bond lengths (Å) and angles (°) for **3.17**.

Bond lengths			
S1-C1	1.70(2)	C5-C6	1.35(2)
S1-C3	1.681(17)	C6-C7	1.45(2)
S2-C3	1.736(17)	I1A-I2	2.935(4)
S2-C2	1.72(2)	I1B-I2	2.914(19)
S3-C5	1.702(15)	I2-I3A	2.902(4)
S3-C4	1.731(17)	I2-I3B	2.887(19)
S4-C4	1.695(17)	I4A-I5	2.921(3)
S4-C6	1.763(17)	I4B-I5	3.09(3)
C1-C2	1.33(3)	I5-I6A	2.918(3)
C3-C4	1.40(2)	I5I6B	2.63(2)
Bond angles			
C1-S1-C3	95.8(9)	S4-C4-S3	115.9(10)
C3-S2-C2	94.5(9)	I1A-I2-I3A	174.76(8)
C5-S3-C4	94.0(8)	I1B-I2-I3B	173.3(7)
C4-S4-C6	96.5(8)	I4A-I5-I6A	176.12(7)
S2-C3-S1	115.4(10)	I4B-I5-I6B	175.3(8)
Dihedral angles			
C5-C6-C7-C11	-14.8(6)	N1-C10-C12-C13	-0.6(5)

In this structure, the derivative molecules pack as 1-D chains of π - π stacked dimers that propagate along the [011] direction of the unit cell. The TTF moieties present short intradimer S \cdots S distances of 3.332(6) and 3.392(6) Å, Figure 3.26 b), and the bipyridine moieties present a centroid-centroid distances of 3.62 Å, indicative of weak π - π interactions.

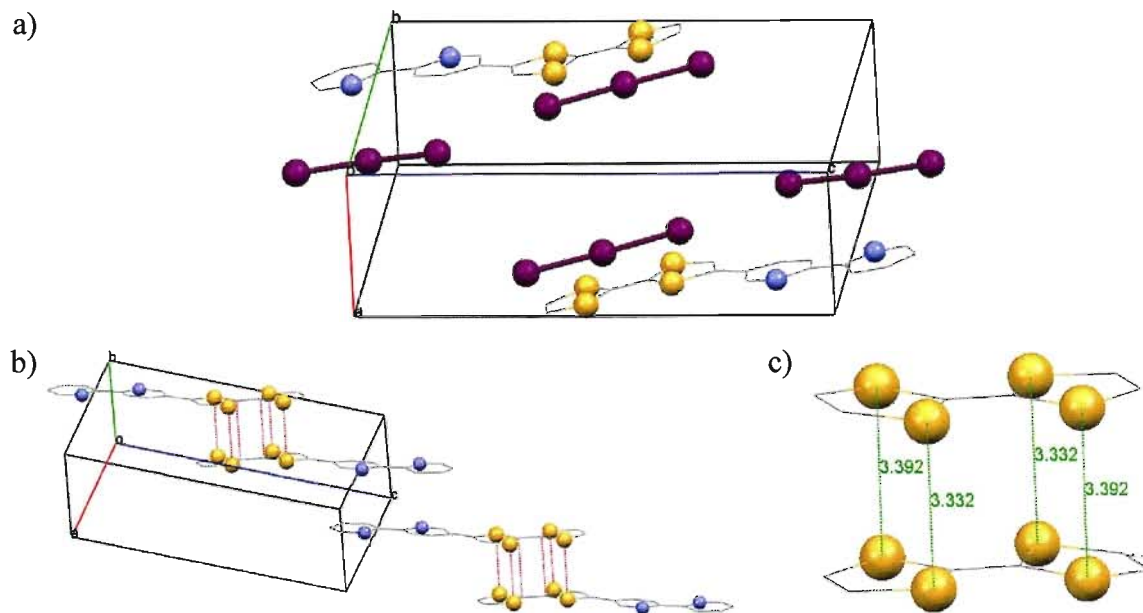


Figure 3.26 a) Unit cell of **3.17**, disorder in the counterions is not shown, b) chains of derivative dimers running along the direction [011], c) TTF dimer S...S short contacts are shown as dashed lines, distances are shown in Å.

The I_3^- anions are arranged as linear dimers with $I\cdots I$ contacts of 3.924(5) Å. These dimers are aligned adjacent to the oxidized **3.8** molecules, with short $S\cdots I$ distances in the range 3.52–3.73 Å that connect chains of dimers running along the b -axis of the unit cell, Figure 3.27 a). Both anions present positional disorder, characterized by the two end iodine atoms pivoting about the central one, Figure 3.27 b). Refinement of the structure indicated 10% and 25% of positional disorder for each anion.

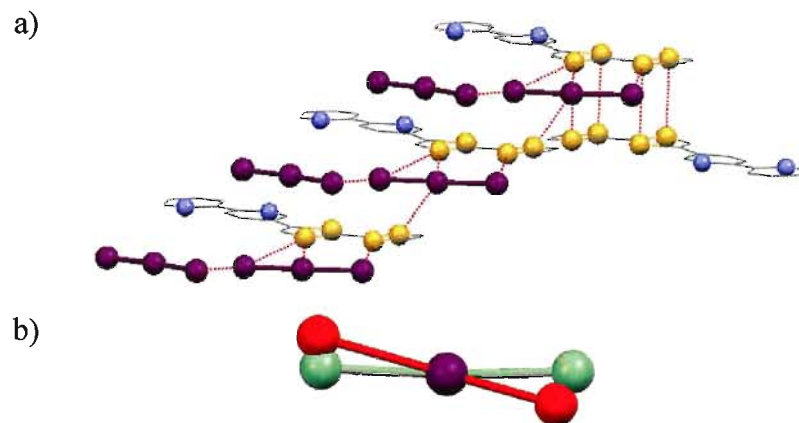


Figure 3.27 a) Short $S\cdots I$ and $I\cdots I$ contacts in **3.17** showing also a TTF dimer, b) molecular model showing, in different colours, the overlapped components of the disorder of a I_3^- anions. The iodine atom in purple is shared by both components of the disorder.

The presence of two anions in the asymmetric unit seems to indicate, based on the charge balance, that the TTF moiety in this CT salt has a charge of +2. Inspection of the crystal structure shows C=C and C-S bond lengths that differ slightly from those expected for a radical cation of **3.8**. Table 3.23 shows a summary of the bond lengths for **3.8** and their changes depending on their oxidation state. The structural changes over two oxidation states, from neutral to a dication state, are significant, and the oxidation of the radical cation to the dication seems to affect mainly bond b due to the strengthening of the C-S bond (see Scheme 3.10 for bond labels).

Table 3.23 Summary of bond lengths of **3.8** and bond length changes for different oxidation states. The column headings indicate bonds as in Scheme 3.10. Bond length changes are compared to the bond lengths of **3.8**²⁺.

	a	Δa	b	Δb	c	Δc	d	Δd
3.8	1.346	-0.054	1.759	0.050	1.750	0.029	1.329	-0.013
3.8 ⁺ (Type A)*	1.351	-0.049	1.755	0.046	1.748	0.027	1.332	-0.011
3.8 ⁺ (Type B)*	1.395	-0.005	1.721	0.012	1.729	0.007	1.335	-0.008
3.8 ²⁺ Dication	1.400	—	1.709	—	1.721	—	1.343	—

*See CT salt **3.21** below.

With no π electrons in the central C-C bond keeping both TTF rings coplanar, a rotation of one of the rings relative to the other would be expected.^{215,216} It is not the case here, where the angle between both rings is about 1.58°, a reasonable value for a radical cation **3.8**⁺. The results of the charge transfer calculation for **3.17** are shown in Table 3.24. Both equations give results that are quite different to the expected charge for **3.17** based on the charge balance of the unit cell. The large uncertainty of the bond lengths caused by the poor quality of the diffraction data and the I₃⁻ disorder may contribute significantly to the error in this CT calculation. In our opinion the argument of charge neutrality prevails and the charge of the TTF moiety in this case is assigned as +2.

Table 3.24 CT calculations for **3.17**.

	Eq. (3.1)	Eq. (3.2)
3.8	+0.14	+0.12
3.17	+1.15	+1.22

3.4.5.2 X-ray characterization of the CT salt 3.21

The single crystal structure of the PF_6^- CT salt of the bipyridine derivative **3.8**, **3.21**, was determined from X-ray diffraction studies at 150 K. The asymmetric unit comprises one trimer of TTF-bipy donors and two PF_6^- counterions, Figure 3.28. This derivative crystallizes in the triclinic space group $P-1$, Figure 3.29 a). All TTF moieties are almost planar, with swivel angles at the S atoms in the range 0.1 – 5.0° . All bipyridine moieties have their pyridine rings in the *anti* conformation as observed in the crystal structure of the neutral donor **3.8**.

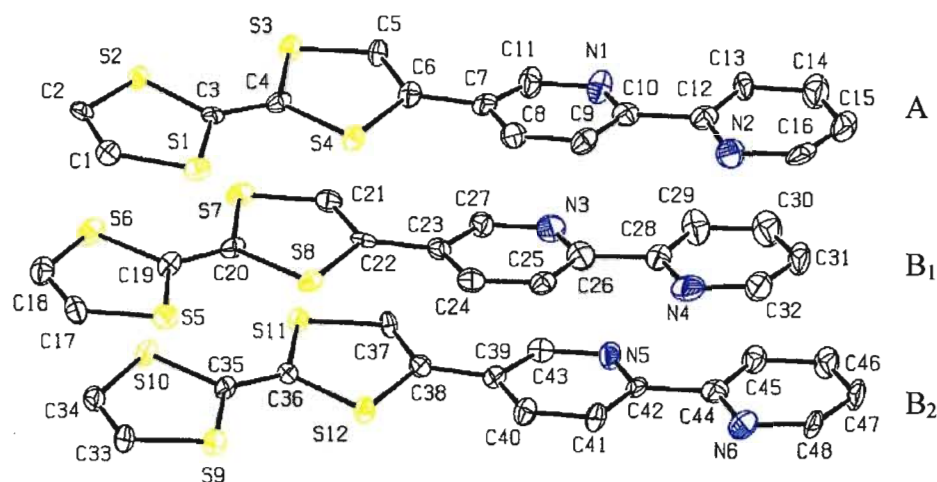


Figure 3.28 ORTEP plot of the asymmetric unit of **3.21**, showing the corresponding numbering scheme and type of donor A and B. Thermal ellipsoids plotted at 50% probability. Hydrogen atoms and PF_6^- counterions are omitted for clarity.

Close inspection of the bond lengths for each donor and the intratrimer distances indicates that there are two types of TTF moieties, type A and type B, which have different oxidation states, Figure 3.28. TTF moiety type A presents C=C and C-S bond lengths similar to those observed in neutral **3.8**, Figure 3.29 b). Also, the intrastack S...S distances involving this molecule are longer than the sum of the *van der Waals* radii for two sulfur atoms. All these observations seem to indicate that the oxidation state of this molecule is zero. On the other hand, for type B TTF moieties, the C=C and C-S bond lengths are longer and shorter respectively than those observed for the neutral donor **3.8**, as expected for an oxidized TTF molecule. The intrastack S...S distances between type B TTF moieties are also much shorter than the sum of their *van der Waals* radii, indicating

the formation of a B₁-B₂ dimer. Assuming that the type A donors are neutral, the presence of two counterions indicates that the type B donors are radical cations, each with a charge of +1. Selected bond lengths and bond angles for these donors are presented in Table 3.17.

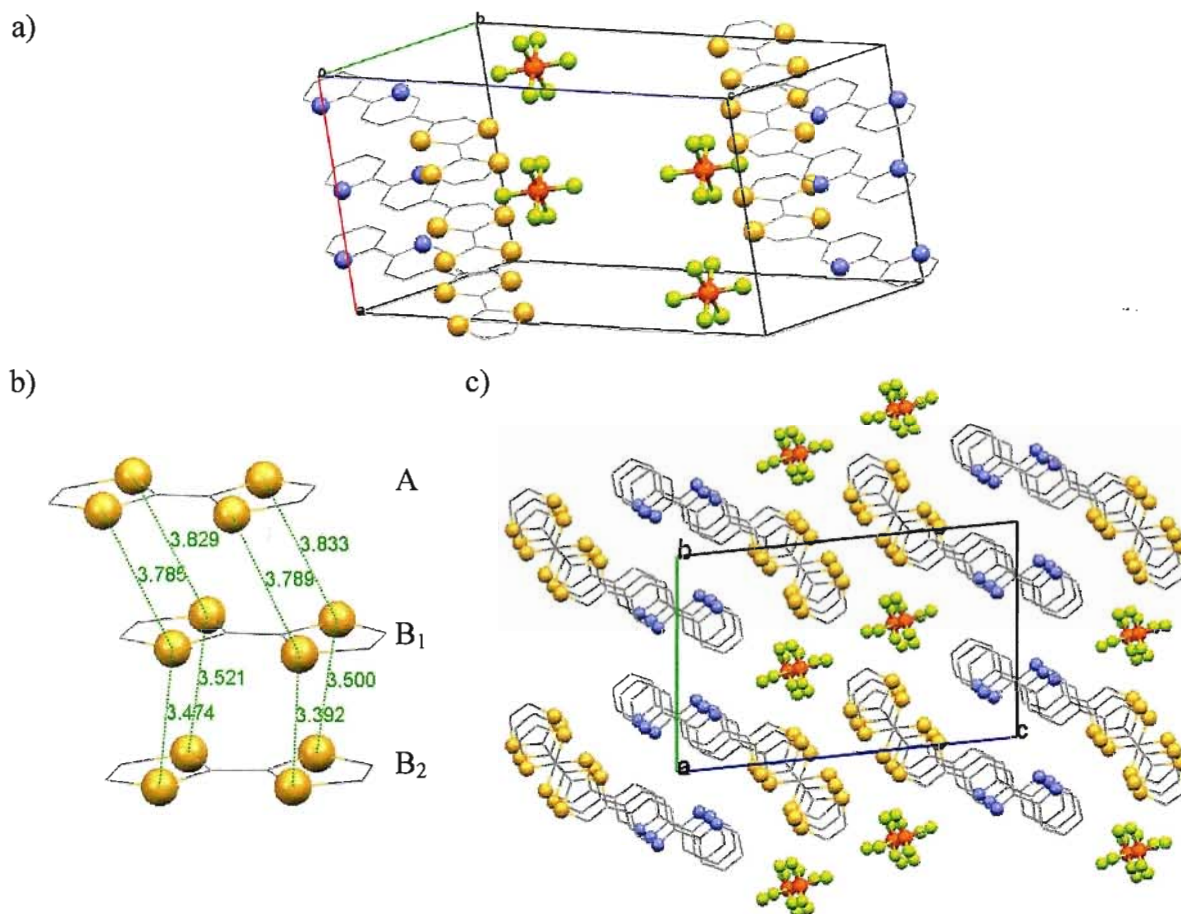


Figure 3.29 a) Unit cell of **3.21**, b) view of the intratrimer S...S distances shown as green dashed lines, distances are in Å c) view of the stacks down the *a*-axis.

For all three independent donors, the pyridine rings of the bipyridine moieties adopt an *anti* conformation and are almost coplanar, presenting dihedral angles in the range 2.0-6.1° between their respective best planes. The TTF and bipyridine moieties deviate from coplanarity, presenting a dihedral angle in the range of 8-11° between their respective best planes.

The trimers of donors pack in an offset stacking arrangement down the *a*-axis of the unit cell, Figure 3.29 c). The arrangement of the stacks is not regular due to the off-set

position of the type A monomer with respect to the type B dimer. The interstack S...S distances are longer than the sum of the *van der Waals* radii. The PF₆[−] anions occupy the space between the donors, forming segregated stacks.

Table 3.25 Selected bond lengths (Å) and angles (°) for **3.21**.

Bond lengths			
S1-C1	1.729(8)	S8-C20	1.727(7)
S1-C3	1.723(7)	S8-C22	1.762(7)
S2-C3	1.728(7)	C17-C18	1.319(11)
S2-C2	1.721(8)	C19-C20	1.394(11)
S3-C5	1.701(8)	C21-C22	1.350(10)
S3-C4	1.721(8)	C22-C23	1.462(11)
S4-C4	1.715(7)	S9-C33	1.738(8)
S4-C6	1.740(8)	S9-C35	1.751(7)
C1-C2	1.333(11)	S10-C34	1.739(8)
C3-C4	1.391(11)	S10-C35	1.770(7)
C5-C6	1.368(10)	S11-C36	1.742(7)
C6-C7	1.471(11)	S11-C37	1.740(7)
S5-C17	1.723(8)	S12-C36	1.756(7)
S5-C19	1.708(8)	S12-C38	1.775(8)
S6-C18	1.716(9)	C33-C34	1.319(11)
S6-C19	1.727(7)	C35-C36	1.351(10)
S7-C20	1.721(7)	C37-C38	1.344(10)
S7-C21	1.712(8)	C38-C39	1.460(10)
Bond angles			
C1-S1-C3	95.0(4)	C34-S10-C35	94.1(4)
C3-S2-C2	95.5(4)	C36-S11-C37	94.9(4)
C5-S3-C4	95.2(4)	C36-S12-C38	94.8(3)
C4-S4-C6	95.7(4)	S2-C3-S1	115.0(4)
C17-S5-C19	94.7(4)	S4-C4-S3	115.8(5)
C18-S6-C19	94.8(4)	S6-C19-S5	115.6(4)
C20-S7-C21	95.3(4)	S8-C20-S7	115.2(5)
C20-S8-C22	95.9(4)	S9-C35-S10	114.4(4)

Table 3.25 Continued.

Bond angles			
C33-S9-C35	95.0(4)	S11-C36-S12	115.4(4)
Dihedral angles			
C5-C6-C7-C11	-14.2(12)	N3-C26-C28-C29	2.8(12)
N1-C10-C12-C13	6.1(11)	C37-C38-C39-C43	-9.4(12)
C21-C22-C23-C27	-10.5(12)	N5-C42-C44-C45	2.0(11)

The results of the CT calculation for the three TTF donors (type A, type B) in the radical cation salt and the neutral donor **3.8** are shown in Table 3.26. The calculations support the observations from the crystal structure that the type A donor in the CT complex is neutral and the remaining type B donors are both radical cations each with a +1 oxidation state.

Table 3.26 CT calculation for **3.21**.

	Eq. (3.1)	Eq. (3.2)
3.8	+0.14	+0.12
Type A	+0.15	+0.23
Type B ₁	+0.99	+0.98
Type B ₂	+0.94	+1.10

3.4.5.3 X-ray characterization of the CT salt **3.22**

The molecular crystal structure of the radical cation salt **3.22** of the TTF-biphenyl donor **3.10** was determined from single crystal X-ray studies at 150 K. This CT salt is isostructural with the previously discussed bipyridine analogue **3.21**, and comprises of three independent **3.10** donors and two PF₆⁻ counterions in the asymmetric unit, Figure 3.30. The molecules also crystallize in the triclinic space group *P*-1, Figure 3.23 a). All three TTF moieties are almost planar, with swivel angles at the S atoms in the range 0.6-6.8°. The TTF and the phenyl ring attached to it present torsion angles in the range -0.2-6.0°. The aromatic rings of the biphenyl moiety are twisted away from coplanarity, showing dihedral angles in the range 27.4-30.7°.

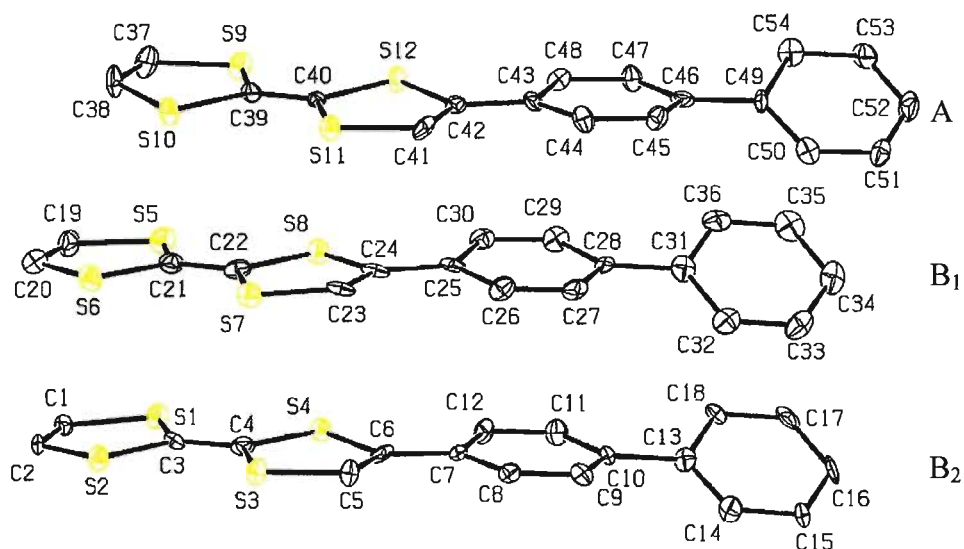


Figure 3.30 ORTEP plot of the asymmetric unit of **3.22**, showing the corresponding numbering scheme and type of donor A and B. Thermal ellipsoids plotted at 50% probability. Hydrogen atoms and PF_6^- anions are omitted for clarity.

Although the crystal structure of the neutral biphenyl derivative **3.10** is not available, the structural similarities between **3.21** and **3.22** indicate that, again, the structure presents two types of TTF moieties, type A and type B, with different oxidation states, Figure 3.30. The type A TTF moiety presents C=C and C-S bond lengths similar to those observed in neutral TTF and to the type A monomer in **3.21**. Also, the intrastack S...S distances of this derivative molecule are longer than the sum of the *van der Waals* radii for sulfur. Based on these observations an oxidation state of zero can be assigned for this type of TTF moiety. The lengthening and shortening of the C=C and C-S bonds, respectively, in the type B TTF moieties can be attributed to an oxidized TTF molecule. The intrastack S...S distances between type B TTF moieties are also much shorter than the sum of the *van der Waals* radii, indicating that B₁ and B₂ form a dimer. Assuming that the type A TTF moieties are not oxidized, the presence of two counterions indicates that the oxidation state of each of the type B TTF moieties is +1. See Table 3.27 for selected bond lengths and bond angles.

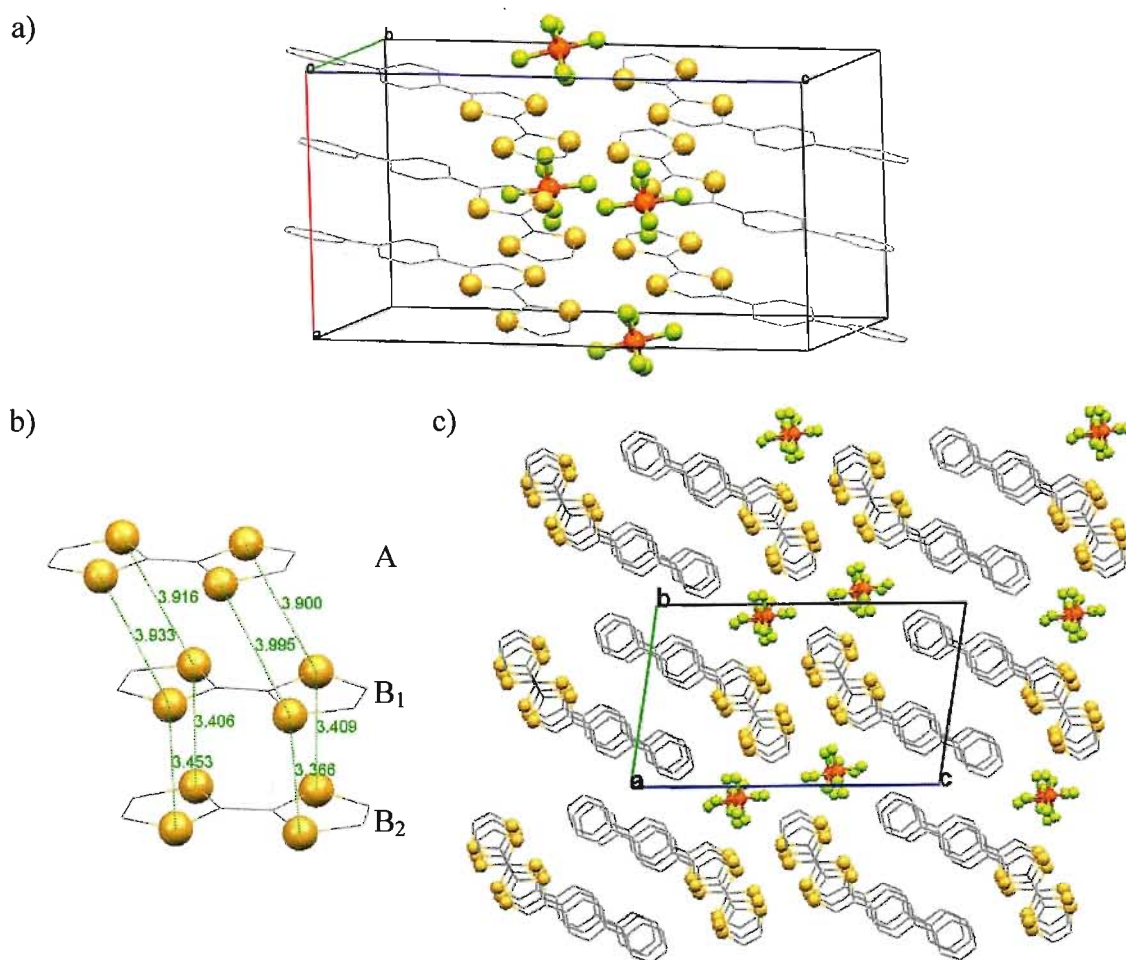


Figure 3.31 a) Unit cell of **3.22**, b) view of the intratrimer S...S distances shown as green dashed lines, distances are in Å, c) view of the stacks in **3.22** down the *a*-axis. The disorder of the PF₆⁻ anions is not shown.

As in **3.21**, the trimers in the CT salt **3.22** form slightly slanted stacks down the *a*-axis. The arrangement of the stacks is not regular due to the off-set position of the type A monomer respect the type B dimer. The stacks present no interstack short contacts other than the ones present in the type B dimers, and the interstack S...S distances are longer than the sum of the *van der Waals* radii. The PF₆⁻ anions occupy the space between the donors, forming segregated stacks.

Table 3.27 Selected bond lengths (Å) and angles (°) for **3.22**.

Bond lengths			
S1-C1	1.727(8)	S8-C22	1.730(9)
S1-C3	1.731(8)	S8-C24	1.762(9)
S2-C3	1.722(8)	C19-C20	1.353(12)
S2-C2	1.731(8)	C21-C22	1.373(12)
S3-C5	1.714(8)	C23-C24	1.335(11)
S3-C4	1.720(8)	C24-C25	1.454(12)
S4-C4	1.727(8)	S9-C37	1.737(9)
S4-C6	1.762(8)	S9-C39	1.756(8)
C1-C2	1.325(12)	S10-C38	1.754(9)
C3-C4	1.372(11)	S10-C39	1.765(8)
C5-C6	1.355(11)	S11-C40	1.765(8)
C6-C7	1.457(12)	S11-C41	1.739(9)
S5-C19	1.730(9)	S12-C40	1.755(8)
S5-C21	1.716(8)	S12-C42	1.760(8)
S6-C20	1.727(9)	C37-C38	1.319(12)
S6-C21	1.728(9)	C39-C40	1.341(11)
S7-C22	1.723(8)	C41-C42	1.352(12)
S7-C23	1.705(9)	C42-C43	1.467(12)
Bond angles			
C1-S1-C3	95.6(4)	C38-S10-C39	94.1(4)
C3-S2-C2	95.3(4)	C40-S11-C41	94.2(4)
C5-S3-C4	95.9(4)	C40-S12-C42	95.9(4)
C4-S4-C6	96.0(4)	S2-C3-S1	114.6(5)
C19-S5-C21	95.8(4)	S4-C4-S3	115.0(5)
C20-S6-C21	96.1(4)	S6-C21-S5	114.9(5)
C22-S7-C23	95.9(4)	S8-C22-S7	114.2(5)
C22-S8-C24	96.2(4)	S9-C39-S10	114.4(5)
C37-S9-C39	95.0(4)	S11-C40-S12	114.8(5)
Dihedral angles			
C5-C6-C7-C8	0.3(13)	C27-C28-C31-C32	27.4(12)
C9-C10-C13-C14	29.0(12)	C41-C42-C43-C45	-4.0(14)
C23-C24-C25-C26	8.7(13)	C45-C46-C49-C50	30.8(12)

One of the PF_6^- counterions in the structure shows some minor disorder. Figure 3.32 shows the counterion that presents no disorder (a) and the disordered counterion (b). The disorder was refined as a positional disorder, with 63% of the PF_6^- ions on that site occupying one position and 37% occupying the other position. All the intramolecular distances of the anions were restrained using a DFIX command in SHELX in order to maintain a chemically reasonable geometry during the refinement process. Although the model seemed reasonable, the refinement of the electronic density to obtain an anisotropic model was not stable, so both components of the disorder were left isotropic.

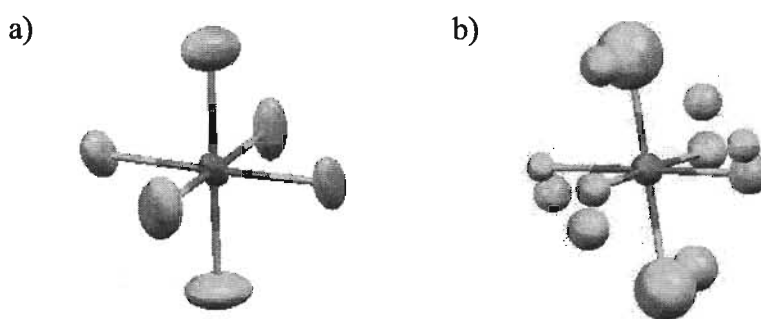


Figure 3.32 The PF_6^- counterions in the structure of **3.22**: a) anisotropic PF_6^- showing no disorder, b) isotropic PF_6^- showing the positional disorder of fluoride atoms as small green spheres not bonded to the central phosphorus atom.

The results of the charge transfer calculation for the type A and type B TTF derivatives are shown on Table 3.28. The charges of the type A TTF moieties are overestimated by equation (3.2), whereas both equations give charges close to the expected value for the type B TTF moieties.

Table 3.28 CT calculations for **3.22**.

	Eq. (3.1)	Eq. (3.2)
3.8	+0.14	+0.12
Type A	+0.06	+0.25
Type B ₁	+0.81	+0.88
Type B ₂	+0.82	+0.95

3.4.6 Additional characterization of the CT salts 3.19-3.22

The UV-Vis spectra of an acetonitrile solution of the CT salts **3.19-3.22** are shown in Figure 3.33. The presence of a neutral TTF derivative and two radical cation molecules in the asymmetric unit of these salts results in the superimposition of the spectra of both species. The band at $\lambda = 275$ nm corresponds to the overlapped local transitions of TTF (neutral and radical cation) and the corresponding *bis*-aryl or cyanopyridyl moieties. The bands at $\lambda = 425$, 450 and 640 nm are indicative of the presence of the radical cation species,^{213,214} although the band at longer wavelengths is also overlapped with the corresponding ICT band. The spectrum of **3.19** presents a very strong band at $\lambda = 260$ nm, which partially overlaps with the TTF and the cyanopyridyl band. This band is not present for any other electrocrystallized CT salt, and we would tentatively assign it to a high energy transition usually over $\lambda = 200$ nm that has become stabilized due to the extended π conjugation of the donor.

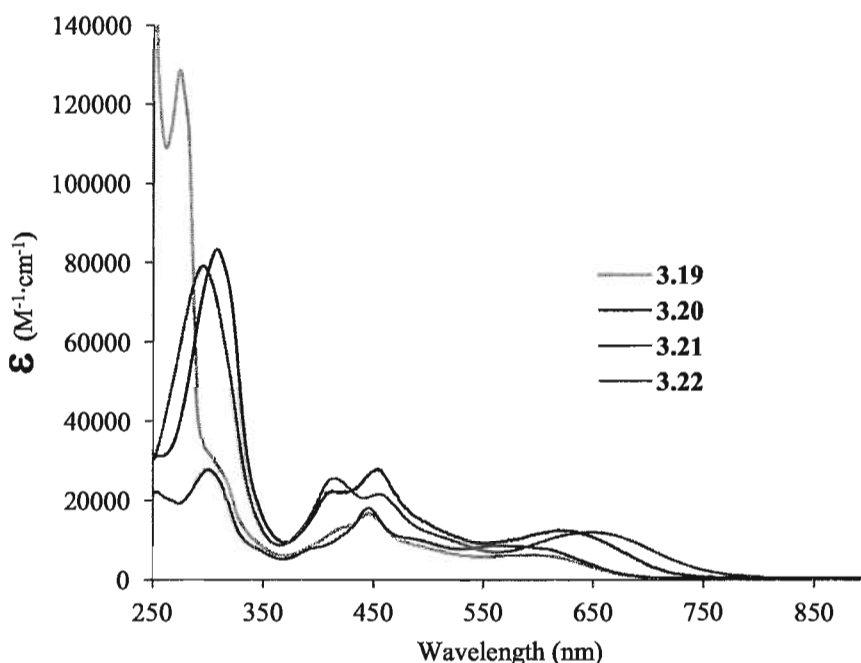


Figure 3.33 UV-Vis spectra of 10^{-5} M solutions of CT salts **3.19-3.22** in acetonitrile.

Powder samples of CT salts **3.19**, **3.20**, **3.21** and **3.22** were pressed into pellets and their electrical conductivities were measured in the range 77-293K, Table 3.29. All

the samples display semiconducting behaviour with conductivities ranging 2.94×10^{-7} to $1.960 \times 10^{-3} \text{ S cm}^{-1}$ at room temperature. Although no crystal structure is available for **3.19** and **3.20**, the similar composition of these CT salts to the composition of **3.21** and **3.22** makes it reasonable to assume the presence of mixed valence trimers of derivatives in the cyanopyridyl CT salts. This would explain the similar electrical conductivities, and the semiconducting behaviour could be explained by the presence of a neutral donor in the trimer. The much lower conductivity of **3.22** can be explained by the longer distances between the neutral donor and its neighbours, caused by the twist present in the biphenyl ring.

Table 3.29 Electrical conductivity measurements (S cm^{-1}) at room temperature of pressed pellets of the CT salts **3.19**, **3.20**, **3.21** and **3.22**.

	Conductivity
3.19	1.960×10^{-3}
3.20	8.255×10^{-4}
3.21	1.490×10^{-3}
3.22	2.940×10^{-7}

3.5 Conclusions

A series of π -extended TTF derivatives have been synthesized and fully characterized. The crystal structure of derivatives **3.2-3.5** is controlled by the substitution of the cyanopyridyl moieties and not simply by the overall shape of the molecule. This is clearly visible for the pairs **3.2/3.4** and **3.3/3.5**. Although in the pair **3.2/3.4** the TTF moiety is *para* respect of the CN group the derivatives stack in parallel and antiparallel arrangements respectively. For the couple **3.3/3.5** the crystal structure transitions from regular stacks of antiparallel derivatives to slipped stacks. The redox potential of these derivatives can be tuned depending on the nature of the substituents appended to the TTF donor. Derivatives **3.2-3.5** and **3.8** crystallize in a flat conformation, which is very desirable for the formation of stacks once the donors have been oxidized. The UV-Vis spectra of derivatives **3.2-3.10** present an ICT band, indicative of the transfer of electron density from the TTF donor moiety to the aryl acceptor moiety. In derivatives **3.2-3.5**, the position of the ICT band is influenced by the relative position of the electron withdrawing

CN and N_{pyridine} in the pyridine ring. The CN str frequency shifts to higher frequencies as the ICT band moves to shorter wavelengths, indicating a strengthening of the CN bond as the energy necessary for the ICT process increases. Oxidation of derivatives **3.2-3.4** and **3.8** with iodine afforded the CT salts **3.15a-c**, **3.16a**, **3.16b** and **3.18a-c**. The UV-Vis characterization of solutions of **3.15c**, **3.16a**, **3.18b**, **3.18c** shows the expected bands for a TTF radical cation. X-ray characterization of **3.15a**, **3.16a** and **3.17** shows the presence of TTF dimers in the solid state. Variable temperature conductivity measurements between 77 and 293 K of the CT salts **3.15c**, **3.16a**, **3.18b** and **3.18c** revealed that these salts display semiconducting behaviour with conductivities ranging from 1.852×10^{-7} to $9.620 \times 10^{-3} \text{ S cm}^{-1}$ at room temperature. The CT salts **3.19-3.22** were successfully electrocrystallized. The UV-Vis characterization of these CT salts in solution shows the expected bands for a TTF radical cation. The crystal structures of **3.21** and **3.22** show that these two CT salts are isostructural and pack in stacks formed by trimers of donors. CT calculations based on the bond lengths of TTF show the presence of two donors with a +1 charge and one neutral donor in the trimer. Variable temperature conductivity measurements between 77 and 293 K on **3.19-3.22** show that these salts display semiconducting behaviour with conductivities ranging from 2.94×10^{-7} to $1.960 \times 10^{-3} \text{ S cm}^{-1}$ at room temperature. In conclusion, we have prepared a series of structurally related π -extended derivatives of TTF. All the neutral derivatives adopt a planar conformation in the solid state, and the CT salts studied by X-ray diffraction present regular stacks of dimers or trimers of functionalized TTF donors. This is a very encouraging result, as the formation of stacks of donors is desirable for the preparation of TTF-based organic molecular conductors. The preparation of CT salts of these donors using different counterions and in different conditions will be necessary in order to achieve higher electrical conductivities.

CHAPTER 4

Synthesis and characterization of a family of electroactive TTF-based transition metal complexes

4.1 Introduction

As mentioned in Chapter 1, the *through bond* approach for the preparation of molecular materials, presenting interplay between electrical conductivity and magnetism, consists of having π - and d -magnetic spins coexisting within one molecular entity. Therefore, it is necessary to design the appropriate molecular architectures in order to: i) maximize the exchange coupling between both kinds of spins, ii) present a conduction pathway in the solid state that will allow for the movement of π -itinerant electrons that gives rise to electrical conductivity. In the literature we can find examples of stable families of π -radicals such as include nitronyl nitroxide,^{217,218} verdazyl,^{218,219} DTDA (1,2,3,5-dithiadiazolyl)^{218,220,221} or 3,5-di-tert-butyl-*o*-quinone,^{218,222} Figure 4.1. Some members of these families have been synthetically modified for the chelation of paramagnetic transition metal ions. The resulting complexes usually present extremely desirable large exchange coupling constants between the spins of the itinerant electrons and the spins of the d electrons, but usually these radicals are often sterically hindered to keep them from dimerizing in the solid state.^{217,218,220-222}

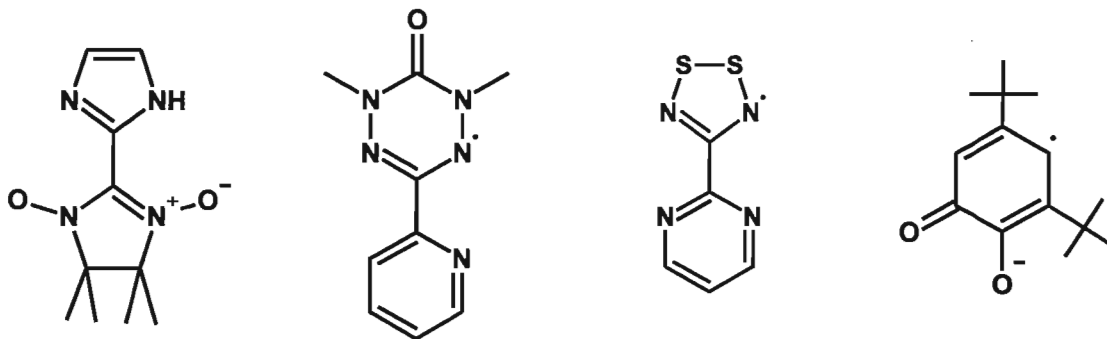
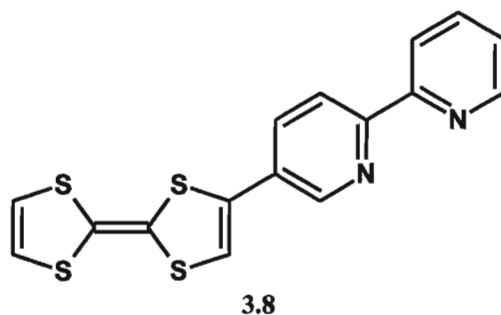


Figure 4.1 Sample radical ligands. From left to right: nitronyl nitroxide, verdazyl, DTDA and 3,5-di-tert-butyl-*o*-quinone.

As discussed in previous Chapters, TTF is well known for the formation of conductive salts in which the presence of conduction pathways for π -electrons gives rise to semiconductor, metal or superconductor behaviour.⁵ TTF does not have any binding sites that can coordinate directly to transition metal cations. With this challenge in mind, we have prepared the ligand **3.8**. The goal of this research project was to exploit the coordination chemistry of this donor ligand. We report herein the crystallographic, electronic and spectroscopic study of a new family of coordination complexes with this ligand.

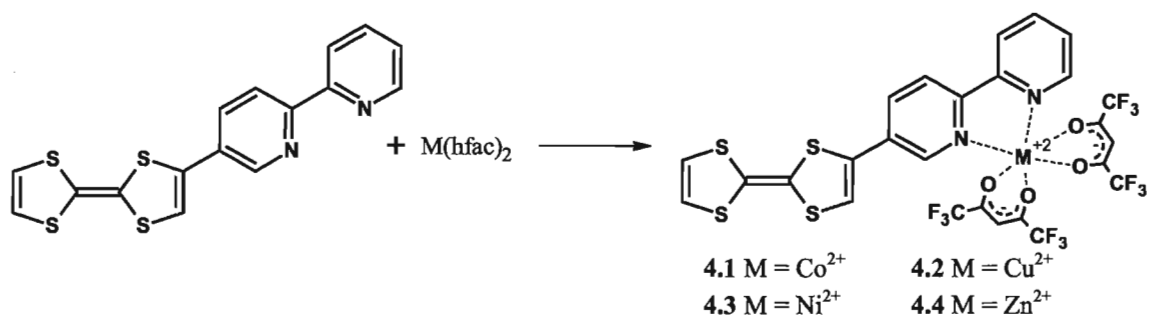


A review of the literature reveals that there are examples of bipyridine-based stable radicals displaying exchange coupling with coordinated metal centres *via* a spin polarization mechanism.¹⁴⁹⁻¹⁵¹ The complexes presented below are the precursors to systems presenting π and d magnetic spins upon oxidation of the TTF donor.

4.2 Coordination of **3.8** and characterization of complexes 4.1-4.4

4.2.1 Coordination of ligand **3.8**

Coordination of **3.8** to the hfac salts of paramagnetic transition metal ions was carried out by mixing equimolar THF solutions of the corresponding salts and refluxing the reaction mixture overnight, Scheme 4.1. In all cases the reaction products were isolated as solids and recrystallized from acetonitrile, giving analytically pure polycrystalline samples in reasonable yields.



Scheme 4.1 Reaction scheme for the preparation of **4.1-4.4**. Reagents and conditions: 1.0 eq. M(hfac)₂, THF, reflux, overnight.

We chose hfac salts since the hfac ligand would block four of the coordination sites of an octahedral metal centre, disavouring the self assembly of polynuclear complexes. We considered that the size of an hfac mononuclear complex would allow the donor complexes to stack, yet the steric hindrance of the hfac ligands would minimize magnetic interactions between metal centres by keeping them separated. The final objective of this project is the preparation of the radical cation CT salts of the complexes **4.1-4.4**. Oxidation of the TTFs derivatives to afford the CT salts **4.1⁺-4.4⁺** would be carried out chemically or electrochemically. The magnetic characterization of the resulting salts would also be simplified due to the magnetically isolated nature of the transition metal centres.

4.2.2 Single-crystal X-ray diffraction

4.2.2.1 Characterization of complex 4.1

Purple needles of the Co²⁺ complex **4.1** suitable for single crystal X-ray diffraction were obtained by slow evaporation of a THF solution. The crystal structure of the complex was determined at 150 K, Figure 4.2 a). The complex crystallizes in the triclinic space group *P*-1, with one crystallographically independent molecule in the unit cell, Figure 4.2 b). The neutral TTF moiety adopts a boat-like conformation similar to the conformation of the free ligand. The bipyridine and TTF moieties are almost coplanar, presenting an torsion angle of about 5.6°. The bipyridine ligand chelates the Co²⁺ ion through the lone pairs on its pyridine nitrogens. The Co²⁺ adopts a distorted octahedral

geometry that is completed by the four oxygen ligands from two hfac ligands. See Table 3.10 for selected bond lengths and angles.

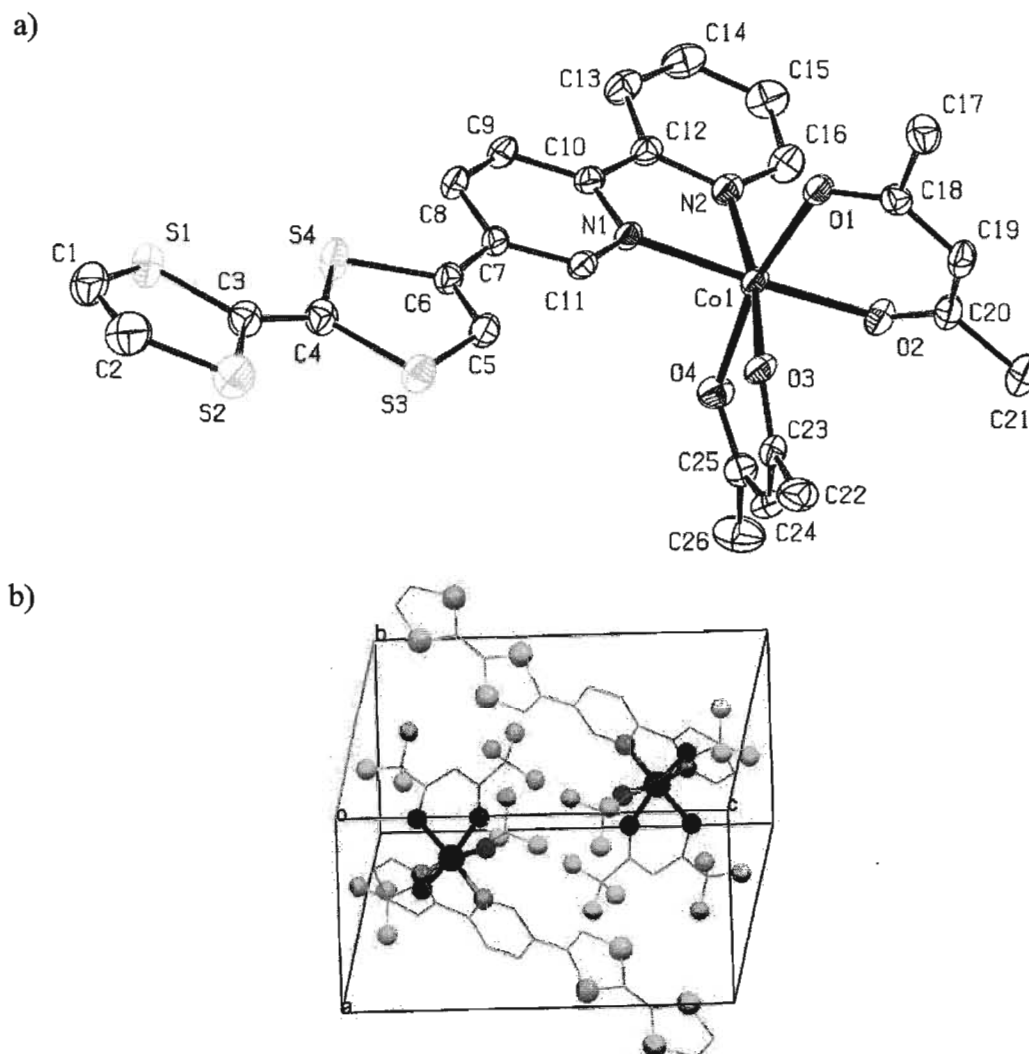


Figure 4.2 a) ORTEP plot of the molecular structure of **4.1** showing the corresponding numbering scheme, b) unit cell of **4.1**. Thermal ellipsoids plotted at 50% probability. Hydrogen and fluorine atoms are omitted for clarity.

Table 4.1 Selected bond lengths (Å) and angles (°) for complex **4.1**.

Bond lengths			
Co1-N1	2.0868(18)	S2-C2	1.743(3)
Co1-N2	2.0973(19)	S3-C5	1.724(2)
Co1-O1	2.0783(15)	S3-C4	1.763(2)
Co1-O2	2.0481(15)	S4-C4	1.760(2)
Co1-O3	2.0713(15)	S4-C6	1.764(2)
Co1-O4	2.0994(15)	C1-C2	1.325(4)
S1-C1	1.738(3)	C3-C4	1.337(3)
S1-C3	1.761(3)	C5-C6	1.339(3)
S2-C3	1.762(3)	C6-C7	1.465(3)
Bond angles			
O1-Co1-N1	92.98(6)	O1-Co1-N2	95.41(7)
O3-Co1-N1	92.98(6)	O2-Co1-O4	82.56(6)
N1-Co1-N2	77.61(7)	O3-Co1-O4	86.31(6)
O4-Co1-N1	98.22(7)	C1-S1-C3	94.56(19)
O4-Co1-N2	93.82(7)	C3-S2-C2	94.68(19)
O2-Co1-N2	97.26(7)	C5-S3-C4	94.87(18)
O2-Co1-O1	86.91(6)	C4-S4-C6	95.84(18)
O3-Co1-O1	86.08(6)	S2-C3-S1	114.5(2)
O2-Co1-O3	91.87(6)	S4-C4-S3	114.2(2)
Dihedral angles			
C5-C6-C7-C11	5.6(4)	N1-C10-C12-N2	4.4(3)

Complex **4.1** stacks in a head-to-tail arrangement of dimers that run down the *a*-axis of the unit cell, Figure 4.3 a) and b). The dimers present short contacts between C9...C7a and C12...C5a of 3.398(9) and 3.376(7) Å respectively. The shortest distance between the best planes of the **3.8** ligand within a dimer is 3.70 Å, indicating the presence of weak π - π stacking interactions. The shortest distance between paramagnetic metal centres is the interdimer Co...Co distance of 8.688(6) Å, with a slightly longer Co...Co intradimer distance of 8.904(6) Å. Based on these distances, we can anticipate that any magnetic interaction between paramagnetic metal centres would be weak at best. Due to the head-to-tail arrangement of the complex molecules, all of the observed S...S distances

in the crystal structure are longer than the sum of their respective *van der Waals* radii. The chelated part of the molecule together with the two hfac ligands occupy the spaces between the stacks of TTF derivatives, Figure 4.3 c). This is reminiscent of the stacking of radical cation salts of unsubstituted TTF donors, where the anions occupy channels between stacks of TTF donors. This coordination mode prevents any lateral interstack S...S short contacts.

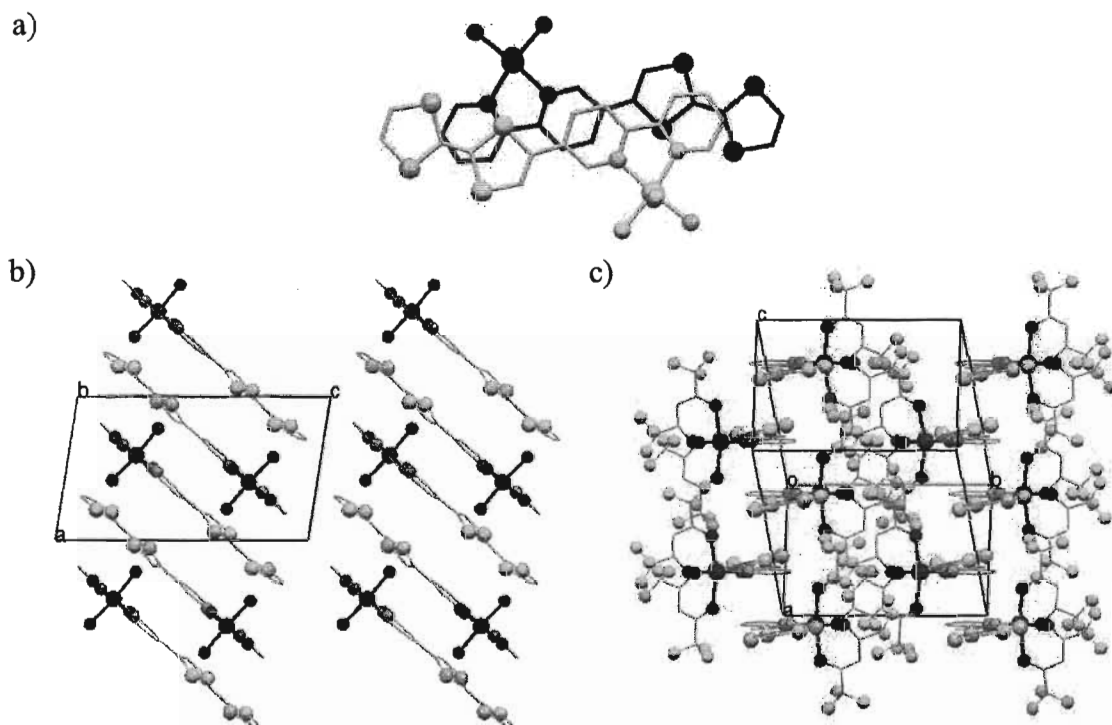


Figure 4.3 a) Top view of a dimer of **4.1**, showing the green molecule is on top of the red molecule. b) View of the slanted stacks of TTF dimers on the *ac* plane, c) view of the same slanted stacks along the *b*-axis showing the chelated Co^{2+} centered occupying the space between adjacent stacks of donors. Hfac ligands omitted when necessary for clarity, except for their oxygen atoms. Hydrogen atoms are omitted for clarity.

4.2.2.2 Characterization of complex 4.2

Slow cooling of a saturated acetonitrile solution of the Cu^{2+} complex **4.2** afforded dark red needles suitable for X-ray diffraction. The crystal structure of **4.2** was determined at 150 K, Figure 4.4. This complex is isostructural with complex **4.1**, crystallizing also in the triclinic space group *P*-1, and presents one crystallographically independent molecule in the unit cell, Figure 4.5 a). Once again the TTF moiety adopts a

boat-like conformation similar to the conformation of the free ligand. The bipyridine and TTF moieties are almost coplanar, presenting a rotation angle of 10.3° . The Cu^{2+} ion is chelated by the bipyridine ligand and its distorted octahedral coordination sphere is completed by two hfac ligands. The axial Cu-O bonds are much longer than the equatorial ones due to the *Jahn-Teller* distortion, with bond lengths of 2.294(3) and 2.360(3) Å for the axial bonds and 1.960(2) and 1.975(2) Å for the equatorial Cu-O bonds. See Table 4.2 for selected bond lengths and angles.

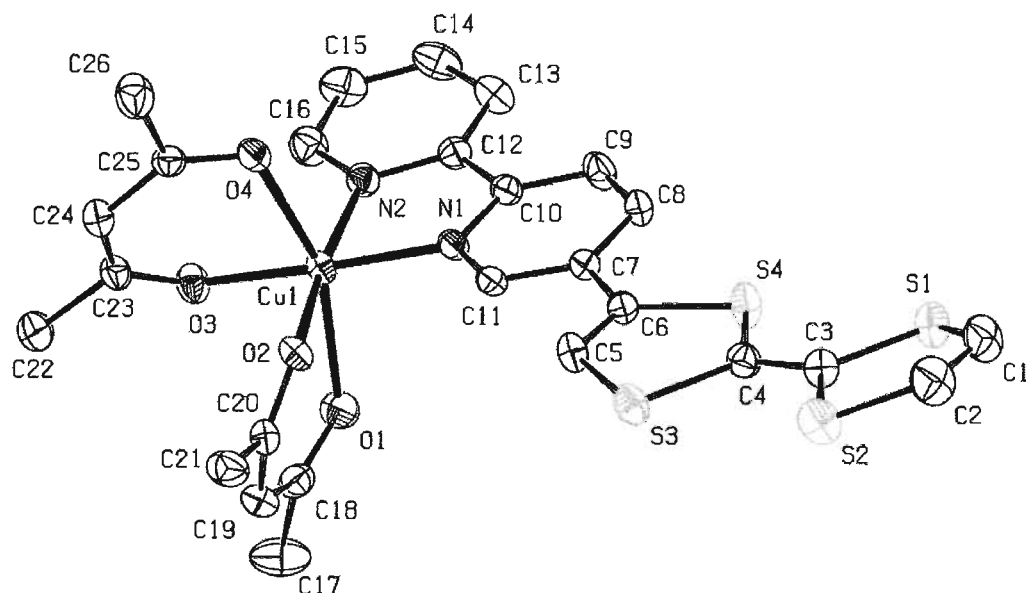


Figure 4.4 ORTEP plot of the molecular structure of **4.2** showing the corresponding numbering scheme. Thermal ellipsoids plotted at 50% probability. Hydrogen and fluorine atoms are omitted for clarity.

Table 4.2 Selected bond lengths (Å) and angles (°) for complex **4.2**.

Bond lengths			
Cu1-N1	1.985(3)	S2-C2	1.741(4)
Cu1-N2	1.990(3)	S3-C5	1.730(4)
Cu1-O1	2.361(2)	S3-C4	1.755(3)
Cu1-O2	1.975(2)	S4-C4	1.753(3)
Cu1-O3	1.960(2)	S4-C6	1.754(3)
Cu1-O4	2.294(2)	C1-C2	1.316(6)
S1-C1	1.739(4)	C3-C4	1.343(5)
S1-C3	1.752(3)	C5-C6	1.337(5)
S2-C3	1.756(3)	C6-C7	1.463(5)
Bond angles			
O1-Cu1-N1	100.92(10)	O1-Cu1-N2	97.11(10)
O3-Cu1-N1	175.08(11)	O2-Cu1-O4	83.98(9)
N1-Cu1-N2	81.28(11)	O3-Cu1-O4	85.21(9)
O4-Cu1-N1	95.64(10)	C1-S1-C3	94.01(17)
O4-Cu1-N2	96.87(10)	C3-S2-C2	94.06(18)
O2-Cu1-N2	173.05(10)	C5-S3-C4	94.49(16)
O2-Cu1-O1	83.91(9)	C4-S4-C6	95.06(16)
O3-Cu1-O1	79.29(9)	S2-C3-S1	114.48(19)
O2-Cu1-O3	93.14(10)	S4-C4-S3	114.52(19)
Dihedral angles			
C5-C6-C7-C11	-10.3(5)	N1-C10-C12-N2	0.5(4)

Complex **4.2** forms head-to-tail dimers that stack down the a -axis, much like complex **4.1**. Image b) of Figure 4.5 shows the slanted stacks of dimers in the ac planes of the crystal structure. The distance between the best planes of the **3.8** ligand within a dimer is ca. 3.48 Å, indicative of weak π - π interactions. This structure presents no short contacts between complex molecules in a stack. In this structure the shortest Cu...Cu distance is 8.5656(8) Å. This distance is slightly shorter than the shortest Co...Co distance of **4.1**, of 8.688(6) Å, but still long enough to anticipate weak magnetic interaction at most between neighbouring paramagnetic metal centres.

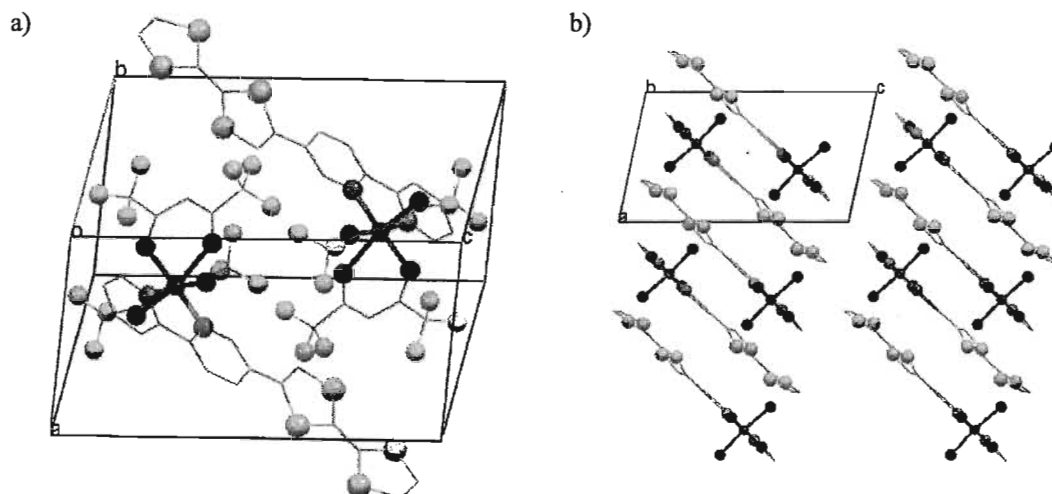


Figure 4.5 a) Unit cell of complex 4.2, b) view of the slanted stacks on the *ac* plane. Hfac ligands omitted when necessary for clarity, with the exception of their oxygen atoms. Hydrogen atoms are omitted for clarity.

As can be seen in image b) from Figure 4.5, the head-to-tail arrangement of the complex molecules and the steric hindrance of the hfac ligands keep all TTF moieties far from each other. As a consequence all of the S...S distances in the crystal structure are longer than the sum of their *van der Waals* radii.

4.2.2.3 Characterization of complex 4.3

Slow cooling of a saturated acetonitrile solution of the Ni^{2+} complex 4.3 afforded purple needles suitable for X-ray diffraction. The crystal structure of 4.3 was determined at 150 K. This complex crystallizes in the triclinic space group *P*-1, with two crystallographically independent molecules and two acetonitrile solvent molecules in the unit cell, Figure 4.6 a). A view of the unit cell of 4.3 is presented in Figure 4.6 b).

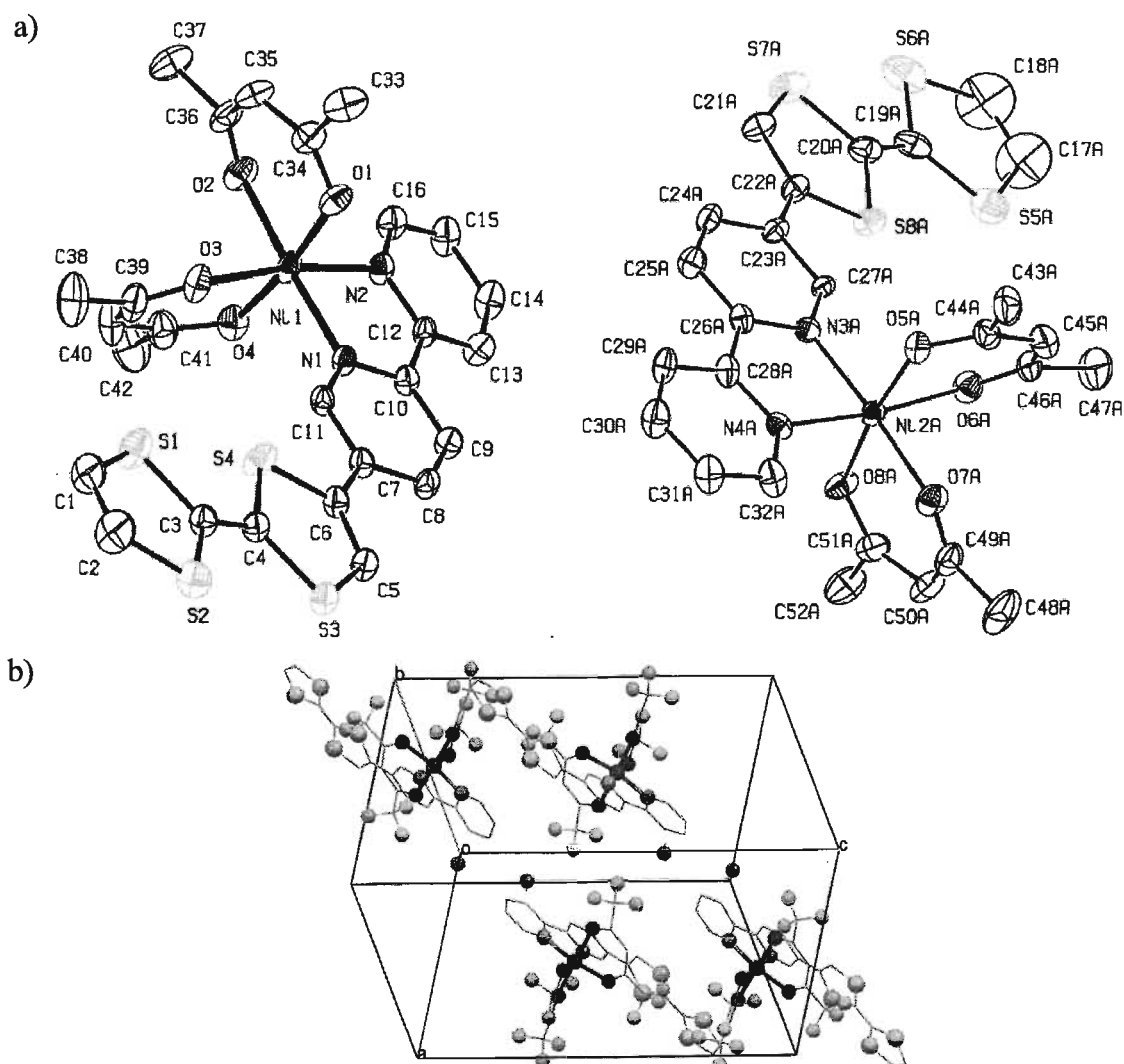


Figure 4.6 a) ORTEP plot of the molecular structure of the two independent molecules of **4.3** showing the corresponding numbering scheme. b) Unit cell of **4.3**. No disorder shown for clarity. Thermal ellipsoids plotted at 50% probability. Hydrogen and fluorine atoms are omitted for clarity.

One of the two complex molecules in the asymmetric unit is disordered over two positions. This positional disorder was not obvious during the first stages of the structure refinement. Although initially the two molecules in the asymmetric unit had all of their atoms located and all atoms seemed to be properly assigned, the value of the refinement parameter $R_1 = 0.193$ was not satisfactory. Close inspection of the additional electron density peaks close to one of the TTF moieties revealed the presence of a group of seven electron density peaks, shown with blue labels in image a) of Figure 4.7, whose arrangement looks like an incomplete and misshapen TTF molecule.

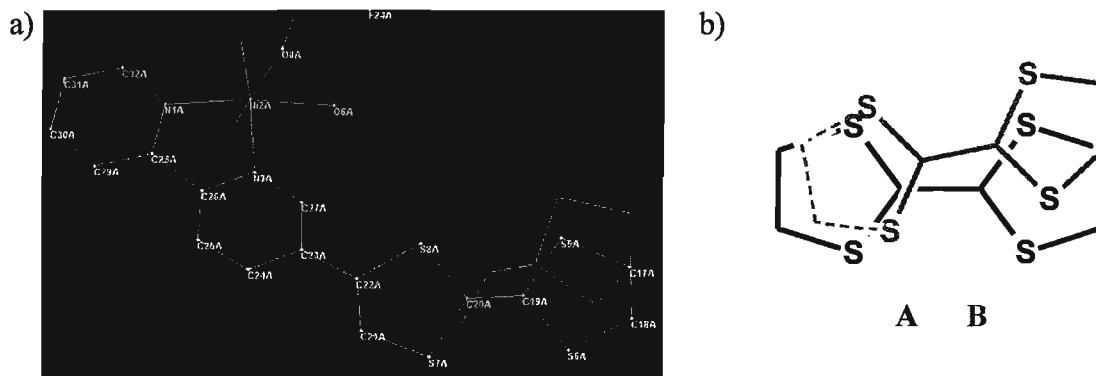


Figure 4.7 a) Image showing in blue the first signs of B component during refinement of **4.3**, overlapped with the A component of the disorder. b) Diagram showing the overlap of TTF-A with an incomplete, misshapen TTF-B (right).

The additional electron density pointed to the presence of extended disorder between two positions of one Ni^{2+} complex. After applying geometrical constraints to the disordered molecule, the refinement of the structure gave an improved $R_1 = 0.0938$ with an occupancy factor for the disorder of 75%. The complex showing the remaining 25% of the occupancy factor was left isotropic during refinement in order to reach a stable solution. Refinement of the disorder afforded a better final structure, with minimized errors to the bond lengths and angles.

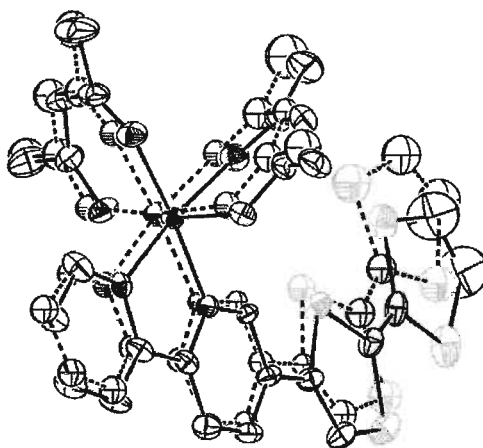


Figure 4.8 Overlapped component of the disorder A (solid bonds) and B (dashed bonds) of **4.3**. Thermal ellipsoids plotted at 50% probability. Hydrogen and fluorine atoms are omitted for clarity.

Despite the fact that both molecules in the asymmetric unit are crystallographically independent, they have some general structural traits in common.

The TTF moieties in both complexes adopt a boat-like conformation. In contrast with **4.1** and **4.2**, the ligand molecules in **4.3** have the TTF moiety oriented towards the side of the metal complex, Figure 4.9 a). The anisotropically refined complex presents a rotation of 18.56(12)° between the best planes of the bipyridine and TTF donors, making them almost coplanar. In both complexes, the Ni²⁺ ion is chelated by the bipyridine, and its distorted octahedral coordination sphere is completed by two hfac ligands. See Table 4.3 for selected bond lengths and angles of the anisotropic molecule.

Table 4.3 Selected bond lengths (Å) and angles (°) for the molecule of **4.3** showing no disorder.

Bond lengths			
Ni1-N1	2.044(4)	S2-C2	1.755(7)
Ni1-N2	2.053(4)	S3-C5	1.735(5)
Ni1-O1	2.057(4)	S3-C4	1.760(5)
Ni1-O2	2.026(4)	S4-C4	1.753(5)
Ni1-O3	2.046(4)	S4-C6	1.755(5)
Ni1-O4	2.048(4)	C1-C2	1.319(9)
S1-C1	1.717(6)	C3-C4	1.336(7)
S1-C3	1.770(5)	C5-C6	1.345(7)
S2-C3	1.748(5)	C6-C7	1.463(6)
Bond angles			
O1-Ni1-N1	176.47(16)	O1-Ni1-N2	97.10(17)
O3-Ni1-N1	93.55(15)	O2-Ni1-O4	84.64(17)
N1-Ni1-N2	79.40(16)	O3-Ni1-O4	89.34(16)
O4-Ni1-N1	95.78(17)	C1-S1-C3	95.7(3)
O4-Ni1-N2	86.22(17)	C3-S2-C2	94.1(3)
O2-Ni1-N2	97.14(16)	C5-S3-C4	95.4(2)
O2-Ni1-O1	176.47(16)	C4-S4-C6	96.2(2)
O3-Ni1-O1	88.26(16)	S2-C3-S1	114.1(3)
O2-Ni1-O3	89.96(16)	S4-C4-S3	113.9(3)
Dihedral angles			
C5-C6-C7-C8	-5.8(9)	N1-C10-C12-N2	8.7(7)

The crystal packing of complex **4.3** shows that, once again, the coordinated TTF donors stack in a head-to-tail arrangement of dimers that run down the *c*-axis of the unit cell, Figure 4.9 b). In this case, dimers of disordered complex molecules alternate with dimers of non-disordered complex molecules to form a stack. The shortest intradimer distance between the best planes of the **3.8** ligands is ca. 3.34 Å, and π - π stacking interactions give rise to short contacts between C9...C7a and C12...C5a of 3.398(9) and 3.376(7) Å respectively, Figure 4.10. Although it is not possible to measure with certainty the intradimer distance for the disordered dimers, a tentative approximation made by measuring the distance between the best planes of the anisotropically refined complex molecules of **4.3** gives a distance of 3.46 Å. Also, measured in a tentative manner, short contacts of about 3.30 Å present between the TTF and bipyridine moieties of neighbouring ligands are consistent with the presence of π - π stacking interactions within the dimer. The high degree of coplanarity between both components of the disorder makes this distance a good estimate for the intradimer distance for the dimers of disordered complex molecules. The shortest interdimer distance between the two independent molecules is 3.54 Å. The head-to-tail arrangement of the complexes and the bulkiness of the hfac ligands force all S...S distances beyond the *van der Waals* threshold for short contacts in the crystal structure.

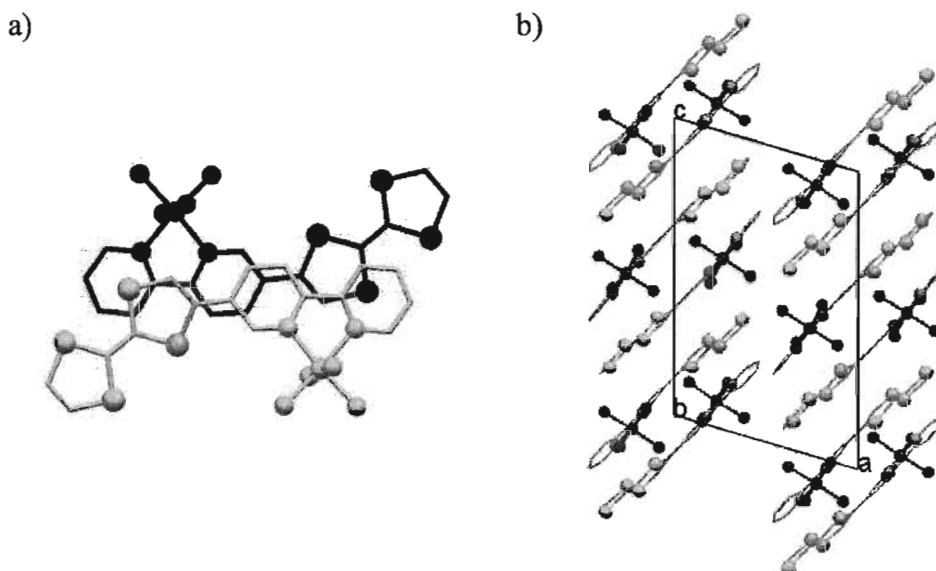


Figure 4.9 a) Top view of a dimer of **4.3**, showing the green molecule is on top of the red molecule. b) View of the slanted stacks in the *ac* plane. Hfac ligands omitted when necessary for clarity, except for their oxygen atoms. Hydrogen atoms are omitted for clarity. The B component of disorder is not shown for clarity.

The shortest Ni...Ni distance can be found between non-disordered dimers, with distance of 8.7039(13) Å. The Ni...Ni shortest distance between two disordered complexes is estimated to be about 8.94 Å. These distances are long enough to anticipate only weak magnetic interactions between metal centres at best.

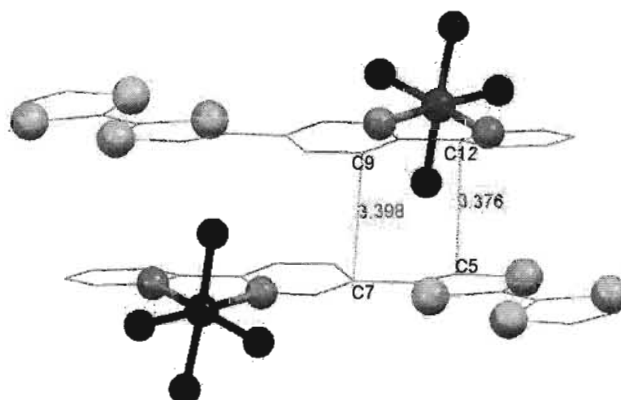


Figure 4.10 Short contacts between the rings of non-disordered **4.3** complexes.

4.2.2.4 Characterization of complex **4.4**

The Zn^{2+} complex **4.4** was prepared as a model complex that would not have paramagnetic d electrons but would retain the same overall molecular shape when compared with complexes **4.1-4.3**. Oxidation of this complex would afford the CT salt **4.4⁺**, whose magnetic properties would come from the π unpaired electrons of the TTF radical cation. In this respect, understanding the electrical conductivity and magnetism properties for this CT salt would enable us to interpret more easily the influence of paramagnetic transition metals on the electrical conductivity and magnetic properties of the CT salts **4.1⁺-4.3⁺**.

Dark red needles of complex **4.4** were prepared by the slow cooling of a saturated acetonitrile solution. X-ray diffraction studies carried out at 150 K afforded the crystal structure of **4.4**, shown in Figure 4.11 a). In contrast to the previously discussed structures, this complex crystallizes in the monoclinic space group $P2_1/c$, with one crystallographically independent molecule in the unit cell, Figure 4.11 b). The bipyridine and TTF moieties are almost coplanar, presenting a slight rotation of about 10.6° . The

Zn^{2+} ion presents a distorted octahedral coordination environment formed by a bipyridine moiety and two hfac ligands. See Table 4.4 for selected bond lengths and angles.

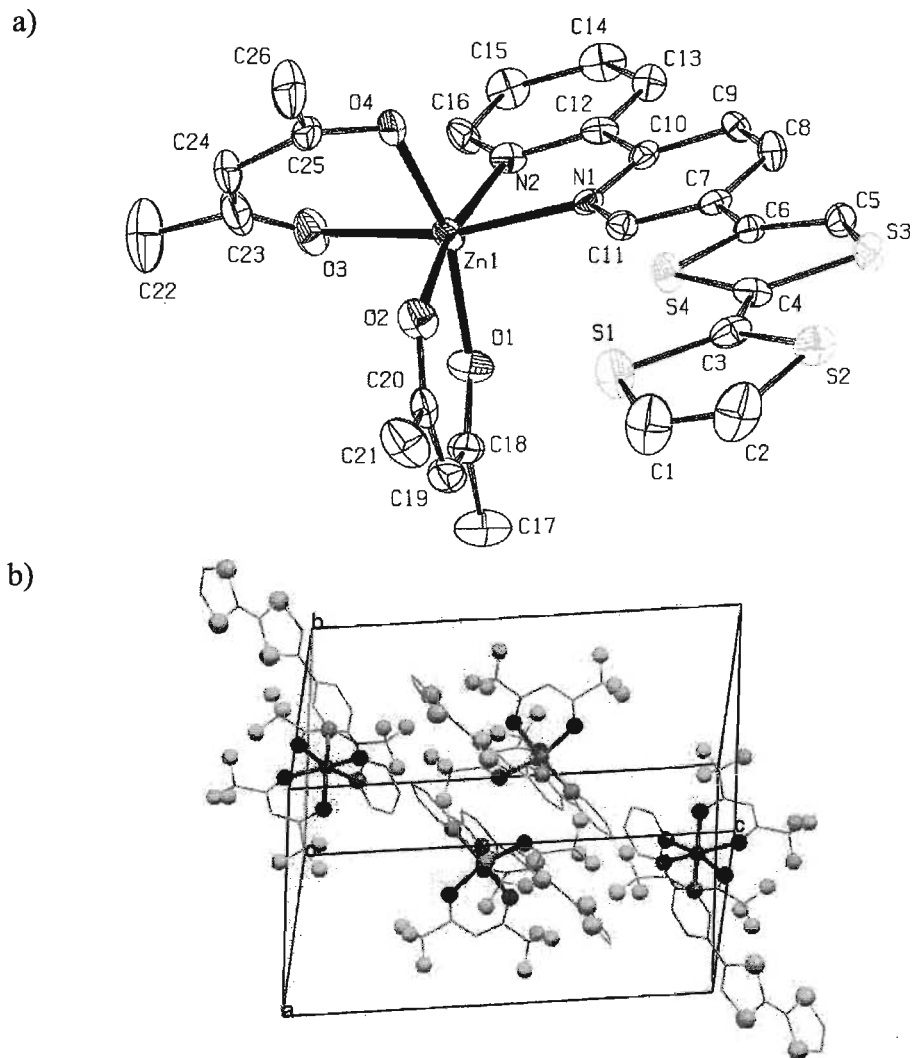


Figure 4.11 a) ORTEP plot of the molecular structure of **4.4** showing the corresponding numbering scheme. Thermal ellipsoids plotted at 50% probability. b) Unit cell of **4.4**. Hydrogen and fluorine atoms are omitted for clarity when necessary.

Table 4.4 Selected bond lengths (Å) and angles (°) for complex **4.4**.

Bond lengths			
Zn1-N1	2.129(6)	S2-C2	1.738(10)
Zn1-N2	2.104(6)	S3-C5	1.730(8)
Zn1-O1	2.101(5)	S3-C4	1.763(8)
Zn1-O2	2.101(5)	S4-C4	1.753(7)
Zn1-O3	2.097(5)	S4-C6	1.762(8)
Zn1-O4	2.133(5)	C1-C2	1.306(14)
S1-C1	1.736(10)	C3-C4	1.337(11)
S1-C3	1.746(9)	C5-C6	1.338(11)
S2-C3	1.760(8)	C6-C7	1.465(10)
Bond angles			
O1-Zn1-N1	102.1(2)	O1-Zn1-N2	168.2(2)
O3-Zn1-N1	166.2(2)	O2-Zn1-O4	80.0(2)
N1-Zn1-N2	77.7(2)	O3-Zn1-O4	84.2(2)
O4-Zn1-N1	89.3(2)	C1-S1-C3	94.7(4)
O4-Zn1-N2	105.2(2)	C3-S2-C2	94.1(4)
O2-Zn1-N2	168.2(2)	C5-S3-C4	94.7(4)
O2-Zn1-O1	85.1(2)	C4-S4-C6	95.4(4)
O3-Zn1-O1	87.5(2)	S2-C3-S1	114.3(4)
O2-Zn1-O3	98.9(2)	S4-C4-S3	114.4(4)
Dihedral angles			
C5-C6-C7-C8	-10.0(12)	N1-C10-C12-N2	0.2(10)

The crystal packing of complex **4.4** reveals that, much as in the previous complexes, the molecules stack in a head-to-tail arrangement down the *a*-axis, Figure 4.12. In this case, however, the structure can be regarded as a *quasi* regular stack of monomers rather than a stack of dimers. The distances between the best planes of molecules in a stack are 3.41 and 3.44 Å, a much smaller difference than in the previous complexes. The slanted stacks of TTF donors running down the *b*-axis of the unit cell, Figure 4.12. The shortest Zn...Zn distances in this structure are 8.7672(13) Å between two neighbouring complexes within a stack.

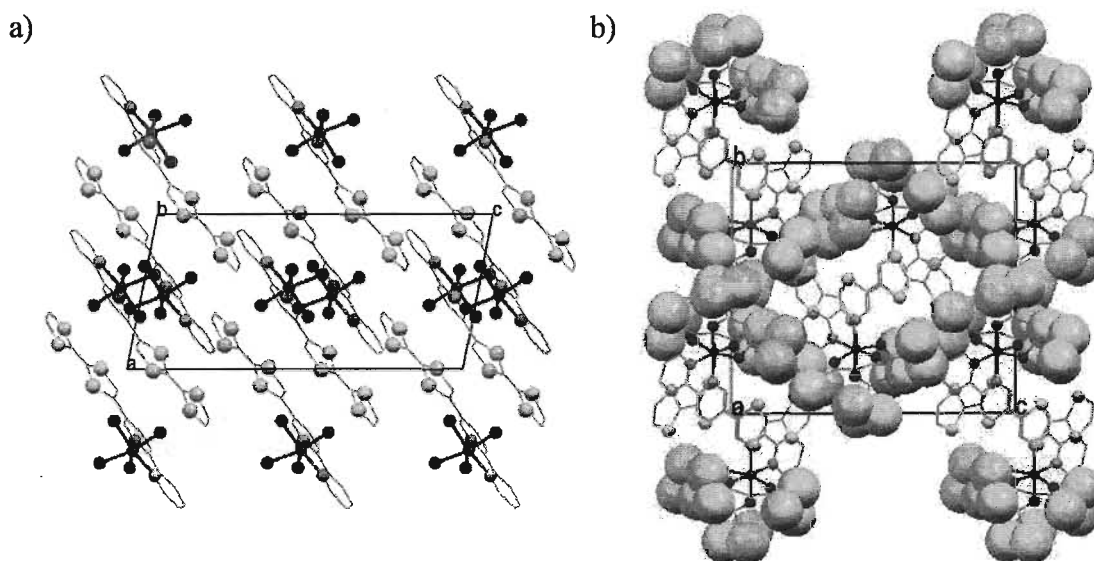


Figure 4.12 a) View of the stacks of **4.4** down the *b*-axis. b) View of the stacks down the *a*-axis showing the fluorine atoms as green spheres. Hydrogen and hfac ligands are omitted for clarity when necessary.

Due to the head-to-tail arrangement of the complex molecules, all the S...S distances in the crystal structure are longer than the sum of the *van der Waals* radii. Image b) in Figure 4.12 shows how the hfac ligands isolate each stack, since the TTF donors are essentially encapsulated within a 'fluorine channel', precluding any interstack S...S short contacts

In summary, although the Zn^{2+} **4.4** crystallizes in a different space group from complexes **4.1-4.3**, the packing of all the complexes is very similar. Therefore it is reasonable to expect that, upon oxidation of the TTF moiety, the CT salt **4.4**⁺ will be a suitable model to compare with the CT salts **4.1**⁺-**4.3**⁺.

4.2.3 Spectroscopic characterization

The diamagnetic properties of complex **4.4** allowed for the characterization of the complex by ¹H NMR spectroscopy. The protons of the dithiole rings of the TTF moiety are observed as sharp singlets between 6.90-6.40 ppm. The aromatic pyridyl protons are visible between 8.77 and 7.69 ppm, similar to the chemical shifts observed for the free

TTF ligand **3.8**. The singlet found at 6.02 ppm integrates to two hydrogen atoms that can be tentatively assigned to the hfac protons.

The UV-Vis spectra of these complexes are shown in Figure 4.13. All derivatives present two absorption bands, the first at $\lambda = 310$ nm and a second broader band between $\lambda = 415$ and 510 nm. The first band together with its shoulders can be assigned to the overlap of the transitions within the TTF donor, based on the spectra of the neutral ligand **3.8** and of related TTF derivatives reported in the literature.^{120,126,199} The broad band at lower energy is not present in solutions containing a mixture of unsubstituted TTF and bromobipyridine. This indicates that this absorption is due to an intramolecular charge transfer (ICT) interaction and highlights the electronic communication between the donor and acceptor moieties in these derivatives. As expected for ICT bands, the position of the band depends on the polarity of the solvents used, Table 4.5.

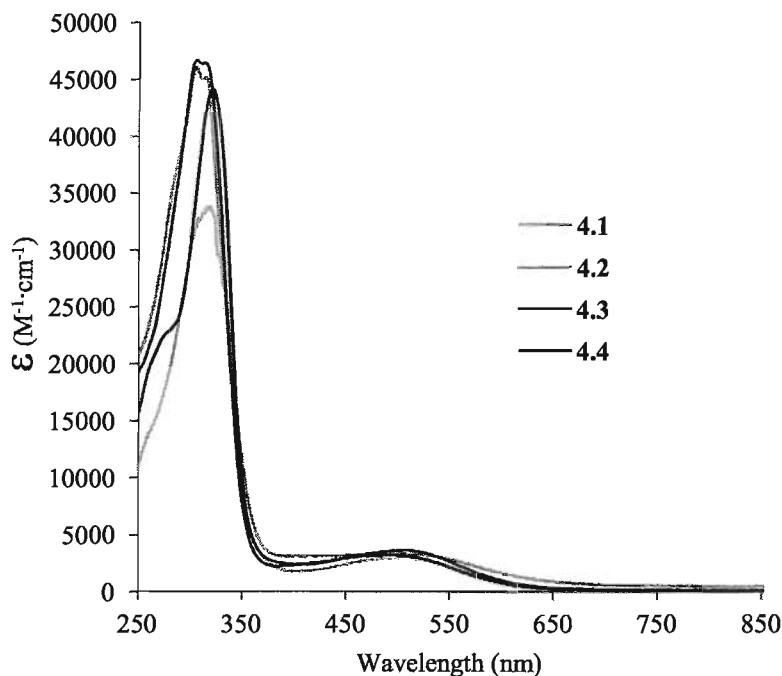


Figure 4.13 UV-Vis spectra of 10^{-5} M solutions of derivatives **4.1–4.4** in acetonitrile.

Table 4.5 UV-Vis ICT λ_{max} (nm) in different solvents for complexes **4.1-4.4**.

	3.8	4.1	4.2	4.3	4.4
Benzene	445	525	528	551	530
MeOH	434	519	521	544	457
Acetonitrile	427	500	509	504	489

4.2.4 Electrochemical characterization

All complexes show the expected two-step reversible oxidation potentials corresponding to the sequential formation of the TTF radical cation and dication species, Table 4.6. Both oxidation potentials are slightly higher for the complexes than for the free ligand due to the stabilization of the electron density of TTF caused by the electron-withdrawing effect of the covalently appended complex. All the complexes have very similar first oxidation potentials, and they share the same value for the second oxidation potential.

Table 4.6 Cyclic voltammetry oxidation potentials (V) for complexes **4.1-4.4**.

	$E_{1/2}^1$	$E_{1/2}^2$
3.8	0.45	0.82
4.1	0.49	0.85
4.2	0.50	0.85
4.3	0.50	0.85
4.4	0.49	0.85

Experimental conditions: 0.1 mM solution in acetonitrile, 0.1 mM TBAPF₆.

4.2.5 Magnetic characterization

4.2.5.1 Characterization of complex **4.1**

Magnetic susceptibility measurements of the Co²⁺ complex **4.1** were carried out in an applied field of 1000 Oe on polycrystalline sample between 2-300 K. Figure 4.14 shows that the magnetic susceptibility rises as the temperature decreases. It is clearly visible that the experimental data does not follow the Curie law ($g = 2.3$) shown as a red line. This is caused by the spin orbit coupling present in Co²⁺ that causes the splitting of

the 4T_1 term into three states, $J_{eff} = 5/2$, $J_{eff} = 3/2$ and $J_{eff} = 1/2$, which are further split due to Zeeman splitting.^{9,11}

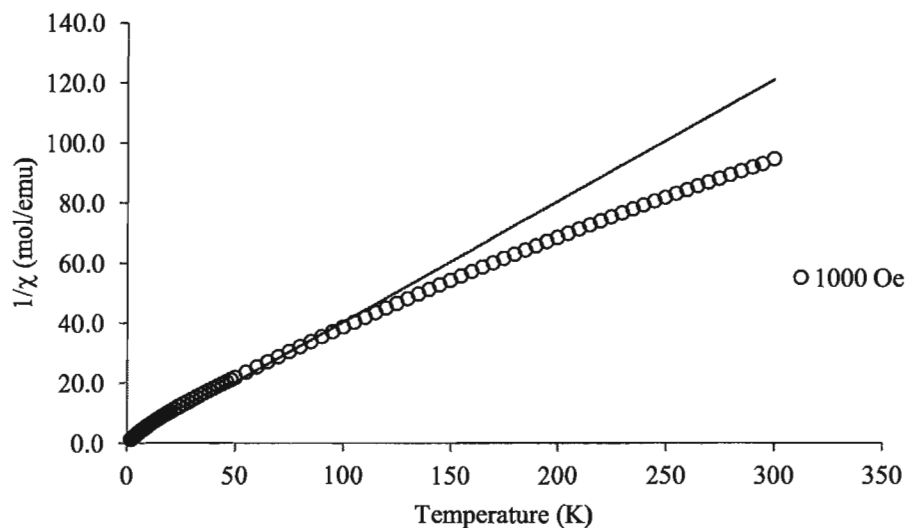


Figure 4.14 Variation of $1/\chi$ versus temperature for 4.1. The fit to the Curie law is shown as a red line.

The deviation of Co^{2+} from a purely paramagnetic behaviour can also be seen in Figure 4.15. The χT value for 4.1 at 300 K is 3.17 emu K/mol, larger than the expected 2.47 emu K/mol for a non-interacting $S = 3/2$ Co^{2+} cation. The larger value of χT is caused by the large orbital momentum contribution to the magnetic moment of the cation. As the temperature is decreased, the value of χT decreases steadily, reaching a value of 1.47 emu K/mol at 2 K. Although this behaviour would normally indicate antiferromagnetic interactions between neighbouring magnetic centres, in this case, it is a characteristic behaviour of mononuclear Co^{2+} complexes (which, incidentally, can mask minor intermolecular antiferromagnetic interactions).⁹ This decrease in χT is caused by the thermal depopulation of the states mentioned above as the sample is cooled.^{9,11} Modelling the magnetic behaviour of Co^{2+} is a very complex problem,^{9,11} and no attempt was made to model this system.

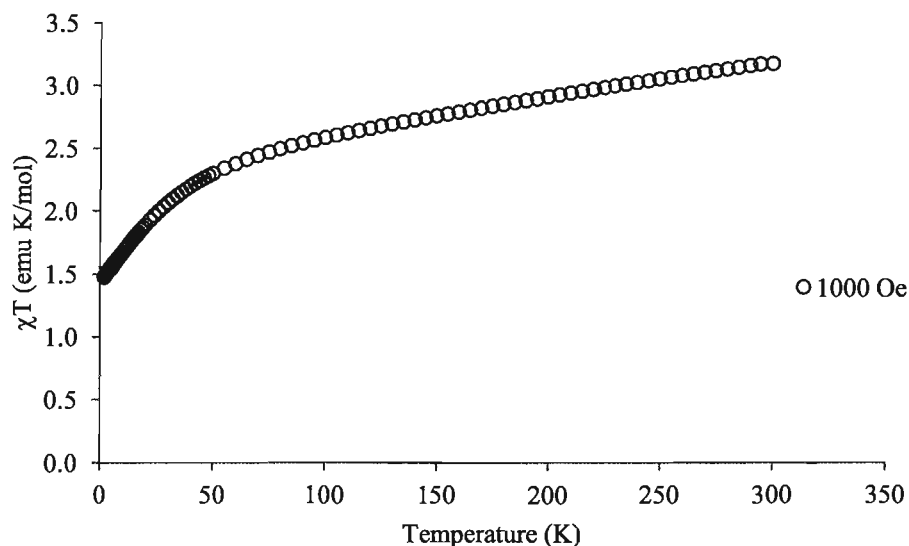


Figure 4.15 Variation of χT versus temperature for complex 4.1.

4.2.5.2 Characterization of complex 4.3

Magnetic susceptibility measurements of the Ni^{2+} complex **4.3** were carried out in an applied field of 1000 Oe on a polycrystalline sample between 2-300 K. Figure 4.16 shows that the magnetic susceptibility rises as the temperature decreases. It is clearly visible that the experimental data does not follow the Curie law (shown as a red line, $g = 2.3$) at high temperature. This is a common situation for $3d$ transition metal ions with an 3A ground term such as Ni^{2+} . The different symmetry of the d_{z^2} and $d_{x^2-y^2}$ quenches any contribution of the first order spin orbit coupling to the magnetic moment of Ni^{2+} . In this case, the mixing of excited states into the ground state introduces a small amount of orbital contribution to the magnetic moment of Ni^{2+} , causing it to deviate from the Curie law.^{9,223} This generates a temperature independent contribution to the paramagnetism of the sample that must be accounted for in order to model the magnetic behaviour of this compound.

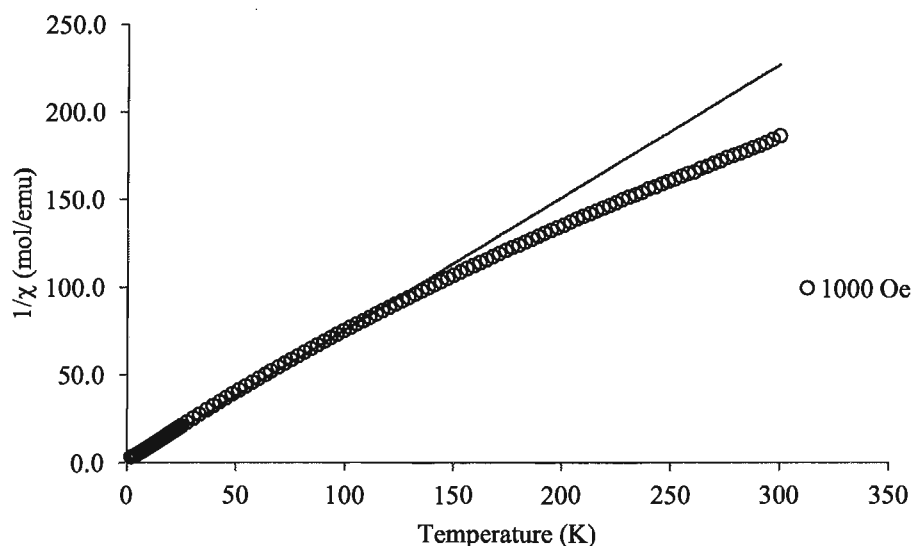


Figure 4.16 Variation of $1/\chi$ versus temperature for **4.3**. The fit to the Curie law is shown as a red line.

The deviation of Ni^{2+} from a purely paramagnetic behaviour can also be seen in Figure 4.17. The χT value for **4.3** at 300 K is 1.61 emu K/mol, larger than the expected 1.32 emu K/mol for a non-interacting $S = 1$ Ni^{2+} cation. The larger value of χT is caused by the orbital momentum contribution to the magnetic moment of the cation gained by the mixing of excited states with the ground state. As the temperature is decreased, the value of χT decreases steadily, reaching a value of 0.58 emu K/mol at 2 K. Given that the shortest $\text{Ni}\cdots\text{Ni}$ distances are greater than 8.7 Å, we can assume that this decrease in χT is not caused by intermolecular antiferromagnetic interactions but rather due to depopulation of thermally populated excited states with $S = 1$. At sufficiently low temperature, the value of χT would be zero because the only populated state would be the Ni^{2+} ground state with $S = 0$.

The loss of degeneracy of these states is the result of zero-field splitting (zfs). In order to find a suitable expression of the van Vleck equation for this system, it is necessary to account for zfs and the temperature independent paramagnetism (T.I.P.) present in this compound. A suitable expression for the magnetic susceptibility of **4.3** is equation (4.1),

$$\chi = \frac{Ng^2\beta^2}{k_B(T-\theta)} \frac{\exp\left(\frac{-D}{k_BT}\right)}{1 + 2\exp\left(\frac{-D}{k_BT}\right)} + N\alpha \quad (4.1)$$

where D is the axial zfs parameter, $N\alpha$ is the T.I.P. parameter, θ is the intermolecular interaction parameter and the rest of parameters have their usual meanings. Figure 4.17 shows the fit (red line) to the experimental data using equation (4.1). The simulated data fits the experimental data all the way down to 25 K, where the fit deviates somewhat from the experimental data. The fit to the experimental data expression for χT yielded $D = 2.1$ K with $g = 2.18$, $\theta = 0.1$ K and T.I.P. = $1.4 \cdot 10^{-4}$. These values are consistent with the values found in the literature.^{9,10,11}

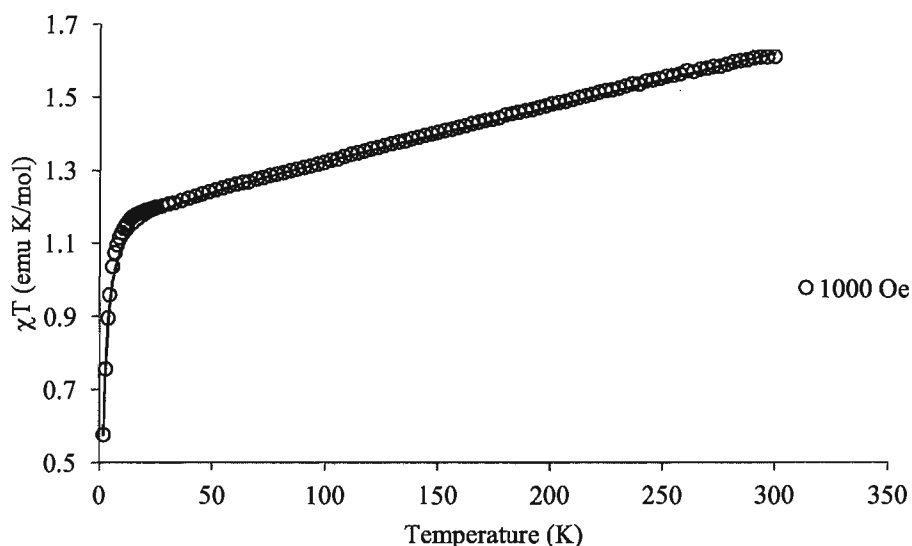


Figure 4.17 Variation of χT versus temperature for complex **4.3**. The fit to the van Vleck equation is shown as a red line.

4.3 Conclusions

Ligand **3.8** has been successfully coordinated to afford the coordination complexes **4.1-4.4**. The crystal structures of complexes **4.1-4.4** show the stacking arrangement of the TTF and bipyridine moieties, placing the metal centres and hfac ligands on the outside of the stacks. This kind of arrangement is similar to the arrangement in sublattices of the structures of TTF radical-ion salts containing organic donors and inorganic anions in independent lattices. UV-Vis and CV characterization of

these complexes show that the electronic properties of the ligand can be tuned by coordination to transition metal ions. The magnetic characterization of complexes **4.1** and **4.3** indicates that the metal centres seem to be well isolated from each other, as seen by single crystal X-ray diffraction experiments. As expected, the hfac counterions maintain the paramagnetic metal centres away from each other, precluding any magnetic interactions between them. The preparation and characterization of these complexes enables us to proceed with the preparation of their corresponding radical cation salts **4.1⁺**-**4.4⁺**.

CHAPTER 5

Summary and outlook

Molecular magnetism and molecule-based organic conductors are two fields that have undergone a dramatic expansion over the last two decades. The work presented in this thesis contributes to both fields by developing and studying new molecular building blocks for the preparation of materials with targeted and tailored physical properties. In this Chapter we will summarize the results obtained in each project, and we will outline their long term objectives.

In Chapter 2 we introduced a family of novel *bis*-imine ligands based on 3,3'-diamino-2,2'-bipyridine bearing 2-pyridyl (**1.40**), 2-phenol (**2.2**) or 2,5-dihydroxyphenyl (**2.3**) arms. X-ray diffraction studies of **2.2** and **2.3** reveal that their crystal packing is dominated by π - π and hydrogen bonding interactions, in contrast to the molecular structure of the 2-pyridyl ligand **1.40**. Upon coordination to metal salts, ligand **2.2** either underwent an intramolecular cyclization (**2.4**, **2.6**, **2.7**), become partially hydrolyzed (**2.8**) or remained intact (**2.11**), depending on the reaction conditions. The paramagnetic coordination complexes display weak antiferromagnetic interactions between metal centres. The long term objectives for this project are as follows: i) further exploration of the coordination chemistry of the *bis*-imine ligands presented in this thesis; ii) enhancing the stability of the imine bonds in 3,3'-diamino-2,2'-bipyridine-based *bis*-imine ligands and iii) synthesis of new ligands through careful choice of aryl aldehydes or aryl ketones. The preparation of new polynuclear complexes with ligands **1.40**, **2.2** and **2.3** in strict anhydrous conditions may ensure the stability of the ligands and afford clusters with interesting magnetic properties, especially if SCO complexes could be assembled. The additional hydroxyl groups on the arms of ligand **2.3** could afford magnetic hysteresis in its SCO complexes through intermolecular hydrogen bonding. The electron-withdrawing nature of the pyridine rings in **1.40** enhances the sensitivity of its imine bonds towards hydrolysis. Ligands **2.2** and **2.3** are more stable because of the electron richer phenol rings on the arms of the ligands. Using different electron-rich aldehydes for the synthesis of new ligands would, at least, ensure that the new ligands would be as stable to

hydrolysis as **2.2** and **2.3**. Additionally, it is possible that the inductive effect of methyl groups could help stabilize the imine bonds in the ligands. Substituting methyl groups on the bipyridine rings and using aryl ketones instead of aryl aldehydes could result in an increase of the imine stability. Finally, aryl aldehydes and aryl ketones bearing multiple groups such as hydroxyl or methoxide could be introduced in order to increase the denticity of the ligand and enhance the overall nuclearity of the resulting complexes.

In Chapter 3 we presented a family of π -extended TTF donors bearing cyanoaryl and *bis*-aryl moieties. The X-ray structure of the cyanopyridyl donors **3.2-3.5** indicate that the substitution of the pyridyl ring influenced their stacking in the solid state. A series of CT salts of **3.2-3.4** and **3.8** were obtained by chemical oxidation in single crystal and powder forms. The single crystal X-ray structure of the CT salts **3.15a**, **3.16a** and **3.17** comprise of dimers of oxidized TTF donors oriented in an antiparallel manner. Samples of the CT salts **3.15c**, **3.16a**, **3.18b**, **3.18c** and **3.19-3.22** pressed into pellets behaved as semiconductors, displaying low electrical conductivities in the range 10^{-7} - 10^{-3} S cm⁻¹. X-ray diffraction studies of single crystals of compounds **3.21** and **3.22** revealed that the derivatives crystallize in regular stacks of trimeric units, where one TTF derivative is neutral and the other two derivatives each have a charge of +1 based on CT calculations. The long term objectives of this project include: i) the preparation of new CT salts of the cyanoaryl donors described in this thesis using different counterions, ii) determine the counterion effect on the solid state structures of the CT salts and, iii) study the correlation between their structure and their electrical properties. The nitrile functional group in the cyanoaryl derivatives can be synthetically modified into a second heterocycle such as imidazole or tetrazole rings. These new derivatives, in turn, could be used to prepare new CT salts whose physical properties will be studied.

In Chapter 4 we introduced a family of M(hfac)₂ coordination complexes prepared from the TTF ligand **3.8**. These compounds crystallize in stacks of head-to-tail dimers of complex molecules. The metal centres are arranged at opposite ends of the dimer, forming stacks of TTF ligand segregated from the coordination sites and metal centres. Variable temperature magnetic susceptibility measurements revealed that the magnetic ions were well isolated. The long term objectives of this project are the synthesis and characterization of hybrid ferromagnetic conducting materials. The next step in this

project would be to oxidize the TTF donor in complexes **4.1-4.4** and study the electrical conductivity and magnetic properties of the resulting CT salts. Furthermore the preparation of complexes from other less bulky metal salts might afford materials in which the metal centers are closer, thus facilitating ferro- or anti-ferromagnetic exchange interactions. Understanding how to tune the functionality of the molecule in order to facilitate ferromagnetic exchange interactions is a long term goal of the research in the Pilkington group.

CHAPTER 6

Experimental

6.1 General considerations

Unless stated otherwise, all experiments were performed under a nitrogen atmosphere using standard Schlenk line techniques, or in a glovebox. All chemicals were purchased from Sigma Aldrich, Alfa Aesar and Matrix Scientific and were used as received unless otherwise stated. Dry solvents were obtained from a Puresolve PS MD-4 solvent purification system.

6.2 Instrumentation

Conductivity: All the samples were pressed into 1cm diameter pellets using 8 tons pressure in a pellet press for 3 minutes. The pellets were broken into smaller pieces and two 0.025 mm diameter gold wire electrodes were glued to the fragments using conducting carbon resin. The two probe DC resistance measurements were carried out at room temperature. The equipment used to measure the conductivity of the samples consisted of an Oxford Instruments Optistat-CF cryostat, an Oxford Instruments ITC503 temperature controller and a Keithley 2001 multimeter. The process was controlled by Labview 7 software using an in house program.

Cyclic voltammetry: Measurements were carried out on a BAS Epsilon potentiostat at room temperature in acetonitrile containing 0.1 M of $n\text{-Bu}_4\text{NPF}_6$. Platinum wire was used as the counter electrode, AgCl/Ag was used as reference electrode and a 3 mm diameter platinum electrode was used as the working electrode. The glassy carbon working electrode was polished on alumina before use. iR compensation was applied for all experiments for potential measurements.

Electrocrystallization: Experiments were carried out at room temperature using a homemade constant current generator with variable output (0.1-10 μA). Platinum electrodes of 1 mm diameter were used. All the electrocrystallization experiments were carried out in a sand box in order to minimize vibrations.

Elemental analysis: Samples for elemental analysis were measured by Atlantic Microlab, Norcross, GA.

FT-IR spectroscopy: Infrared samples were pressed as KBr pellets and the spectra were recorded using a ThermoMattson RS-1 FT-IR spectrometer.

Magnetic susceptibility measurements: Magnetic susceptibility data were collected on a Quantum Design SQUID magnetometer MPMS in an applied field of 5000 G between 5 and 300 K. DC analyses were performed on polycrystalline samples, carefully weighed into gelatine capsules, which were loaded into plastic straws and attached to the sample transport rod. Diamagnetic corrections to the paramagnetic susceptibilities were applied using Pascal's constants.

Mass spectroscopy: EI/FAB mass spectra were obtained using a Kratos Concept 1S High Resolution E/B mass spectrometer. MALDI mass spectra were obtained using a Bruker Autoflex TOF/TOF MALDI spectrometer.

Melting Point: All solids were determined using a Stuart Scientific SMP 10 melting point apparatus.

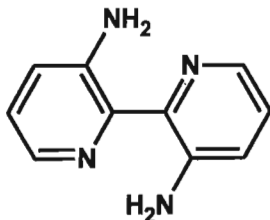
NMR spectroscopy: ^1H and ^{13}C NMR spectra were recorded using either a Bruker Avance AV 600 Digital NMR spectrometer with a 14.1 Tesla Ultrashield Plus magnet or a Bruker Avance AV 300 Digital NMR spectrometer with a 7.05 Tesla Ultrashield magnet. The software TOPSPIN 3.1 was used for data analysis.

UV-Vis spectroscopy: UV-Vis spectra were recorded using a ThermoSpectronic/Unicam UV-4 UV-VIS spectrometer.

X-ray structure determination: Single crystal X-ray diffraction experiments were carried out using a Bruker Apex II CCD diffractometer equipped with a Kryoflex Oxford variable temperature device using graphite monochromated Mo K α radiation ($\lambda = 0.71073 \text{ \AA}$). Frames were integrated using the SAINT package and corrected with SADABS.²²⁴ The data were processed using the Bruker SHELXTL software package.²²⁴ The structures were solved by direct methods using the SHELXS-97 program.²²⁵ The structures were refined using the SHELX-97 program in the Bruker SHELXTL suite.²²⁴

6.3 Experimental for Chapter 2

6.3.1 Synthesis of 3,3'-diamino-2,2'-bipyridine

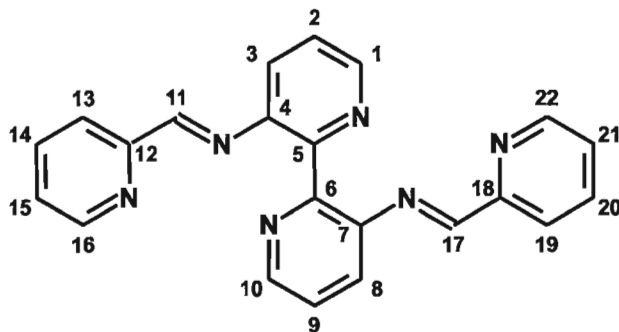


The preparation of 3,3'-diamino-2,2'-bipyridine was carried out following the synthetic procedure reported by Pilkington *et al.*²²⁶ Yield: 0.3 g (51%).

M.p.: 133-134 °C; Lit [133-134 °C]

¹H NMR (600 MHz, CDCl₃, ppm): 7.95 (dd, *J* = 7.0, 3.0 Hz, 2H), 7.03 (m, 4H), 6.29 (s, 4H).

6.3.2 Synthesis of *E,E*-N3,N3'-Bis(2-pyridylmethylene)-(2,2'-bipyridine)-3,3'-diamine (1.40)

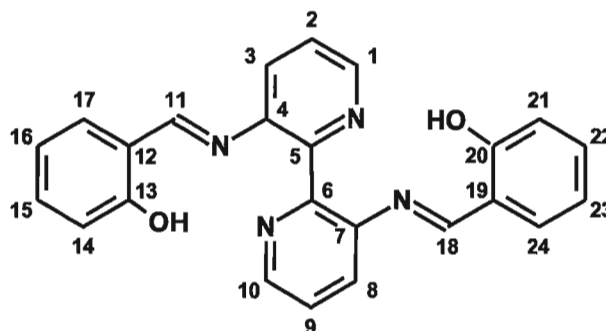


The synthesis of **1.40** was carried out following the method reported by Pilkington *et al.*²²⁷ Yield: 0.11 g (40%),

M.p._{dec.}: 79-81 °C; Lit. [80-81 °C]

¹H NMR (600 MHz, CDCl₃, ppm): 8.71 (dd, *J* = 4.7, 1.2 Hz, 2H), 8.51 (d, *J* = 4.7 Hz, 2H), 8.34 (s, 2H), 7.79 (d, *J* = 7.8 Hz, 2H), 7.69 (dd, *J* = 7.8, 1.2 Hz, 2H), 7.47 (dd, *J* = 7.8, 1.2 Hz, 2H), 7.43 (dd, *J* = 7.8, 4.6 Hz, 2H), 7.30 (dd, *J* = 7.8, 4.7 Hz, 2H).

6.3.3 Synthesis of *E,E*-N3,N3'-Bis(phenol-2-ylmethylene)-(2,2'-bipyridine)-3,3'-diamine (2.2)



Salicyl aldehyde (5.81 g, 0.047 mol) was added dropwise into a solution of 3,3'-diamino-2,2'-bipyridine (4.04 g, 0.021 mmol) in methanol (160 mL).. The resulting yellow reaction mixture was stirred overnight at room temperature. After completion of the reaction, a yellow precipitate was isolated by filtration. The precipitate was washed with methanol (3 x 20 mL) followed by diethyl ether (3 x 20 mL) and dried in air.. An additional crop of the ligand was obtained by evaporating the filtrate to dryness affording an additional 2.43 g of the ligand. Following this procedure, the ligand was isolated as a pale yellow crystalline solid. Yield: 7.54 g (88%). Single crystals suitable for X-Ray diffraction were obtained *via* the slow evaporation of a saturated solution of **2.2** in dichloromethane.

M.p.: 213-214 °C

¹H NMR (600 MHz, CDCl₃, ppm): 12.11 (s, 2H, OH), 8.67 (dd, *J* = 4.74, 1.47 Hz, 2H, H1 and H10), 8.45 (s, 2H, H11 and H18), 7.57 (dd, *J* = 8.19, 1.47 Hz, 2H, H3 and H8), 7.41 (dd, *J* = 8.19, 4.74 Hz, 2H, H2 and H9), 7.26 (qd, *J* = 8.52, 7.11, 1.56 Hz, 2H, H15 and H22), 7.05 (dd, *J* = 7.74, 1.56 Hz, 2H, H17 and H24), 6.82 (dd, *J* = 8.52, 1.08 Hz, 2H, H14 and H21), 6.76 (qd, *J* = 7.74, 7.11, 1.08 Hz, 2H, H16 and H23).

¹³C NMR (150 MHz, CDCl₃, ppm): 164.72 (C11 and 18), 160.74 (C13 and C20), 151.74 (C5 and C6), 148.07 (C1 and C10), 143.44 (C4 and C7), 133.68 (C15 and C22), 132.58 (C17 and C24), 125.96 (C3 and C8), 124.60 (C2 and C9), 119.22 (C16 and C12), 119.04 (C12 and C19), 117.08 (C14 and C21).

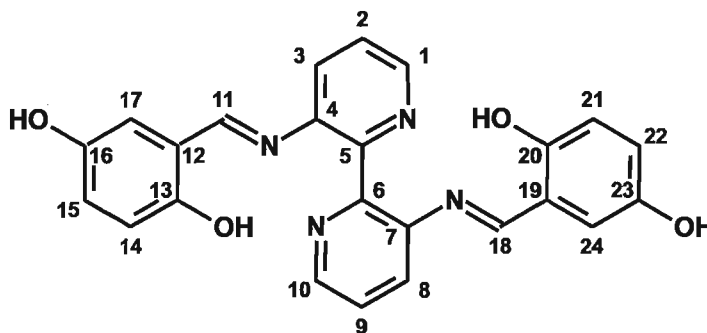
FT-IR (KBr, cm^{-1}): 3448, 3055, 1612, 1567, 1492, 1456, 1419, 1398, 1365, 1278, 1145, 908, 761.

UV-Vis (CH_3CN , nm, ϵ , $\text{M}^{-1} \text{cm}^{-1}$): 279 (30800), 346 (19510).

Elemental analysis (%): calculated for $\text{C}_{22}\text{H}_{16}\text{N}_6$: C, 72.50; H, 4.43; N, 23.07; found C, 71.97; H, 4.43; N, 23.43%.

MS (FAB, m/z): 394 ($[\text{M}]^+$, 35%), 395 ($[\text{M}+\text{H}]^+$, 100%)

6.3.4 Synthesis of *E,E*-N3,N3'-Bis(phen-1,4-diol-2-ylmethylene)-(2,2'-bipyridine)-3,3'-diamine (2.3)



2,5-dihydroxybenzaldehyde (0.3 g, 2.2 mmol) and 3,3'-diamino-2,2'-bipyridine (0.19 g, 1.0 mmol) were dissolved in methanol (20 mL). The resulting orange solution was refluxed overnight after which time the solvent was evaporated under vacuum until the product started to precipitate out from the reaction mixture as a cream-coloured solid. Diethyl ether (100 mL) was then added to facilitate the precipitation of the remainder of the product. The solid was then collected by filtration, washed with diethyl ether (3 x 10 mL) and dried in air. Yield: 0.30 g (69%). Single crystals suitable for X-Ray diffraction were obtained by slowly cooling a hot isopropanol solution of the ligand to room temperature.

M.p.: 216-217 °C

^1H NMR (600 MHz, CD_3OD , ppm): 8.62 (s, 2H, H11 and H18), 8.61 (d, $J = 1.20$ Hz, 2H, H1 and H10), 7.95 (dd, $J = 8.19, 1.20$ Hz, 2H, C3 and C8), 7.67 (dd, $J = 8.19, 4.86$

Hz, 2H, H2 and H9), 6.84 (dd, $J = 8.82, 3.00$ Hz, 2H, H15 and H22), 6.70 (d, $J = 3.00$ Hz, 2H, H17 and H24), 6.65 (d, $J = 8.82$ Hz, 2H, H14 and H21).

^{13}C NMR (150 MHz, CD_3OD , ppm): 165.63 (C11 and C18), 153.67 (C13 and C20), 151.15 (C4 and C7), 149.66 (C16 and C23), 146.68 (C1 and C10), 144.27 (C5 and C6), 126.84 (C2 and C9), 125.24 (C3 and C8), 121.62 (C15 and C22), 118.90 (C12 and C19), 117.07 (C17 and C24), 116.88 (C14 and C21).

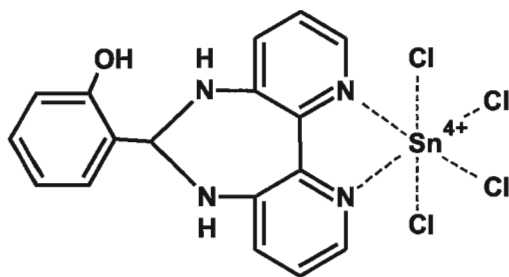
FT-IR (KBr, cm^{-1}): 3293, 3066, 1619, 1586, 1564, 1488, 1460, 1427, 1294, 1261, 1197, 1155, 785, 732, 629.

UV-Vis (CH_3CN , nm, $\epsilon/\text{M}^{-1}\text{cm}^{-1}$): 242 (28340), 286 (26680), 384 (11843).

Elemental analysis (%): calculated for $(\text{C}_{24}\text{H}_{18}\text{N}_4\text{O}_4 \cdot 0.4\text{CH}_3\text{OH})$: C, 66.72; H, 4.5; N, 12.76; found: C, 66.74; H, 4.40; N, 12.70.

MS (FAB, m/z): 426 ($[\text{M}]^+$, 63%), 427 ($[\text{M}+\text{H}]^+$, 100%)

6.3.5 Synthesis of complex $\text{Sn}(\mathbf{2.5})\text{Cl}_4$ ($\mathbf{2.4}$)



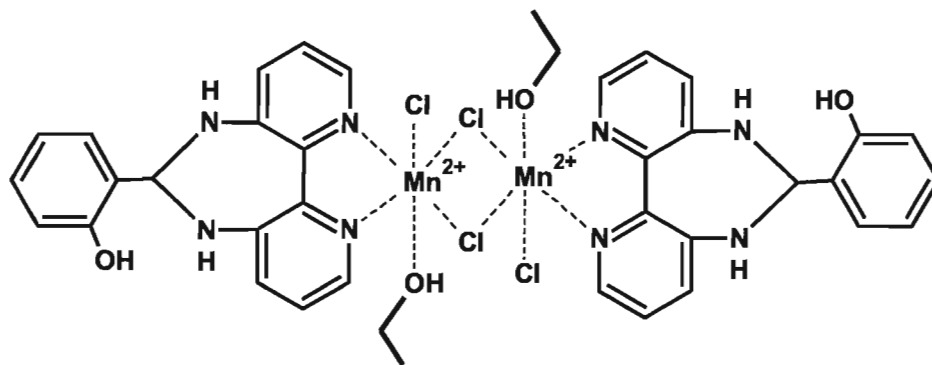
A suspension of **2.2** (0.39 g, 1.0 mmol) in ethanol (10 mL) was added to a solution of SnCl_2 (0.38 g, 2.0 mmol) in ethanol (10 mL). The resulting orange reaction mixture was stirred at room temperature for 30 minutes. After completion, the solution was filtered and the filtrate was evaporated slowly, affording red crystalline blocks of **2.4** suitable for X-ray diffraction. Yield: 0.0672 g (12%).

FT-IR (KBr, cm^{-1}): 3347, 3070, 1636, 1577, 1458, 1271, 1200, 809, 755, 706, 655.

UV-Vis [MeOH , nm]: 245, 280, 440.

MS (FAB, m/z): 291 ($[M+H]^+$, 48%), 515 ($[M-Cl]^+$, 4%)

6.3.6 Synthesis of complex $[Mn(2.5)Cl(\mu-Cl)OHEt]_2$ (2.6)



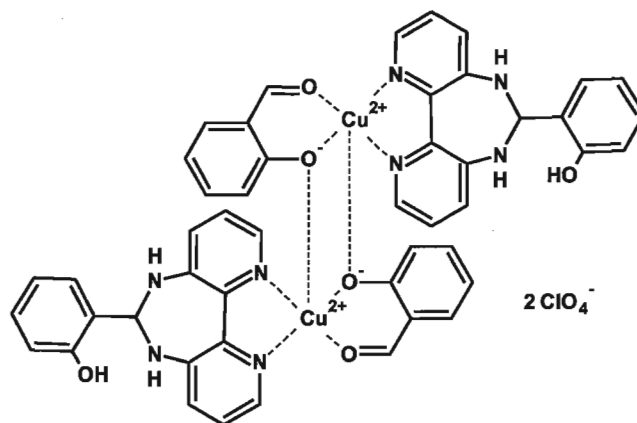
A suspension of **2.2** (0.39 g, 1.0 mmol) in ethanol (10 mL) was added to a solution of anhydrous $MnCl_2$ (0.28 g, 2.2 mmol) in ethanol (10 mL). The resulting orange reaction solution was stirred at room temperature for 30 minutes. Then the solution was then filtered and the filtrate was allowed to evaporate slowly, affording the Mn^{2+} complex as orange plates that were suitable for single crystal X-Ray diffraction. Yield: 0.0752 g (16%).

FT-IR (KBr, cm^{-1}): 3343, 2943, 2833, 2733, 2623, 1569, 1511, 1460, 1401, 1169, 1021, 995, 809, 765, 724, 639.

UV-Vis [MeOH, nm): 240, 283, 406.

MS (MALDI-TOF, m/z): 797 ($[M-2xEtOH-Cl]^+$, 1%), 634 ($[M-2.5]^+$, 100%).

6.3.7 Synthesis of complex $[\text{Cu}(\mathbf{2.5})(\mu\text{-sal})]_2(\text{ClO}_4)_2$ (**2.7**)



$\text{Cu}(\text{ClO}_4)_2 \cdot 6\text{H}_2\text{O}$ (0.39 g, 1.05 mmol) and **2.2** (0.2 g, 0.50 mmol) were dissolved in methanol (30 mL) affording a brown solution that was stirred overnight at room temperature. The reaction solution was then left undisturbed for 48 h after which time it was filtered. The filtrate was then left to evaporate slowly over a period of three weeks. The complex was then isolated as black block shaped single crystals that were suitable for X-ray diffraction. Yield: 0.0821 g. (28%).

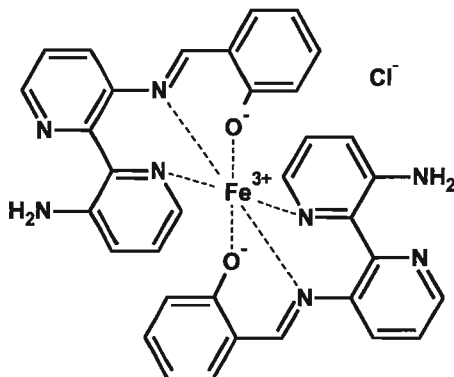
FT-IR (KBr, cm^{-1}): 3347, 3366, 3336, 3271, 3091, 3017, 2924, 1614, 1525, 1465, 1433, 1398, 1338, 1311, 1206, 1094, 1027, 804, 757, 623.

UV-Vis [MeOH, nm, $\epsilon/\text{M}^{-1}\text{cm}^{-1}$]: 239 (68000), 275 (47000), 405 (18500).

Elemental analysis (%): calculated for $(\text{Cu}_2(\mathbf{2.5})_2\text{sal}_2(\text{ClO}_4)_2 \cdot 1\text{MeOH})$: C, 49.84; H, 3.58; N, 9.49; found C, 49.59; H, 3.58; N, 9.59.

MS (MALDI-TOF, m/z): 695 ($[2\text{xCu}^{+2} + \mathbf{2.5} + 2 \text{ x salicyl aldehyde}]^+$, 29%).

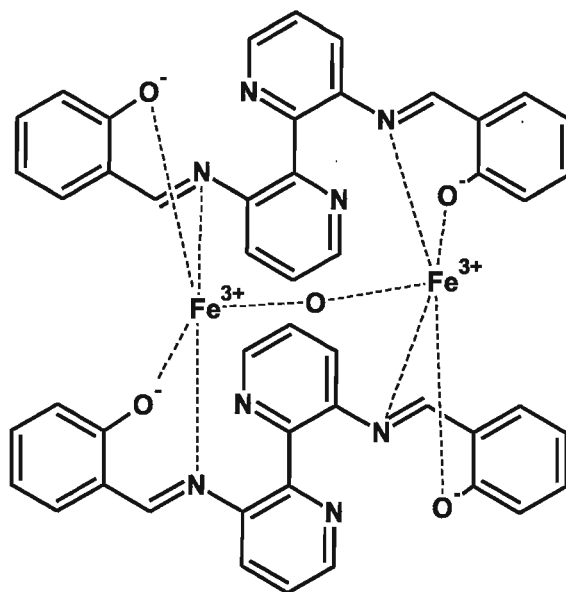
6.3.8 Synthesis of complex [Fe(2.9)₂]Cl (2.8)



Dry triethylamine (1.0 mL) was added dropwise to a solution of **2.2** (0.39 g, 1.0 mmol) in hot, dry acetonitrile (20 mL). After refluxing the reaction mixture for 5 minutes, a solution of FeCl₃ (0.33 g, 2.0 mmol) in dry acetonitrile (10 mL) was added dropwise, turning the resulting solution a deep red colour and resulting in the formation of a dark brown precipitate. The reaction mixture was refluxed for an additional hour, then it was cooled to room temperature and filtered. Slow evaporation of the filtrate over several weeks afforded red needles of **2.8** suitable for X-ray diffraction. Yield: 0.0197 g (6%).

MS (MALDI-TOF, *m/z*, intensity): 634.1036 ([M-Cl]⁺, 100).

6.3.9 Synthesis of complex $\text{Fe}_2(2.2)_2(\mu\text{-O})$ (2.11)



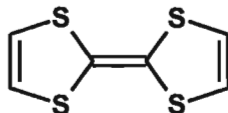
Dry triethylamine (0.25 mL) was added dropwise to a solution of **2.2** (0.1 g, 0.25 mmol) in hot, dry acetonitrile (25 mL). The solution was stirred at 50°C for 10 minutes. A solution of FeCl_3 (86 mg, 0.5 mmol) in dry acetonitrile was then added dropwise affording a dark brown solid that precipitated out of a deep red solution.. The reaction mixture was then refluxed for an additional hour. After this, dry pyridine (0.12 mL) was added dropwise to the reaction mixture and the solution was refluxed for an additional hour before it was allowed to slowly cool to room temperature. The reaction mixture was filtered and the filtrate was then cooled in a fridge for two weeks, affording a few red rhombohedral single crystals suitable for X-ray diffraction. Yield: 3 mg.

FT-IR (KBr, cm^{-1}): 3052, 1610, 1538, 1467, 1446, 1413, 1392, 1344, 1313, 1255, 1178, 1149, 1124, 1105, 1070, 1033, 979, 921, 850, 819, 755, 617, 541, 480, 445.

UV-Vis [MeOH, nm, $\epsilon/\text{M}^{-1}\text{cm}^{-1}$): 237 (62330), 269 (53340), 348 (16870), 426 (6430), 492 (5030).

6.4 Experimental for Chapter 3

6.4.1 Synthesis of tetrathiafulvalene, TTF (1.47)



The large scale preparation of TTF was carried out following the synthetic procedure reported by Bryce *et al.*²²⁸ TTF was obtained as orange needles. Yield: 13 g (65%).

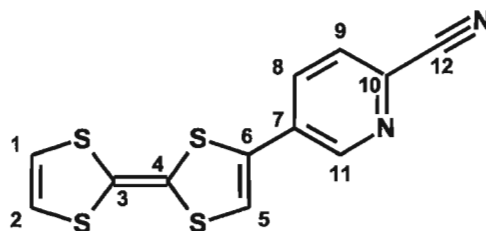
M.p.: 119-120 °C; Lit. [119-119.5 °C]

¹H NMR (600 MHz, CDCl₃, ppm): 6.33 (s, 4H).

6.4.2 General procedure for the preparation of TTF-cyanopyridines 3.2-3.5

A solution of TTF (1.02 g, 4.9 mmol) in dry THF (60 mL) was cooled to -83°C. LDA (3.3 mL, 6.0 mmol) was then added dropwise to the solution, causing the formation of a yellow precipitate. After stirring for 1 h at -83°C, a solution of ZnCl₂ (1.03 g, 7.5 mmol) in dry THF (15 mL) was added dropwise, affording a yellow solution. After an additional 1 h of stirring at -83°C, a solution of Pd(PPh₃)₄ (0.59 g, 0.5 mmol) and 5-bromocyanopyridine (1.29 g, 7.0 mmol) in dry THF (20 mL) was added dropwise to the reaction solution. The resulting orange solution was kept at -83°C for 1 h before being allowed to slowly warm up to room temperature. The reaction mixture was stirred for a total of 48 h at room temperature after which time water and DCM were added. The organic phase was then collected, washed with water and dried over anhydrous MgSO₄. The solvent was evaporated under reduced pressure and the resulting crude product was purified by column chromatography (neutral alumina, ethyl acetate/hexane (1:3)). The product was isolated as dark purple crystalline solid.

6.4.2.1 Synthesis of 5-(2-(1,3-dithiol-2-ylidene)-1,3-dithiol-4-yl)pyridine-2-carbonitrile (3.2)



This product was prepared following the general procedure described above and was obtained as a dark purple powder. Yield: 1.28 g (84%).

M.p._{dec.}: 219 °C

¹H NMR (600 MHz, CDCl₃, ppm): 8.79 (d, *J* = 2.2 Hz, 1H, H11), 7.76 (dd, *J* = 8.31, 2.2 Hz, 1H, H8), 7.71 (d, *J* = 8.31 Hz, 1H, H9), 6.87 (s, 1H, H5), 6.39 (s, 2H, H1-2).

¹³C NMR (150 MHz, CDCl₃, ppm): 147.97 (C11), 133.56 (C8), 132.21 (C10), 131.30 (C6), 130.93 (C7), 128.42 (C9), 120.08 (C5), 119.13 (C1-2), 116.99 (C12), 115.16 (C3), 105.98 (C4).

FT-IR (KBr, cm⁻¹): 3068, 2228, 1563, 1526, 1378, 1088, 1023, 830, 775, 658, 518, 435.

UV-Vis (CH₃CN, nm, ε/M⁻¹ cm⁻¹): 304 (28300), 480 (3870).

Elemental analysis (%): calculated for C₁₂H₆N₂S₄: C, 47.03; H, 1.97; N, 9.14; S, 41.85; found C, 46.81; H, 1.86; N, 9.16; S, 41.16.

MS (EI, *m/z*): 306 ([M]⁺, 78%).

CV (*E*_{1/2} vs. Ag/AgCl, V, CH₃CN, 0.1 mM TBAPF₆): 0.48, 0.85.

The chemical structure shows a central pyridine ring (atoms 7-11) substituted at the 2 and 6 positions with 2-thienyl groups. The pyridine ring has a nitrogen atom at position 11. The 2-thienyl groups are thiophene rings (atoms 1-6) attached at their 2-positions (atoms 4 and 6). A nitrile group (atoms 12 and 13) is attached to the pyridine ring at position 4 (atom 9). The atoms are numbered as follows: 1 and 2 are the outer ring carbons of the left thiophene; 3 and 4 are the bridgehead carbons; 5 and 6 are the outer ring carbons of the right thiophene; 7 and 8 are the ortho carbons of the pyridine ring; 9 is the para carbon of the pyridine ring; 10 and 11 are the meta carbons of the pyridine ring, with 11 being the nitrogen atom; 12 is the nitrile carbon, and 13 is the nitrile nitrogen.

M.p._{dec.}: 219 °C

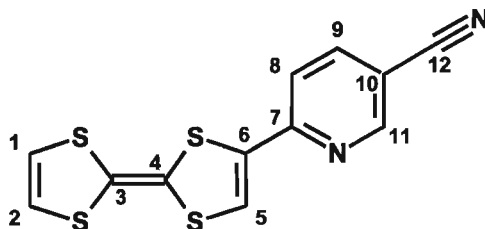
¹³C NMR (150 MHz, CDCl₃, ppm): 151.03 (C10), 149.94 (C11), 135.91 (C8), 130.07 (C6), 128.83 (C7), 119.15 and 119.11 (C1 and C2), 119.00 (C5), 115.97 (C9), 115.20 (C3), 110.24 (C12), 105.99 (C4).

UV-Vis (CH₃CN, nm, ε/M⁻¹ cm⁻¹): 295 (18300), 317 (16400), 415 (2900).

MS (EI, m/z): 306 ($[M]^+$, 100%).

198

6.4.2.3 Synthesis of 6-(2-(1,3-dithiol-2-ylidene)-1,3-dithiol-4-yl)pyridine-3-carbonitrile (3.4)



This product was prepared as described above and was obtained as a purple powder. Yield: 0.48 g (75%).

M.p._{dec.}: 217 °C

¹H NMR (600 MHz, CDCl₃, ppm): 8.82 (s, 1H, H11), 7.93 (dd, *J* = 7.9, 1.8 Hz, 1H, H9), 7.52 (d, *J* = 7.9 Hz, 1H, H8), 7.26 (s, 1H, H5), 6.38 (d, *J* = 6.4 Hz, 1H, H1 or H2), 6.37 (s, *J* = 6.4, 1H, H1 or H2).

¹³C NMR (150 MHz, CDCl₃, ppm): 152.81 (C7), 152.29 (C11), 139.33 (C9), 136.39 (C6), 123.13 (C5), 119.35 (C1-2), 118.88 (C8), 116.50 (C12), 113.90 (C3), 107.52 (C10), 107.23 (C4).

FT-IR (KBr, cm^{-1}): 3062, 3038, 2220, 1586, 1559, 1534, 1468, 1377, 1259, 1203, 1092, 1020, 835, 797, 738, 652.

UV-Vis (CH₃CN, nm, ε/M⁻¹ cm⁻¹): 307 (28250), 510 (3910).

Elemental analysis (%): calculated for $C_{12}H_6N_2S_4$: C, 47.03; H, 1.97; N, 9.14; S, 41.85; found C, 46.77; H, 1.86; N, 8.90; S, 41.60.

HR-MS (EI): calculated for $[\text{C}_{13}\text{H}_6\text{N}_1\text{S}_4]^+$: 305.94139, found 304.94152.

CV ($E_{1/2}$ vs. Ag/AgCl, V, CH₃CN, 0.1 mM TBAPF₆): 0.46, 0.84.

M.p._{dec.}: 217 °C

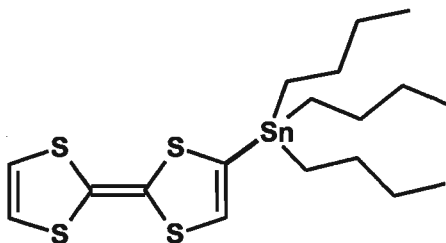
¹³C NMR (150 MHz, CDCl₃, ppm): 151.62 (C7), 137.47 (C9), 135.96 (C6), 133.41 (C11), 126.65 and 122.39 (C8 and C10), 121.47 (C5), 119.35 and 118.86 (C1 and C2), 116.78 (C12), 113.79 (C3), 107.72 (C4).

UV-Vis (CH₃CN, nm, $\epsilon/\text{M}^{-1} \text{ cm}^{-1}$): 300 (29300), 430 (4570).

MS (EI, m/z): 306 ($[M]^+$, 31%).

200

6.4.3 Synthesis of stannyl-tetrathiafulvalene (3.11)



TTF (1.98 g, 9.7 mmol) was dissolved in dry THF (20 mL) with constant stirring and the resulting solution was cooled to -83°C in an ethyl acetate/liquid nitrogen bath. LDA (6.5 mL, 11.7 mmol) was then added dropwise over 15 minutes and the resulting suspension was stirred for 1 hour at -83°C . After that time tributyltin chloride (4.8 mL, 17.7 mmol) was added dropwise over a 5 minute period, and the resulting orange solution was stirred at -83°C for 1 hour. The solution was then allowed to warm slowly to room temperature and stirred overnight. On completion the reaction mixture was diluted with water (50 mL), and extracted with DCM (3 x 30 mL). The organic extracts were dried over anhydrous MgSO_4 and the solvent was removed under vacuum to afford the crude product as a golden oil. Purification by column chromatography over deactivated silica gel eluting with a (95:5) mixture of pentane/DCM afforded **3.11** as a pale yellow oil. Yield: 2.98 g (62%).

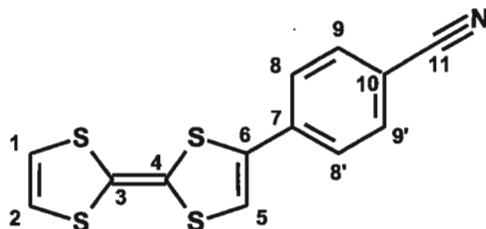
^1H NMR (600 MHz, CDCl_3 , ppm): 6.32 (d, $J = 6.78$ Hz, 2H, H1 and H2), 6.13 (s, 1H, H5), 1.57 (m, 6H, $\text{SnBu}_3\text{-H}$), 1.34 (m, 6H, $\text{SnBu}_3\text{-H}$), 1.11 (t, 6H, $\text{SnBu}_3\text{-H}$), 0.91 (t, 9H, $\text{SnBu}_3\text{-H}$).

6.4.4 General procedure for the preparation of TTF-benzonitriles 3.6, 3.7

Tetrakis(triphenylphosphine)palladium (0.04 g, 0.04 mmol) was added as a solid portion to a solution of tributylstannylTTF (0.2 g, 0.4 mmol) and 4-bromobenzonitrile (0.088, 0.40 mmol) in dry toluene (14 mL), and the reaction mixture was refluxed for 12 hrs in the dark. The solvent volume was then reduced under vacuum until a precipitate started to form. At this point petroleum ether was added to facilitate the precipitation of the product as an orange solid. The solid was collected by filtration and purified by

column chromatography on silica gel eluting with DCM to afford the the desired product as an orange powder.

6.4.4.1 Synthesis of 4-(2-(1,3-dithiol-2-ylidene)-1,3-dithiol-4-yl)benzonitrile (3.6)



This product was prepared as described above and was obtained as an orange powder. Yield: 0.0762g (62%).

M.p._{dec.}: 214 °C

¹H NMR (600 MHz, CDCl₃, ppm): 7.66 (d, *J* = 7.95 Hz, 2H, H9 and H9'), 7.50 (d, *J* = 7.95 Hz, 2H, H8 and H8'), 6.73 (s, 1H), 6.37 (s, 2H).

¹³C NMR (150 MHz, CDCl₃, ppm): 136.40 (C7), 134.23 (C6), 132.66 (C9, C9'), 126.55 (C8, C8') 119.11 and 119.08 (C1 and C2), 118.45 (C11), 117.80 (C5), 113.64 (C3), 111.53 (C10), 107.22 (C4).

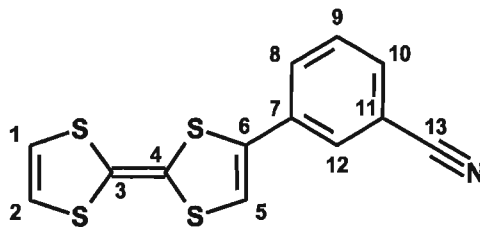
FT-IR (KBr, cm⁻¹): 3059, 2224, 1575, 1535, 1405, 1312, 1285, 1176, 1092, 831, 796, 766, 631, 553, 517, 436.

UV-Vis (CH₃CN, nm, ε/M⁻¹ cm⁻¹): 290 (19100), 438 (2990).

HR-MS (ED): calculated for [C₁₃H₇N₁S₄]⁺: 304.94614, found 304.94606.

CV (*E*_{1/2} vs. Ag/AgCl, V, CH₃CN, 0.1 mM TBAPF₆): 0.45, 0.82.

6.4.4.2 Synthesis of 3-(2-(1,3-dithiol-2-ylidene)-1,3-dithiol-4-yl)benzonitrile (3.7)



This product was prepared as described above and was obtained as an orange powder. Yield: 0.0537g (54%)

M.p._{dec.}: 216 °C

¹H NMR (600 MHz, CDCl₃, ppm): 8.70 (s, 1H, H12), 7.63 (d, *J* = 7.85 Hz, 1H, H8), 7.61 (d, *J* = 7.93 Hz, 1H, H10), 7.50 (t, *J* = 7.93, 1H, H5), 6.65 (s, 1H, H5), 6.65 (s, 2H, H1-2).

¹³C NMR (150 MHz, CDCl₃, ppm): 133.62 and 133.58 (C6 and C7), 131.52 (C10), 130.25 (C8), 129.78 (C9), 129.56 (C12), 119.13 and 119.08 (C1 and C2), 118.18 (C13), 116.51 (C5), 113.55 (C3), 113.25 (C11), 107.35 (C4).

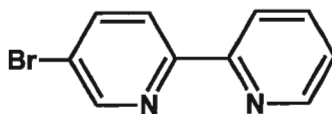
FT-IR (KBr, cm⁻¹): 3070, 2223, 1573, 1539, 1516, 1474, 1416, 1256, 1156, 914, 845, 797, 756, 671, 638, 612, 429.

UV-Vis (CH₃CN, nm, ε/M⁻¹ cm⁻¹): 287 (13200), 311 (11370), 414 (2080).

HR-MS (EI): calculated for [C₁₃H₇N₁S₄]⁺: 304.94614, found 304.94606.

CV (*E*_{1/2} vs. Ag/AgCl, V, CH₃CN, 0.1 mM TBAPF₆): 0.45, 0.82.

6.4.5 Synthesis of 4-bromo-2,2'-bipyridine (3.12)



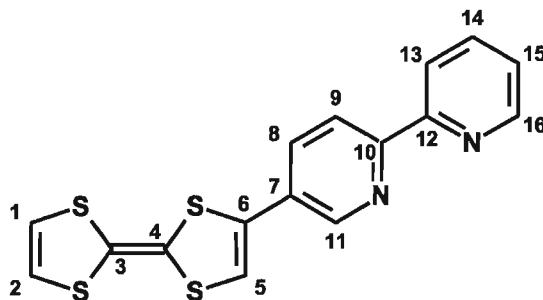
A solution of 2-bromopyridine (1.2 mL, 12.5 mmol) in dry THF (40 mL) was cooled to -83°C in an ethyl acetate/liquid nitrogen bath after which time a BuLi (8.0 mL, 12.8 mmol) solution was added dropwise over a period of 15 minutes. The resulting orange solution was further stirred for 1 hour -83°C . A solution of ZnCl_2 (1.82 g, 13.5 mmol) in THF (15 mL) was then added dropwise over 5 minutes and the resulting orange solution was stirred at -83°C for an additional hour. A solution of 2,5-dibromopyridine (3.1 g, 13.0 mmol) and tetrakis(triphenylphosphine)palladium (0.61 g, 0.5 mmol) in THF (20 mL) was added dropwise to the reaction mixture over 5 min. The resulting solution was stirred for 1 h at -83°C and then allowed to warm up to room temperature overnight. A saturated bicarbonate solution containing 1.2 eq of Na_2EDTA (respect of ZnCl_2) was added and the mixture was stirred vigorously for 2 h. The resulting phases were then extracted with diethyl ether (3x40 mL) and the organic extracts were collected and dried under vacuum. The crude product was isolated as a yellow solid. Purification by column chromatography on alumina gel, eluting with a (10:1) mixture of hexane/ethyl acetate afforded the desired product as a white solid. Yield: 1.48 g (50%).

^1H NMR (600 MHz, CDCl_3 , ppm): 8.77 (m, 1H), 8.71 (m, 1H), 8.43 (m, 2H), 7.84 (m, 2H), 7.35 (m, 1H), 6.72 (s, 1H), 6.38 (s, 2H).

UV-Vis (CH_3CN , nm, $\epsilon/\text{M}^{-1}\text{cm}^{-1}$): 245 (13500), 251 (13500), 287 (17600).

MS (EI, m/z): 235 ($[\text{M}]^+$, 71%).

6.4.6 Synthesis of 5-(2-(1,3-dithiol-2-ylidene)-1,3-dithiol-4-yl)-2,2'-bipyridine (3.8)



Tetrakis(triphenylphosphine)palladium (0.43 g, 0.37 mmol) was added as a solid portion to a solution of tributylstannylTTF (1.38 g, 2.79 mmol) and 4-bromo-2,2'-bipyridine (0.97 g, 4.12 mmol) in dry toluene (50 mL). The reaction mixture was then refluxed in the dark for 24 hours. On completion, the deep red solution was cooled first to room temperature and then to -8°C in the freezer overnight. The red precipitate obtained was collected by filtration, washed with petroleum ether (3 x 10 mL) and dried in air. The product was obtained as a red powder. Yield: 1.00 g (67%). Orange needles were obtained by sublimation of the powder at 100°C for 24 hours.

M.p._{dec.}: 224°C

^1H NMR (600 MHz, CDCl_3 , ppm): 8.76 (d, $J = 2.22$ Hz, 1H, H11), 8.71 (d, $J = 4.80$ Hz, 1H, H16), 8.43 (d, $J = 8.28$ Hz, 1H, H9), 8.42 (d, $J = 7.72$ Hz, 1H, H13), 7.85 (td, $J = 1.68, 7.72$ Hz, 1H, H14), 7.82 (dd, $J = 2.22, 8.28$ Hz, 1H, H8), 7.34 (dd, $J = 4.80, 7.72$ Hz, 1H, H15), 6.72 (s, 1H, H5), 6.38 (s, 2H, H1-2).

^{13}C NMR (150 MHz, CDCl_3 , ppm): 155.50, 155.33, 149.27, 146.45, 137.06, 134.14, 132.61, 128.42, 123.98, 121.22, 120.89, 119.12, 119.08, 115.93, 113.15, 107.89.

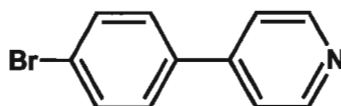
FT-IR (KBr, cm^{-1}): 3070, 1654, 1637, 1572, 1458, 1431, 1382, 1141, 1089, 1018, 790, 757, 639.

UV-Vis (CH_3CN , nm, $\epsilon/\text{M}^{-1}\text{cm}^{-1}$): 304 (22600), 427 (2700).

HR-MS (EI): calculated for $[\text{C}_{16}\text{H}_{10}\text{N}_2\text{S}_4]^+$: 357.97269, found 357.97287.

CV ($E_{1/2}$ vs. Ag/AgCl, V, CH_3CN , 0.1 mM TBAPF₆): 0.45, 0.82.

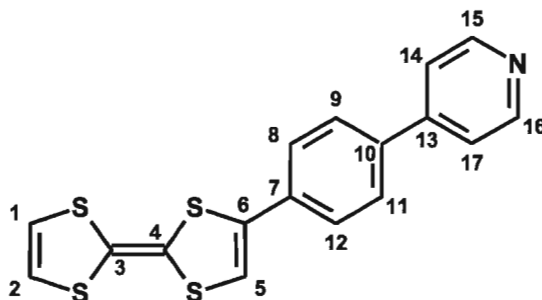
6.4.7 Synthesis of 4-(p-bromophenyl)pyridine (3.13)



The synthesis of 4-(p-bromophenyl)pyridine was carried out following the method reported by Wang *et al.*²⁰⁴ Yield: 0.24 g (40%).

¹H NMR (600 MHz, CDCl₃, ppm): 8.67 (d, *J* = 6.0 Hz, 2H), 7.62 (d, *J* = 8.0 Hz, 2H), 7.51 (d, *J* = 8.0 Hz, 4H), 7.47 (d, *J* = 6.0 Hz, 2H).

6.4.8 Synthesis of 4-{4-(2-(1,3-dithiol-2-ylidene)-1,3-dithiol-4-yl)phenyl}pyridine (3.9)



4-(p-bromophenyl)pyridine (95.0 mg, 0.40 mmol), stannyl-TTF **3.11** (23.4 mg, 0.46 mmol) and tetrakis(triphenylphosphine)palladium (103 mg, 0.34 mmol) were dissolved in dry toluene (20 mL) and the solution was refluxed for 12 h. The solvent was then removed under vacuum, and the resulting crude product was dissolved in DCM (30 mL) and washed with distilled water (3 x 20 mL). The organic phase was dried over anhydrous Na₂SO₄ and the solvent was evaporated under vacuum to afford the crude product as a dark brown solid. Purification *via* flash column chromatography on silica gel eluting with a (1:4) mixture of ethyl acetate/DCM afforded the product as a red solid. Yield: 20 mg (13%).

¹H NMR (600 MHz, CDCl₃, ppm): 8.69 (d, *J* = 6.04 Hz, 2H, H15, H16), 7.66 (d, *J* = 7.93 Hz, 2H, H8, H12), 7.54 (m, 4H, H9-17), 6.64 (s, 1H, H5), 6.37 (s, 2H, H1-2).

^{13}C NMR (150 MHz, CDCl_3 , ppm): 150.39 (C15, C16), 147.26 (C13), 137.89 (C10), 135.27 (C7), 133.12 (C6), 127.43 (C8, C12), 126.9 (C9, C11), 121.37 (C14, C17), 119.11 and 119.09 (C1 and C2), 114.7 (C5), 112.28 (C4), 108.51 (C3).

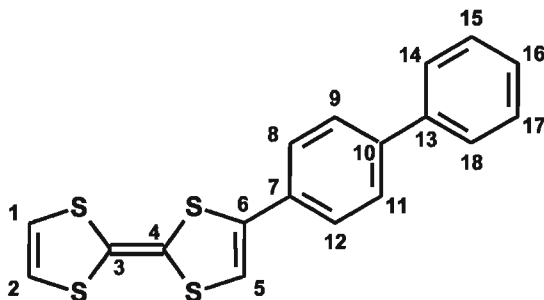
FT-IR (KBr, cm^{-1}): 3066, 3026, 1594, 1565, 1536 1482, 1401, 1330, 1221, 1091, 1028, 992, 921, 887, 801, 761, 650, 532, 453.

UV-Vis (CH_3CN , nm, $\epsilon/\text{M}^{-1}\text{cm}^{-1}$): 296 (30500), 417 (4300).

HR-MS (EI): calculated for $[\text{C}_{17}\text{H}_{11}\text{N}_1\text{S}_4]^+$: 356.97704, found 356.97706.

CV ($E_{1/2}$ vs. Ag/AgCl, V, CH_3CN , 0.1 mM TBAPF₆): 0.42, 0.80.

6.4.9 Synthesis of 4-(biphenyl-4-yl)-2-(1,3-dithiol-2-ylidene)-1,3-dithiole (3.10)



Tetrakis(triphenylphosphine)palladium (0.11 g, 0.1 mmol) was added as a solid portion to a solution of tributylstannylTTF (0.49 g, 0.9 mmol) and 4-bromo-biphenyl (0.2561 g, 1.1 mmol) in dry toluene (20 mL) and the reaction mixture was refluxed for 24 hours in the dark. The resulting deep red mixture was dried under vacuum affording the crude product as a dark red oil. Purification by flash column chromatography on silica gel eluting with a (10:1) mixture of hexane/ethyl acetate afforded an orange powder that was dissolved in the minimum amount of a (1:1) mixture of DCM/ petroleum ether until the solution became cloudy. The solution was then cooled to -8°C in the freezer overnight. The resulting orange powder was collected by filtration, washed with cold petroleum ether (3 x 10 mL) and dried in air. Yield: 0.14 g (40%).

M.p._{dec.}: 222°C

^1H NMR (600 MHz, CDCl_3 , ppm): 7.62 (d, $J = 7.55$ Hz, 2H, H14, H18), 7.61 (d, $J = 8.31$ Hz, 2H, H8, H12), 7.50 (d, $J = 8.31$ Hz, 2H, H9, H11), 7.47 (dd, $J = 7.55, 7.20$ Hz, 2H, H15, H17), 7.39 (t, $J = 7.20$ Hz, 1H, H16), 6.58 (s, 1H, H5), 6.37 (s, 2H, H1-2).

^{13}C NMR (150 MHz, CDCl_3 , ppm): 141.17 (C10), 140.15 (C13), 135.78 (C7), 131.40 (C6), 128.90 (C15, C17), 127.67 (C16), 127.47 (C8, C12), 126.99 (C14, C18), 126.66 (C9, C11), 119.12 and 119.07 (C1 and C2), 113.47 (C5), 111.66 (C4), 109.09 (C3).

FT-IR (KBr, cm^{-1}): 3066, 3027, 1561, 1535, 1482, 1444, 1404, 1255, 1207, 1159, 1076, 1030, 945, 920, 863, 833, 798, 777, 751, 691, 640, 560, 521, 441.

UV-Vis (CH_3CN , nm, $\epsilon/\text{M}^{-1} \text{cm}^{-1}$): 290 (31900), 402 (4300).

Elemental analysis (%): calculated for ($\text{C}_{18}\text{H}_{12}\text{S}_4$): C, 60.63; H, 3.39; S, 35.97; found C, 60.46; H, 3.30; S, 35.70.

HR-MS (EI): calculated for $[\text{C}_{18}\text{H}_{12}\text{S}_4]^+$: 355.98219, found 355.98262.

CV ($E_{1/2}$ vs. Ag/AgCl, V, CH_3CN , 0.1 mM TBAPF₆): 0.40, 0.78.

6.4.10 General procedure for the preparation of single crystals of CT salts

A solution of **3.2** (20 mg, 0.06 mmol) in DCM (10 mL) was added to a test tube. A solution of I_2 (30 mg, 0.11 mmol) in acetone (10 mL) was then carefully layered over the top of the DCM solution and both phases were allowed to mix slowly at room temperature in a sealed tube. After two weeks a few black crystals suitable for single crystal X-ray diffraction were isolated from the test tube. The molecular structure of the charge transfer salt was characterized by X-ray crystallography.

6.4.11 General procedures for the preparation CT salts as powders

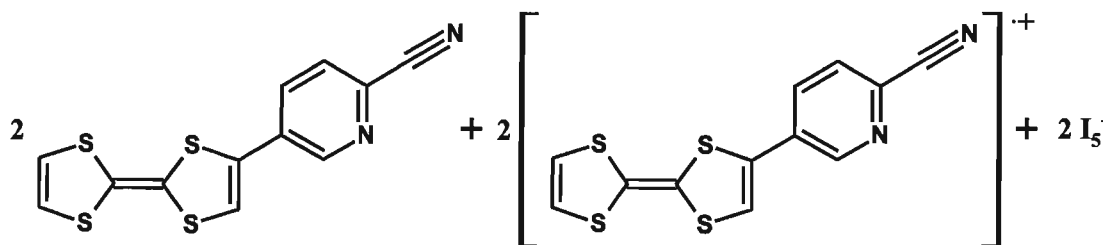
Two different procedures were followed in order to prepare CT salts as microcrystalline powders:

- I_2 (0.09 g, 0.34 mmol) in 10 mL of dry acetone was added dropwise to a solution of **3.2** (0.10 g, 0.32 mmol) in 25 mL of dry DCM, under nitrogen. The reaction

mixture was then refluxed for 3 hours. The black powder present in suspension was isolated by filtration, washed with petroleum ether (3 x 10 mL) and dried in air.

ii) I₂ (0.067 g, 0.26 mmol) was added as a solid portion to a warm solution of **3.2** (0.050 g, 0.16 mmol) in 15 mL of dry DCM, under nitrogen, causing the immediate formation of a black precipitate. After refluxing the solution for 3h, the black powder present in suspension was isolated by filtration and washed with 50 mL of hexane and 2 mL of DCM.

6.4.11.1 Preparation of single crystals of the CT salt (3.2)₄I₁₀ (**3.15a**)



Single crystals of the CT salt (3.2)₄I₁₀, **3.15a**, were prepared following the general procedure described above.

6.4.11.2 Preparation of the CT salt (3.2)₂I₇ (**3.15b**)

I₂ (0.36 g, 1.4 mmol) in 10 mL of dry acetone was added dropwise to a solution of **3.2** (0.34 g, 1.1 mmol) in 20 mL of dry DCM, under nitrogen. The reaction mixture was heated to 35° for 40 minutes and then it was stirred at room temperature for 3 days. The black powder present in suspension was isolated by filtration and dried under air. Yield: 0.55 g (90%).

M.p.: 265 °C

FT-IR (KBr, cm⁻¹): 3046, 2229, 1577, 1552, 1498, 1465, 1338, 1247, 1207, 1137, 1081, 1022, 925, 863, 835, 790, 744, 734, 692, 674, 566, 553, 528, 489, 458.

Elemental analysis (%): calculated for (C₂₄H₁₂I₇N₄S₈): C, 19.20; H, 0.81; N, 3.73; S, 17.09; I, 59.17; found: C, 19.37; H, 0.87; N, 3.88; S, 35.70; I, 50.87.

6.4.11.3 Preparation of the CT salt (3.2)₂I₅ (3.15c)

The CT salt (3.2)₂I₅, **3.15c** was prepared following the general procedure ii) described above. Yield: 0.074 g (66%).

M.p.: 268 °C

FT-IR (KBr, cm⁻¹): 3046, 2229, 1654, 1637, 1577, 1552, 1498, 1340, 1247, 1209, 1126, 1081, 1020, 927, 835, 790, 734, 690, 673, 568, 555, 528, 491, 457.

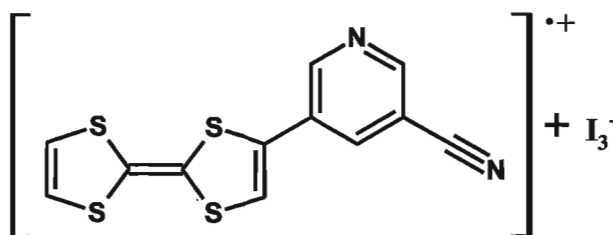
Elemental analysis (%): calculated for (C₂₄H₁₂I₅N₄S₈·0.25 CH₂Cl₂): C, 22.96; H, 0.99; N, 4.42; S, 20.22; I, 50.02; found: C, 22.72; H, 1.06; N, 4.33; S, 20.20; I, 50.21.

6.4.11.4 Alternative preparation of the CT salt (3.2)₂I₅ (3.15c)

A sample of CT salts (3.2)₂I₇, **3.15b** was placed under vacuum overnight, giving the CT salt (3.2)₂I₅, **3.15c** as a black powder.

Elemental analysis (%): calculated for (C₂₄H₁₂I₅N₄S₈): C, 23.11; H, 0.97; N, 4.49; S, 20.56; I, 50.87; found: C, 22.89; H, 0.93; N, 4.28; S, 20.74; I, 50.59.

6.4.11.5 Preparation of single crystals of the CT salt (3.3)I₃ (3.16a)



Single crystals of the CT salt (3.3)I₃, **3.16a**, were prepared following the general procedure described above.

6.4.11.6 Preparation of the CT salt (3.3)I₃ (3.16a)

The CT salt (3.3)I₃, **3.16a**, were prepared following a modification of the general procedure ii), using 0.12 mg (0.50 mmol) of I₂ and 0.10 mg (0.33 mmol) of **3.3** in DCM (30 mL). Yield: 0.1617 g (78%).

M.p.: 271 °C

FT-IR (KBr, cm^{-1}): 3039, 3022, 2226, 1558, 1515, 1493, 1467, 1424, 1339, 1269, 1246, 1156, 1078, 1020, 990, 940, 896, 874, 812, 742, 708, 686, 629, 600, 488, 462, 439.

Elemental analysis (%): calculated for ($\text{C}_{12}\text{H}_6\text{I}_3\text{N}_2\text{S}_4$): C, 20.97; H, 0.88; N, 4.08; S, 18.67; I, 55.40; found: C, 21.04; H, 0.76; N, 4.11; S, 18.90; I, 55.12.

LC-MS (ESI^+ , CH_3CN , m/z): 305.8 $[\text{M}]^+$.

6.4.11.7 Preparation of the CT salt $(\mathbf{3.3})_3\text{I}_7$ (**3.16b**)

The CT salt $(\mathbf{3.3})_2\text{I}_7$, **3.16b** was prepared following the general procedure i) described above. Yield: 0.0851 g (50%)

M.p.: 269 °C

FT-IR (KBr, cm^{-1}): 3041, 3025, 2233, 1558, 1515, 1463, 1449, 1422, 1339, 1293, 1246, 1150, 1077, 1024, 993, 942, 896, 872, 807, 774, 735, 706, 685, 666, 629, 597, 512, 486, 469, 428.

Elemental analysis (%): calculated for ($\text{C}_{36}\text{H}_{18}\text{I}_7\text{N}_6\text{S}_{12}$): C, 23.92; H, 1.00; N, 4.65; S, 21.29; I, 49.14; found: C, 23.54; H, 1.05; N, 4.58; S, 21.03; I, 49.69.

LC-MS (ESI^+ , CH_3CN , m/z): 305.8 $[\text{M}]^+$.

6.4.11.8 Preparation of the CT salt $(\mathbf{3.4})_2\text{I}_7$ (**3.18a**)

The CT salt $(\mathbf{3.4})_2\text{I}_7$ **3.18a** was prepared following the general procedure i) but using 0.21 mg (0.83 mmol) of I_2 . Yield: 0.2019 g (84%).

M.p.: 263 °C

FT-IR (KBr, cm^{-1}): 3058, 2233, 1585, 1461, 1413, 1378, 1342, 1294, 1268, 1209, 1141, 1103, 1081, 1022, 944, 833, 788, 746, 694, 636, 565, 526, 487, 460.

Elemental analysis (%): calculated for ($\text{C}_{24}\text{H}_{12}\text{I}_7\text{N}_4\text{S}_8$): C, 19.20; H, 0.81; N, 3.73; S, 17.09; I, 59.17; found: C, 19.24; H, 0.86; N, 3.50; S, 15.99; I, 59.12.

LC-MS (ESI⁺, CH₃CN, *m/z*): 305.7 [M]⁺.

6.4.11.9 Preparation of the CT salt (3.4)₂I₅ (3.18b)

The CT salt (3.4)₂I₅ **3.18b** was prepared following a modification of the general procedure ii), using 0.12 mg (0.49 mmol) of I₂ and 0.10 mg (0.33 mmol) of **3.3** in DCM (30 mL). Yield: 0.1601 g (63%).

M.p.: 270 °C

FT-IR (KBr, cm⁻¹): 3042, 2232, 1583, 1534, 1504, 1462, 1398, 1379, 1341, 1294, 1264, 1241, 1203, 1078, 1019, 834, 774, 740, 692, 634, 561, 520, 486, 432.

Elemental analysis (%): calculated for (C₂₄H₁₂I₅N₄S₈•H₂O): C, 23.01; H, 1.01; N, 4.47; S, 20.47; found: C, 22.76; H, 0.89; N, 4.44; S, 20.25.

LC-MS (ESI⁺, CH₃CN, *m/z*): 305.8 [M]⁺.

6.4.11.10 Preparation of the CT salt (3.4)I₃ (3.18c)

The CT salt (3.4)I₃ **3.18c** was prepared following a modification of the general procedure ii), using 0.12 mg (0.49 mmol) of I₂. Yield: 0.0887 g (80%).

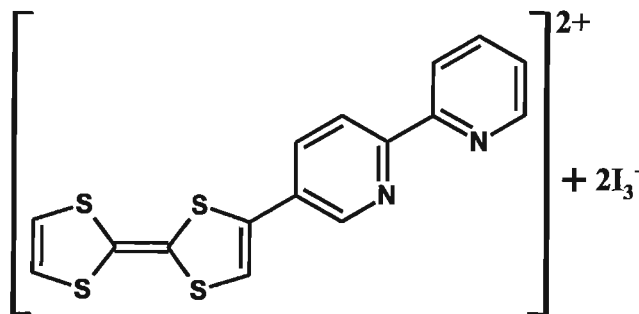
M.p.: 272 °C

FT-IR (KBr, cm⁻¹): 3050, 2233, 1585, 1535, 1490, 1463, 1429, 1378, 1342, 1295, (1267, 1205, 1141, 1083, 1024, 941, 877, 835, 790, 742, 692, 632, 565, 526, 487, 439.

Elemental analysis (%): calculated for (C₁₂H₆I₃N₂S₄): C, 20.97; H, 0.88; N, 4.08; S, 18.67; I, 55.40; found: C, 20.84; H, 0.74; N, 4.11; S, 18.52; I, 55.21.

LC-MS (ESI⁺, CH₃CN, *m/z*): 305.9 [M]⁺.

6.4.11.11 Synthesis of single crystals of the CT salt $3.8(I_3)_2$ (3.17)



A solution of **3.8** (0.020 g, 0.05 mmol) in dry DCM (10 mL) was placed in a test tube. After that 2 mL of acetone containing no solute were carefully layered on top of this solution. Finally, a solution of I_2 (0.020 g, 0.08 mmol) in acetone was carefully placed as the top layer. The test tube was then sealed and after 2 weeks a few black single crystals suitable for X-ray diffraction were collected.

6.4.11.12 Synthesis of the CT salt $(3.2)_3(PF_6)_2$ (3.19)

Compound **3.2** (76 mg, 0.24 mmol) was dissolved in a 0.22 M solution of $TBAPF_6$ in dry $CHCl_3$ (10 mL). The solution was filtered and then added to one arm of an H cell, filling the other arm with 0.22 M solution of $TBAPF_6$ in dry $CHCl_3$. The electrolysis was carried out using platinum electrodes with an initial current intensity of 2 μA for 4 days before being increased to 10 μA . The experiments were carried out in the dark and the H-cells were placed in a sandbox in order to minimize vibrations. The experiment was left undisturbed, at room temperature for 2 weeks. After this time the radical cation salt was isolated from the anode as a black polycrystalline powder. Yield: 69.7 mg (23%).

FT-IR (KBr, cm^{-1}): 3075, 2225, 1558, 1465, 1411, 1351, 1261, 1243, 1218, 1118, 1076, 1054, 1027, 885, 844, 796, 744, 557, 493, 447.

UV-Vis (DCM, nm, $\epsilon/M^{-1} cm^{-1}$): 274 (128000), 417 (12500), 446 (16500), 595 (61800).

MS (FAB, m/z): 306 ($[M]^+$, 20%).

Elemental analysis (%): calculated for (C₃₆H₁₈F₁₂N₆P₂S₁₂·0.2CHCl₃): C, 35.26; H, 1.49; F, 18.85; N, 6.82; S, 31.20; found C, 35.03; H, 1.43; F, 18.19; N, 6.76; S, 31.47.

6.4.11.13 Synthesis of the CT salt (3.4)₃(PF₆)₂ (3.20)

Compound **3.4** (69 mg, 0.22 mmol) was dissolved in a 0.22 M solution of TBAPF₆ in dry CHCl₃. The solution was filtered and then added to one arm of the H cell, filling the other arm with 0.22 M solution of TBAPF₆ in dry CHCl₃. The electrolysis was carried out using platinum electrodes with an initial current intensity of 2 μA for 4 days before it was increased to 10 μA. The electrocrystallization setup was placed in a sandbox in order to minimize vibrations and the experiment was left undisturbed for two weeks. After this time the product was collected from the anode as a black polycrystalline powder. Yield: 34.5 mg (12%).

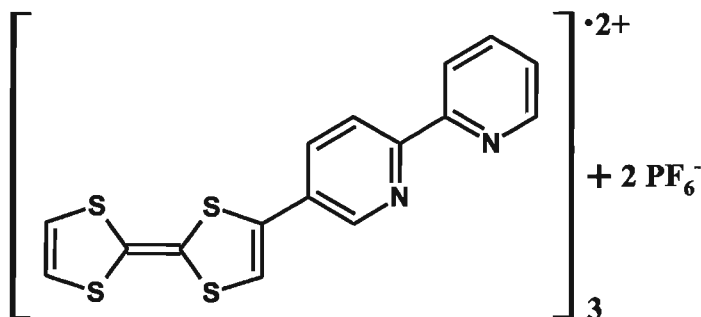
FT-IR (KBr, cm⁻¹): 3095, 2231, 1585, 1504, 1463, 1351, 1301, 1263, 1216, 1145, 1093, 1020, 848, 748, 673, 555, 489.

UV-Vis (DCM, nm, ε/M⁻¹ cm⁻¹): 297 (27400), 393 (7800), 442 (17500), 578 (8500).

MS (FAB, *m/z*): 306 ([M]⁺, 50%).

Elemental analysis: calculated for (C₃₆H₁₈F₁₂N₆P₂S₁₂·0.15CHCl₃): C, 35.38; H, 1.49; N, 6.85; S, 31.82; found C, 35.38; H, 1.49; N, 6.85; S, 31.35.

6.4.11.14 Synthesis of the CT salt (3.8)₃(PF₆)₂ (3.21)



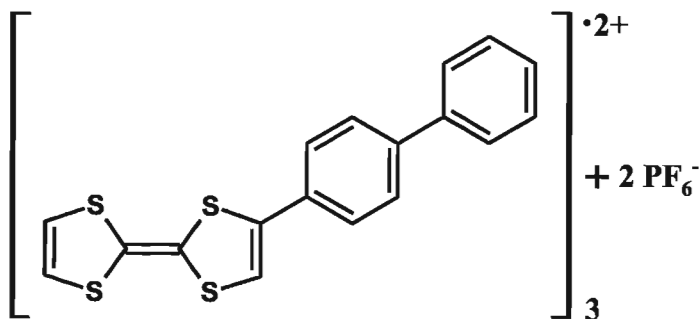
Compound **3.8** (10 mg, 0.22 mmol) was dissolved in a 0.01 M solution of TBAPF₆ in dry CHCl₃. The solution was filtered and then added to one arm of the H cell, filling the other arm with a 0.01 M solution of TBAPF₆ in dry CHCl₃. The electrolysis was carried out using platinum electrodes with an initial current intensity of 0.1 μ A. The experiments were left undisturbed in the dark at room temperature for 2 weeks. The electrocrystallization setup was placed in a sandbox in order to minimize vibrations. Black needles of the radical cation salt were collected from the anode.

FT-IR (KBr, cm⁻¹): 3090, 1582, 1499, 1432, 1357, 1224, 1121, 1092, 1064, 990, 925, 911, 841, 777, 736, 674, 556, 511, 492, 443.

UV-Vis (DCM, nm, ϵ /M⁻¹ cm⁻¹): 304 (81500), 408 (21600), 449 (27300), 618 (12500).

MS (EI, m/z): 358 ([M]⁺, 15%).

6.4.11.15 Synthesis of the CT salt (3.10)₃(PF₆)₂ (3.22)



Compound **3.10** (10 mg, 0.22 mmol) was dissolved in a 0.01 M solution of TBAPF₆ in dry CHCl₃. The solution was filtered and then added to one arm of the H cell, filling the other arm with 0.01 M solution of TBAPF₆. The electrolysis was carried out using platinum electrodes with an initial current intensity of 0.1 μ A. The electrocrystallization setup was placed in a sandbox in order to minimize vibrations. The experiments were left undisturbed in the dark at room temperature for 1 week, affording single crystals that grew on the electrodes as black needles.

FT-IR (KBr, cm^{-1}): 3093, 3025, 1644, 1600, 1523, 1475, 1403, 1353, 1268, 1216, 1101, 1076, 1000, 921, 835, 755, 690, 555, 491, 466.

UV-Vis (DCM, nm, $\epsilon/\text{M}^{-1} \text{cm}^{-1}$): 292 (78200), 409 (24800), 453 (21500), 645 (11900).

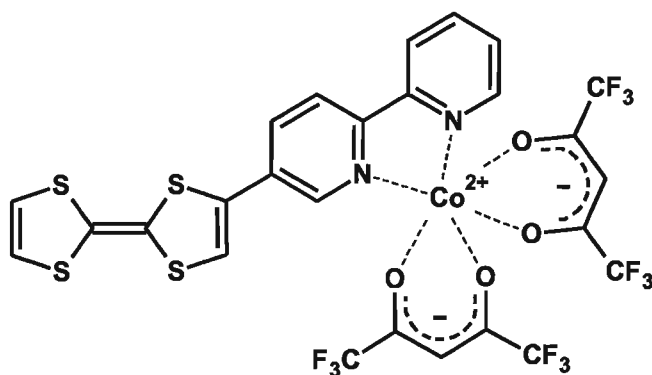
MS (EI, m/z): 356 ($[\text{M}]^+$, 19%).

6.5 Experimental for Chapter 4

6.5.1 General procedure for the preparation of complexes 4.1-4.4

In a typical reaction, compound **3.8** (50 mg, 0.14 mmol) was dissolved in THF (14 mL) and added to a solution of 1 eq. of metal salt dissolved in THF (6 mL). The resulting solution was refluxed overnight. Once the reaction had cooled to room temperature it was filtered affording the corresponding complex as a dark purple solid that was recrystallized from acetonitrile.

6.5.1.1 Synthesis of $\text{Co}(\text{3.8})(\text{hfac})_2$ complex (**4.1**)



The Co^{2+} complex **4.1** was prepared following the general procedure described above. Single crystals suitable for X-ray diffraction were obtained *via* the slow evaporation of a THF solution of the product. Yield 0.22 g (85%).

FT-IR (KBr, cm^{-1}): 3139, 3117, 1643, 1600, 1558, 1534, 1498, 1471, 1257, 1209, 1144, 1099, 1031, 908, 839, 795, 764, 667, 647, 585.

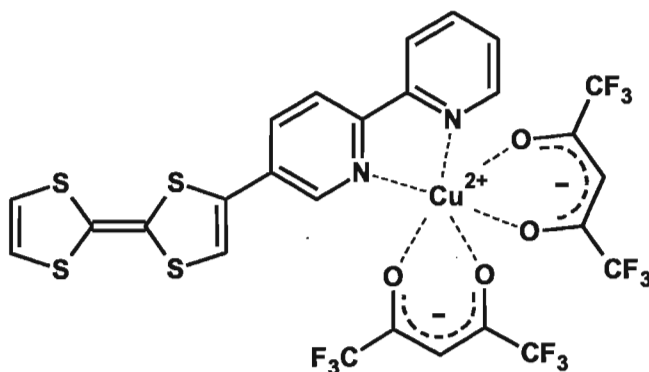
UV-Vis (CH_3CN , nm, $\epsilon/\text{M}^{-1} \text{cm}^{-1}$): 314 (36700), 500 (3000).

Elemental analysis: calculated for (C₂₆H₁₂F₁₂N₂O₄S₄Co): C, 37.55; H, 1.45; N, 3.37; S, 15.42; found C, 37.44; H, 1.29; N, 3.43; S, 15.22.

MS (MALDI-TOF, *m/z*): 624 ([M-hfac]⁺, 100).

CV (*E*_{1/2} vs. Ag/AgCl, V, CH₃CN, 0.1 mM TBAPF₆): 0.495, 0.851.

6.5.1.2 Synthesis of Cu(3.8)(hfac)₂ complex (4.2)



The Cu²⁺ complex 4.2 was prepared following the general procedure described above. Single crystals suitable for X-ray diffraction were obtained *via* the slow cooling of a hot acetonitrile solution of the product. Yield before recrystallization: 0.0734 g (62%).

FT-IR (KBr, cm⁻¹): 3077, 1669, 1603, 1552, 1530, 1494, 1468, 1397, 1372, 1337, 1261, 1229, 1199, 1128, 1088, 1024, 948, 912, 799, 767, 693, 665, 582, 526.

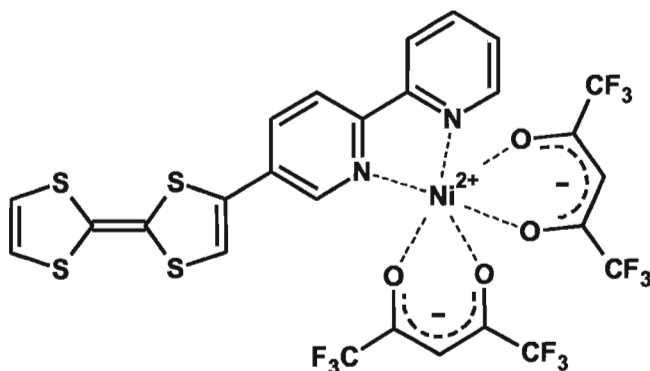
UV-Vis (CH₃CN, nm, ε/M⁻¹ cm⁻¹): 302 (45500), 313 (45000), 509 (3300).

Elemental analysis: calculated for (C₂₆H₁₂F₁₂N₂O₄S₄Cu) C, 37.35; H, 1.45; N, 3.35; found C, 37.40; H, 1.36; N, 3.45

MS (FAB, *m/z*): 836 [M]⁺, 2%), 629 ([M - hfac]⁺, 7%).

CV (*E*_{1/2} vs. Ag/AgCl, V, CH₃CN, 0.1 mM TBAPF₆): 0.505, 0.856.

6.5.1.3 Synthesis of Ni(3.8)(hfac)₂ complex (4.3)



The Ni²⁺ complex **4.3** was prepared following the general procedure described above. Single crystals suitable for X-ray diffraction were obtained *via* the slow cooling of a hot acetonitrile solution of the product. Yield before recrystallization: 0.0910 g (78%).

FT-IR (KBr, cm⁻¹): 3078, 1646, 1554, 1527, 1497, 1473, 1258, 1201, 1143, 1097, 1026, 942, 797, 765, 704, 669, 609, 585, 522.

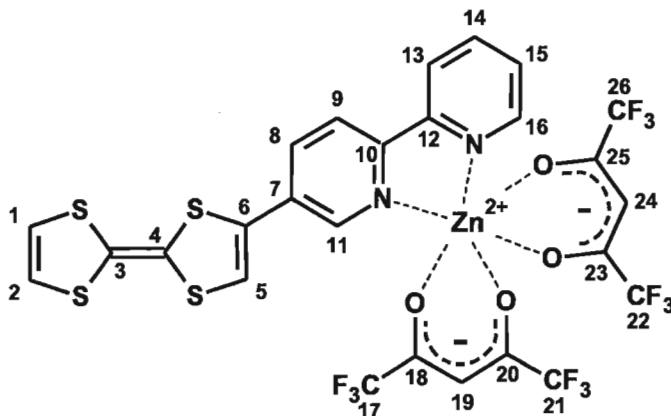
UV-Vis (CH₃CN, nm, ε/M⁻¹ cm⁻¹): 317 (44100), 504 (3600).

Elemental analysis: calculated for (C₂₆H₁₂F₁₂N₂O₄S₄Ni): C, 37.56; H, 1.45; N, 3.37; S, 15.43; found C, 37.39; H, 1.31; N, 3.49; S, 15.43.

MS (FAB, *m/z*): 693 ([M - 2xCF₃]⁺, 10%), 623 ([M - hfac]⁺, 28%)

CV (*E*_{1/2} vs. Ag/AgCl, V, CH₃CN, 0.1 mM TBAPF₆): 0.500, 0.855.

6.5.1.4 Synthesis of Zn(3.8)(hfac)₂ complex (4.4)



The Zn²⁺ complex **4.4** was prepared following the general procedure described above. Single crystals suitable for X-ray diffraction were obtained *via* the slow cooling of a hot acetonitrile solution of the product. Yield before recrystallization: 0.0896 g (76%).

¹H NMR (600 MHz, CDCl₃, ppm): 8.77 (d, *J* = 2.27 Hz, 1H, H11), 8.70 (d, *J* = 4.16 Hz, 1H, H16), 8.24 (d, *J* = 7.93 Hz, 1H, H9), 8.22 (d, *J* = 8.69 Hz, 1H, H13), 8.16 (m, 1H, H14), 7.98 (m, *J* = 8.69, 2.27 Hz, 1H, H8), 7.69 (m, *J* = 7.93, 4.16 Hz, 1H, H15), 6.90 (s, 1H, H5), 6.40 (s, 2H, H1-2), 6.02 (s, 2H, H19 and H24).

FT-IR (KBr, cm⁻¹): 3079, 1652, 1602, 1558, 1531, 1498, 1471, 1379, 1322, 1257, 1202, 1143, 1097, 1030, 939, 917 798, 765, 721, 665, 609, 583, 523.

UV-Vis (CH₃CN, nm, ε/M⁻¹ cm⁻¹): 303 (46300), 311 (46300), 489 (3200).

Elemental analysis: calculated for (C₂₆H₁₂F₁₂N₂O₄S₄Zn) C, 37.26; H, 1.44; N, 3.34; found C, 36.98; H, 1.65; N, 3.32.

MS (FAB, *m/z*): 699 ([M - 2xCF₃]⁺, 10%), 629 ([M - hfac]⁺, 7%).

CV (*E*_{1/2} vs. Ag/AgCl, V, CH₃CN, 0.1 mM TBAPF₆): 0.495, 0.851.

CHAPTER 7

References

1. G. Saito; F. Wudl; R. C. Haddon; K. Tanigaki; T. Enoki; H. E. Katz, Eds.; *Multifunctional Conducting Molecular Materials*; RSC Publishing: Cambridge, **2006**; pp 306.
2. J. S. Miller; M. Drillon, Eds.; *Magnetism: Molecules to Materials V* Wiley-VCH: Weinheim, **2005**; pp 395.
3. D. Gatteschi; L. Bogani; A. Cornia; M. Mannini; L. Sorace; R. Sessoli, *Solid State Sci.*, **2008**, *10*, 1701-1709.
- 4., R. Winpenny, Ed.; *Single-molecule magnets and related phenomena*; Structure and bonding; Springer: Berlin ;; New York, **2006**; *Vol. 122*, pp 262.
5. E. Coronado; P. Day, *Chem. Rev.*, **2004**, *104*, 5419-5448.
6. P. Gülich; H. A. Goodwin, Eds.; *Spin crossover in transition metal compounds*; *Topics in current chemistry*; Springer: Berlin ;; New York, **2004**; *Vol. 233-235*.
7. B. D. Cullity; C. D. Graham , *Introduction to magnetic materials*; IEEE/Wiley: Hoboken, N.J., 2009; , pp 544.
8. A. F. Orchard , *Magnetochemistry*; Oxford chemistry primers ; Oxford University Press: Oxford, 2003; *Vol. 75*, pp 172.
9. O. Kahn , *Molecular Magnetism*; VCH: New York, 1993; , pp 380.
10. F. E. Mabbs and D. J. Machin. , *Magnetism and transition metal complexes*; Dover Publications: Mineola, N.Y., 2008; , pp 206.
11. J. Ribas Gispert. , *Coordination chemistry*; Wiley-VCH: Weinheim, 2008; , pp 600.
12. A. Bousseksou; G. Molnar; L. Salmon; W. Nicolazzi, *Chem. Soc. Rev.*, **2011**, *40*, 3313-3335.

13. J. A. Real; A. B. Gaspar; V. Niel; M. C. Muñoz, *Coord. Chem. Rev.*, **2003**, *236*, 121-141.
14. J. Olguín; S. Brooker, *Coord. Chem. Rev.*, **2011**, *255*, 203-240.
15. A. Caneschi; D. Gatteschi; R. Sessoli; A. L. Barra; L. C. Brunel; M. Guillot, *J. Am. Chem. Soc.*, **1991**, *113*, 5873-5874.
16. M. Soler; W. Wernsdorfer; K. Abboud; J. Huffman; E. Davidson; D. Hendrickson; G. Christou, *J. Am. Chem. Soc.*, **2003**, *125*, 3576-3588.
17. R. Bagai; G. Christou, *Chem. Soc. Rev.*, **2009**, *38*, 1011-1026.
18. D. Gatteschi; R. Sessoli; A. Cornia, *Chem. Commun.*, **2000**, 725-732.
19. O. Roubeau; R. Clérac, *Eur. J. Inorg. Chem*, **2008**, *2008*, 4315-4342.
20. M. Murrie, *Chem. Soc. Rev.*, **2010**, *39*, 1986-1995.
21. G. Aromí; E. Brechin, In *Synthesis of 3d Metallic Single-Molecule Magnets*; R. Winpenny , Ed.; Single-Molecule Magnets and Related Phenomena; Springer Berlin / Heidelberg: 2006; Vol. 122, pp 1-67.
22. G. Christou; D. Gatteschi; D. N. Hendrickson; R. Sessoli, *MRS Bull*, **2011**; **2000**, *25*, 66-71.
23. E. Rodriguez; A. Roig; E. Molins; C. Arus; M. R. Quintero; M. E. Cabanas; S. Cerdan; P. López-Larrubia; C. Sanfeliu, *NMR Biomed.*, **2005**, *18*, 300-307.
24. S. Isaacman; R. Kumar; E. d. Barco; A. D. Kent; J. W. Canary; A. Jerschow, *Polyhedron*, **2005**, *24*, 2691-2694.
25. B. Cage; S. E. Russek; R. Shoemaker; A. J. Barker; C. Stoldt; V. Ramachandaran; N. S. Dalal, *Polyhedron*, **2007**, *26*, 2413-2419.
26. J. E. Mertzman; S. Kar; S. Lofland; T. Fleming; E. Van Keuren; Y. Y. Tong; S. L. Stoll, *Chem. Commun.*, **2009**, (7), 788-790.

27. J. Crossgrove; W. Zheng, *NMR Biomed.*, **2004**, *17*, 544-553.
28. A. L. Gavrilova; B. Bosnich, *Chem. Rev.*, **2004**, *104*, 349-384.
29. E. Pardo; R. Ruiz-Garcia; J. Cano; X. Ottenwaelder; R. Lescouezec; Y. Journaux; F. Lloret; M. Julve, *Dalton Trans.*, **2008**, 2780-2805.
30. M. A. Halcrow, *Chem. Soc. Rev.*, **2011**, *40*, 4119-4142.
31. L. K. Thompson, *Coord. Chem. Rev.*, **2002**, *233-234*, 193.
32. A. Palij; B. Tsukerblat; S. Klokishner; K. R. Dunbar; J. M. Clemente-Juan; E. Coronado, *Chem. Soc. Rev.*, **2011**, *40*, 3130-3156.
33. T. P. Hanusa, In *Cyanide Complexes of the Transition Metals*; Encyclopedia of Inorganic Chemistry; John Wiley & Sons, Ltd: Published Online: 15 MAR 2006, 2006; .
34. X. Wang; C. Avendano; K. R. Dunbar, *Chem. Soc. Rev.*, **2011**, *40*, 3213-3238.
35. M. Pilkington; S. Decurtins, In *A Rational Approach for the Self-Assembly of Molecular Building Blocks in the Field of Molecule-Based Magnetism*; G. R. Desiraju, Ed.; *Crystal design :structure and function*; Wiley: Chichester, West Sussex, England ;; Hoboken, NJ, 2003; Vol. 7, pp 408-324.
36. A. Ludi, *Chimia*, **1972**, *26*, 647-647.
37. M. Pilkington; M. Gross; P. Franz; M. Biner; S. Decurtins; H. Stoeckli-Evans; A. Neels, *J. Solid State Chem.*, **2001**, *159*, 262.
38. W. D. Geiebler; D. Badel, *Z. Naturforsch, Teil B*, **1982**, *87*, 832-835.
39. S. M. Holmes; G. S. Girolami, *J. Am. Chem. Soc.*, **1999**, *121*, 5593-5594.
40. O. Sato; T. Iyoda; A. Fujishima; K. Hashimoto, *Science*, **1996**, *272*, 704-705.

41. M. Ohba; H. Ōkawa; N. Fukita; Y. Hashimoto, *J. Am. Chem. Soc.*, **1997**, *119*, 1011-1019.
42. J. A. Smith; J. Galán-Mascarós; R. Clérac; J. Sun; X. Ouyang; K. R. Dunbar, *Polyhedron*, **2001**, *20*, 1727.
43. K. V. Langenberg; S. R. Batten; K. J. Berry; D. C. R. Hockless; B. Moubaraki; K. S. Murray, *Inorg. Chem.*, **1997**, *36*, 5006-5015.
44. E. Colacio; M. Ghazi; H. Stoeckli-Evans; F. Lloret; J. M. Moreno; C. Pérez, *Inorg. Chem.*, **2001**, *40*, 4876-4883.
45. E. Colacio; J. M. Dominguez-Vera; M. Ghazi; J. M. Moreno; R. Kivekas; M. Klinga, *Chem. Commun.*, **1998**, 1071-1072.
46. T. Mallah; C. Auberger; M. Verdaguer; P. Veillet, *Chem. Commun.*, **1995**, 61-62.
47. S. Decurtins; R. Pellaux; G. Antorrena; F. Palacio, *Coord. Chem. Rev.*, **1999**, *190-192*, 841.
48. M. Clemente-Léon; E. Coronado; C. Martí-Gastaldo; F. M. Romero, *Chem. Soc. Rev.*, **2011**, *40*, 473-497.
49. H. Tamaki; M. Mitsumi; K. Nakamura; N. Matsumoto; S. Kida; H. Okawa; S. Iijima, *Chem. Lett.*, **1992**, *10*, 1975-1978.
50. C. Mathonière; C. J. Nuttall; S. G. Carling; P. Day, *Inorg. Chem.*, **1996**, *35*, 1201-1206.
51. H. Tamaki; Z. J. Zhong; N. Matsumoto; S. Kida; M. Koikawa; N. Achiwa; Y. Hashimoto; H. Okawa, *J. Am. Chem. Soc.*, **1992**, *114*, 6974-6979.
52. C. J. Nuttall; C. Bellitto; P. Day, *Chem. Commun.*, **1995**, 1513-1514.
53. M. Clemente-Léon; E. Coronado; M. C. Giménez-López; A. Soriano-Portillo; J. C. Waerenborgh; F. S. Delgado; C. Ruiz-Pérez, *Inorg. Chem.*, **2008**, *47*, 9111-9120.

54. R. Clément; S. Decurtins; M. Gruselle; C. Train, *Monatsh. Chem.*, **2003**, *134*, 117-135.
55. R. S. Fishman; M. Clemente-León; E. Coronado, *Inorg. Chem.*, **2009**, *48*, 3039-3046.
56. R. Sieber; S. Decurtins; H. Stoeckli-Evans; C. Wilson; D. Yufit; J. A. K. Howard; S. C. Capelli; A. Hauser, *Chem. Eur. J.*, **2000**, *6*, 361-368.
57. G. Wilkinson; R. D. Gillard; J. A. McCleverty, Eds.; , *Comprehensive coordination chemistry :the synthesis, reactions, properties, and applications of coordination compounds*; Pergamon Press: Oxford, England ;; New York, **1987**; Vol. 2.
58. E. C. Constable; P. J. Steel, *Coord. Chem. Rev.*, **1989**, *93*, 205-223.
59. C. Kaes; A. Katz; M. W. Hosseini, *Chem. Rev.*, **2000**, *100*, 3553-3590.
60. G. Newkome; A. Patri; E. Holder; U. Schubert, *Eur. J. Org. Chem.*, **2004**, *2004*, 235-254.
61. N. C. Fletcher, *J. Chem. Soc. Perkin Trans. 1*, **2002**, 1831-1842.
62. R. Ziessel, *Coord. Chem. Rev.*, **2001**, *216-217*, 195-223.
63. M. H. Keefe; K. D. Benkstein; J. T. Hupp, *Coord. Chem. Rev.*, **2000**, *205*, 201-228.
64. P. D. Beer; J. Cadman, *Coord. Chem. Rev.*, **2000**, *205*, 131-155.
65. U. Knof; A. von Zelewsky, *Angew. Chem. Int. Ed.*, **1999**, *38*, 302-322.
66. M. D. Ward; C. M. White; F. Barigelletti; N. Armaroli; G. Calogero; L. Flamigni, *Coord. Chem. Rev.*, **1998**, *171*, 481-488.
67. K. Kalyanasundaram; M. Grätzel, *Coord. Chem. Rev.*, **1998**, *177*, 347-414.
68. D. C. Craig; H. A. Goodwin; D. Onggo, *Aust. J. Chem.*, **1988**, *41*, 1157-1169.
69. R. Goddard; B. Hemalatha; M. V. Rajasekharan, *Acta Cryst.*, **1990**, *C46*, 33-35; S. Menon; M. V. Rajasekharan; J. -. Tuchagues, *Inorg. Chem.*, **1997**, *36*, 4341-4346; K.

- Ravikumar; G. Swamy; N. Lakshmi; K. Chandramohan, *J. Chem. Cryst.*, **1997**, *27*, 119-124; K. Ravikumar; G. Y. S. K. Swamy; N. Venkata Lakshmi, *Acta Cryst.*, **1995**, *C51*, 608-611; J. Yoo; J. Kim; Y. S. Sohn; Y. Do, *Inorg. Chim. Acta*, **1997**, *263*, 53-60; C. Zhang; H. Mao; J. Wang; H. Zhang; J. Tao, *Inorg. Chim. Acta*, **2007**, *360*, 448-454; G. Zhang; Y. Wei; P. Wang; H. Guo, *Acta Cryst.*, **2002**, *C58*, m605-m607; Z. J. Zhong; X. You; T. C. W. Mak, *Polyhedron*, **1994**, *13*, 2157; Z. J. Zhong; X. You; Q. Yang, *Polyhedron*, **1994**, *13*, 1951-1955.
70. S. Decurtins; H. W. Schmalle; L. Zheng; J. Ensling, *Inorg. Chim. Acta*, **1996**, *244*, 165-170; E. A. M. Geary; L. J. Yellowlees; L. A. Jack; I. D. H. Oswald; S. Parsons; N. Hirata; J. R. Durrant; N. Robertson, *Inorg. Chem.*, **2005**, *44*, 242-250; V. M. Miskowski; V. H. Houlding; C. M. Che; Y. Wang, *Inorg. Chem.*, **1993**, *32*, 2518-2524; L. Toupet; P. Dixneuf; M. Akkurt; M. Daoudi; N. Sam; A. Kerbal; Z. Chohan; T. Hadda, *J. Chem. Cryst.*, **2009**, *39*, 423-427; B. Wu; Y. Zhou; L. Han; M. Hong, *Acta Cryst.*, **2004**, *E60*, m1365-m1366; C. Zhang; H. Mao; J. Wang; H. Zhang; J. Tao, *Inorg. Chim. Acta*, **2007**, *360*, 448-454.
71. T. Bugarcic; A. Habtemariam; J. Stepankova; P. Heringova; J. Kasparikova; R. J. Deeth; R. D. L. Johnstone; A. Prescimone; A. Parkin; S. Parsons; V. Brabec; P. J. Sadler, *Inorg. Chem.*, **2008**, *47*, 11470-11486; C. Hou; J. Shi; Y. Sun; W. Shi; P. Cheng; L. Liu, **2008**, 5970-5976; M. D. Stephenson; M. J. Hardie, **2007**, *9*, 496-502; S. G. Zhang; C. Hou, *Acta Cryst.*, **2008**, *E64*, m1131.
72. a) S. S. Alguindigue; M. A. Khan; M. T. Ashby, *Inorg. Chim. Acta*, **2000**, *310*, 156-162; b) S. J. Min; C. J. Na; L. L. Dong, *Acta Cryst.*, **2006**, *E62*, m1810-m1811; c) C. Rice; S. Onions; N. Vidal; J. Wallis; M. Senna; M. Pilkington; H. Stoeckli-Evans, *Eur. J. Inorg. Chem.*, **2002**, *2002*, 1985-1997; d) J. Shi; J. Chen; L. Liu, *Acta Cryst.*, **2006**, *E62*, m2094-m2095; e) J. Shi; J. Chen; L. Liu, *Acta Cryst.*, **2006**, *E62*, m2151-m2152; f) C. Wu; J. Chen; J. Shi, *Acta Cryst.*, **2007**, *E63*, m2668-m2668; g) S. Zhang; J. Chen; J. Shi, *Acta Cryst.*, **2007**, *E63*, m1945-m1945.
73. A. M. W. C. Thompson; J. C. Jeffery; D. J. Liard; M. D. Ward, *J. Chem. Soc., Dalton Trans.*, **1996**, 879-884.

74. K. Rurack; R. Radeglia, *Eur. J. Inorg. Chem.*, **2000**, 2000, 2271-2282.
75. D. Parker; R. S. Dickins; H. Puschmann; C. Crossland; J. A. K. Howard, *Chem. Rev.*, **2002**, 102, 1977-2010.
76. C. M. G. d. Santos; A. J. Harte; S. J. Quinn; T. Gunnlaugsson, *Coord. Chem. Rev.*, **2008**, 252, 2512-2527.
77. L. Sorace; C. Benelli; D. Gatteschi, *Chem. Soc. Rev.*, **2011**, 40, 3092-3104.
78. O. Jung; S. H. Park; Y. Lee; D. C. Kim, *J. Mol. Struct.*, **2003**, 645, 281-285.
79. Ł. John; P. Sobota, In *Chapter 4: Alkoxide Molecular Precursors for Nanomaterials: A One Step Strategy for Oxide Ceramics*; Wunderlich, W., Ed.; Ceramic Materials; Sciyo: www.intechopen.com, 2010; pp 69-86.
80. T. J. Boyle; L. A. M. Ottley; M. A. Rodriguez, *Polyhedron*, **2008**, 27, 3079-3084.
81. R. J. Kuppler; D. J. Timmons; Q. Fang; J. Li; T. A. Makal; M. D. Young; D. Yuan; D. Zhao; W. Zhuang; H. Zhou, *Coord. Chem. Rev.*, **2009**, 253, 3042-3066.
82. M. Kurmoo, *Chem. Soc. Rev.*, **2009**, 38, 1353-1379.
83. J. L. C. Rowsell; O. M. Yaghi, *Microporous Mesoporous Mater.*, **2004**, 73, 3-14.
84. B. Ji; D. Deng; H. Lan; C. Du; S. Pan; B. Liu, *Crystal Growth & Design*, **2010**, 10, 2851-2853.
85. C. J. Baylies; J. C. Jeffery; T. A. Miller; R. Moon; C. R. Rice; T. Riis-Johannessen, *Chem. Commun.*, **2005**, 4158-4160.
86. C. J. Baylies; T. Riis-Johannessen; L. P. Harding; J. C. Jeffery; R. Moon; C. R. Rice; M. Whitehead, *Angew. Chem. Int. Ed.*, **2005**, 44, 6909-6912.
87. C. J. Baylies; L. P. Harding; J. C. Jeffery; R. Moon; C. R. Rice; T. Riis-Johannessen, *New J. Chem.*, **2007**, 31, 1525-1529.

88. C. R. Rice; C. J. Baylies; L. P. Harding; J. C. Jeffery; R. L. Paul; M. D. Ward, *J. Chem. Soc. , Dalton Trans.*, **2001**, 3039-3044.
89. C. R. Rice; S. Worl; J. C. Jeffery; R. L. Paul; M. D. Ward, *J. Chem. Soc. , Dalton Trans.*, **2001**, 550-559.
90. C. Rice; S. Onions; N. Vidal; J. Wallis; M. Senna; M. Pilkington; H. Stoeckli-Evans, *Eur. J. Inorg. Chem.*, **2002**, 2002, 1985-1997.
91. H. J. Clayton; L. P. Harding; J. P. Irvine; J. C. Jeffery; T. Riis-Johannessen; A. P. Laws; C. R. Rice; M. Whitehead, *Chem. Commun.*, **2008**, 108-110.
92. J. Rebek; T. Costello; R. Wattle, *J. Am. Chem. Soc.*, **1985**, 107, 7487-7493.
93. C. E. Felton; L. P. Harding; J. E. Jones; B. M. Kariuki; S. J. A. Pope; C. R. Rice, *Chem. Commun.*, **2008**, 6185-6187.
94. P. G. Cozzi, *Chem. Soc. Rev.*, **2004**, 33, 410-421; R. E. P. Winpenny, *Chem. Soc. Rev.*, **1998**, 27, 447-452; A. D. Garnovskii; I. S. Vasilchenko; D. A. Garnovskii; B. I. Kharisov, **2009**, 62, 151-204; L. F. Lindoy, **1971**, 25, 379-391; C. D. Meyer; C. S. Joiner; J. F. Stoddart, *Chem. Soc. Rev.*, **2007**, 36, 1705-1723; P. A. Vigato; S. Tamburini, *Coord. Chem. Rev.*, **2004**, 248, 1717; S. Yamada, *Coord. Chem. Rev.*, **1999**, 190-192, 537.
95. J. Wang; S. Onions; M. Pilkington; H. Stoeckli-Evans; J. C. Halfpenny; J. D. Wallis, *Chem. Commun.*, **2007**, 3628-3630.
96. J. Wang; B. Djukic; J. Cao; A. Alberola; F. S. Razavi; M. Pilkington, *Inorg. Chem.*, **2007**, 46, 8560-8568.
97. J. Yamada and T. Sugimoto. , *TTF chemistry :fundamentals and applications of tetrathiafulvalene*; Kodansha ;: Tokyo, 2004; , pp 445.
98. M. R. Bryce, *Chem. Soc. Rev.*, **1991**, 20, 355-390.
99. M. Bendikov; F. Wudl; D. F. Perepichka, *Chem. Rev.*, **2004**, 104, 4891-4946.

100. J. L. Segura; N. Martín, *Angew. Chem. Int. Ed.*, **2001**, *40*, 1372-1409.
101. J. O. Jeppesen; M. B. Nielsen; J. Becher, *Chem. Rev.*, **2004**, *104*, 5115-5132.
102. T. Enoki; A. Miyazaki, *Chem. Rev.*, **2004**, *104*, 5449-5478.
103. M. R. Bryce, *Adv Mater*, **1999**, *11*, 11-23.
104. J. Ferraris; D. O. Cowan; V. Walatka; J. H. Perlstein, *J. Am. Chem. Soc.*, **1973**, *95*, 948-949.
105. a) D. Jérôme, *Chem. Rev.*, **2004**, *104*, 5565-5592; b) A. J. Schultz; G. D. Stucky; R. H. Blessing; P. Coppens, *J. Am. Chem. Soc.*, **1976**, *98*, 3194-3201.
106. K. Bechgaard; C. S. Jacobsen; K. Mortensen; H. J. Pedersen; N. Thorup, *Solid State Commun.*, **1980**, *33*, 1119-1125.
107. H. Kobayashi; H. Cui; A. Kobayashi, *Chem. Rev.*, **2004**, *104*, 5265-5288.
108. P. Day; M. Kurmoo; T. Mallah; I. R. Marsden; R. H. Friend; F. L. Pratt; W. Hayes; D. Chasseau; J. a. Gaultier, *J. Am. Chem. Soc.*, **1992**, *114*, 10722-10729.
109. H. Kobayashi; H. Tomita; T. Naito; A. Kobayashi; F. Sakai; T. Watanabe; P. Cassoux, *J. Am. Chem. Soc.*, **1996**, *118*, 368-377.
110. E. Coronado; J. Galán-Mascarós; C. Gomez-Garcia; V. Laukhin, *Nature*, **2000**, *408*, 447-449.
111. M. Kurmoo; A. W. Graham; P. Day; S. J. Coles; M. B. Hursthouse; J. L. Caulfield; J. Singleton; F. L. Pratt; W. a. Hayes, *J. Am. Chem. Soc.*, **1995**, *117*, 12209-12217.
112. T. Sugimoto; H. Fujiwara; S. Noguchi; K. Murata, *Sci. Technol. Adv. Mater.*, **2009**, *10*, 024302.
113. L. Ouahab; F. Iwahori; S. Golhen; R. Carlier; J. Sutter, *Synth. Met.*, **2003**, *133-134*, 505-507.

114. J. Balandier; A. Belyasmine; M. Sallé, *Eur. J. Org. Chem.*, **2008**, 2008, 269-276.
115. S. Bouguessa; A. K. Gouasmia; L. Ouahab; S. Golhen; J. Fabre, *Synth. Met.*, **2010**, *160*, 361-367.
116. L. Wang; B. Zhang; J. Zhang, *Inorg. Chem.*, **2006**, *45*, 6860-6863.
117. T. Devic; N. Avarvari; P. Batail, *Chem. Eur. J.*, **2004**, *10*, 3697-3707.
118. T. Murata; Y. Morita; K. Fukui; K. Sato; D. Shiomi; T. Takui; M. Maesato; H. Yamochi; G. Saito; K. Nakasuji, *Angew. Chem. Int. Ed.*, **2004**, *43*, 6343-6346.
119. G. Huang; D. Zhang; G. Zhang; D. Zhu, *Chin. J. Chem.*, **2010**, *28*, 1743-1750.
120. C. Goze; S. Liu; C. Leiggener; L. Sanguinet; E. Levillain; A. Hauser; S. Decurtins, *Tetrahedron*, **2008**, *64*, 1345-1350.
121. Q. Wang; P. Day; J. Griffiths; H. Nie; J. D. Wallis, **2006**, *30*, 1790-1800.
122. L. K. Keniley; L. Ray; K. Kovnir; L. A. Dellinger; J. M. Hoyt; M. Shatruk, *Inorg. Chem.*, **2010**, *49*, 1307-1309.
123. N. Bellec; J. Massue; T. Roisnel; D. Lorcy, *Inorg. Chem. Commun.*, **2007**, *10*, 1172-1176.
124. L. Jia; G. Zhang; D. Zhang; J. Xiang; W. Xu; D. Zhu, *Chem. Commun.*, **2011**, *47*, 322-324.
125. P. Pellon; G. Gachot; J. Le Bris; S. Marchin; R. Carlier; D. Lorcy, *Inorg. Chem.*, **2003**, *42*, 2056-2060.
126. Y. Zhao; L. Wu; G. Si; Y. Liu; H. Xue; L. Zhang; C. Tung, *J. Org. Chem.*, **2007**, *72*, 3632-3639.
127. G. Cosquer; F. Pointillart; Y. Le Gal; S. Golhen; O. Cador; L. Ouahab, *Dalton Trans.*, **2009**, 3495-3502; J. Galán-Mascarós; E. Coronado; P. A. Goddard; J. Singleton; A. I. Coldea; J. D. Wallis; S. J. Coles; A. Alberola, *J. Am. Chem. Soc.*,

- 2010, 132, 9271-9273; S. Ichikawa; K. Takahashi; M. Matsuda; H. Tajima; H. Mori, 2010, 20, 10130-10134; J. Qin; C. Qian; N. Zhou; R. Zhu; Y. Li; J. Zuo; X. You, 2012, 2012, 234-245; S. Wang; W. He; W. Huang, *J. Chem. Cryst.*, 2011, 41, 430-433; Y. Wang; S. Cui; B. Li; J. Zhang; Y. Zhang, 2009, 9, 3855-3858.
128. M. Chahma; N. Hassan; A. Alberola; H. Stoeckli-Evans; M. Pilkington, *Inorg. Chem.*, 2007, 46, 3807-3809.
129. S. Bakhta; M. Guerro; B. Kolli; F. Barrière; T. Roisnel; D. Lorcy, *Tetrahedron Lett.*, 2010, 51, 4497-4500.
130. F. Pointillart; T. Cauchy; Y. L. Gal; S. Golhen; O. Cador; L. Ouahab, *Inorg. Chem.*, 2010, 49, 1947-1960.
131. M. Shatruk; L. Ray, *Dalton Trans.*, 2010, 39, 11105-11121.
132. D. Lorcy; N. Bellec; M. Fourmigué; N. Avarvari, *Coord. Chem. Rev.*, 2009, 253, 1398-1438.
133. N. Benbellat; K. S. Gavrilenko; Y. Le Gal; O. Cador; S. Golhen; A. Gouasmia; J. Fabre; L. Ouahab, *Inorg. Chem.*, 2006, 45, 10440-10442.
134. K. S. Gavrilenko; Y. L. Gal; O. Cador; S. Golhen; L. Ouahab, *Chem. Commun.*, 2007, 280-282.
135. F. Setifi; L. Ouahab; S. Golhen; Y. Yoshida; G. Saito, *Inorg. Chem.*, 2003, 42, 1791-1793.
136. K. Hervé; Y. L. Gal; L. Ouahab; S. Golhen; O. Cador, *Synth. Met.*, 2005, 153, 461.
137. S. Golhen; O. Cador; L. Ouahab, In *Electroactive Paramagnetic Complexes as Molecular Bricks for π -d Conducting Magnets*; Fourmigué, M., Ouahab, L., Eds.; Conducting and Magnetic Organometallic Molecular Materials; Springer Berlin / Heidelberg: 2009; Vol. 27, pp 55-75.

138. S. Ichikawa; S. Kimura; H. Mori; G. Yoshida; H. Tajima, *Inorg. Chem.*, **2006**, *45*, 7575-7577.
139. M. Y. Ogawa; B. M. Hoffman; S. Lee; M. Yudkowsky; W. P. Halperin, *Phys. Rev. Lett.*, **1986**, *57*, 1177-1180.
140. M. Fourmigué; P. Batail, *Chem. Rev.*, **2004**, *104*, 5379-5418.
141. T. Devic; D. Rondeau; Y. Sahin; E. Levillain; R. Clérac; P. Batail; N. Avarvari, *Dalton Trans.*, **2006**, 1331-1337.
142. K. Hervé; S. Liu; O. Cador; S. Golhen; Y. Le Gal; A. Bousseksou; H. Stoeckli-Evans; S. Decurtins; L. Ouahab, *Eur. J. Inorg. Chem.*, **2006**, *2006*, 3498-3502.
143. A. Alberola; M. Pilkington, *Curr. Org. Synth.*, **2009**, *6*, 66-78.
144. R. Kumai; M. M. Matsushita; A. Izuoka; T. Sugawara, *J. Am. Chem. Soc.*, **1994**, *116*, 4523-4524.
145. J. Nakazaki; M. M. Matsushita; A. Izuoka; T. Sugawara, *Tetrahedron Lett.*, **1999**, *40*, 5027-5030.
146. F. Matsuoka; Y. Yamashita; T. Kawakami; Y. Kitagawa; Y. Yoshioka; K. Yamaguchi, *Polyhedron*, **2001**, *20*, 1169-1176.
147. V. Polo; A. Alberola; J. Andres; J. Anthony; M. Pilkington, *Phys. Chem. Chem. Phys.*, **2008**, *10*, 857-864.
148. M. Kitano; Y. Ishimaru; K. Inoue; N. Koga; H. Iwamura, *Inorg. Chem.*, **1994**, *33*, 6012-6019.
149. Y. Ishimaru; M. Kitano; H. Kumada; N. Koga; H. Iwamura, *Inorg. Chem.*, **1998**, *37*, 2273-2280.
150. H. Kumada; A. Sakane; N. Koga; H. Iwamura, *J. Chem. Soc. , Dalton Trans.*, **2000**, 911-914.

151. S. Adugna; K. Revunova; B. Djukic; S. I. Gorelsky; H. A. Jenkins; M. T. Lemaire, *Inorg. Chem.*, **2010**, *49*, 10183-10190.
152. M. Dul; E. Pardo; R. Lescouëzec; Y. Journaux; J. Ferrando-Soria; R. Ruiz-García; J. Cano; M. Julve; F. Lloret; D. Cangussu; C. L. M. Pereira; H. O. Stumpf; J. Pasán; C. Ruiz-Pérez, *Coord. Chem. Rev.*, **2010**, *254*, 2281-2296.
153. M. Kettunen; C. Vedder; H. Brintzinger; I. Mutikainen; M. Leskelä; T. Repo, *Eur. J. Inorg. Chem.*, **2005**, 1081-1089.
154. H. Zhang; L. Chen; H. Song; G. Zi, *Inorg. Chim. Acta*, **2011**, *366*, 320-336.
155. H. L. Li, *Acta Cryst.*, **2009**, *E65*, o2290.
156. M. Aydemir; F. Durap; A. Baysal; N. Meric; A. Buldağ; B. Gümgüm; S. Özkar; L. T. Yıldırım, *J. Mol. Catal. A: Chem.*, **2010**, *326*, 75-81.
157. A. Orita; J. Otera, In *Tin in Organic Synthesis*; Yamamoto, H., Oshima, K., Eds.; Main Group Metals in Organic Synthesis; Wiley-VCH Verlag GmbH & Co. KGaA: Weinheim, Germany, 2005; pp 621-720.
158. T. Mukaiyama; S. Kobayashi, In Trost, B. M., Ed.; *Stereocontrolled Organic Synthesis*; Blackwell Scientific Publications: Oxford, 1994; pp 37-65.
159. T. N. Mitchell, In *Organotin reagents in cross-coupling*; Meijere, A. d., Diederich, F., Eds.; Wiley-VCH Verlag GmbH: Weinheim, Germany, 1998; pp 167-202.
160. D. A. Atwood; J. A. Jegier; K. J. Martin; D. Rutherford, *J. Organomet. Chem.*, **1995**, *503*, 4-C7.
161. M. C. Kuchta; J. M. Hahn; G. Parkin, *J. Chem. Soc. , Dalton Trans.*, **1999**, 3559-3563.
162. D. Agustin; G. Rima; H. Gornitzka; J. Barrau, *J. Organomet. Chem.*, **1999**, *592*, 1-10.
163. A. van den Bergen; R. J. Cozens; K. S. Murray, *J. Chem. Soc. A*, **1970**, 3060-3064.

164. C. Qi; X. Sun; S. Gao; S. Ma; D. Yuan; C. Fan; H. Huang; W. Zhu, *Eur. J. Inorg. Chem.*, **2007**, 2007, 3663-3668.
165. A. Majumder; M. Westerhausen; A. N. Kneifel; J. Sutter; N. Daro; S. Mitra, *Inorg. Chim. Acta*, **2006**, 359, 3841-3846.
166. A. B. P. Lever. , *Inorganic electronic spectroscopy*;
; Elsevier: Amsterdam ;; New York, 1984; Vol. 33, pp 863.
167. B. Shin; Y. Kim; M. Kim; J. Han, *Polyhedron*, **2007**, 26, 4557-4566.
168. L. Wang; C. Zhang; Z. Liu; D. Liao; Z. Jiang; S. Yan, *Inorg. Chem. Commun.*, **2003**, 6, 1255-1258.
169. P. L. Pawlak; M. Panda; R. Loloee; B. E. Kucera; J. Costes; J. Tuchagues; F. A. Chavez, **2011**, 40, 2926-2931.
170. S. Onaka; L. Hong; M. Ito; T. Sunahara; H. Imai; K. Inoue, *J. Coord. Chem.*, **2005**, 58, 1523-1530.
171. G. A. v. Albada; A. Mohamadou; W. L. Driessen; R. d. Gelder; S. Tanase; J. Reedijk, *Polyhedron*, **2004**, 23, 2387-2391.
172. S. Ma; S. Ren; Y. Yang, *J. Inorg. Organomet. Polym.*, **2010**, 20, 104-109.
173. K. D. Karlin; B. I. Cohen, *Inorg. Chim. Acta*, **1985**, 107, 17-20.
174. T. N. Sorrell; C. O'Connor; O. P. Anderson; J. H. Reibenspies, *J. Am. Chem. Soc.*, **1985**, 107, 4199-4206.
175. E. Spodine; A. M. Atria; O. Pena; H. L'Helgouach; M. T. Garland, *J. Chem. Soc. , Dalton Trans.*, **1989**, 1435-1438.
176. M. T. Garland; J. Y. Le Marouille; E. Spodine, *Acta Cryst.*, **1986**, C42, 1518-1520.
177. H. P. Berends; D. W. Stephan, *Inorg. Chem.*, **1987**, 26, 749-754.

178. E. Spodine; A. M. Atria; O. Pena; H. L'Helgouach; M. T. Garland, *J. Chem. Soc., Dalton Trans.*, **1989**, 1435-1438.
179. R. K. Dean; C. I. Fowler; K. Hasan; K. Kerman; P. Kwong; S. Trudel; D. B. Leznoff; H. Kraatz; L. N. Dawe; C. M. Kozak, **2012**, *41*, 4806-4816.
180. J. Nishio; H. Ōkawa; S. Ohtsuka; M. Tomono, *Inorg. Chim. Acta*, **1994**, *218*, 27-32.
181. R. E. Norman; R. C. Holz; S. Menage; L. Que; J. H. Zhang; C. J. O'Connor, *Inorg. Chem.*, **1990**, *29*, 4629-4637.
182. A. W. Addison; T. N. Rao; J. Reedijk; J. van Rijn; G. C. Verschoor, *J. Chem. Soc., Dalton Trans.*, **1984**, 1349-1356.
183. M. Chahma; X. Wang; A. van der Est; M. Pilkington, *J. Org. Chem.*, **2006**, *71*, 2750-2755.
184. Fourmigué, M. In *Halogen Bonding in Conducting or Magnetic Molecular Materials*; Metrangolo, P., Resnati, G., Eds.; Structure and Bonding; Springer Berlin / Heidelberg: 2008; Vol. 126, pp 181-207.
185. T. Devic; J. N. Bertran; B. Domercq; E. Canadell; N. Avarvari; P. Auban-Senzier; M. Fourmigué, *New J. Chem.*, **2001**, *25*, 1418-1424.
186. N. Terkia-Derdra; R. Andreu; M. Sallé; E. Levillain; J. Orduna; J. Garín; E. Ortí; R. Viruela; R. Pou-Amérigo; B. Sahraoui; A. Gorgues; J. Favard; A. Riou, *Chem. Eur. J.*, **2000**, *6*, 1199-1213.
187. Z. J. Zhong; X. -. You; K. Yu, *Acta Cryst.*, **1996**, *B52*, 449-451.
188. G. Cooke; A. K. Powell; S. L. Heath, *Synthesis*, **1995**, 1411-1413.
189. B. A. Scott; F. B. Kaufman; E. M. Engler, *J. Am. Chem. Soc.*, **1976**, *98*, 4342-4344.
190. S. Yoneda; T. Kawase; M. Inaba; Z. Yoshida, *J. Org. Chem.*, **1978**, *43*, 595-598.

191. M. Iyoda; Y. Kuwatani; N. Ueno; M. Oda, *J. Chem. Soc. , Chem. Commun.*, **1992**, 158-159.
192. P. K. Poddutoori; A. S. D. Sandanayaka; N. Zarrabi; T. Hasobe; O. Ito; A. van der Est, *J. Phys. Chem. A*, **2011**, *115*, 709-717.
193. B. Albinsson; J. Mårtensson, *J. Photochem. Photobiol. , C*, **2008**, *9*, 138-155.
194. B. Noda; M. Katsuhara; I. Aoyagi; T. Mori; T. Taguchi; T. Kambayashi; K. Ishikawa; H. Takezoe, *Chem. Lett.*, **2005**, *34*, 392-393.
195. B. Noda; H. Wada; K. Shibata; T. Yoshino; M. Katsuhara; I. Aoyagi; T. Mori; T. Taguchi; T. Kambayashi; K. Ishikawa; H. Takezoe, *Nanotechnology*, **2007**, *18*, 424009-424019.
196. H. Tamura; T. Watanabe; K. Imanishi; M. Sawada, *Synth. Met.*, **1999**, *107*, 19-25.
197. G. Schukat; Le Van Hinh; E. Fanghaenel; L. Libera, *J. Prakt. Chem.*, **1978**, *320*, 404-412.
198. M. Iyoda; M. Hasegawa; J. Takano; K. Hara; Y. Kuwatani, *Chem. Lett.*, **2002**, *31*, 590-591.
199. F. Riobé; P. Grosshans; H. Sidorenkova; M. Geoffroy; N. Avarvari, *Chem. Eur. J.*, **2009**, *15*, 380-387.
200. M. Bryce; A. Green; A. Moore; D. Perepichka; A. Batsanov; J. K. Howard; I. Ledoux-Rak; M. Gonzalez; N. Martin; J. Segura; J. Garin; J. Orduna; R. Alcalá; B. Villacampa, *Eur. J. Org. Chem.*, **2001**, *2001*, 1927-1935.
201. A. S. Batsanov; M. R. Bryce; J. N. Heaton; A. J. Moore; P. J. Skabara; J. A. K. Howard; E. Orti; P. M. Viruela; R. Viruela, *J. Mater. Chem.*, **1995**, *5*, 1689-1696.
202. E. Pretsch, P. Bühlmann and C. Affolter. , *Structure determination of organic compounds : tables of spectral data*; Springer: Berlin ;; New York, 2000; , pp 421.
203. X. Shen; T. Moriuchi; T. Hirao, *Tetrahedron Lett.*, **2003**, *44*, 7711-7714.

204. Y. Wang; D. L. Frattarelli; A. Facchetti; E. Cariati; E. Tordin; R. Ugo; C. Zuccaccia; A. Macchioni; S. L. Wegener; C. L. Stern; M. A. Ratner; T. J. Marks, *J. Phys. Chem. C*, **2008**, *112*, 8005-8015.
205. T. C. Umland; S. Allie; T. Kuhlmann; P. Coppens, *J. Phys. Chem.*, **1988**, *92*, 6456-6460.
206. P. Guionneau; C. J. Kepert; G. Bravic; D. Chasseau; M. R. Truter; M. Kurmoo; P. Day, *Synth. Met.*, **1997**, *86*, 1973-1974.
207. P. Batail; K. Boubekeur; M. Fourmigué; J. P. Gabriel, *Chem. Mater.*, **1998**, *10*, 3005-3015.
208. A. Deluzet; S. Perruchas; H. Bengel; P. Batail; S. Molas; J. Fraxedas, *Adv. Funct. Mater.*, **2002**, *12*, 123-128.
209. T. Akutagawa; Y. Abe; Y. Nezu; T. Nakamura; M. Kataoka; A. Yamanaka; K. Inoue; T. Inabe; C. A. Christensen; J. Becher, *Inorg. Chem.*, **1998**, *37*, 2330-2331.
210. M. A. Beno; U. Geiser; K. L. Kostka; H. H. Wang; K. S. Webb; M. A. Firestone; K. D. Carlson; L. Nunez; M. H. Whangbo; J. M. Williams, *Inorg. Chem.*, **1987**, *26*, 1912-1920.
211. P. H. Svensson; L. Kloo, *Chem. Rev.*, **2003**, *103*, 1649-1684.
212. J. S. Chappell; A. N. Bloch; W. A. Bryden; M. Maxfield; T. O. Poehler; D. O. Cowan, *J. Am. Chem. Soc.*, **1981**, *103*, 2442-2443.
213. Y. Zhou; H. Wu; L. Qu; D. Zhang; D. Zhu, *J. Phys. Chem. B*, **2006**, *110*, 15676-15679.
214. J. B. Torrance; B. A. Scott; B. Welber; F. B. Kaufman; P. E. Seiden, *Phys. Rev. B*, **1979**, *19*, 730-741.
215. B. A. Scott; S. J. La Placa; J. B. Torrance; B. D. Silverman; B. Welber, *J. Am. Chem. Soc.*, **1977**, *99*, 6631-6639.

216. P. R. Ashton; V. Balzani; J. Becher; A. Credi; M. C. T. Fyfe; G. Mattersteig; S. Menzer; M. B. Nielsen; F. M. Raymo; J. F. Stoddart; M. Venturi; D. J. Williams, *J. Am. Chem. Soc.*, **1999**, *121*, 3951-3957.
217. M. T. Lemaire, *Pure Appl. Chem.*, **2004**, *76*, 277-293.
218. R. Hicks; R. Hicks, Eds.; , *Stable radicals :fundamentals and applied aspects of odd -electron compounds*; Wiley; Wiley: Chichester, West Sussex, U.K., **2010**; pp 588.
219. B. D. Koivisto; R. G. Hicks, *Coord. Chem. Rev.*, **2005**, *249*, 2612-2630.
220. K. E. Preuss, **2007**, 2357-2369.
221. A. J. Banister; I. May; J. M. Rawson; J. N. B. Smith, *J. Organomet. Chem.*, **1998**, *550*, 241.
222. E. Evangelio; D. Ruiz-Molina, *Eur. J. Inorg. Chem.*, **2005**, *2005*, 2957-2971.
223. F. E. Mabbs and D. J. Machin. , *Magnetism and transition metal complexes*; Dover Publications: Mineola, N.Y., 2008; , pp 206.
224. SHELXTL, PCV6.14, Siemens Analytical X-ray Instruments, Madison, WI, 1995.
225. G. M. Sheldrick, *Act. Cryst. Sec. A*, **1990**, *46*, 47, 73.
226. C. Rice; S. Onions; N. Vidal; J. Wallis; M. Senna; M. Pilkington; H. Stoeckli-Evans, *Eur. J. Inorg. Chem.*, **2002**, *2002*, 1889-1901.
227. J. Wang; S. Onions; M. Pilkington; H. Stoeckli-Evans; J. C. Halfpenny; J. D. Wallis, *Chem. Commun.*, **2007**, *2007*, 3628-3630.
228. A. J. Moore; M. R. Bryce, *Synthesis*, **1997**, *4*, 407-409.

Appendix A

Crystallographic tables

Table I Crystal data and structure refinement parameters for compounds **1.40**, **2.2** and **2.3**.

	1.40	2.2	2.3
Empirical formula	C ₂₂ H ₁₆ N ₆	C ₂₄ H ₁₈ N ₄ O ₂	C ₃₀ H ₃₄ N ₄ O ₆
Formula weight	364.41	394.42	546.61
Temperature	150 K	150(2) K	150(2) K
Wavelength	0.71073 Å	0.71073 Å	0.71073 Å
Crystal system, space group	Monoclinic, P21/c	Triclinic, P-1	Monoclinic, C2/c
Unit cell dimensions	a = 10.9614(6) Å α = 90° b = 20.1743(11) Å β = 101.490(3)° c = 8.7356(5) Å γ = 90°	a = 8.2616(5) Å α = 69.313(4)° b = 11.0442(7) Å β = 76.743(4)° c = 11.8712(7) Å γ = 71.691(4)°	a = 21.339(2) Å α = 90° b = 25.993(3) Å β = 123.198(4)° c = 12.4196(13) Å γ = 90°
Volume, density (calculated)	1893.06(18) Å ³ , 1.279 Mg/m ³	953.45(10) Å ³ , 1.374 Mg/m ³	5764.2(10) Å ³ , 1.260 Mg/m ³
Z	4	2	8
Absorption coefficient	0.080 mm ⁻¹	0.090 mm ⁻¹	0.089 mm ⁻¹
F(000)	760	412	2320
Crystal size	0.50 x 0.20 x 0.05 mm ³	0.20 x 0.12 x 0.07 mm	0.50 x 0.20 x 0.20 mm
Theta range for data collection	2.77 to 28.55°	1.85 to 28.38°	1.82 to 20.00°
Index ranges	-13 ≤ h ≤ 14, -11 ≤ l ≤ 11	-25 ≤ k ≤ 25, -10 ≤ h ≤ 11, -15 ≤ l ≤ 15	-14 ≤ k ≤ 14, -18 ≤ h ≤ 20, -11 ≤ l ≤ 11
Reflections collected / unique	29931 / 4286 [R(int) = 0.0466]	17671 / 4582 [R(int) = 0.0429]	17258 / 2673 [R(int) = 0.0435]
Completeness to theta	25.00°, 99.8 %	28.38°, 96.2 %	20.00°, 99.1 %
Absorption correction	Semi-empirical from equivalents	Semi-empirical from equivalents	Semi-empirical from equivalents
Max. and min. transmission	0.9960 and 0.9399	0.746 and 0.619	0.9825 and 0.9570
Refinement method	Full-matrix least-squares on F ²	Full-matrix least-squares on F ²	Full-matrix least-squares on F ²
Data / restraints / parameters	4286 / 0 / 253	4582 / 0 / 271	2673 / 0 / 367
Goodness-of-fit on F ²	1.098	1.376	1.180
Final R indices [I > 2σ(I)]	R ₁ = 0.0529, wR ₂ = 0.0994	R ₁ = 0.0518, wR ₂ = 0.1435	R ₁ = 0.0596, wR ₂ = 0.1645
R indices (all data)	R ₁ = 0.0869, wR ₂ = 0.1110	R ₁ = 0.0836, wR ₂ = 0.1585	R ₁ = 0.0703, wR ₂ = 0.1717
Largest diff. peak and hole	0.224 and -0.212 e.Å ⁻³	0.485 and -0.259 e.Å ⁻³	0.382 and -0.243 e.Å ⁻³

Table II Crystal data and structure refinement parameters for compounds **2.4** and **2.6**.

	2.4	2.6
Empirical formula	C ₂₁ H ₂₆ Cl ₄ N ₄ O ₃ Sn	C ₃₈ H ₄₀ Cl ₄ Mn ₂ N ₈ O ₄
Formula weight	642.95	924.46
Temperature	150(2) K	150(2) K
Wavelength	0.71073 Å	0.71073 Å
Crystal system	Monoclinic	Triclinic
Space group	P21/c	P-1
Unit cell dimensions	a = 8.3486(14) Å α = 90° b = 27.473(5) Å β = 93.665(4)° c = 11.3936(17) Å γ = 90°	a = 9.4410(5) Å α = 64.848(3)° b = 10.9557(6) Å β = 88.440(4)° c = 10.9598(6) Å γ = 72.810(3)°
Volume	2607.9(7) Å ³	973.92(9) Å ³
Z	4	2
Density (calculated)	1.638 Mg/m ³	1.576 Mg/m ³
Absorption coefficient	1.420 mm ⁻¹	0.976 mm ⁻¹
F(000)	1288	474
Crystal size	0.30 x 0.15 x 0.03 mm	0.30 x 0.15 x 0.05 mm
Theta range for data collection	1.48 to 28.36°	2.25 to 28.39°
Index ranges	-10 ≤ h ≤ 11, -14 ≤ l ≤ 6	-36 ≤ k ≤ 36, -12 ≤ h ≤ 12, -14 ≤ l ≤ 14
Reflections collected	15273	12488
Independent reflections	6104 [R(int) = 0.0421]	4811 [R(int) = 0.0299]
Completeness to theta	25.00°, 95.4 %	28.39°, 98.4 %
Absorption correction	Semi-empirical from equivalents	Semi-empirical from equivalents
Max. and min. transmission	0.9237 and 0.6172	0.746 and 0.603
Refinement method	Full-matrix least-squares on F ²	Full-matrix least-squares on F ²
Data / restraints / parameters	6104 / 7 / 298	4811 / 10 / 265
Goodness-of-fit on F ²	1.156	1.026
Final R indices [I > 2σ(I)]	R ₁ = 0.0533, wR ₂ = 0.1327	R ₁ = 0.0334, wR ₂ = 0.0784
R indices (all data)	R ₁ = 0.0731, wR ₂ = 0.1478	R ₁ = 0.0448, wR ₂ = 0.0846
Largest diff. peak and hole	1.775 and -0.990 e.Å ⁻³	0.428 and -0.405 e.Å ⁻³

Table III Crystal data and structure refinement parameters for compounds **2.7**, **2.8** and **2.11**.

	2.7	2.8	2.11
Empirical formula	C ₄₉ H ₄₂ Cl ₂ Cu ₂ N ₈ O ₁₅	C ₃₈ H ₃₂ ClFeN ₁₀ O ₂	C ₂₆ H ₁₉ FeN ₅ O ₃
Formula weight	1180.88	752.04	497.31
Temperature	150(2) K	150(2) K	150(2) K
Wavelength	0.71073 Å	0.71073 Å	0.71073 Å
Crystal system, space group	Orthorhombic, Pnna	Monoclinic, C2/c	Triclinic, P-1
Unit cell dimensions	a = 15.2508(10) Å α = 90° b = 23.2887(16) Å β = 90° c = 12.9853(8) Å γ = 90°	a = 13.163(3) Å α = 90° b = 19.772(5) Å β = 92.198(7)° c = 13.268(2) Å γ = 90°	a = 13.0767(8) Å α = 100.563(2)° b = 13.4441(8) Å β = 107.325(2)° c = 14.3843(8) Å γ = 98.963(3)°
Volume	4612.0(5) Å ³	3450.4(13) Å ³	2312.8(2) Å ³
Z	4	4	4
Density (calculated)	1.701 Mg/m ³	1.448 Mg/m ³	1.428 Mg/m ³
Absorption coefficient	1.123 mm ⁻¹	0.566 mm ⁻¹	0.688 mm ⁻¹
F(000)	2416	1556	1024
Crystal size	0.15 x 0.14 x 0.10 mm	0.38 x 0.05 x 0.01 mm	0.24 x 0.21 x 0.10 mm
Theta range for data collection	2.06 to 28.39°	2.06 to 28.41°	1.67 to 28.50°
Index ranges	-20 ≤ h ≤ 20, -31 ≤ k ≤ 30, 17 ≤ l ≤ 14	-- -16 ≤ h ≤ 17, -26 ≤ k ≤ 26, -7 ≤ l ≤ 17	-17 ≤ h ≤ 16, -19 ≤ k ≤ 17, -19 ≤ l ≤ 19
Reflections collected / unique	43292 / 5768 [R(int) = 0.0596]	10375 / 4219 [R(int) = 0.0470]	78503 / 11424 [R(int) = 0.0390]
Completeness to theta	28.39°, 99.6 %	28.41°, 97.3 %	28.50°, 97.5 %
Absorption correction	Semi-empirical from equivalents	Semi-empirical from equivalents	Semi-empirical from equivalents
Max. and min. transmission	0.746 and 0.676	0.746 and 0.649	0.9344 and 0.8522
Refinement method	Full-matrix least-squares on F ²	Full-matrix least-squares on F ²	Full-matrix least-squares on F ²
Data / restraints / parameters	5768 / 23 / 389	4219 / 0 / 238	11424 / 0 / 624
Goodness-of-fit on F ²	1.033	0.997	1.266
Final R indices [I > 2σ(I)]	R ₁ = 0.0399, wR ₂ = 0.0959	R ₁ = 0.0420, wR ₂ = 0.0898	R ₁ = 0.0719, wR ₂ = 0.1842
R indices (all data)	R ₁ = 0.0619, wR ₂ = 0.1077	R ₁ = 0.0745, wR ₂ = 0.1016	R ₁ = 0.0852, wR ₂ = 0.1990
Largest diff. peak and hole	0.859 and -0.753 e.Å ⁻³	0.425 and -0.373 e.Å ⁻³	1.266 and -0.837 e.Å ⁻³

Table IV Crystal data and structure refinement parameters for compounds **3.2** and **3.3**.

	3.2	3.3
Empirical formula	C ₁₂ H ₆ N ₂ S ₄	C ₁₂ H ₆ N ₂ S ₄
Formula weight	306.43	306.43
Temperature	220(2) K	298(2) K
Wavelength	0.71073 Å	0.71073 Å
Crystal system	Monoclinic	Orthorhombic
Space group	P2 ₁ /c	Pbca
Unit cell dimensions	a = 3.9321(5) Å α = 90° b = 11.3945(11) Å β = 91.376(7)° c = 27.653(3) Å γ = 90°	a = 7.7240(6) Å α = 90° b = 11.3417(9) Å β = 90° c = 28.465(2) Å γ = 90°
Volume	1238.6(2) Å ³	2493.6(3) Å ³
Z	4	8
Density (calculated)	1.643 Mg/m ³	1.632 Mg/m ³
Absorption coefficient	0.746 mm ⁻¹	0.741 mm ⁻¹
F(000)	624	1248
Crystal size	0.50 x 0.12 x 0.01 mm	0.40 x 0.10 x 0.10 mm
Theta range for data collection	1.93 to 22.49°	1.43 to 28.34°
Index ranges	-4 ≤ h ≤ 4, -29 ≤ l ≤ 29	-12 ≤ k ≤ 12, -10 ≤ h ≤ 10, -37 ≤ l ≤ 37
Reflections collected	13564	44122
Independent reflections	1613 [R(int) = 0.0753]	3087 [R(int) = 0.0426]
Completeness to theta	22.49°, 99.9 %	28.34°, 99.1 %
Absorption correction	Semi-empirical from equivalents	Semi-empirical from equivalents
Max. and min. transmission	0.9926 and 0.7068	0.9296 and 0.7560
Refinement method	Full-matrix least-squares on F ²	Full-matrix least-squares on F ²
Data / restraints / parameters	1613 / 119 / 164	3087 / 0 / 163
Goodness-of-fit on F ²	1.171	1.162
Final R indices [I > 2σ(I)]	R ₁ = 0.1433, wR ₂ = 0.3247	R ₁ = 0.0302, wR ₂ = 0.0840
R indices (all data)	R ₁ = 0.1542, wR ₂ = 0.3305	R ₁ = 0.0541, wR ₂ = 0.1053
Largest diff. peak and hole	1.202 and -0.891 e.Å ⁻³	0.305 and -0.294 e.Å ⁻³

Table V Crystal data and structure refinement parameters for compounds **3.4** and **3.5**.

	3.4	3.5
Empirical formula	C ₁₂ H ₆ N ₂ S ₄	C ₁₂ H ₆ N ₂ S ₄
Formula weight	306.43	306.43
Temperature	150(2) K	150(2) K
Wavelength	0.71073 Å	0.71073 Å
Crystal system	Monoclinic	Monoclinic
Space group	P21/c	P21/n
Unit cell dimensions	a = 13.9706(11) Å α = 90° b = 7.2149(5) Å β = 93.952(4)° c = 12.2020(9) Å γ = 90°	a = 7.0832(4) Å α = 90° b = 13.6308(8) Å β = 99.295(3)° c = 13.3145(8) Å γ = 90°
Volume	1226.99(16) Å ³	1268.63(13) Å ³
Z	4	4
Density (calculated)	1.659 Mg/m ³	1.604 Mg/m ³
Absorption coefficient	0.753 mm ⁻¹	0.728 mm ⁻¹
F(000)	624	624
Crystal size	0.40 x 0.15 x 0.02 mm	0.40 x 0.15 x 0.02 mm
Theta range for data collection	1.46 to 28.37°	2.15 to 28.39°
Index ranges	-18 ≤ h ≤ 18, -16 ≤ l ≤ 16	-9 ≤ k ≤ 9, -9 ≤ h ≤ 9, -17 ≤ l ≤ 17
Reflections collected	54583	24131
Independent reflections	3052 [R(int) = 0.0309]	3163 [R(int) = 0.0302]
Completeness to theta	28.37°, 99.5 %	28.39°, 99.4 %
Absorption correction	Semi-empirical from equivalents	Semi-empirical from equivalents
Max. and min. transmission	0.9851 and 0.7528	0.9856 and 0.7594
Refinement method	Full-matrix least-squares on F ²	Full-matrix least-squares on F ²
Data / restraints / parameters	3052 / 0 / 163	3163 / 0 / 163
Goodness-of-fit on F ²	1.231	1.056
Final R indices [I > 2σ(I)]	R ₁ = 0.0216, wR ₂ = 0.0654	R ₁ = 0.0277, wR ₂ = 0.0678
R indices (all data)	R ₁ = 0.0270, wR ₂ = 0.0811	R ₁ = 0.0401, wR ₂ = 0.0746
Largest diff. peak and hole	0.419 and -0.295 e.Å ⁻³	0.355 and -0.250 e.Å ⁻³

Table VI Crystal data and structure refinement parameters for compounds **3.8** and **3.15a**.

	3.8	3.15a
Empirical formula	C ₁₆ H ₁₀ N ₂ S ₄	C ₂₄ H ₁₂ I ₅ N ₄ S ₈
Formula weight	358.50	1247.44
Temperature	150(2) K	100(2) K
Wavelength	0.71073 Å	0.71073 Å
Crystal system	Monoclinic	Triclinic
Space group	P2 ₁ /n	P-1
Unit cell dimensions	a = 3.8842(2) Å α = 90° b = 32.8021(19) Å β = 94.539(3)° c = 11.4879(7) Å γ = 90°	a = 14.6149(19) Å α = 96.594(3)° b = 15.401(2) Å β = 111.003(4)° c = 15.993(2) Å γ = 91.459(3)°
Volume	1459.08(14) Å ³	3329.6(8) Å ³
Z	4	4
Density (calculated)	1.632 Mg/m ³	2.488 Mg/m ³
Absorption coefficient	0.646 mm ⁻¹	5.198 mm ⁻¹
F(000)	736	2308
Crystal size	0.40 x 0.10 x 0.10 mm	0.41 x 0.32 x 0.26 mm
Theta range for data collection	2.48 to 28.35°	1.33 to 28.35°
Index ranges	-5 ≤ h ≤ 5, -15 ≤ l ≤ 15	-43 ≤ k ≤ 43, -11 ≤ h ≤ 19, -21 ≤ l ≤ 14, -20 ≤ k ≤ 20,
Reflections collected	34231	34196
Independent reflections	3630 [R(int) = 0.0714]	15942 [R(int) = 0.0369]
Completeness to theta	28.35°, 99.6 %	28.35°, 95.8 %
Absorption correction	Semi-empirical from equivalents	Semi-empirical from equivalents
Max. and min. transmission	0.9382 and 0.7821	0.3457 and 0.2249
Refinement method	Full-matrix least-squares on F ²	Full-matrix least-squares on F ²
Data / restraints / parameters	3630 / 0 / 199	15942 / 7 / 831
Goodness-of-fit on F ²	1.089	1.119
Final R indices [I > 2σ(I)]	R ₁ = 0.0556, wR ₂ = 0.1436	R ₁ = 0.0696, wR ₂ = 0.1912
R indices (all data)	R ₁ = 0.0834, wR ₂ = 0.1578	R ₁ = 0.1020, wR ₂ = 0.2056
Largest diff. peak and hole	0.822 and -0.565 e.Å ⁻³	2.608 and -1.631 e.Å ⁻³

Table VII Crystal data and structure refinement parameters for compounds **3.16a** and **3.17a**.

	3.16a	3.17a
Empirical formula	C ₁₂ H ₆ I ₃ N ₂ S ₄	C ₁₆ H ₁₀ I ₆ N ₂ S ₄
Formula weight	687.17	1119.90
Temperature	273(2) K	150(2) K
Wavelength	0.71073 Å	0.71073 Å
Crystal system	Monoclinic	Triclinic
Space group	P2 ₁ /n	P-1
Unit cell dimensions	a = 12.1387(13) Å α = 90° b = 20.388(2) Å β = 110.823(6)° c = 15.2846(17) Å γ = 90°	a = 7.8720(9) Å α = 76.589(6)° b = 10.0650(12) Å β = 84.468(6)° c = 17.446(2) Å γ = 74.023(6)°
Volume	3535.6(6) Å ³	1291.9(3) Å ³
Z	8	2
Density (calculated)	2.582 Mg/m ³	2.879 Mg/m ³
Absorption coefficient	5.770 mm ⁻¹	7.545 mm ⁻¹
F(000)	2520	1004
Crystal size	0.15 x 0.14 x 0.12 mm	.1 x 0.05 x 0.05 mm
Theta range for data collection	2.05 to 28.79°	2.40 to 22.50°
Index ranges	-16 ≤ h ≤ 16, -20 ≤ l ≤ 20	-27 ≤ k ≤ 26, -8 ≤ h ≤ 8, -16 ≤ l ≤ 18, -10 ≤ k ≤ 10,
Reflections collected	89182	20007
Independent reflections	8945 [R(int) = 0.0436]	3341 [R(int) = 0.0395]
Completeness to theta	28.79°, 97.0 %	22.50°, 98.7 %
Absorption correction	Semi-empirical from equivalents	Semi-empirical from equivalents
Max. and min. transmission	0.5444 and 0.4782	0.7457 and 0.6079
Refinement method	Full-matrix least-squares on F ²	Full-matrix least-squares on F ²
Data / restraints / parameters	8945 / 0 / 379	3341 / 216 / 291
Goodness-of-fit on F ²	1.079	1.395
Final R indices [I > 2σ(I)]	R ₁ = 0.0255, wR ₂ = 0.0518	R ₁ = 0.0666, wR ₂ = 0.1222
R indices (all data)	R ₁ = 0.0357, wR ₂ = 0.0591	R ₁ = 0.0727, wR ₂ = 0.1244
Largest diff. peak and hole	2.894 and -1.499 e.Å ⁻³	1.343 and -0.988 e.Å ⁻³

Table VIII Crystal data and structure refinement parameters for compounds **3.21** and **3.22**.

	3.21	3.22
Empirical formula	C ₄₈ H ₃₀ F ₁₂ N ₆ P ₂ S ₁₂	C ₅₄ H ₃₆ F ₁₂ P ₂ S ₁₂
Formula weight	1365.56	1359.61
Temperature	150(2) K	150(2) K
Wavelength	0.71073 Å	0.71073 Å
Crystal system	Triclinic	Triclinic
Space group	P-1	P-1
Unit cell dimensions	a = 10.6521(7) Å α = 83.751(3)° b = 12.4482(9) Å β = 85.507(3)° c = 19.6789(14) Å γ = 83.910(3)°	a = 10.9719(5) Å α = 81.130(2)° b = 12.0742(5) Å β = 87.988(2)° c = 20.2586(9) Å γ = 87.364(2)°
Volume	2573.4(3) Å ³	2647.8(2) Å ³
Z	2	2
Density (calculated)	1.762 Mg/m ³	1.705 Mg/m ³
Absorption coefficient	0.661 mm ⁻¹	0.639 mm ⁻¹
F(000)	1380	1380
Crystal size	0.25 x 0.10 x 0.10 mm	0.40 x 0.10 x 0.02 mm
Theta range for data collection	2.04 to 30.38°	1.71 to 25.00°
Index ranges	-13 ≤ h ≤ 14, -28 ≤ l ≤ 26	-17 ≤ k ≤ 16, -12 ≤ h ≤ 13, -24 ≤ l ≤ 24
Reflections collected	45198	35516
Independent reflections	13118 [R(int) = 0.0818]	9100 [R(int) = 0.0856]
Completeness to theta	30.38°, 84.5 %	25.00°, 97.8 %
Absorption correction	Semi-empirical from equivalents	Semi-empirical from equivalents
Max. and min. transmission	0.9368 and 0.8521	0.9873 and 0.7840
Refinement method	Full-matrix least-squares on F ²	Full-matrix least-squares on F ²
Data / restraints / parameters	13118 / 0 / 721	9100 / 332 / 705
Goodness-of-fit on F ²	1.124	1.247
Final R indices [I > 2σ(I)]	R ₁ = 0.1228, wR ₂ = 0.1944	R ₁ = 0.1109, wR ₂ = 0.1658
R indices (all data)	R ₁ = 0.2012, wR ₂ = 0.2219	R ₁ = 0.1669, wR ₂ = 0.1853
Largest diff. peak and hole	0.896 and -0.628 e.Å ⁻³	1.108 and -0.817 e.Å ⁻³

Table IX Crystal data and structure refinement parameters for compounds **4.1** and **4.2**.

	4.1	4.2
Empirical formula	C ₂₆ H ₁₂ CoF ₁₂ N ₂ O ₄ S ₄	C ₂₆ H ₁₂ CuF ₁₂ N ₂ O ₄ S ₄
Formula weight	831.55	836.16
Temperature	150(2) K	150(2) K
Wavelength	0.71073 Å	0.71073 Å
Crystal system	Triclinic	Triclinic
Space group	P-1	P-1
Unit cell dimensions	a = 8.6880(5) Å α = 95.300(3)° b = 11.7019(6) Å β = 98.465(3)° c = 15.2395(8) Å γ = 90.555(3)°	a = 8.7591(6) Å α = 94.691(2)° b = 11.4671(7) Å β = 101.358(2)° c = 15.2353(9) Å γ = 91.988(2)°
Volume	1525.48(14) Å ³	1493.24(16) Å ³
Z	2	2
Density (calculated)	1.810 Mg/m ³	1.860 Mg/m ³
Absorption coefficient	0.948 mm ⁻¹	1.125 mm ⁻¹
F(000)	826	830
Crystal size	0.40 x 0.02 x 0.02 mm	0.40 x 0.20 x 0.01 mm
Theta range for data collection	2.37 to 28.44°	1.78 to 28.64°
Index ranges	-11 ≤ h ≤ 11, -20 ≤ l ≤ 20	-15 ≤ k ≤ 15, -11 ≤ h ≤ 11, -20 ≤ l ≤ 19
Reflections collected	63086	20782
Independent reflections	7530 [R(int) = 0.0565]	7181 [R(int) = 0.0407]
Completeness to theta	28.44°, 97.9 %	28.64°, 93.4 %
Absorption correction	Semi-empirical from equivalents	Semi-empirical from equivalents
Max. and min. transmission	0.9813 and 0.7029	0.9888 and 0.6617
Refinement method	Full-matrix least-squares on F ²	Full-matrix least-squares on F ²
Data / restraints / parameters	7530 / 0 / 442	7181 / 0 / 442
Goodness-of-fit on F ²	1.011	1.097
Final R indices [I > 2σ(I)]	R ₁ = 0.0370, wR ₂ = 0.0719	R ₁ = 0.0519, wR ₂ = 0.1048
R indices (all data)	R ₁ = 0.0758, wR ₂ = 0.0839	R ₁ = 0.0762, wR ₂ = 0.1143
Largest diff. peak and hole	0.375 and -0.355 e.Å ⁻³	0.523 and -0.631 e.Å ⁻³

Table X Crystal data and structure refinement parameters for compounds **4.3** and **4.4**.

	4.3	4.4
Empirical formula	C ₅₆ H ₁₂ F ₂₄ N ₆ Ni ₂ O ₈ S ₈	C ₂₆ H ₁₂ F ₁₂ N ₂ O ₄ S ₄ Zn
Formula weight	1726.66	837.99
Temperature	150(2) K	150(2) K
Wavelength	0.71073 Å	0.71073 Å
Crystal system	Triclinic	Monoclinic
Space group	P-1	P21/c
Unit cell dimensions	a = 12.1030(12) Å α = 107.877(3)° b = 15.3947(15) Å β = 103.963(3)° c = 19.584(2) Å γ = 95.546(4)°	a = 9.2555(5) Å α = 90° b = 17.1219(9) Å β = 100.922(2)° c = 19.7057(11) Å γ = 90°
Volume	3312.1(6) Å ³	3066.2(3) Å ³
Z	2	4
Density (calculated)	1.731 Mg/m ³	1.815 Mg/m ³
Absorption coefficient	0.946 mm ⁻¹	1.185 mm ⁻¹
F(000)	1708	1664
Crystal size	0.38 x 0.07 x 0.03 mm	0.20 x 0.06 x 0.05 mm
Theta range for data collection	1.76 to 28.63°	2.38 to 22.49°
Index ranges	-16 ≤ h ≤ 16, -25 ≤ l ≤ 26	-20 ≤ k ≤ 20, -9 ≤ h ≤ 9, -21 ≤ l ≤ 21
Reflections collected	62285	69150
Independent reflections	16046 [R(int) = 0.0474]	3996 [R(int) = 0.0690]
Completeness to theta	28.63°, 94.3 %	22.49°, 99.9 %
Absorption correction	Semi-empirical from equivalents	Semi-empirical from equivalents
Max. and min. transmission	0.9722 and 0.7151	0.9431 and 0.7975
Refinement method	Full-matrix least-squares on F ²	Full-matrix least-squares on F ²
Data / restraints / parameters	16046 / 2841 / 1134	3996 / 0 / 442
Goodness-of-fit on F ²	1.109	1.319
Final R indices [I > 2σ(I)]	R ₁ = 0.0938, wR ₂ = 0.2230	R ₁ = 0.0763, wR ₂ = 0.1746
R indices (all data)	R ₁ = 0.1230, wR ₂ = 0.2412	R ₁ = 0.0807, wR ₂ = 0.1769
Largest diff. peak and hole	3.428 and -0.949 e.Å ⁻³	1.024 and -0.499 e.Å ⁻³